Snapshot Hyperspectral Imaging:

Near-Infrared Image Replicating Imaging Spectrometer and Achromatisation of Wollaston Prisms

Gerald Wong

MPHYS MINSTP MIET

Thesis submitted for the degree;
Doctor of Engineering – EngD

Heriot-Watt University, City of Edinburgh
School of Engineering & Physical Sciences

MAY 2012

Abstract

Conventional hyperspectral imaging (HSI) techniques are time-sequential and rely on temporal scanning to capture hyperspectral images. This temporal constraint can limit the application of HSI to static scenes and platforms, where transient and dynamic events are not expected during data capture.

The **N**ear-**I**nfrared **I**mage **R**eplicating **I**maging **S**pectrometer (N-IRIS) sensor described in this thesis enables snapshot HSI in the short-wave infrared (SWIR), without the requirement for scanning and operates without rejection in polarised light. It operates in eight wavebands from 1.1μm to 1.7μm with a 2.0° diagonal field-of-view. N-IRIS produces spectral images directly, without the need for prior topographic or image reconstruction. Additional benefits include compactness, robustness, static operation, lower processing overheads, higher signal-to-noise ratio and higher optical throughput with respect to other HSI snapshot sensors generally.

This thesis covers the IRIS design process from theoretical concepts to quantitative modelling, culminating in the N-IRIS prototype designed for SWIR imaging. This effort formed the logical step in advancing from peer efforts, which focussed upon the visible wavelengths. After acceptance testing to verify optical parameters, empirical laboratory trials were carried out. This testing focussed on discriminating between common materials within a controlled environment as proof-of-concept. Significance tests were used to provide an initial test of N-IRIS capability in distinguishing materials with respect to using a conventional SWIR broadband sensor.

Motivated by the design and assembly of a cost-effective visible IRIS, an innovative solution was developed for the problem of chromatic variation in the splitting angle (CVSA) of Wollaston prisms. CVSA introduces spectral blurring of images. Analytical theory is presented and is illustrated with an example N-IRIS application where a six-fold reduction in dispersion is achieved for wavelengths in the region 400nm to 1.7μm, although the principle is applicable from ultraviolet to thermal-IR wavelengths. Experimental proof of concept is demonstrated and the spectral smearing of an achromatised N-IRIS is shown to be reduced by an order of magnitude. These achromatised prisms can provide benefits to areas beyond hyperspectral imaging, such as microscopy, laser pulse control and spectrometry.

Dedication of Thesis

This EngD thesis is dedicated to my wife, Anastasia, whose patience and support during difficult times is tremendously appreciated indeed. Her strength of character helped me to persevere and boost my motivation to succeed during the most challenging periods.

Acknowledgements

ACADEMIC REGISTRY
Research Thesis Submission

Name:	**GERALD WONG**		
School/PGI:	School of Engineering and Physical Sciences		
Version: (i.e. First, Resubmission, Final)	**First**	Degree Sought (Award and Subject area)	*EngD Engineering Doctorate* in Optics and Photonic Technologies

Declaration

In accordance with the appropriate regulations, I hereby submit my thesis and I declare that:

1) The thesis embodies the results of my own work and has been composed by myself
2) Where appropriate, I have made acknowledgement of the work of others and have referred to work carried out in collaboration with other persons
3) The thesis is the correct version of the thesis for submission and is the same version as any electronic versions submitted*.
4) My thesis for the award referred to, deposited in the Heriot-Watt University Library, should be made available for loan or photocopying and be available via the Institutional Repository, subject to such conditions as the Librarian may require
5) I understand that as a student of the University, I am required to abide by the Regulations of the University and to conform to its discipline.

* Please note that it is the responsibility of the candidate to ensure that the correct version of the thesis is submitted.

Signature of Candidate:		Date:	

Submission

Submitted By (name in capitals):	**GERALD WONG**
Signature of Individual Submitting:	
Date Submitted:	

For Completion in the Student Service Centre (SSC)

Received in the SSC by (in capitals):			
Method of Submission (Handed in to SSC; posted through internal/external mail):			
E-thesis Submitted (mandatory for final theses)			
Signature:		Date:	

Table of Contents

List of Tables

Glossary of Abbreviations

1D	One-dimensional
2D	Two-dimensional
3D	Three-dimensional
ACHRO-IRIS	Achromatised image replicating imaging spectrometer
ADU	Analogue to digital units
AOTF	Acousto-optic tuneable filter
AMD	Advanced Micro Devices Inc
ANOVA	Analysis of variance
ASTER	Advanced spaceborne thermal emission & reflection radiometer
AVIRIS	Airborne visible and infrared imaging spectrometer
CASSI	Coded aperture snapshot spectral imager
CCD	Charge-coupled device
CGH	Computer generated hologram
COTS	Commercial off-the-shelf
CTIS	Computed tomographic imaging spectrometer
CVSA	Chromatic variation in splitting angle
DD-CASSI	Double-dispersive coded aperture snapshot spectral imager
DFC	Fraunhofer spectral lines (589, 486 and 656 nm respectively)
DIS	Direct-imaging spectrometry
DoF	Degrees of freedom
EMS	Error mean squares
EngD	Engineering doctorate
EPICS	Exo-planet imaging camera and spectrograph
FHI	Flash hyperspectral imaging
FoV	Field-of-view
FPA	Focal plane array
FTIS	Fourier-transform imaging spectrometry
FWHM	Full-width half-maximum
GmbH	Gesellschaft mit beschränkter Haftung
GPU	Graphics processing unit
GSL	Ground spread length
GUI	Graphical user interface
HDPE	High-density polyethylene
HPU	Hyperspectral prototype unit
HSI	Hyperspectral imaging
I3A	International Imaging Industry Association
ICBM	Intercontinental ballistic missile
IRBM	Intermediate range ballistic missile
IED	Improvised explosive device
IFS	Integral field spectroscopy
IFU	Integral field unit
IR	Infrared (general)

IRIS	Image replicating imaging spectrometer
ISO	International Organization for Standardization
LCTF	Liquid crystal tuneable filter
LWIR	Long-wave infrared
MSSI	Miniature snapshot hyperspectral imager
MTF	Modulation transfer function
MWIR	Mid-wave infrared
NASA	National Aeronautics and Space Administration
NIR	Near infrared
N-IRIS	Near-infrared image replicating imaging spectrometer
NIST	National Institute of Standards and Technology
OPD	Optical path difference
OPO	Optical parametric oscillator
PSF	Point spread function
PSL	Pixel spread length
PSU	Power supply unit
PVC	Polyvinyl chloride
RGB	Red-green-blue
RMS	Root mean square
RX	Reed and Yu (developers)
SAR	Search and rescue
SD-CASSI	Single-dispersive coded aperture snapshot spectral imager
SLR	Single-lens reflex
SNR	Signal to noise ratio
SpA	Società per Azioni
SSE	Error sum of squares
SST	Sum of squares between treatments
SSY	Sum of squares
STC	Spectral transmission curve
STF	Spectral transmission function
SWIR	Short-wave infrared
TDP	Thermal design power
TMS	Treatment mean square
TV	Television
UAV	Unmanned air vehicle
UN	United Nations
US	United States
USB	Universal serial bus
USGS	United States Geological Survey
UV	Ultraviolet
VIS-IRIS	Visible image replicating imaging spectrometer
VNIR	Visible and near infrared
WS	Waterfall Solutions Ltd

Publications and Conferences

Gerald Wong, **Roger Pilkington** and **A R Harvey**, "Achromatization of Wollaston polarizing beam splitters" Optics Letters, volume **36:8**, pages 1332 – 1334 (April 2011)

Gerald Wong, **Andrew R Harvey** and **Roger Pilkington**, "Achromatic Wollaston Prisms for Snapshot Multispectral Imaging" *oral presentation*, IoP *Spectral Imaging* meeting, *Photonex-10* conference, Telford International Centre (November 2010)

Gerald Wong, **Andrew R Harvey**, **Roger Pilkington** and **Rick Rickman**, "Real-Time Hyperspectral Imaging in the SWIR Band" *oral slide presentation*, Institute of Physics *Photon-10* conference, University of Southampton (August 2010)

Gerald Wong, **AR Harvey**, **Roger Pilkington** and **Rick Rickman**, "Real-Time SWIR Hyperspectral Imaging with Polarimetric Capability" Proceedings of SPIE, volume **7812**, paper 781204 (August 2010)

Gerald Wong, "Low-Cost Snapshot Hyperspectral Imaging with the N-IRIS Sensor" *oral presentation*, *Fifth* Annual PGR Conference, Heriot-Watt University (June 2010)

Gerald Wong, **A R Harvey** and **Roger Pilkington**, "Snapshot Hyperspectral Imaging within the SWIR Waveband" *poster presentation*, First UK-HSI Conference, University of Strathclyde (April 2010)

Gerald Wong, "Hyperspectral Imaging" Nexus News: *Institute of Physics*, autumn 2nd edition, featured article **#4**, pages 27-30 (December 2009)

Gerald Wong, "Spectral Imaging with N-IRIS: Optical Design and Spiral Upgrades" *oral presentation*, EngD Annual Conference, Heriot-Watt University (August 2009)

Gerald Wong, "Anomaly Detection Rudiments for the Application of Hyperspectral Sensors in Aerospace Remote Sensing" Journal of Physics: *Conference Series*, volume **178**, paper 012051 (July 2009)

Gerald Wong, "Snapshot Hyperspectral Imaging and Practical Applications" Journal of Physics: *Conference Series*, volume **178**, paper 012048 (July 2009)

Gerald Wong, "Hyperspectral Imaging: Multi-Band IRIS Snapshot Imager" *oral slide presentation*, EngD Annual Conference, Heriot-Watt University (August 2008)

Gerald Wong, "IRIS Hyperspectral Imaging: Photonics EngD Research Project" *poster presentation*, EngD Annual Conference, Heriot-Watt University (August 2007)

Chapter 1:
Introduction and Motivation for Research

ABSTRACT – This chapter introduces hyperspectral imaging (HSI) and differentiates it from conventional panchromatic imaging, by highlighting the potential ability of HSI to discriminate between otherwise indistinguishable image elements through their spectral signatures. The phenomenology and background of two defence applications, landmine detection and low-light rescue operations, are considered as the motivation for research. Seven requirements for such HSI applications are explained as the main driver for the development of a SWIR snapshot hyperspectral imager. This chapter is concluded with a brief outline and summary of the remaining thesis structure.

1.1 Panchromatic and Hyperspectral Imaging

Traditional colour imaging generally involves the representation of a scene by using a reduced colour space, which is sufficient to meet the needs of human perception. This use of reduced colour spaces is motivated by the biological responses of the human eye, which responds in three visible wavebands. This limited spectral information can make certain image elements appear indistinguishable to the human eye, which does not reflect the underlying spectral diversity. This is a key problem in cases where spectral responses are as critical as spatial structure in discriminating between image elements. Motivating applications are discussed in the next section, but such an example could be detecting camouflaged military vehicles that are partially obscured by tree canopies.

Hyperspectral imaging (HSI) on the other hand, has an increased spectral resolution, which better reflects the dimensionality of spectra, rather than a limited subset of three or four colours [1]. The objective is increased spectral information with respect to traditional panchromatic imaging. This can solve the problem in discriminating image elements whose spectral response can be more significant than their spatial structure. HSI is often achieved by dispersive methods that resolve the spectral components of image elements while retaining spatial information. The main conventional techniques that are generally used for HSI are discussed in Chapter Two.

Space-based and high-attitude HSI is currently used within the geophysical community for environmental monitoring, agricultural surveys and locating natural resources. This is achieved through a time-sequential application of HSI, where hyperspectral images are recorded and transmitted for future processing.

Current spectral imagers are generally used in time-sequential HSI for remote sensing spectroscopy [2,3]. Such imagers involved raster scanning the surface of the Earth, followed by subsequent image assembly of the scanned areas. Contemporary HSI systems can involve up to several hundred wavebands, when compared with the early LandSat Thematic Mapper with seven wavebands. Figure 1-1 is an example of a generic method using raster scanning to generate the hypercubes, which are the counterparts of traditional panchromatic images that usually either use one or three colors.
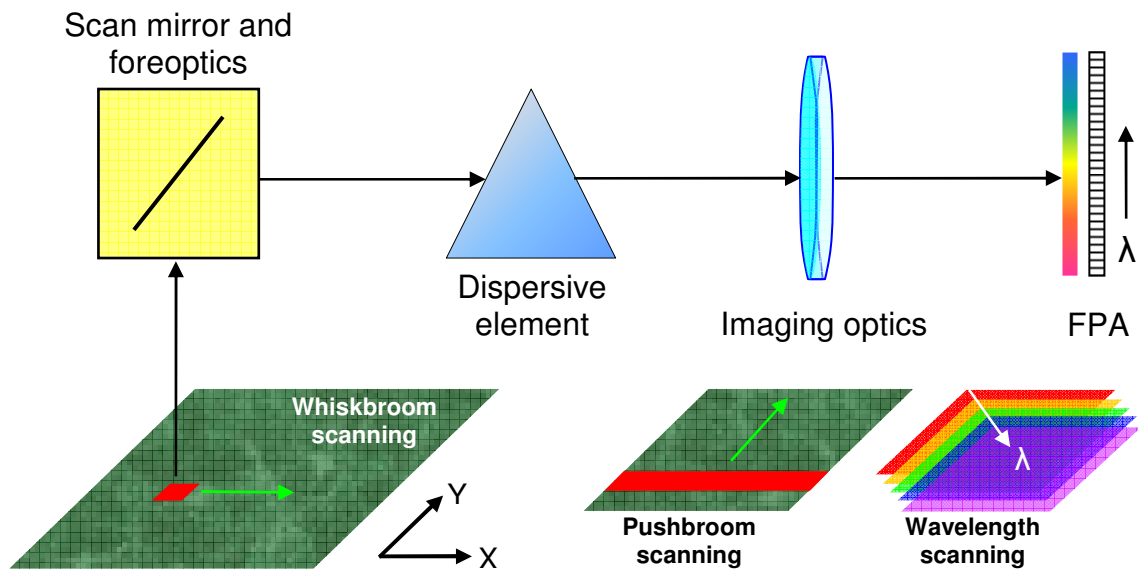
Figure 1-1: Diagram of a basic imaging spectrometer, using prism dispersion and raster scanning [2]

Each type of natural or synthetic terrain feature typically has a unique spectral signature, with a characteristic form and notable absorption bands that can allow discrimination and identification. Figure 1-2 highlights common examples of spectral signatures for vegetation, natural terrain and surface minerals. The ultimate goal of this project in the longer-term is anomaly detection, rather than only the positive identification or classification of materials. HSI anomaly detection involves highlighting those elements of a particular scene that appear to be spectrally alien to the global image. This type of spectral discrimination is usually set by an arbitrary user-defined metric or requirement dependent on the desired application.
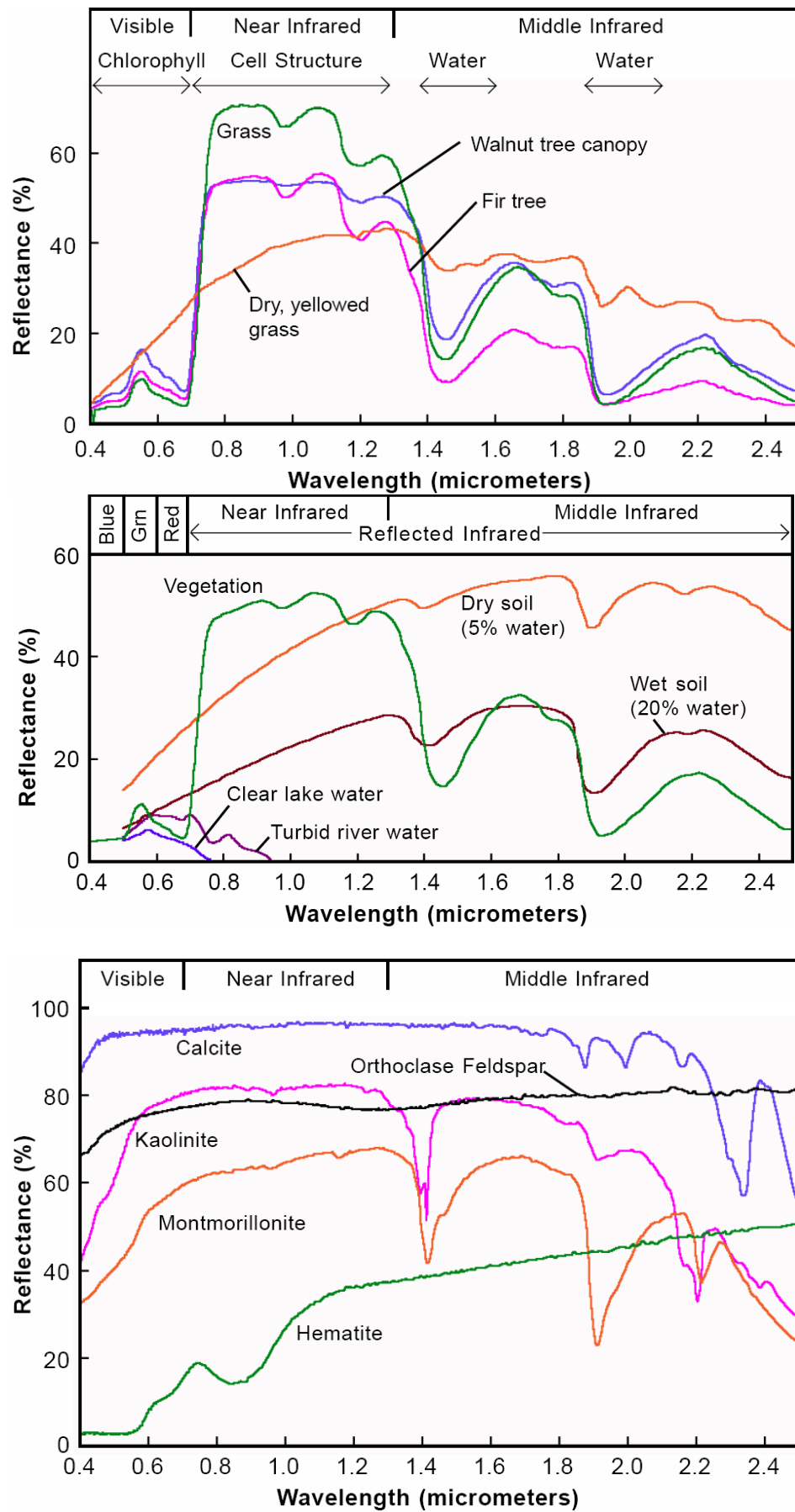
Figure 1-2: Reflectance spectra examples for common vegetation, natural terrain and surface minerals [2]

1.2 HSI Phenomenology for Defence Applications

1.2.1 Snapshot Landmine Detection

An opportunity exists for the development of snapshot HSI to airborne landmine detection, which could satisfy a requirement within NATO and Allied armed forces. The threat of landmines is the underlying motivation for this thesis, where the problem posed is that surface and buried devices may not exhibit sufficient contrast within panchromatic imagery for reliable detection with respect to their surroundings. This is a result of both the intentional design of these devices and the methods for emplacing them under soil or disguising their presence among environmental clutter.

The phenomenology of landmines and improvised explosive devices (IEDs) suggests that although panchromatic contrast can be very low, distinguishing IR spectral features exist and can be significant for detection purposes [4]. This empirical observation is applicable for landmines and IEDs by virtue of the spectral response of disturbed soil that is created during device emplacement [5]. The specific nature of these signatures or interpretation thereof was not available or accessible to the author at the time of writing.

Further published findings suggest that snapshot passive HSI offers the potential for landmine and IED detection, motivating the research in this thesis. Significant spectral differences exist between camouflaged targets and the background in the infrared region, for both desert environments and vegetation clutter [4]. Studies have also indicated that multispectral infrared sensors offer significant detection improvement over single panchromatic and narrow-band sensors [6].

The usage of landmines is a force-multiplier factor where the effectiveness of a combat operation is increased materially, without requiring significantly more personnel or resources [7]. The two central roles of minefields are to provide a tactical barrier near fortified positions and as an area-denial weapon to prevent free manoeuvre. Landmine removal during wartime is relatively straightforward, involving rapid and destructive mine clearance by combat engineers using armoured vehicles [8,9]. These dedicated brigades can however become a prime target for an enemy that exploits landmines as a key asset. An HSI system to identify landmines ahead of land formations could potentially be mounted upon unmanned air vehicles (UAV). This capability could assist in reducing the risk to combat engineers, by exposing them only when a positive

landmine threat has been identified. Two additional problems arising from landmines, involving unmarked minefields and asymmetric warfare will be commented upon as specific and defined opportunities for HSI applications.

Unmarked Minefields

Unmarked minefields pose a challenge, as they constitute a persisting threat to the local population [10]. Civilian causalities can be incurred by landmines even after the cessation of hostilities and facilitating economic redevelopment requires removal [11]. Demining methods in a civilian context is far more restrictive than military means, where only manual disarmament meets the UN (United Nations) ethical criteria for International Mine Action Standards [12]. Demining is a prerequisite for humanitarian operations and manually clearing one square kilometer of land can cost between \$2M and \$39M USD [13]. This is due to metal detection yielding typically 1×10^3 false positives for every mine, even assuming that low-metals mines are not present [14].

Deploying an HSI detector onto a low-altitude small UAV for civilian applications could potentially reduce the cost of demining. Manual minesweepers could be able to locate unmarked minefields from unaffected areas and hence concentrate their efforts on areas of the greatest threat to the civilian population. When manual minesweepers are unable to attend a given area, then at a minimum the minefield can be clearly defined and marked, thus preventing more loss of human life in the near-term.

Asymmetric Warfare

Landmines and IEDs pose a significant threat to friendly forces [7]. This threat can involve devices emplaced in unexpected positions, ahead of a friendly convoy or a footpath taken by a squad patrol. Prior knowledge may not be available on these opportunistic attacks and scouting may not be an appropriate solution. This scouting could invite attack upon the scouting party itself or signal the approach of a valuable target to a concealed enemy.

An HSI system mounted onto a UAV operating ahead of friendly forces could provide a useful tool for situational awareness. The key advantage is that skilled personnel do not require direct exposure to the threat itself in order to identify it. HSI could provide the potential for rapid detection of landmines using a low-observable aerial platform, thus preventing an enemy the opportunity to plan a direct assault.

1.2.1 Search and Rescue Operations

HSI can provide an enhancement to low-light Search and Rescue (SAR) operations, by negating the debilitating effects of thermal crossover in infrared imagery [15]. This occurs under certain environmental conditions such that the temperature, absorptivity, reflectivity, transmissivity, and emissivity differences between two adjacent surfaces or objects interact to cancel out the panchromatic thermal contrast between them. It causes a target and background to become indiscernible within panchromatic imagery.

Thermal crossover normally occurs on a diurnal cycle when conditions are such that there is a contrast loss between adjacent objects, as illustrated in Figure 1-3. This phenomenon is an interaction between weather effects and solar heating, which normally becomes apparent during the early morning and late afternoon. Dense clouds can reduce the contrast caused by solar heating, while strong winds equalise the surface temperature of objects towards that of the ambient air and henceforth each other. During calm conditions of intense sunlight without cloud cover, thermal crossover may only ideally persist for a few seconds at most. Unfavourable conditions of dense cloud, strong winds and heavy precipitation can extend this effect for several minutes.
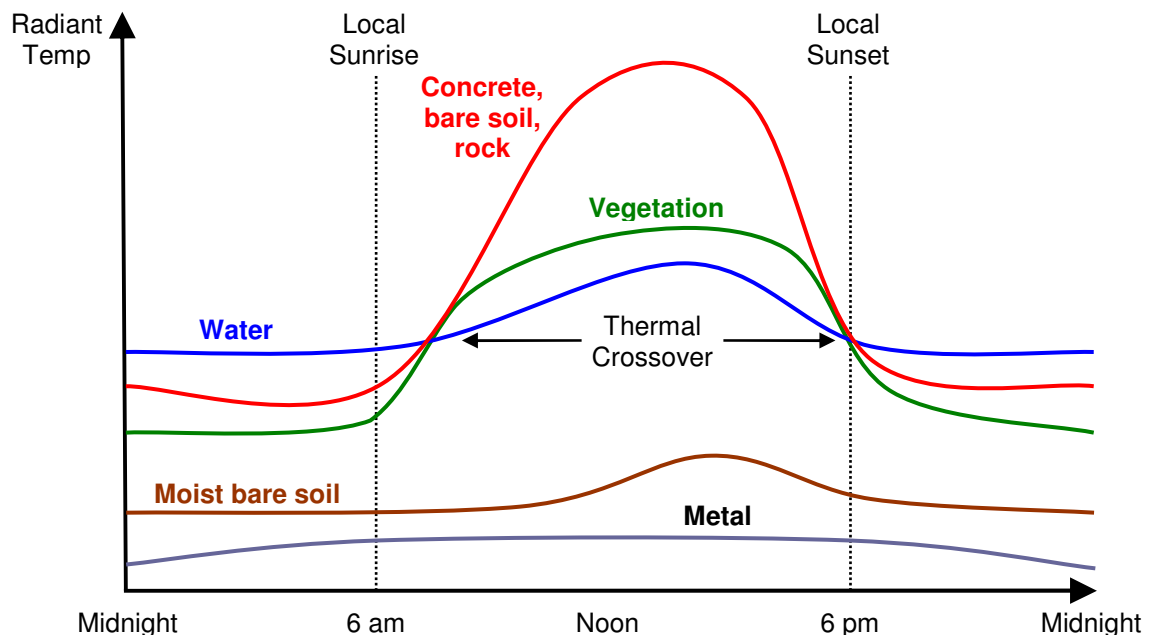
Figure 1-3: Generic diurnal radiant temperature cycles for selected materials – image adapted from [16]

Thermal crossover could effectively render a SAR operation as blind, especially in very low-light conditions when visual image intensifiers are not effective. During time-critical SAR operations, whether on the open seas or difficult terrain, thermal crossover

could potentially cause rescue aircraft to miss injured persons. An HSI sensor operating in even only two bands may reduce thermal crossover. Although a panchromatic imager may suffer from thermal crossover at any one particular time, there will be bands that still exhibit thermal contrast. Exploiting HSI to negate this debilitating effect for SAR operations could potentially enhance the ability of rescuers to locate injured persons.

Another defence-related application of significant interest but not discussed in this EngD (Engineering Doctorate) thesis is the detection of heavily camouflaged objects or targets exploiting active countermeasures for deception. There are known to be materials and techniques that actively reduce the thermal signatures of armoured vehicles by using thermal panels for instance. Military aircraft and intercontinental ballistic missiles (ICBMs) are also known to exploit lasers and flares respectively to deceive or disrupt an attacker.

1.3 Suggested Requirements for Applications

The following requirements from unpublished sources are suggested as pivotal for an HSI sensor to enable anomaly detection, for landmine detection and SAR operations. Actual detailed requirements are not made publicly available by defence and military bodies. They are suggested here to outline the motivation for this EngD project and highlight the potential benefits of N-IRIS for HSI anomaly detection over other sensors.

1) Passive and snapshot HSI without any spectral or spatial scanning

2) Operation beyond visual wavelengths into the IR spectrum with $1\mu m \leq \lambda \leq 2 \ \mu m$

3) Maximise transmission and signal-to-noise ratio (SNR) over the operation range

4) Compact size, low mass and power-efficient with respect to alternatives

5) Static operation without any moving parts or elements sensitive to vibration

6) Minimise processing overhead and resource requirements to extract hypercubes

7) Raw imagery to be interpretable by an operator at video rates

The first requirement prevents the sensor being detected through active illumination and to minimise the time exposed to danger or hostile detection. One major determinant of success in military operations is to detect an opponent before they detect the operator. The requirement reduces the possibility that an operator is detected by using active illumination or during the time interval needed to complete spectral or spatial scanning.

The second requirement recognises that low-light operation is important for military operations. Although SWIR is dependent on external illumination, it is an incremental improvement from daytime operation in the visible regime toward thermal operation at night. This is also aimed at reducing visual retro-reflection, should certain tasks require covert operation. Although retro-reflection is still applicable in the SWIR, it is often likely that more human opponents or visual cameras are present within an imaged scene than SWIR arrays and can perhaps be the most likely source of counter-detection.

The third requirement encourages optical efficiency and SNR to reduce the time needed to capture images, again to reduce opportunity for counter-detection by an opponent. It also indirectly promotes higher frame rates in situations where loitering is not an issue, thus enabling the time-domain to be exploited for dynamic and transient events. These first three requirements are likely the most important, given that detection by an opponent regardless of other characteristics can compromise the outcome of a mission.

The fourth requirement recognises that UAVs have payload limitations, which is important for UAV range and the time that can be spent within an area of interest. These are both key factors in maximising the potential benefit that an HSI sensor can provide. For reference, unclassified sensor payload limits for small tactical UAVs are typically 20kg with a maximum power supply of 100W, though medium UAVs are also known to accommodate sensors up to 45kg with a maximum power supply of 1kW [17,18].

The fifth requirement ensures that any sensors are reliable in terms of operating on a vibrating aircraft, while implicitly acknowledging the stringent safely rules and regulations on flight-qualified devices by aviation authorities. These fourth and fifth requirements are next in relative important, since the HSI sensor must be capable of actually being safely flown to an area of interest before it can start collecting imagery.

The sixth requirement is aimed to reduce associated infrastructure such as processing hardware, with respective payload and power needs that could otherwise negate the benefits of a sensor that satisfies all other requirements. This requirement acknowledges that limitations on data bandwidth and radio spectrum usage encourage that two-dimensional (2D) anomaly maps are preferable to hypercubes for transmission to a ground operator. Reducing processing needs will enable anomaly detection to be completed onboard the UAV and thus reduce the dimensionality of the data to be transmitted elsewhere.

The seventh requirement will enable an operator to recognise and interpret raw imagery streaming at video rates, independent of subsequent processing. This will allow timely decisions to be made on reported anomalies, potential false alarms and the interpretation of information within an image not readily apparent to algorithms. The human operator will be able to compare and contrast the raw imagery with the output from an anomaly detection algorithm. Aside from the numerous differing approaches taken by algorithm designers, the variability in the performance of algorithms is dependent on many factors. These include the selection of test imagery, processing capability and the choice of performance metrics. This requirement separates the optical characteristics of N-IRIS from the variable performance of classification and anomaly detection algorithms. The following section now describes the outline of the main content in this thesis.

1.4 Structure and Outline of Thesis

This EngD thesis describes research aiming to provide proof-of-concept for snapshot HSI in the SWIR region as a precursor to operating at longer wavelengths. It is desired that the Image-Replicating-Imaging-Spectrometer (IRIS) prototype described here can act as an initial step towards this long-term goal. This could allow IRIS to operate in synergy with algorithms developed for anomaly detection, along with those emerging applications not covered in this thesis in the industrial and agricultural sectors [19].

As an adjunct, the achromatisation of Wollaston prisms as a component of IRIS for polarizing beamsplitting is also described later in this thesis. This novel development significantly improves upon the chromatic variation in splitting angle (CVSA), which is a significant degrading factor in image quality. Achromatic Wollaston prisms can also provide benefits for areas beyond HSI such as laser applications, microscopy and interferometry.

The context and motivation for this EngD research was outlined in this chapter, in terms of enabling the optical detection of camouflaged and hidden threats that would otherwise not be detected by panchromatic imagers. An adjunct is the potential for the negation or reduction of thermal crossover in infrared imagery, which can degrade image contrast for critical tasks such as search and rescue. A brief outline of the informal key requirements for an effective HSI sensor indicates that IRIS could provide a useful capability for the potential applications envisaged.

The concept and theory of IRIS is described in Chapter Two. The alternative approaches to snapshot HSI are also considered, along with their respective advantages and disadvantages. For completeness, a brief consideration of traditional non-snapshot HSI techniques is included, such as spectral filter wheels and narrow-band adaptive filters.

The engineering design and optical modelling from first principles is detailed in Chapter Three, including the selection of wavebands and birefringent materials. Lens aberration is considered ahead of assembling the first infrared IRIS prototype, which is followed by basic optical testing to demonstrate proof-of-concept. This prototype was then upgraded with bespoke lenses and the improvement was verified by basic testing of the modulation transfer function.

Basic studies into fundamental experiments and testing is detailed in Chapter Four, including simulated spectral responses for generic materials and significance testing with example materials. A collaborative joint project into video-rate anomaly detection using streaming N-IRIS imagery is also described [20,21].

The development of a visible IRIS sensor from low-cost components to accompany the SWIR prototype is outlined in Chapter Five, which was originally a cost-efficiency exercise. CVSA emerged as a major degrading factor in image quality, even more so than with the SWIR prototype, which provided the motivation to research a solution for CVSA. This chapter then describes the invention and development of achromatic Wollaston prisms [22,23]. Chapter Six concludes the thesis by summarising the key developments and considering future research, along with opportunities to exploit the IRIS sensor in emerging applications.

> CONCLUSION – This chapter introduced the background behind HSI and its advantage over traditional panchromatic imaging, in terms of spectral discrimination between otherwise indistinguishable elements. Snapshot landmine detection and low-light rescue were considered as motivating applications for HSI, due to the phenomenology behind their respective issues. Seven requirements were discussed as pivotal for an HSI sensor to enable anomaly detection for the given applications. A brief outline and summary of the remaining thesis structure was then described.

Chapter 2:
IRIS in Context of Snapshot Methods

ABSTRACT – This chapter considers the prevalent techniques and methods for snapshot HSI, beginning with an outline of time-sequential methods for completeness. Spectral multiplexing techniques with inversion are considered, followed by spatial multiplexing techniques. The advantages and drawbacks of each such method are discussed, before reaching the conclusion that the *Image-Replicating-Imaging-Spectrometer* is optimal in meeting the application requirements of the preceding chapter. The EngD research to be described in this thesis is placed within context with respect to previous developments.

2.1 Traditional Time-Sequential Techniques

Traditional HSI techniques require time-sequential scanning across the spectral or spatial dimensions [24,25,26,27]. This introduces time-dependence to the collection of two spatial and one spectral dimension. Only snapshot HSI for the applications outlined in Chapter One is of interest given the goal of capturing transient and dynamic events, but traditional techniques will nonetheless be briefly considered here for completeness. For the present discussion, conventional methods can be divided into four categories:

1) Dispersive spectrometers – prisms and grating elements
2) Adaptive filters – liquid crystal and acousto-optical
3) Fourier transform interferometers – Sagnac and Michelson
4) Sequential mechanical methods – rotating filter wheels

Dispersive spectrometers are prevalent and involve pushbroom scanning in one spatial dimension, which is usually the direction of platform travel. Spectral dispersion is achieved through using either gratings or prisms. An objective focuses an image onto a slit, followed by collimation through the dispersive element, with final condensing onto a detector array. Prisms generally exhibit low scatter and uniform high efficiency, while grating-based systems are optically simpler in design. A number of innovative designs beyond the generic layout described have emerged over recent years, but all still require dispersive prisms or gratings along with the necessary scanning involved [28].

Tuneable filters for HSI systems offer the advantage of narrow wavebands and fast random access of spectral bins, but require time-sequential scanning. The two prevalent filtering techniques are liquid crystal and acousto-optical tuneable filters, also known as

LCTF and AOTF respectively. LCTF systems are based upon the Lyot filter, with liquid crystals providing the variable retardance. It is also possible to stack them sequentially to achieve higher spectral resolution, although individual transmissions are relatively low at approximately 40%. The basis of AOTF systems is that a sound wave applied to a suitable crystal creates a density pattern within that material. Only certain wavelengths are diffracted to the detector array by this density pattern. Tuneable Fabry-Perot etalons, circular and linear variable filters are other less common techniques.

Although Michelson interferometry has been employed for over a hundred years, the use of Fourier-imaging techniques has only been enabled relatively recently. Sagnac and Michelson imagers coupled to fast Fourier-transform algorithms have now become widespread in spectral imaging. The key principle is that incoming radiation is subject to beam splitting and then recombined, after a controlled path difference has been introduced. Sagnac imagers require spatial scanning in one dimension, while Michelson systems involve scanning across the spectrum of interest. The trade-off is that Sagnac systems can be robustly compact, while Michelson systems can yield higher resolution at the cost of vulnerable moving parts. Both techniques are limited to a maximum transmission of 50%, whereas the other techniques mentioned here can achieve typical efficiencies of 80% to 90% with the exception of LCTFs.

The use of mechanical filter wheels is a low-cost technique for HSI. Such systems employ several wavebands, each of could be relatively broad and may be discontinuous in spectral distribution. The rotating wheel sequentially filters the flux reaching an imager, thus dividing the spectral response into various bands, which are specifically chosen for the particular task. This fixed nature of the temporal scanning coupled with mechanical concerns with reliability or vibration entails limited flexibility when attempting to capture transient or dynamic events.

2.2 Spectral Multiplexing with Inversion

2.2.1 Computed Tomography Imaging Spectrometer

The Computed Tomography Imaging Spectrometer (CTIS) provides snapshot HSI and uses a 2D dispersive grating in the pupil [29,30]. Figure 2-4 illustrates the key CTIS components. The 2D dispersive grating is a computer-generated hologram (CGH) that replicates images and simultaneously disperses them [31]. These images are incident on a focal plane array (FPA) and collected for reconstruction by tomographic algorithms. Such reconstruction is necessary due to the radial dispersion of images as depicted in Figure 2-5. The central zeroth order is a spectrally unaltered image, which serves as the focus reference [32].

The CTIS system is being developed for ophthalmology at the time of writing, but has been considered previously for astronomy and geology [32]. It is envisaged that CTIS will enable functional rather than structural mapping to diagnose sight-threatening conditions. This is achieved by creating oxygen saturation maps of the retina, in order to locate diseased or damaged areas for medical treatment.

Although no journal publications on CTIS research into anomaly detection have been found, it is known that continued military research is being conducted into its development for ballistic missile defence. This research has focussed on SWIR and UV (ultraviolet) plume detection of intermediate-range ballistic missiles (IRBM), along with mid-wave infrared (MWIR) detection of CO_2 combustion products [33,34,35].

The advantage of CTIS is that aside from the single custom component of the 2D-CGH, only two lenses are required with a camera. The central zeroth order and paraxial arrangement make the alignment, focusing and image cueing of CTIS possible by eye alone. There are however two problems with the use of CTIS, which can be challenging for any potential application for real-time anomaly detection. The precise details of these issues have not been made publicly available by the CTIS researchers, but other publications provide some useful detail as to their nature and possible impact on HSI.
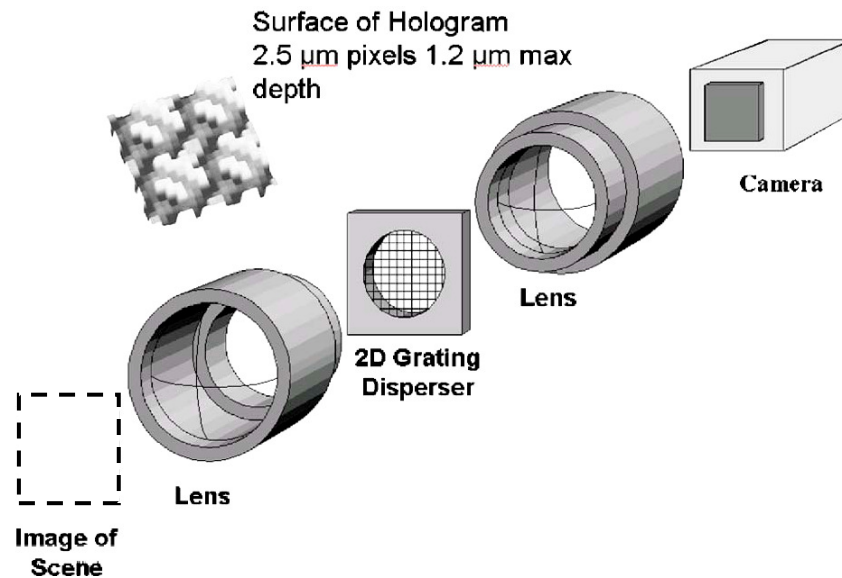
Figure 2-4: Schematic illustration of the CTIS system, where diffractive grating disperses the collimated input image in two dimensions, followed by a second lens re-imaging the pattern onto the focal plane – image reproduced from reference [32].
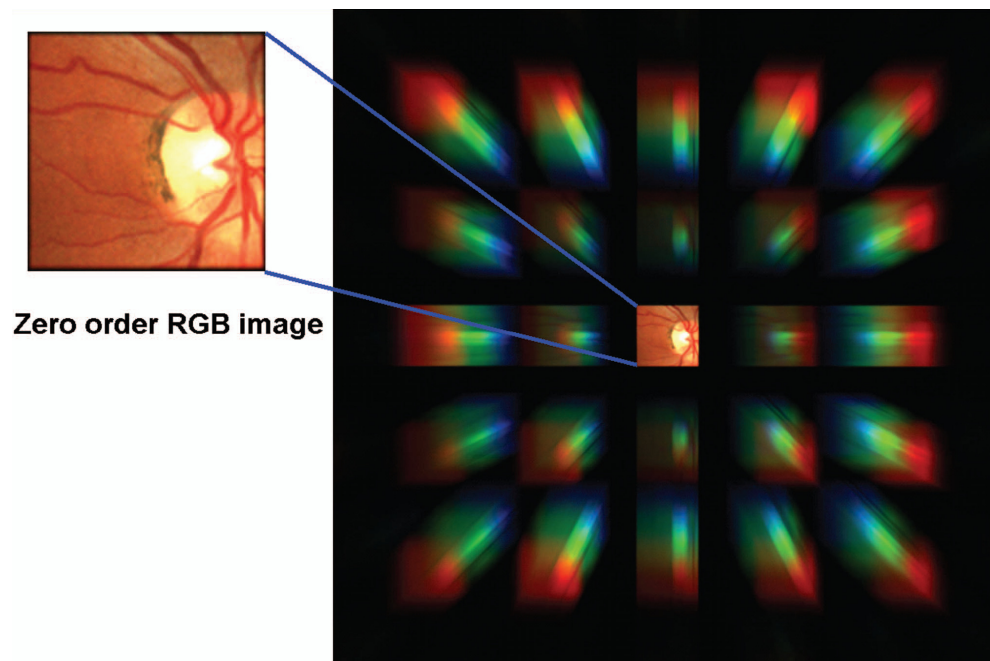
Figure 2-5: Colour CTIS diffraction pattern formed by an image of an optic disk and the surrounding vascular structure – note the intense radial dispersion. Image reproduced from reference [32].

The first difficulty is stated as a lack of sensitivity, likely due to the low intensities incident on each pixel, which would limit the resolution of sub-pixel targets such as landmines, without operating at extremely low altitudes [36]. The second problem is the computational overhead required for the reconstruction of dispersed images, even before anomaly detection algorithms are applied. A single iteration of a reconstruction algorithm employed six minutes of continuous processing on a 1.0 GHz Pentium-3 core,

while eight such iterative passes where required for the published results [37]. Such intense processing demands could render CTIS as only suitable for flash hyperspectral imaging (FHI), where processing lag could produce a pipelining output unless high-performance computing is available in-situ, such as multi-threading on parallel GPUs (graphics processing unit).

An excerpt reproduced in verbatim from United States Patent 7092088 for an imaging spectrometer is most concise in describing further inherent difficulties with CTIS:

> *"While the CTIS solved the problem of providing imagery in many spectral bands, it had several limitations. First, it demonstrated inefficient use of the focal plane, providing images in small numbers of pixels. A 1024×1024 pixel focal plane yielded only an 80×80 pixel image in 108 colour bands. Second, the CTIS had poor signal to noise ratio (SNR) caused by the design which required all diffraction orders to not overlap thus presenting low intensity to each pixel. Third, it had high instrument self-radiance caused by the CTIS design that employed an intermediate focal plane with collimation stage. Furthermore, the CTIS showed very poor performance in the infrared spectrum, and the mechanical layout resulted in a device that was too large for many applications. Plus, the technology could not be retrofit into existing sensor packages."* [38]

CTIS is likely not suitable for airborne applications requiring snapshot HSI, where power and payload restrictions limit the availability of processing. From the few published hardware details in 2001, it was not accurately possible to determine how many such GPUs would be needed to decrease the single frame rate from 48 min to 40 ms. This requires a 7.2×10^4 factor reduction in processing time to achieve the 25 Hz frame rate requirement. An order-of-magnitude estimate using "Moore's Law" suggests that as of 2011, at least 2,250 GPUs may be required for this.

As an example of power and cooling requirements, one leading GPU processor at the time of writing is the AMD (*Advanced Micro Devices Inc*) Radeon HD-6990, which requires a 1.2 kW power supply and has an upper thermal design point of 450 W (average output under load). Given the large power and cooling needs to support the required processing, it would significantly negate the CTIS advantages of snapshot capability and high optical efficiency. Given these considerations, it suggests CTIS may only be optimal for emplaced HSI in a static ground station, which can support the required processing requirements.

2.2.2 Coded Aperture Snapshot Spectral Imager

A team led by David L Brady from Duke University has developed the Coded Aperture Snapshot Spectral Imager known as CASSI, which captures a compressed 2D projection of the three-dimensional (3D) hypercube. This spectral compression exploits a coded aperture and dispersive elements to measure fewer voxels than is within the final reconstructed hypercube [39,40,41]. The main assumption is that natural remote scenes are sparse on some multiscale basis and hence compressible. This compression relies upon multiplexing that is controlled using the coded aperture and one or two sets of dispersive elements.

Two variants of this HSI sensor exist and include the SD-CASSI and DD-CASSI, which denote Single-Dispersive and Dual-Dispersive modes respectively. The difference is that the latter uses two sets of dispersive elements, with the second set cancelling out dispersion introduced by the first. SD-CASSI effectively trades-off easier alignment and fewer optical elements for more spatial multiplexing and challenging processing requirements. The SD-CASSI prototype gives a hypercube resolution of 128^2 spatial pixels in 28 passbands and operates from 540nm to 620nm, while the corresponding parameters for DD-CASSI are similar. Figure 2-6 are the respective schematics for SD-CASSI and DD-CASSI, while Figure 2-7 shows the corresponding sensing processes.
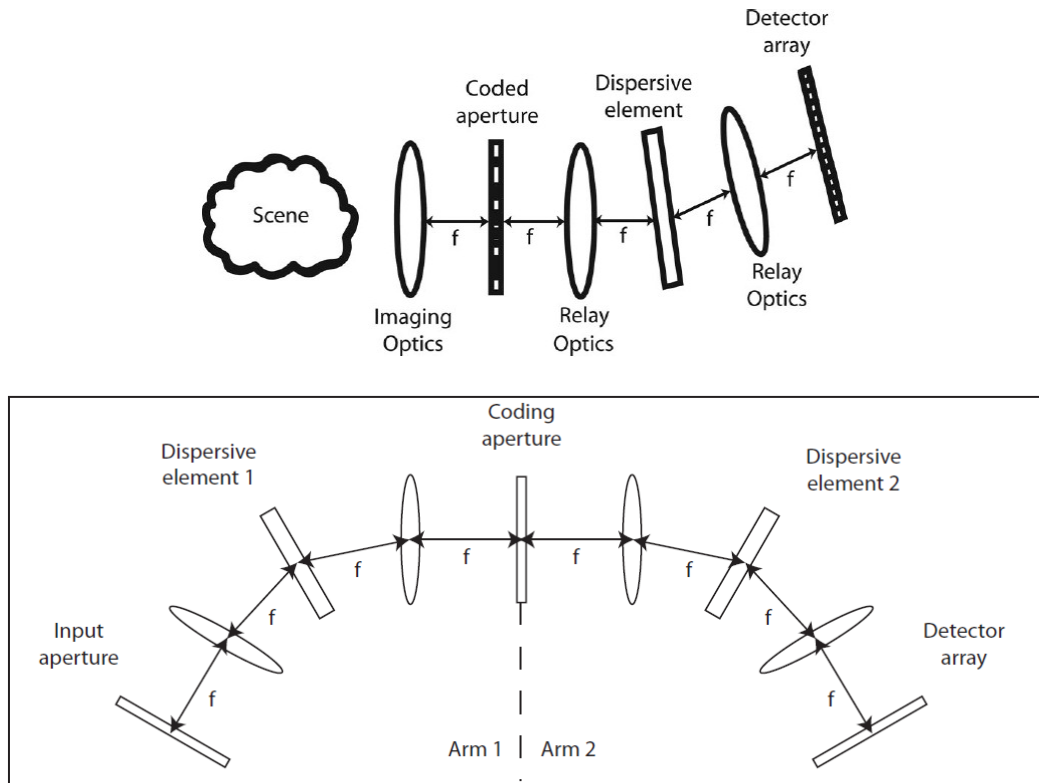
Figure 2-6: Schematics of SD-CASSI and DD-CASSI respectively – images from reference [39,40]
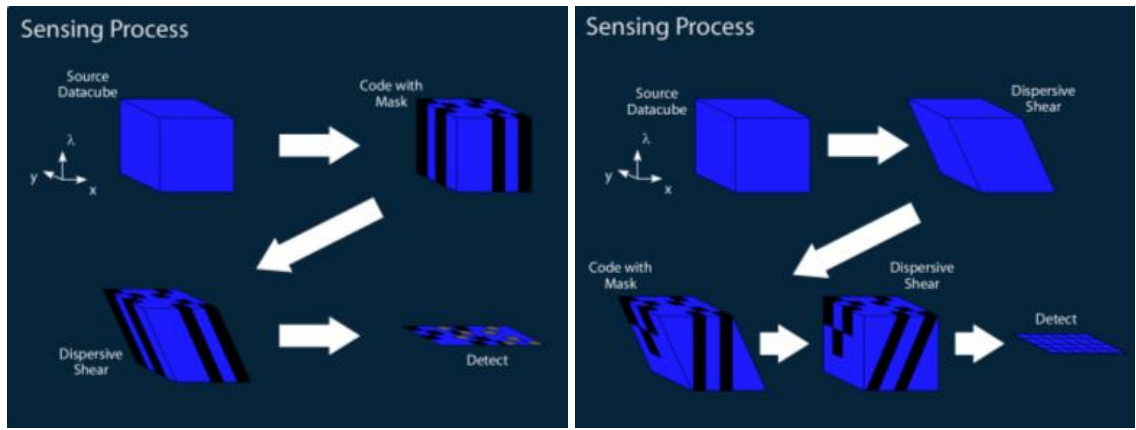
Figure 2-7: Sensing process for SD-CASSI and DD-CASSI respectively – images from reference [41]
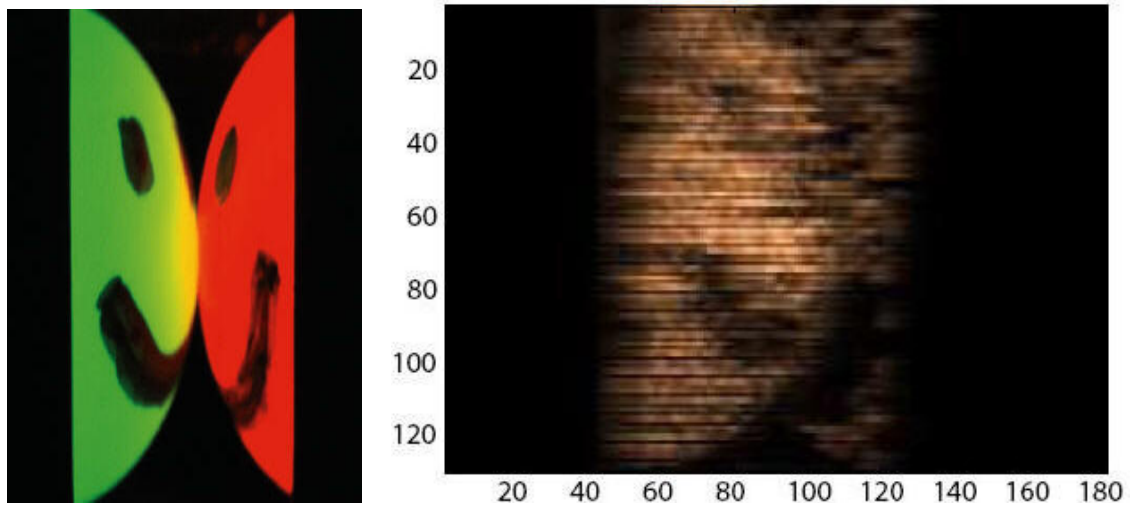
Figure 2-8: Example of two illuminated balls captured by SD-CASSI as viewed on the detector array. There is spatial-spectral overlap of the aperture code-modulated images of each ping-pong ball. Images reproduced from reference [40].

Although offering snapshot imaging as shown in Figure 2-8, some shortcomings are present that reduce the efficacy of CASSI. The authors state that it is impossible for DD-CASSI to reconstruct the spectra of point sources, since only spectral data is multiplexed by the sensor. It is additionally difficult but not impossible for SD-CASSI to achieve this feat, dependent upon the coded input aperture. The snapshot benefits of both sensors are mitigated by the processing time needed for hypercube recovery, with SD-CASSI requiring fourteen minutes of reconstruction on an undisclosed computer of "desktop" standard in 2008 [40]. This yielded only an estimate of the hypercube, which itself was down-sampled spatially by a factor of two, in order to reduce the time required for this initial reconstruction. The reconstructed image shown in Figure 2-9 of a controlled and optimised scene is of also low optical quality.
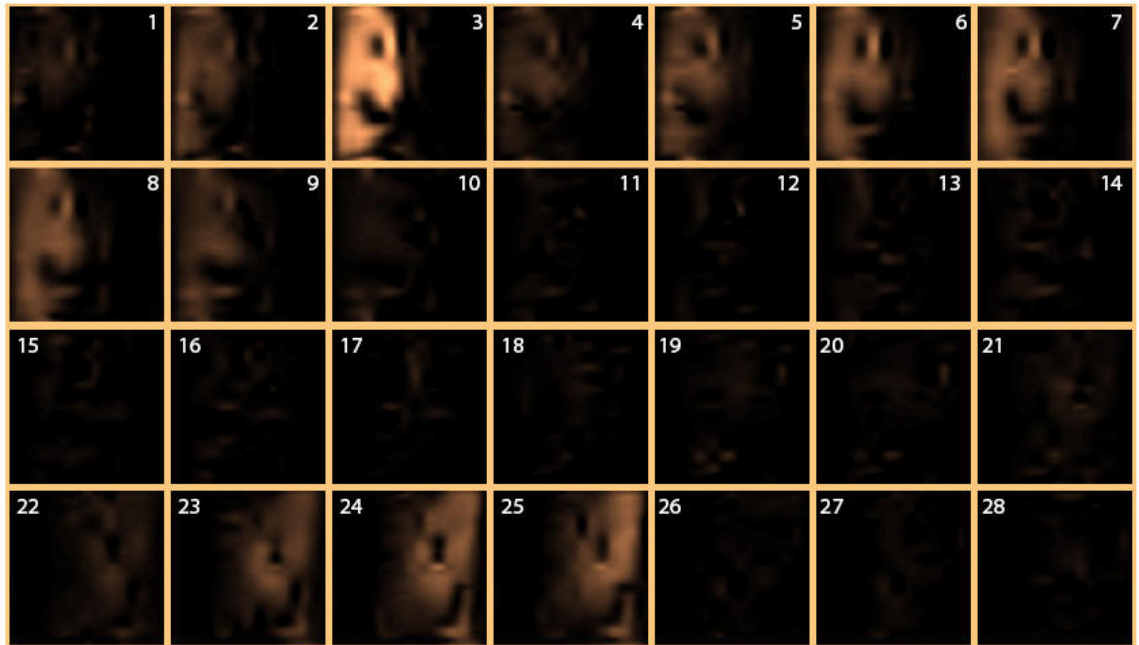
Figure 2-9: Twenty-eight reconstructed spectral channels between 540 nm and 640 nm of the illuminated high-spectral contrast balls with dark background in Figure 2-7 – image reproduced from reference **[40].**

CASSI is likely not suitable for airborne applications requiring snapshot HSI, where power and payload restrictions limit the availability of processing. Limited published information on the hardware used only allows an estimate of the GPUs required to reduce processing by a factor of 2×10^5 to achieve 25 Hz frame rates. Approximately 8×10^4 current GPUs would be required with the pre-requisite power draw and cooling requirements of a 1.2 kW PSU (power supply unit) and 450 Max-TDP (thermal design power) respectively. It suggests that CASSI (like CTIS) may only be optimal for emplaced HSI in a static ground station, which can support the required processing on-site with high-performance computing.

2.3 Spatial Multiplexing Techniques

2.3.1 Integral Field Spectroscopy

HSI image slicing is used for astrophysical imaging, where the technique is also known as Integral Field Spectroscopy (IFS) [42]. The image slicer is also known as an Integral Field Unit (IFU) and is placed in the focal plane of a telescope, where the IFU couples the image to a spectrograph. Using an array of slit mirrors with varying curvatures, tilts and decentres, the 2D image is optically reformatted into a contiguous one-dimensional (1D) array. This array is located at the entrance focal plane of the spectrograph, where typically further rows of pupil mirrors direct the pseudo-slit onto the spectrograph. The spectrograph then returns the spectral information across the long-dimension of each part of the pseudo-slit, which can then be reconstructed into a regular hypercube. The key advantage of this technique is high optical throughput and the spectral resolution of typically up to 256 wavebands as achieved in the SWIR by EPICS (Exo-Planet Imaging Camera and Spectrograph) [42].
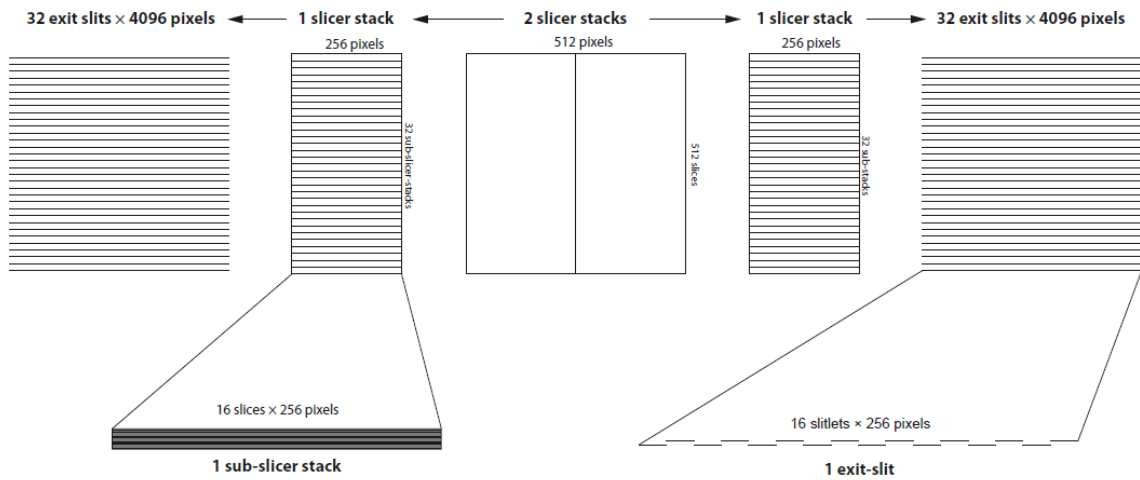
Figure 2-10: Concept schematic of an example IFU in a two-arm arrangement using two slicer stacks, with each comprising 32 sub-slicers with 16 slices each to cover an overall field of 512^2 spatial pixels – image reproduced from reference [42].

The main trade-off with this snapshot technique is the resolution lost in the direction of the slicing. For an IFU using N slicing mirrors, the resultant hypercube has an upper resolution of $N \times Y \times \lambda$, where N, Y and λ are the spatial and spectral resolutions of the spectrograph respectively. Current image slicers provide a resolution in the slicing dimension of 512 spatial elements, but two contiguous slicer stacks are required [42]. This could create potential issues with the complexity of modelling, fabrication cost and

the alignment of both the image slicer and associated optics. The overall system can be prohibitive in terms of its compactness, requiring more volume than other techniques to accommodate the reflection of beams – similar to a Cassegrain reflector in reverse [42].

Another issue is the high F-number of the sliced beam at the micro-mirrors and the relatively low étendue. The spectrograph that disperses the contiguous 1D array into typically 256 bands presents a relatively low intensity to each individual FPA pixel. These factors may combine to generate the requirement for a lengthy integration time at the FPA to overcome detector and shot noise.

Published details are either limited or pertain to stellar phenomena, so it is not known if IFS can generate useful imagery at 25 Hz. The IFS method also requires an FPA with significant resolution in the SWIR region, where for example, the EPICS system required a 16.8 megapixel array for 512^2 spatial pixels in the returned hypercube [42]. Current SWIR arrays are limited to 330k pixels for commercial off-the-shelf (COTS) cameras (640×512 pixels), while the large-format FPA used for EPICS is subject to US (United States) export restrictions with no analogous European source. Along with the undisclosed but anticipated extremely high FPA cost, this legal restriction on security grounds makes the pursuit of IFS for SWIR snapshot HSI prohibitively cumbersome.

2.3.2 Miniature Snapshot Multispectral Imager

The miniature snapshot multispectral imager (MSSI) is based on a monolithic SWIR filter array with 16 elements mounted near the surface of an InGaAs detector array [43]. Using a commercial SWIR camera, the condenser lens is substituted with a telecentric microlens array to multiplex the imaged scene into sixteen channels. These channels are then spectrally filtered by this monolithic array, composed of Fabry-Pérot etalons with two multilayer dielectric mirrors. Figure 2-11 is an illustration of the MSSI system and Figure 2-12 is the measured spectral transmission of the sixteen spectral channels. This technique postdates the research described in this thesis.
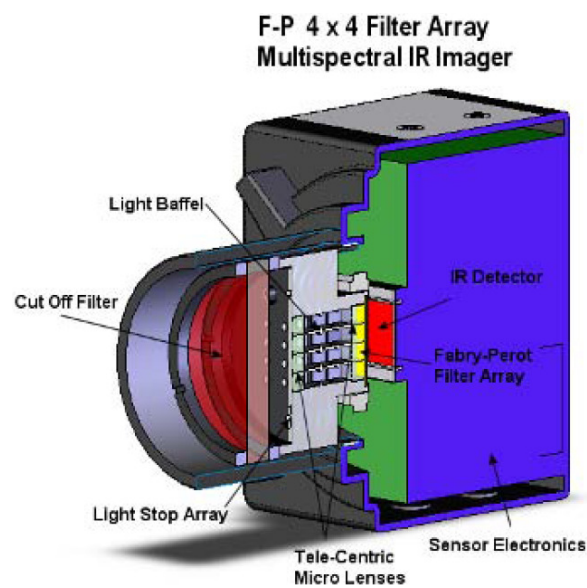
Figure 2-11: An illustration of the MSSI using a commercial camera, with 4×4 filter array in front of the IR-FPA. In front of the filter array is a micro-optic assembly with lenses, baffles and a cut-off filter [44].
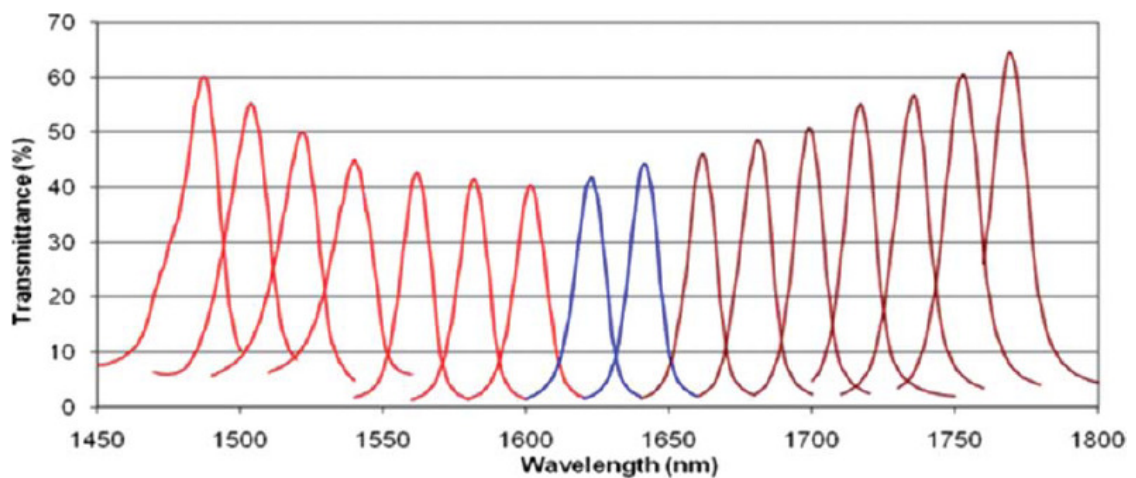
Figure 2-12: Measured spectral transmission of each of the 16 spectral channels in the filter array [43]

MSSI offers the advantage of a compact configuration that is attractive for operating on an aerial platform, which could be used to substitute an already present imager without significant changes or modifications to the aircraft. No image reconstruction is required before a human operator can begin to interpret the direct output, either for cueing onto a remote scene of interest or anomaly detection by eye. Between the sixteen uniformly distributed peaks as observed in Figure 2-12, each channel rejects all other input flux and greatly reduces the net optical efficiency of MSSI. Each channel possesses a peak transmission of between 40% to 60% and a full-width half-maximum (FWHM) of approximately 15nm, leading to a first-order rejection estimate of 97.5% for net incident flux. This net rejection could be an issue for defence applications that require minimal time to capture imagery.

The étendue and angular resolution of MSSI is reduced with respect to the alternatives in this section, since the telecentric microlens and filter array effectively create sixteen concurrent imagers. Each pseudo-imager will have less than $^1/_{16}$ of the maximum étendue for a single lens imager using the same detector FPA. The frame-rate of MSSI for imagery with useful levels of intensity contrast under either laboratory or simulated real-world environments was not reported by the researchers.

With respect to the preceding techniques, MSSI excels in meeting all but one of the requirements detailed in Chapter One, which is the minimisation of rejected input flux. This requirement is important for defence applications to minimise the time needed to capture HSI imagery at standard 25 Hz video rate, which may not be achieved by MSSI. Despite this inherent problem of étendue and light rejection, the MSSI sensor may be very effective in meeting the seven suggested requirements for snapshot HSI.

2.3.3 Image Replicating Imaging Spectrometer

Traditional HSI techniques require time-sequential recording by spatial or spectral scanning to capture hypercubes. This requirement renders snapshot anomaly detection in dynamic or transient situations as challenging if not unfeasible using a time-sequential system.

The *Image-Replicating-Imaging-Spectrometer* (IRIS) is a novel and patented technique invented by AR Harvey *et al* at Heriot-Watt University that offers significant potential for a snapshot HSI sensor in the infrared wavebands [45,46,47,48,49,50]. IRIS systems are currently exploited for ophthalmology in addition to retinal imaging. IRIS involves exploiting Wollaston prisms to achieve two-beam spectral separation, which will be described as shown in Figure 2-13. All symbols from this point onwards represent their regular textbook quantities, unless where otherwise specified or indicated.
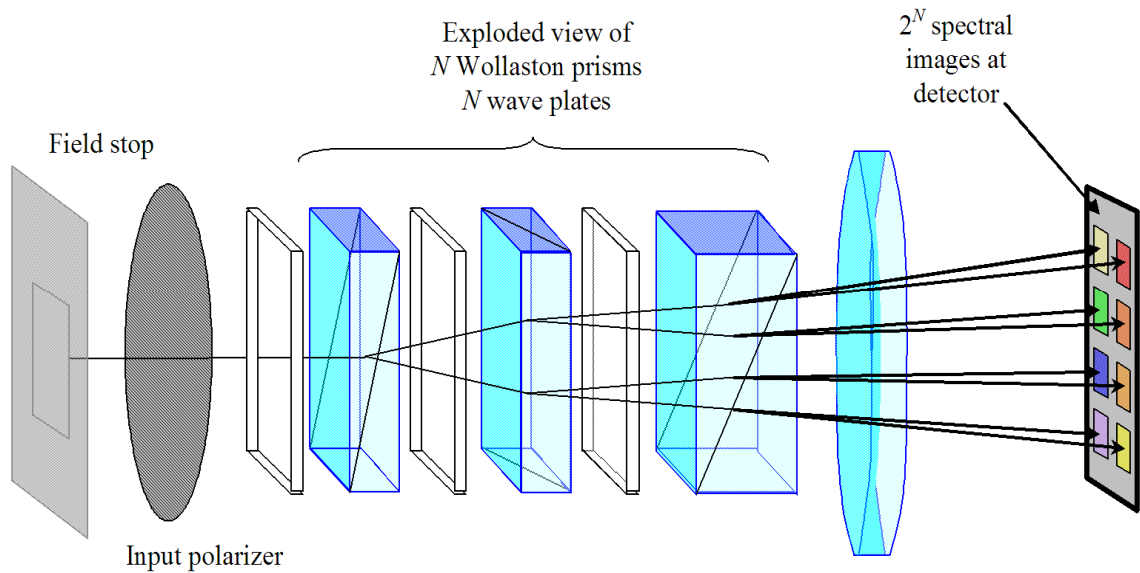
Figure 2-13: Expanded schematic of an eight waveband IRIS sensor minus objective optics [45]

Figure 2-13 is a diagram of an expanded IRIS where the objective and collimator lenses either side are not shown for simplicity, but are considered during the design stage in Chapter 4. After passing through the foreoptics, input flux from an imaged scene is linearly polarised vertically by the input polariser and propagates through a waveplate with the fast-axis rotated by $\pi/4$ with respect to vertical. This tilted waveplate introduces a phase difference of $\Delta\theta(\lambda,d)=[2\pi/\lambda]\{n_e(\lambda)-n_o(\lambda)\}d$ between the orthogonal components, where $n_e(\lambda)$ and $n_o(\lambda)$ are the extraordinary and ordinary refractive indices respectively, with depth d, such that the polarisation state is dependent upon the wavelength λ.

The subsequent Wollaston prism then symmetrically splits this ray into two diverging components, each of which is linearly polarised in mutually orthogonal planes. These diverging rays emerging from the Wollaston prism have relative intensities according to $\cos^2(\Delta\theta/2)$ and $\sin^2(\Delta\theta/2)$ respectively. These two intensities sum to unity in their transmission efficiency without the absorption or rejection of any given polarisation. This concurrent beamsplitting with polarisation discrimination without rejection was a key factor in the use of Wollaston prisms, along with their simplicity and availability. The convenience of approximately collinear replication enables a single detector array.

This wave retardation followed by Wollaston-prism splitting yields 2^N replicated images, according to the number of retarder-prism sets N. Exploiting the wavelength and polarisation dependence of each retarder-prism set causes replication of the image with separate wavebands. Unlike time-sequential methods, the fundamental throughput of the initially polarised light is unity without any rejection in wavelength.

IRIS is characterised by spectral transmission functions (STFs) that describe the wavelength-dependence for each replicated image. For N retarder-prism sets, there are 2^N corresponding STFs for each of the 2^N-replicated images. These STFs express the wavelength dependence of transmission for the replicated sub-images that form the basis of the IRIS concept. For an eight-band system, there are respectively eight STFs with each possessing a different combination of sine and cosine terms. Equations (1) to (8) are the generalised STFs for waveplate depths (d_1, d_2, d_3) when N=3. An instance of the spectral transmission curves (STCs) from these STFs is shown in Figure 2-14, where the waveplate depths are 102, 208 and 408 μm respectively. These depths were found by optimisation that will be discussed in *Chapter Three*.

$$T_1(\lambda, d_1, d_2, d_3) = \cos^2\left[d_1\pi\left\{\frac{n_e(\lambda)\text{-}n_o(\lambda)}{\lambda}\right\}\right]\cos^2\left[d_2\pi\left\{\frac{n_e(\lambda)\text{-}n_o(\lambda)}{\lambda}\right\}\right]\cos^2\left[d_3\pi\left\{\frac{n_e(\lambda)\text{-}n_o(\lambda)}{\lambda}\right\}\right] \quad (1)$$

$$T_2(\lambda, d_1, d_2, d_3) = \cos^2\left[d_1\pi\left\{\frac{n_e(\lambda)\text{-}n_o(\lambda)}{\lambda}\right\}\right]\cos^2\left[d_2\pi\left\{\frac{n_e(\lambda)\text{-}n_o(\lambda)}{\lambda}\right\}\right]\sin^2\left[d_3\pi\left\{\frac{n_e(\lambda)\text{-}n_o(\lambda)}{\lambda}\right\}\right] \quad (2)$$

$$T_3(\lambda, d_1, d_2, d_3) = \cos^2\left[d_1\pi\left\{\frac{n_e(\lambda)\text{-}n_o(\lambda)}{\lambda}\right\}\right]\sin^2\left[d_2\pi\left\{\frac{n_e(\lambda)\text{-}n_o(\lambda)}{\lambda}\right\}\right]\cos^2\left[d_3\pi\left\{\frac{n_e(\lambda)\text{-}n_o(\lambda)}{\lambda}\right\}\right] \quad (3)$$

$$T_4(\lambda, d_1, d_2, d_3) = \cos^2\left[d_1\pi\left\{\frac{n_e(\lambda)\text{-}n_o(\lambda)}{\lambda}\right\}\right]\sin^2\left[d_2\pi\left\{\frac{n_e(\lambda)\text{-}n_o(\lambda)}{\lambda}\right\}\right]\sin^2\left[d_3\pi\left\{\frac{n_e(\lambda)\text{-}n_o(\lambda)}{\lambda}\right\}\right] \quad (4)$$

$$T_5(\lambda,d_1,d_2,d_3)=\sin^2\left[d_1\pi\left\{\frac{n_e(\lambda)\text{-}n_o(\lambda)}{\lambda}\right\}\right]\cos^2\left[d_2\pi\left\{\frac{n_e(\lambda)\text{-}n_o(\lambda)}{\lambda}\right\}\right]\cos^2\left[d_3\pi\left\{\frac{n_e(\lambda)\text{-}n_o(\lambda)}{\lambda}\right\}\right] \quad (5)$$

$$T_6(\lambda,d_1,d_2,d_3)=\sin^2\left[d_1\pi\left\{\frac{n_e(\lambda)\text{-}n_o(\lambda)}{\lambda}\right\}\right]\cos^2\left[d_2\pi\left\{\frac{n_e(\lambda)\text{-}n_o(\lambda)}{\lambda}\right\}\right]\sin^2\left[d_3\pi\left\{\frac{n_e(\lambda)\text{-}n_o(\lambda)}{\lambda}\right\}\right] \quad (6)$$

$$T_7(\lambda,d_1,d_2,d_3)=\sin^2\left[d_1\pi\left\{\frac{n_e(\lambda)\text{-}n_o(\lambda)}{\lambda}\right\}\right]\sin^2\left[d_2\pi\left\{\frac{n_e(\lambda)\text{-}n_o(\lambda)}{\lambda}\right\}\right]\cos^2\left[d_3\pi\left\{\frac{n_e(\lambda)\text{-}n_o(\lambda)}{\lambda}\right\}\right] \quad (7)$$

$$T_8(\lambda,d_1,d_2,d_3)=\sin^2\left[d_1\pi\left\{\frac{n_e(\lambda)\text{-}n_o(\lambda)}{\lambda}\right\}\right]\sin^2\left[d_2\pi\left\{\frac{n_e(\lambda)\text{-}n_o(\lambda)}{\lambda}\right\}\right]\sin^2\left[d_3\pi\left\{\frac{n_e(\lambda)\text{-}n_o(\lambda)}{\lambda}\right\}\right] \quad (8)$$

Aside from the snapshot capability and high optical throughput offered by concurrent spectral filtering and image replication, the IRIS system provides other benefits. The lack of moving parts allows increased reliability and robustness, making IRIS airborne deployment more readily achievable when compared to scanning alternatives, which would also not be able to capture transient or dynamic events. Power requirements can be less than other HSI sensors, as a commercial camera can be used at the image plane without mechanical scanning motors as used on traditional line-scanning sensors.
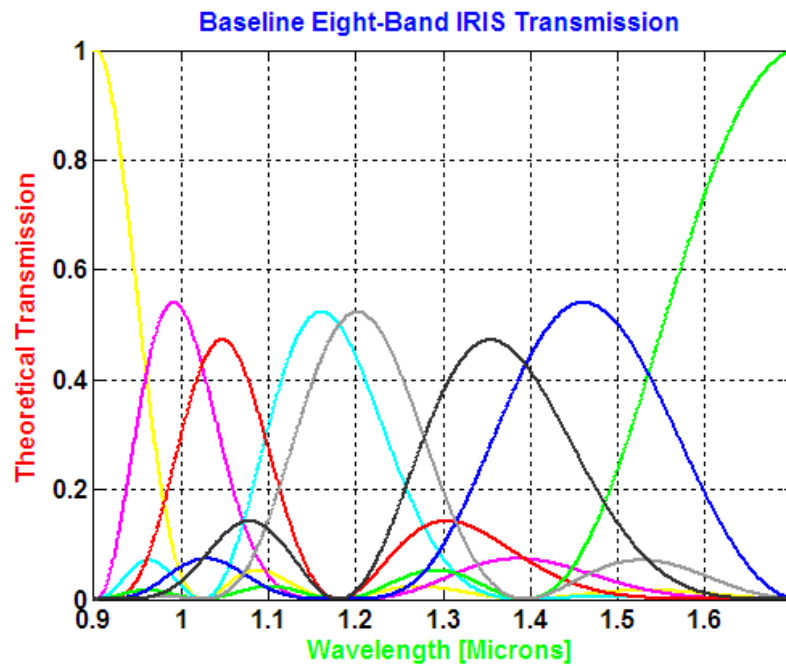
Figure 2-14: Example STCs for an eight band IRIS system, composed of three retarder-prism sets

Two issues arise that require attention and further consideration. The first concern is that pixels within a replicated image must be co-registered with those of all the other corresponding images. This would only require a simple translation if the system were ideal and free from any possible aberrations. The actual situation is more complex, due

to distortions and aberrations introduced by the geometrical optical elements, along with misalignment and variability. Figure 2-15 illustrates the problems introduced by this mis-registration from imaging distortions. The current solution involves a dewarping algorithm to correct the distortion measured during calibration. The design, execution and assessment of this solution have been recently completed by Alistair Gorman at Heriot-Watt University [51].
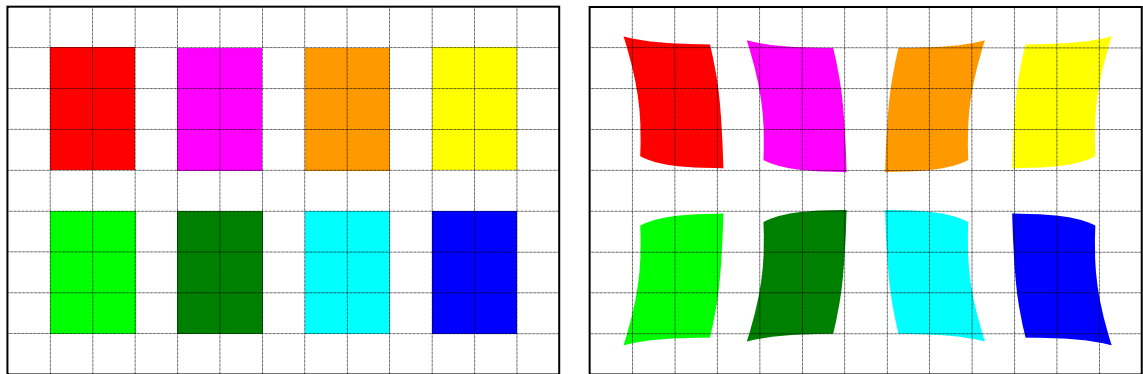
Figure 2-15: Examples of *ideal* co-registration and (pincushion) distorted image mis-registration

The second significant issue is chromatic dispersion, whereby the replicated images are blurred, due to the chromatic variation in splitting angle (CVSA) from Wollaston prisms. This CVSA problem can be exacerbated by the presence of sidelobes in the STCs as shown in Figure 2-14, which are not the idealised and narrow rectangular windows that are generally desirable. The CVSA creates a smeared point-spread function (PSF) in a slanted direction, thus causing a blurred image. Spectral contrast can be greatly reduced and spatial clarity compromised because of smearing. The net effect can potentially be seriously decreased resolution, making it challenging to discern or extract useful spatial information in order to exploit spectral differences.
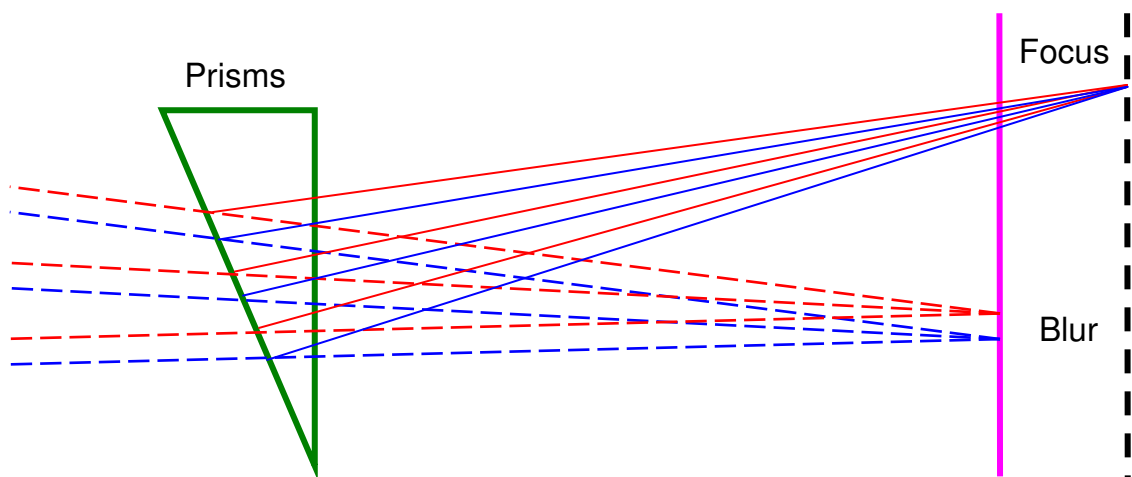
Figure 2-16: The correction of CVSA by a dispersive prism – note that the image plane may shift

2.4 Signal-to-Noise Considerations

Potentially the most significant determinant for the usefulness of a given technique is the achievable signal-to-noise ratio (SNR). For reference, SNR is the ratio of the total number of signal electrons to the sum in quadrate of noise sources. The latter includes detector noise, shot noise on the signal flux and shot noise on the background flux. All imaging spectrometry techniques can be grouped into one of two categories: direct or with inversion. Those that are direct require some combination of spectral or spatial multiplexing or de-multiplexing to record a spectral data cube.

Spectral multiplexing with inversion uses non-orthogonal spectral basis sets, being exemplified by Fourier-transform imaging spectrometry (FTIS) operating sequentially in time. The spectral basis sets are not strictly orthogonal since the interferograms can be represented as a bias with the addition of an orthogonal basis set. CTIS and CASSI belong to the FTIS category, although both are capable of snapshot operation. CTIS especially involves the smearing of spectra rather than the generation of interferograms.

These two techniques involve spectral smearing of the light from one pixel that can largely overlap with the spectrally smeared light from an adjacent pixel. The spectral intensities of objects within a field-of-view (FoV) are not spatially separated at the detector. This spectral overlap on the FPA entails shot-noise is dependent between pixels, such that the contribution by shot-noise is not due to a single spectral bin, but rather the full spectral band of interest. SNR expressions at each wavenumber are dependent on the integral of spectral distribution at the detector. It can be shown from [52] that the SNR can be expressed directly as:

$$SNR(\sigma) = \frac{T\int_{\sigma}^{\sigma+\delta\sigma} k_s(\sigma)\,\mathrm{d}\sigma}{\sqrt{2N\bar{n}_d^2 + T\int_{\sigma_{\min}}^{\sigma_{\max}} k_s(\sigma)\,\mathrm{d}\sigma + T\int_{\sigma_{\min}}^{\sigma_{\max}} k_b(\sigma)\,\mathrm{d}\sigma}} \qquad (9)$$

Where σ is the wavenumber, N is the number of bands, T is the integration time and $\bar{n}_d$ is the noise root-mean square (RMS) of detector electrons. When integrated over a wavenumber range $\mathrm{d}\sigma$, $k_s(\sigma)$ and $k_b(\sigma)$ yield the target radiance and background radiance respectively. $k_s(\sigma)$ and $k_b(\sigma)$ can be complicated and require expressions for the atmospheric transmission, emission, scattering, signal irradiance with wavelength, along with positions of the sensor and target of interest. Sensor parameters are also

required for $k_s(\sigma)$ and $k_b(\sigma)$ that includes étendue, detector area, detector quantum efficiency, optics F-number, optic transmission efficiency, integration time per spectral image and spectral bin width. Commercial software such as *Lowtran* can readily calculate the atmospheric transmission and thermal radiation using generic spectra from databases such as ASTER (Advanced Spaceborne Thermal Emission & Reflection Radiometer). FTIS gives some guide for a specific class of convenient inversion spectrometer. A similar discussion for CTIS or CASSI may give some general indication of the approximate performance for SNR comparison purposes.

Contrast this with the latter category of direct imaging spectrometry (DIS) using multiplexing, where there is generally no overlap at the FPA of spectral features. They produce spatial patterns that are essentially orthogonal and are independent of the signal in all other spectral bins. IFA, MSSI and IRIS spectrally multiplex the input onto spatially distinct detector areas in a form of DIS. It is noted that IRIS is not strictly spectrally orthogonal due to spectral side-lobes, but is clearly a DIS method due to the concurrent spatial replication and spectral separation on an FPA of an input flux. The SNR for DIS techniques can be expressed as:

$$SNR = \frac{e_s}{\sqrt{\overline{n}_d^2 + \overline{e}_s + \overline{e}_b}}$$

(10)

$$e_s = \overline{e}_s = T\int_{\lambda}^{\lambda+d\lambda} k_s\left(\lambda\right) \, \mathrm{d}\lambda$$

$$\overline{e}_b = T\int_{\lambda}^{\lambda+d\lambda} k_b\left(\lambda\right) \, \mathrm{d}\lambda$$

(11)

Where e_s is the number of signal photoelectrons measured during integration, $\overline{n}_d$ is the RMS noise of detector electrons, $\overline{e}_s$ is the shot-noise RMS of the signal, $\overline{e}_b$ is the RMS photon shot-noise of the background flux and T is the total integration time [52]. As with FTIS, $k_s(\lambda)$ and $k_b(\lambda)$ is calculated from optical and sensor parameters.

Lowtran software was not available to the author, while fundamental differences entail that direct contrast or comparison between DIS and FTIS is not trivial [52]. For the latter category, which includes CTIS and CASSI, the SNR for each spectral bin is dependent on the signals within all other spectral bins. This is not generally the case for DIS techniques such as IFA, MSSI and IRIS. One other significant issue is that FTIS techniques tend to a linear spectral resolution in the wavenumber domain, while DIS

has linear resolution that is mostly constant with wavelength. An indirect comparison for this discussion is nonetheless possible, by drawing upon generalised published results [52].

By assuming no detector saturation and that spectral transmissions are constant over wavelength with input spectra are gray, such that total incident flux is the same for both, it can be shown for snapshot imaging that [52]:

$$\frac{SNR_{FTIS}}{SNR_{DIS}} = \frac{\tau^{FTIS}}{\tau^{DIS}} \sqrt{\frac{NT_{tot}^{FTIS}}{T_{tot}^{DIS}}} \sqrt{\frac{N\frac{\overline{T}}{T_{tot}^{DIS}} + \frac{\tau^{DIS}}{N}}{2N_{FTIS}\frac{\overline{T}}{T_{tot}^{FTIS}} + \tau^{FTIS}}} \tag{12}$$

Where the *FTIS* and *DIS* descriptors refer to spectral multiplexing with inversion and spatial multiplexing for convenience, specifically for the snapshot techniques discussed in this chapter. τ are the nominal spectral transmissions, N is the number of spectral bins (snapshot imaging), $\overline{T}$ is the integration time to achieve shot-noise limited imaging per detector read, while T_{Tot} is the total integration time to record the hypercube.

For the purposes of this comparison with respect to the requirements of Section 1.3, the same detector array running at a fixed frame rate with common optics where applicable is assumed for both categories. $\overline{T}$ is equal to T_{Tot} for both snapshot categories for the purposes of this comparison, while τ can be approximated as equal in both cases also. $\overline{T}$ is dependent on the imaged scene and the FPA read-noise, along with the assumption of detector-noise limited imaging for high radiance scenes without detector saturation. Simplification with these assumptions allows the following expression to be found:

$$\frac{SNR_{FTIS}}{SNR_{DIS}} \approx \sqrt{N}\sqrt{\frac{N + \frac{\tau}{N}}{N + \tau}} \propto \sqrt{N}\sqrt{\frac{1}{N^2}} \propto \frac{1}{\sqrt{N}} \tag{13}$$

This suggests that as the number of wavebands is increased for the same detector array under the same circumstances of 2D snapshot imaging, the SNR for DIS techniques is generally superior to FTIS techniques. Although not as rigorous as using *Lowtran* software, this approximation does provide useful insight into SNR that implies DIS techniques are optimal for scaling to increasing numbers of wavebands. It is recognised

here that doing so would reduce the spatial resolution of the hypercube (generally linearly with N), but FPA technology is mature with 32 megapixel arrays now available as a COTS package[1].

Another qualifier to this conclusion is that the two categories of snapshot techniques are assumed as having exactly the same angular FoV and FPA utilisation. The methods within these two categories may also be shot-noise or detector-noise limited and is dependent on rigorous optical modelling and atmospheric simulation. These issues may affect the generalised conclusion that DIS is superior to FTIS for snapshot imaging, but is nonetheless a useful insight for the purposes of this brief consideration.

2.5 Optimal Snapshot Method for Defence Applications

This Chapter covered emerging snapshot HSI techniques after starting from the context of time-sequential methods. The objective was to determine which technique offered the best potential to satisfy the requirements for a SWIR snapshot imager. Aside from the MSSI method, which postdates the EngD research in this thesis, no other discovered technique has been developed for non-visible wavelengths at the time of writing. The contribution of this thesis is hence novel and original, by taking the IRIS technique and further developing it to operate in the SWIR region for non-medical remote sensing.

Table 2-1 summaries the advantages and disadvantages between the HSI techniques that may satisfy the requirements of Section 1.3. It should be noted that the techniques each have potential applications that optimally exploit their inherent advantages. CTIS for example is known to have been developed for ground-based missile defence [33,34,35], where processing needs can be more readily satisfied and low FPA sensitivity can be overcome by staring at an intense missile plume against an uncluttered sky. The central reference image of CTIS is an advantage over other snapshot techniques for maintaining alignment and focus on a fast-moving target of interest.

One potential application for MSSI that would optimally exploit its advantages could be as a spectral analyser cued by another panchromatic sensor with a larger FoV. Such a compact system may be useful for ground vehicles that occasionally require spectral

---

[1] *InfinityX-32* camera from Lumenera Corporation in Canada

inspection of an area, which has been determined or cued by some other sensor device. An IFS imager may be optimal for satellite applications that can incorporate its larger relative volume and enable longer integration times of slowly varying ground scenes. CASSI on the other hand offers a compact solution with the compromise of dozens of wavebands, with respect to the hundreds of IFA wavebands and the eight bands of IRIS.

HSI Technique	Advantages	Disadvantages
Computed Tomography Imaging Spectrometer (CTIS)	Few components Majority COTS Central reference image	Reduced SNR from inversion Processing requirements Inefficient FPA fill-factor Incomplete hypercube projections
Coded Aperture Snapshot Spectral Imager (CASSI)	Dozens of wavebands Compact optical layout	Reduced SNR from inversion Processing requirements Low-quality hypercube Compression inaccuracies
Integral Field Spectroscopy (IFS)	No inversion Hundreds of wavebands	Large physical volume Low sensitivity at FPA Limited availability FPA
Miniature Snapshot Multispectral Imager (MSSI)	Compact layout No inversion or reconstruction	High rejection of incident flux Low angular resolution and FoV
Image Replicating Imaging Spectrometer (IRIS)	No inversion or reconstruction High optical efficiency	Dispersion from prisms Non-orthogonal passbands

Table 2-1: Summary of snapshot techniques, with associated advantages and disadvantages

Aside from potential or optimal applications, although spectral multiplexing techniques such as CTIS and CASSI offer compactness, the processing requirements to generate video-rate imagery are onerous and potentially unfeasible for airborne applications. The payload, cooling and power requirements to enable video-rate imagery imply that these techniques may be optimal for static ground stations. CTIS is relatively inefficient in its FPA fill-factor, while the reconstructed image quality of CASSI is challenging. Further issues with reconstruction errors may also arise due to the incomplete capture of

hypercube projections by CTIS and 2D compression of the 3D hypercube by CASSI. As such, they do not meet the requirements for the applications described in Chapter One.

Spatial multiplexing techniques offer snapshot HSI that generally does not require high-performance computing to generate streaming imagery. Although offering high optical efficiency using reflective optics and no filtering, the IFS method is bulky and relatively costly, notwithstanding US export controls on suitable SWIR FPAs for an IFS system. MSSI and IRIS are the two optimal snapshot methods for the applications described in Chapter One, with the former offering superior compactness and smaller mass. MSSI however rejects a significant proportion of input flux and is complex to fabricate, with respect to its microlens assembly and Fabry-Pérot array at the FPA image plane. IRIS on the other hand, uses only COTS components and simple Wollaston prisms to achieve both spatial multiplexing and spectral separation. IRIS meets the specified requirements and is the optimal solution to requirements for developing a SWIR snapshot HSI sensor.

There are solutions to the problems of IRIS spectral smear that are proposed within literature or applied within practice [51]. Chapter 5 briefly reviews these advances, such as corrective prisms as shown in Figure 2-16, before considering a more fundamental remedy at the initial design stage. This eventual solution to be detailed is the invention of achromatised prisms to reduce chromatic variations in splitting angles.

> CONCLUSION – Beginning with an outline of time-sequential methods, this chapter considered the prevalent methods for snapshot HSI. Spectral multiplexing techniques with inversion such as CTIS and CASSI were considered as problematic with respect to processing requirements despite some advantages. Spatial multiplexing techniques were also considered such as IFU, MSSI and IRIS. The advantages and drawbacks of each such method were discussed, before reaching the conclusion that IRIS was optimal in meeting the application requirements of the preceding chapter. The research to be described in this thesis was placed within the context of previous developments, while highlighting the original contribution to the field of snapshot HSI.

Chapter 3:
Near-Infrared IRIS Design and Verification

ABSTRACT – This chapter describes the design and verification process for N-IRIS, with the supplied SWIR camera and lenses acting as the starting point for the design. The required splitting arrangement to achieve eight subimages is described, along with the necessary field-stop size and resultant pixel-spread length. The choice of quartz is made for the waveplates with their thicknesses optimised to minimise the ratio of sidelobes to main peaks for a uniform passband distribution. Based on cost considerations and image quality, beta barium-borate is selected as the most suitable prism material for N-IRIS. Ray-trace optical modelling is performed for N-IRIS with paraxial and real lenses respectively, with key optical parameters reported. The eventual assembled prototype is tested for basic verification, before and after the integration of upgraded lenses that were later made available to the N-IRIS project.

3.1 N-IRIS Optical Design

Referring to the expanded IRIS layout shown in Figure 3-17, the design for an eight-band SWIR snapshot sensor is described in this Chapter. This new iteration is the first SWIR snapshot prototype. Other known snapshot sensors at the time of writing were not designed for use in the SWIR region and typically operated in visible wavelengths. The definition of SWIR can vary amongst application areas, but is considered here as wavelengths between 700 nm and 1.7 μm inclusive. This is mainly due to the limitations of the SWIR camera provided and described below. This is contrasted with the visible range of previous IRIS sensors, which is usually defined as between 400 and 700 nm. Longer wavelengths form a natural progression and meet the requirements to enable SWIR operation for the applications given in Chapter One.

This near-infrared sensor will be denoted as *N-IRIS*. The first step involved in designing N-IRIS was to consider an appropriate camera for use. The near-infrared camera available was the *XenICs* XEVA sensor, employing an InGaAs array with 256×320 pixels and 30 μm pitch. The 7.68×9.6mm focal plane array (FPA) was cooled thermoelectrically to 263K. The *XenICs* offered a wavelength range of 900 nm to 1.7 μm inclusive, but the specific response curve is not available.

Eight spectral
images at detector

Condenser lens

Exploded view of three
Wollaston prisms and
three waveplates

Linear polarizer

Collimator lens
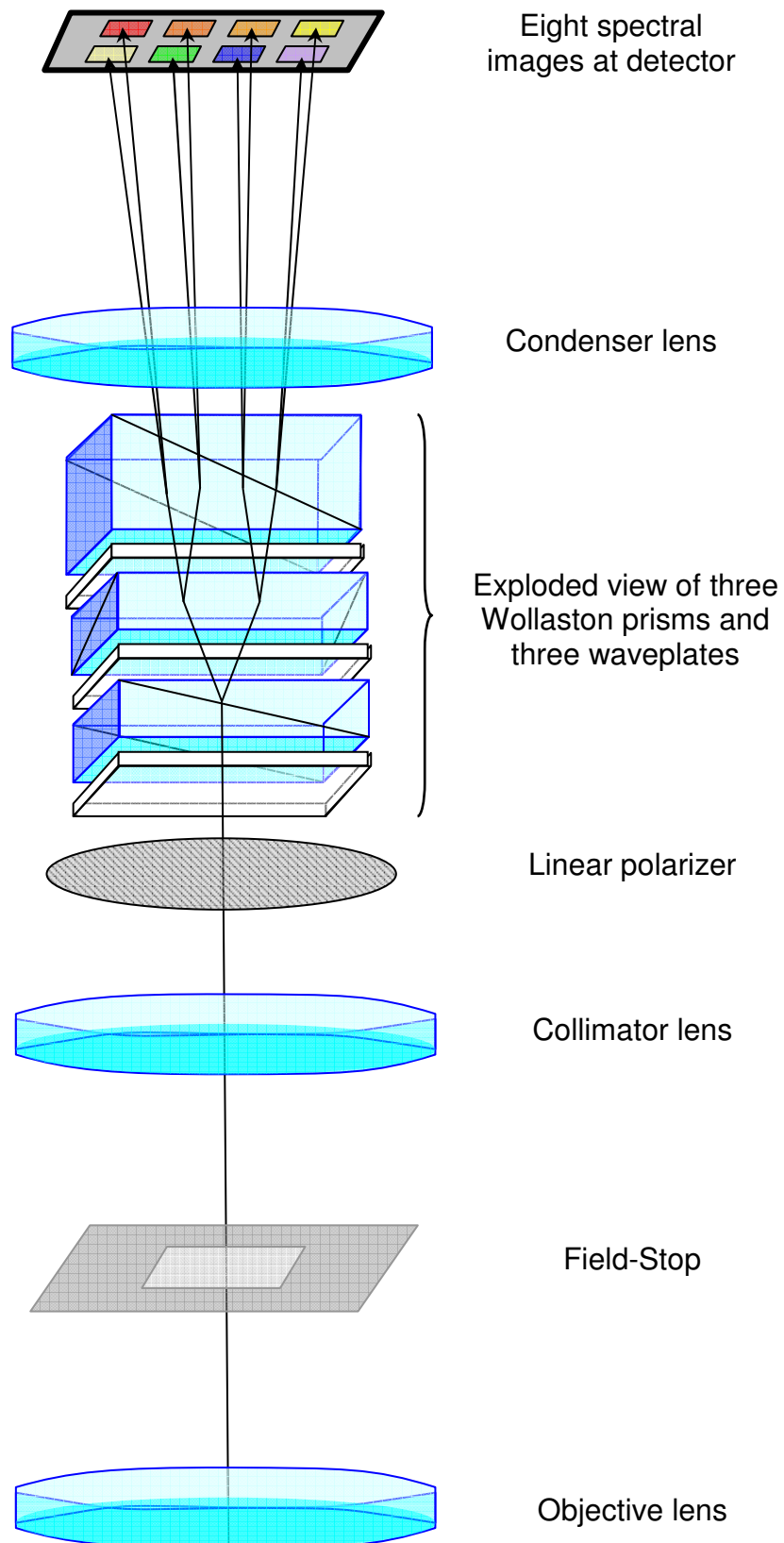
Field-Stop

Objective lens

Figure 3-17: Expanded IRIS layout including lenses, field stop, linear polarizer, detector and exploded view of the Wollaston prism and waveplate pairs – image adapted from [45]

Recalling the description within Chapter Two, N-IRIS follows the precedence of its visible predecessors by using eight wavebands. Resources available were a deciding factor in this arbitrary choice, along with unpublished research suggesting 6-8 bands were optimal for IR-HSI anomaly detection. Since each prism-retarder pair yields a doubling in the number of subimages, three such prism pairs will be required. The selection of passbands is decoupled from the optical design and will be considered in later sections.

Assuming perfect FPA usage, the subimages on the FPA will be 128×80 pixels each as shown in Figure 3-18. Judgement was taken to reduce FPA sizes by 10% in each dimension as contingency to account for aberrations and non-ideal manufacture. This will become more apparent in the following Chapters covering the chromatic variation in splitting angles (CVSA) from the Wollaston prisms. The revised FPA size was taken as 6.91×8.64mm, with eight 3.46×2.16mm sub-images laid out as shown in Figure 3-18.
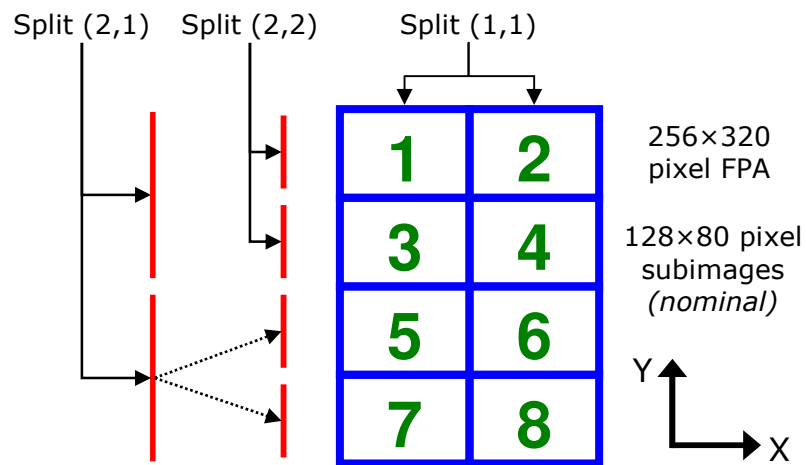
Figure 3-18: Illustration of IRIS subimage layout with splitting notation for eight bands

As with the *XenICs* camera, certain lenses were utilised to reduce project costs. The *XenICs* camera was provided with a 25mm focal length television (TV) condenser lens, for which optical design data could not be obtained. Two COTS lenses were provided for the objective and collimator, with focal lengths of 250mm and 50mm respectively. These were achromatic doublets designed for telecoms use, causing difficulties as discussed later within Section 3.5 regarding off-axis lens aberrations due to their narrow FoV. To generate the configuration shown in Figure 3-18 of two subimages by four, the splitting angle θ is given by:

$$\theta_{i,j}(a_i, f_{\mathrm{con}}, n_{i,j}) = 2\tan^{-1}\left(\frac{c_{i,j}}{2f_{\mathrm{con}}}\right) = 2\tan^{-1}\left(\frac{a_i}{4f_{\mathrm{con}}n_{i,j}}\right) \tag{14}$$

The subscripts *i,j* represent the splitting in the *x,y* directions respectively. This splitting angle θ is needed to split the centroid rays, such that they are incident at the appropriate FPA point. These centroid rays are at the middle of each sub-image, where the spatial extents of sub-images are controlled by a field-stop and not by splitting. The condenser focal length f_{CON} is fixed at 25mm, while the centroid $c_{i,j}$ pertains to that particular subimage under consideration. Subscript *i* can take the values of (1,2) to indicate the direction of splitting as *x* or *y* respectively. Subscript *j* can take the values (1,2) to denote the two respective splittings needed to achieve four subimages in the y-dimension ($i = 1$ only). Using geometry at the image plane, the splitting angle θ can also be found from the array size a_i and number of subimages $n_{i,j}$ in a given direction.

Figure 3-19 indicates the splitting arrangement needed to generate two sub-images in the X-dimension of the FPA, as shown in Figure 3-18. Note that the full field angle is θ and not $\theta/2$, since Wollaston prisms create symmetric splitting either side of the normal plane. This normal plane is shown as the green line on the conceptual diagram in Figure 3-19, which shows the undeviated path of a centroid ray if no IRIS splitting took place.

This concept also applies to the Y-dimension, except that double splitting must be accounted for as on the conceptual diagram in Figure 3-20. The initial vertical split results in two sub-images across the full FPA as with the previous case. The difference is that a second split is required with the size of the FPA is taken as half its value, to create two more sub-images from each initial sub-image. The net result is four separate sub-images landing on the detector array.
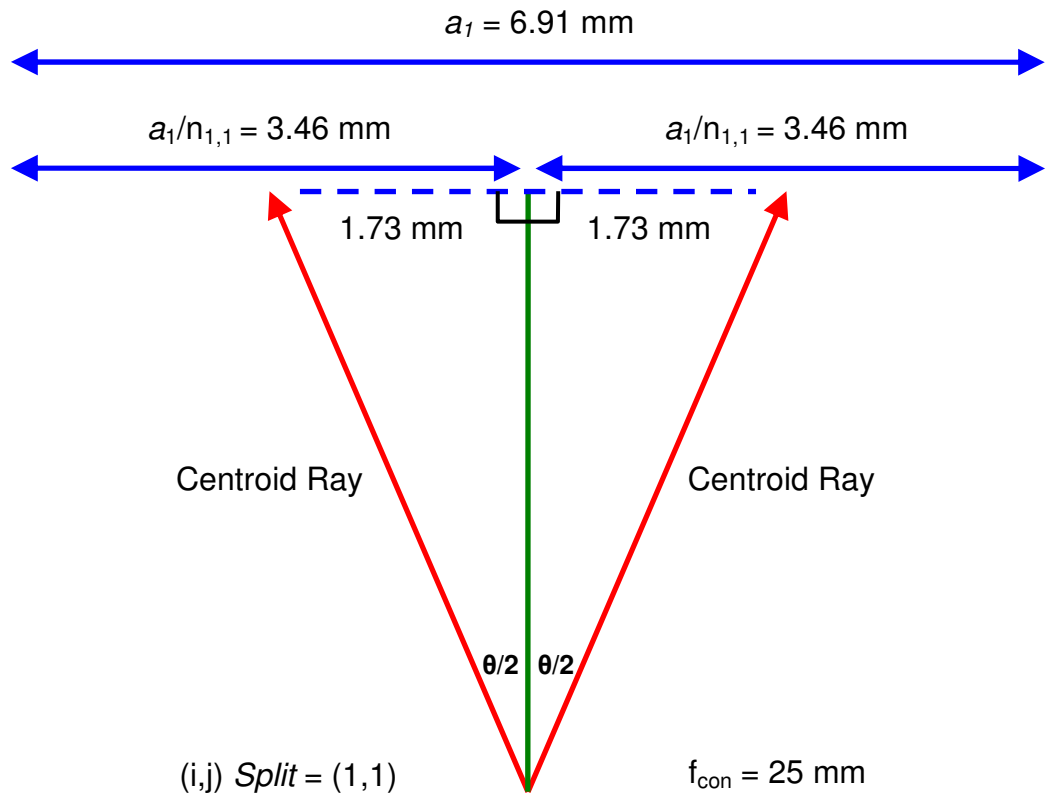
Figure 3-19: Conceptual splitting arrangement for two subimages in the X-dimension of the FPA
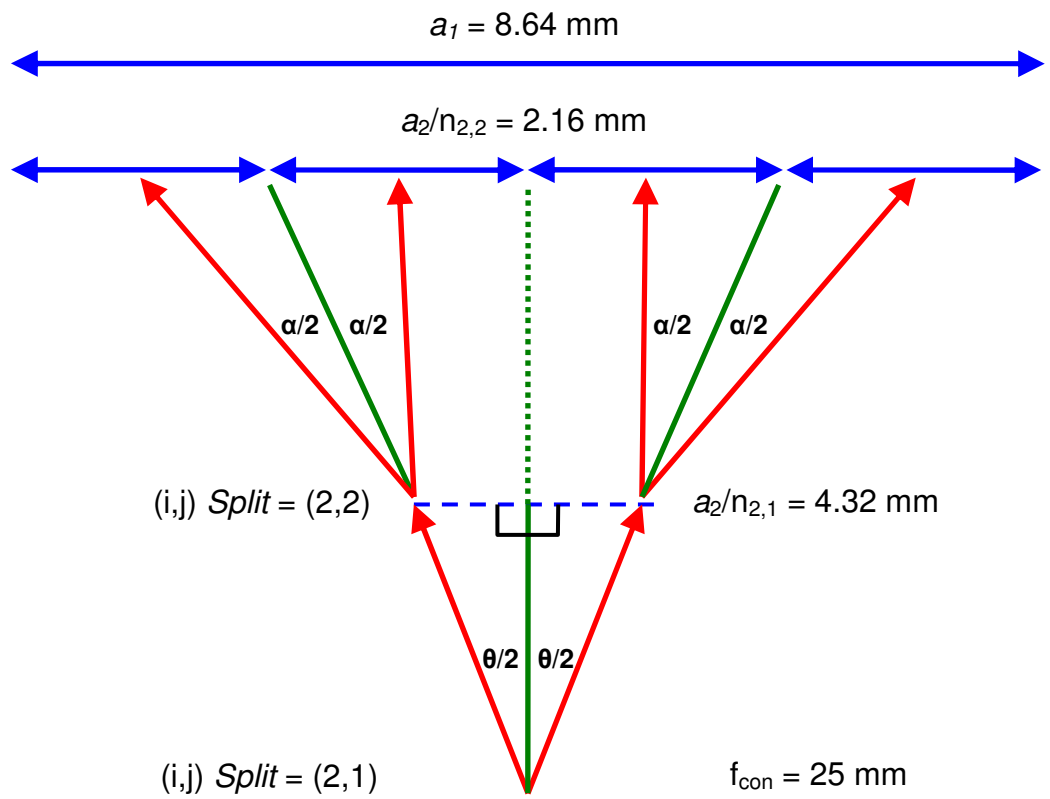

Figure 3-20: Conceptual double-splitting arrangement for four subimages in the Y-dimension of the FPA

Given the 25mm condenser lens and reduced FPA size 6.9×8.64mm, the three splitting angles are given in Table 3-2. The application of these angles is approximately order independent and any combination will result in a 2×4 sub-image layout at the detector array. This is because of the input light being collimated, with ray-tracing analysis in Section 3.4 providing more rigorous modelling as necessary for validation of the design.

Centroid Splitting (i,j)	Centroid Distance From Paraxial (mm)	Splitting Angle (deg)
X-Dimension (1,1)	1.73 mm	7.908°
Initial Y-Split (2,1)	2.16 mm	9.876°
Second Y-Split (2,2)	1.08 mm	4.947°

Table 3-2: Summary of splitting angles required for N-IRIS

The spatial extent of the subimages is limited by a field stop, preventing overlap along shared border regions. The magnification m can be found from the ratio of focal lengths for the collimator and condenser, which are f_{col} and f_{con} respectively. It can also be given by the ratios of object to image heights h or distances d respectively:

$$m\left(f_{col}, f_{con}\right) = \frac{-d_{img}}{d_{obj}} = \frac{h_{img}}{h_{obj}} = \frac{f_{con}}{f_{col}} \qquad (15)$$

The 25mm condenser and 50mm collimator yield a magnification factor of 0.5 in this design. Using the magnification and subimage sizes where $i = $ (x,y) and $j=2$, the necessary field-stop size k_i is calculated by:

$$k_i\left(a_i, f_{col}, f_{con}, n_{i,j}\right) = \frac{s_i}{m} = \left(\frac{f_{col}}{f_{con}} \frac{a_i}{n_{i,j}}\right) \qquad (16)$$

The height and width of the subimages s_i are the ratios of FPA size to the number of subimages in that direction. The former is given by a_i while the latter is denoted by $n_{i,j}$ to account for the necessary differences within the two directions. This leads to an ideal N-IRIS field stop size of 6.91×4.32 mm.

A useful quantity to be aware of is the full field-of-view (FoV) v_i shown in Figure 3-21, which dictates the spatial extent of image captured from the object of interest. It is calculated from the field-stop dimensions and the focal length of the objective lens:

$$v_i\left(a_i, f_{col}, f_{con}, f_{obj}, n_{i,j}\right) = \tan^{-1}\left(\frac{k_i}{f_{obj}}\right) = \tan^{-1}\left(\frac{f_{col}a_i}{f_{obj}n_{i,j}f_{con}}\right) \qquad (17)$$

This gives the full FoV as 1.6°×1.0° degrees, which is potentially suitable for use in long-range applications like those discussed in Chapter Two. The FoV is calculated from the field-stop size and the objective focal length, but the former is dependent upon the following optics. These directly include the FPA size, condenser length, collimator length and the Wollaston splitting angles (indirectly) as shown within Equation 17.
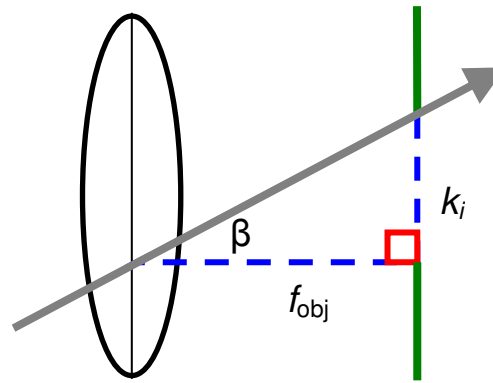
Figure 3-21: Illustration of FoV full-angle β for known field-stop size and objective focal length

The FoV is dominated by the inverse tangent that becomes asymptotic to an upper limit. Although not explicitly stated within the suggested requirements of Section 1.3, FoV is of importance for military applications, with larger FoVs often more useful than smaller FoVs for target detection. For a fixed FPA this must also be balanced with the area that each pixel subtends at a given distance for a known application for target detection. The following discussion considers these potential future needs within the design of N-IRIS.

Changing the objective is generally the most convenient method for increasing the FoV. One typical method for a larger FoV is to decrease the objective length, which creates problems whereby a smaller F-number collimator is required for a given field stop size. This ensures the collection of the larger ray cone, presented by the shorter objective focal length. It could be challenging to locate lenses ($\leq$ F1.2) that are both COTS and relatively affordable. Larger prisms are also required to accept the larger extent of collimated rays, which can create supplier or affordability issues beyond 25mm squared.

Altering the field-stop size to modify the FoV, as given in the preceding equation, also requires changes to the other IRIS optics. The field stop both prevents the overlap of subimages and maximises the usage of the FPA by being of sufficient size. Changing the field stop would require new Wollaston prisms to ensure neither over nor under-splitting. Replacement lenses may also be required for the collimator and condenser, to provide either larger apertures or appropriate focal lengths as the new stop necessitates.

Increasing FoV requires significant optical changes and N-IRIS sensor was designed to maximise cost efficiency given the COTS constraint. This prevented the inclusion of considerable spare capacity in terms of FoV, although minor changes could boost FoV by up to one-fifth with a new objective lens. Another related improvement could be lens replacements to enable the easy integration of a new camera, which may possess both a larger FPA and higher resolution. With the necessary resources, N-IRIS could be designed in future with the ability to accept multiple lenses for given applications known beforehand.

The ground spread length (GSL) g_i and the pixel spread length (PSL) p_i for a given target distance d yield more intuitive measures in addition to FoV. These quantities are useful measures for end-users in defence applications and given here for completeness:

$$g_i\left(a_i, d, f_{\text{col}}, f_{\text{con}}, f_{\text{obj}}, n_{i,j}\right) = 2d \tan\left(\frac{v_i}{2}\right) = 2d \tan\left(\frac{\tan^{-1}\left(\frac{f_{\text{col}} a_i}{f_{\text{obj}} n_{i,j} f_{\text{con}}}\right)}{2}\right) \qquad (18)$$

$$p_i\left(a_i, d, f_{\text{col}}, f_{\text{con}}, f_{\text{obj}}, n_{i,j}\right) = \left(\frac{n_{i,j} g_i}{r_i}\right) = \tan\left[\frac{\tan^{-1}\left(\frac{f_{\text{col}} a_i}{f_{\text{obj}} n_{i,j} f_{\text{con}}}\right)}{2}\right]\left[\frac{2d\left(n_{i,j}\right)^2}{a_i}\right] \qquad (19)$$

GSL as given by Equation (18) yields the length subtended by the FoV at the given distance d. The PSL as given by Equation (19) yields the length subtended by one pixel from r_i pixels in that dimension for the given distance d. As an example, for an arbitrary distance of 5km, the GSL is 138×86 meters and the resultant PSL is 1.0×1.0m. These equations can be used in future N-IRIS prototypes that are optimised for specific defence-related applications, such as anomaly detection of known targets from a given altitude that require a certain resolution for algorithms to be effective (pixels on target).

With the core attributes for N-IRIS determined, the next stage was to consider the choice of materials for the Wollaston prisms and waveplates in the following sections. The optical characteristics such as transmission range or birefringence must be traded-off against both cost and the manufacturing capability of suppliers. The issue of spectral blurring will form one key criterion in selecting appropriate materials, which is the topic of Section 3.3.

3.2 Selection of Wavebands

As previously discussed in Chapter Two, the STFs for an eight-band N-IRIS are of the form given by Equations (1) to (8), leading to STCs of the generic type shown within Figure 3-22. The sidelobes within each passband is an unwanted phenomenon resulting from the forms of the STFs, causing spectral measurements to become mixed between passbands. Optimisation is required to reduce this spectral interference by selecting appropriate waveplate thicknesses (d_1,d_2,d_3), which will reduce the amplitude of sidelobes with respect to the primary peaks. This will yield greater orthogonality of spectral bands, by reducing overlap and thus increasing potential discrimination. In order to achieve the objective of minimised side-lodes, a search methodology and suitable merit function is henceforth required for optimisation.

Three parameters leading to eight wavebands entail a nonlinear problem, necessitating a sampling of 3D thickness space to yield an optimal set of (d_1,d_2,d_3). Although resource intensive, a search was chosen as appropriate for this purpose for simplicity. Such an approach would be capable of dealing with several local minima of a merit function should they arise during computation. The particular merit function chosen here was an eight-band mean of peak power as a ratio of total power, which would be maximised when sidelobes are conversely minimised. As can be observed within Equations (1) to (8), there is both birefringence and wavelength dependence that must be considered beforehand. This requires selection of both a suitable wavelength range coupled to an appropriate material chosen for the waveplates.

From considering previous research with IRIS, quartz was selected as an appropriate material for waveplates [46,49]. This material exhibits the robustness necessary for manufacture on the thicknesses expected from previous studies, which required micron-level accuracy and tolerances. Quartz waveplates are also relatively low-cost and widely available, with greater than 90% transmission over the SWIR region of interest. As previously mentioned, the *XenICs* camera procured for N-IRIS operates from 900 nm to 1.7 µm inclusive. It is known that the birefringence and the associated dispersion are generally larger at shorter wavelengths for quartz, thus potentially leading to an increase in spectral smear [53]. The upper bound at 1.7 µm is taken as fixed; while the lower bound is arbitrary and can be increased to reduce spectral smear. Care must be taken however in order to retain a meaningful wavelength range for specific HSI applications if needed.

$$d_1\left(\lambda_{\text{Min}}, d_2, d_3\right) = \frac{\lambda_{\text{Min}}}{B\left(\lambda_{\text{Min}}\right)} = \frac{d_2}{2} = \frac{d_3}{4} \quad (20)$$

Equation 20 gives a set of initial depth values for (d_1, d_2, d_3), which is a heuristic from previous IRIS research [45]. The successive doubling of waveplate depths create a type of harmonic factor series and is similar to the scheme exploited by Lyot filters. Such a series is notable for periodicity and phase relationship, making it a rational point to begin an algorithmic search in "D-Space" (thickness space) without *a priori* knowledge. These initial STCs are shown in Figure 3-22, using refractive index values calculated for n_e and n_o by [54]:

$$n_e\left(\lambda\right) = \left(2.3849 - 0.0126 \cdot \lambda^2 + \frac{0.0108}{\lambda^2} + \frac{1.65 \times 10^{-4}}{\lambda^4} + \frac{1.95 \times 10^{-6}}{\lambda^6} + \frac{9.36 \times 10^{-8}}{\lambda^8}\right)^{\frac{1}{2}} \quad (21)$$

$$n_o\left(\lambda\right) = \left(2.3573 - 0.0117 \cdot \lambda^2 + \frac{0.0105}{\lambda^2} + \frac{1.34 \times 10^{-4}}{\lambda^4} + \frac{4.45 \times 10^{-7}}{\lambda^6} + \frac{5.92 \times 10^{-8}}{\lambda^8}\right)^{\frac{1}{2}} \quad (22)$$
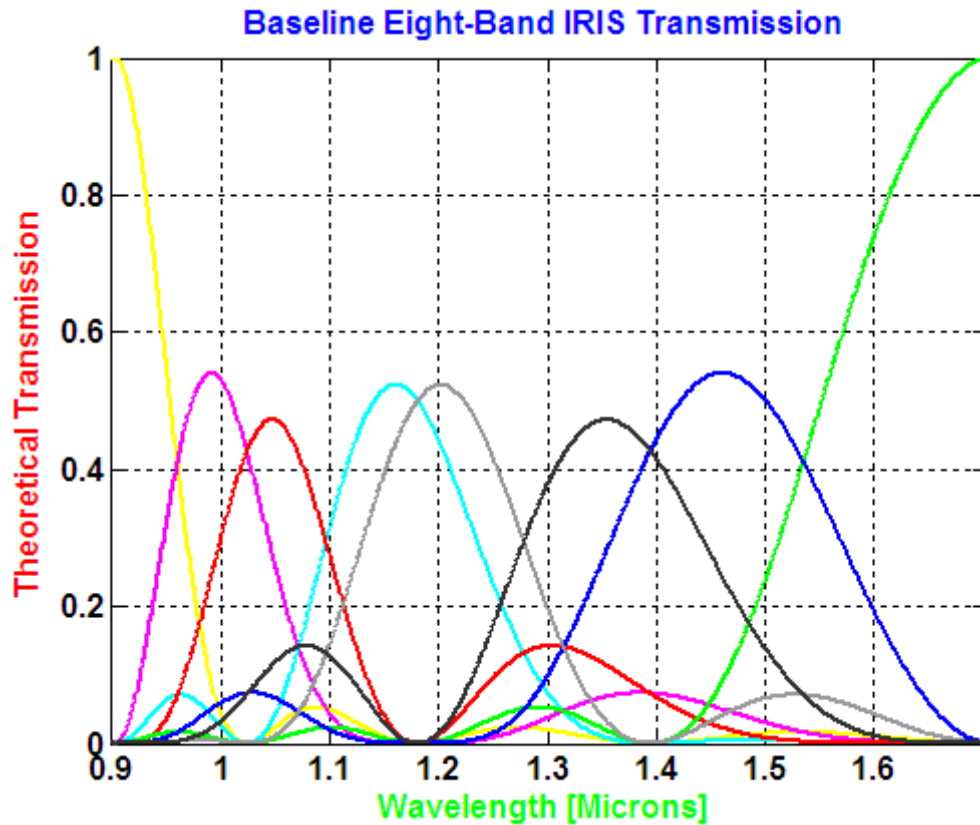

Figure 3-22: Full wavelength range STCs for the initial depths of **102**, **204** and **408 µm**

Judicious empirical testing by cropping upper and lower wavelength limits, while repeating the iterative search, resulted in the operating range being truncated out of the near-infrared (NIR) region of about 0.7 to 1.0 µm. The lower bound was fixed at 1.1 µm

onwards, with the upper bound dictated by the FPA response as before, in order to limit the effects of spectral smear. Most COTS optical elements are also designed around the arbitrary regions of VNIR (visible and near infrared), NIR, and SWIR – thus operating in only one conventional region reduces overall cost.

Figure 3-23 displays the resultant STCs that are deemed optimal given the metric chosen, which was the maximisation of average peak power against total power. This would minimise the power transmitted by side-lobes with respect to the main lobes, in order to limit the effect of spectral dispersion on image quality. Inspection of the STCs confirms indeed that the sidelobes are materially reduced, while peak positions are well distributed. The depths most suitable for N-IRIS from this search are given in Table 3-3, where the designations are arbitrary from smallest to largest.

It should be noted that numerous metrics are possible and the method chosen here is not exclusive, but was asserted as most appropriate. One alternative is the use of peak height equalisation, to exploit the FPA dynamic range through equal intensity sub-images [45]. Depending on the precise interpretation of reducing spectral smear, it is also possible to formulate metrics using different expressions – qualification is required.

Relying upon metrics alone may fail to capture externalities such as manufacturing tolerances. An apparently optimal solution may actually be sub-standard if it is very sensitive to variations in parameters, with volatility destroying any intended advantage. Performing a sensitivity analysis yields the tolerance graph of Figure 3-24, created from an error envelope of 10 µm distributed about the optimal depths. Using 1.0 µm increments, these potential combinations indicate that deviations ≤ 10µm are arbitrarily acceptable and range from 1.4% to 3.6% of the waveplate depth as given in Table 3-3. With the key parameters of the retarders determined, consideration of the second key N-IRIS element in the form of Wollaston prisms is carried out within the next section.

Waveplate	Depth (µm)	Tolerance
A1	275.0	3.6%
B2	384.4	3.3%
C3	700.8	1.4%

Table 3-3: Summary of quartz waveplate depths with absolute 10 µm error tolerance represented as a percentage of the respective waveplate depth
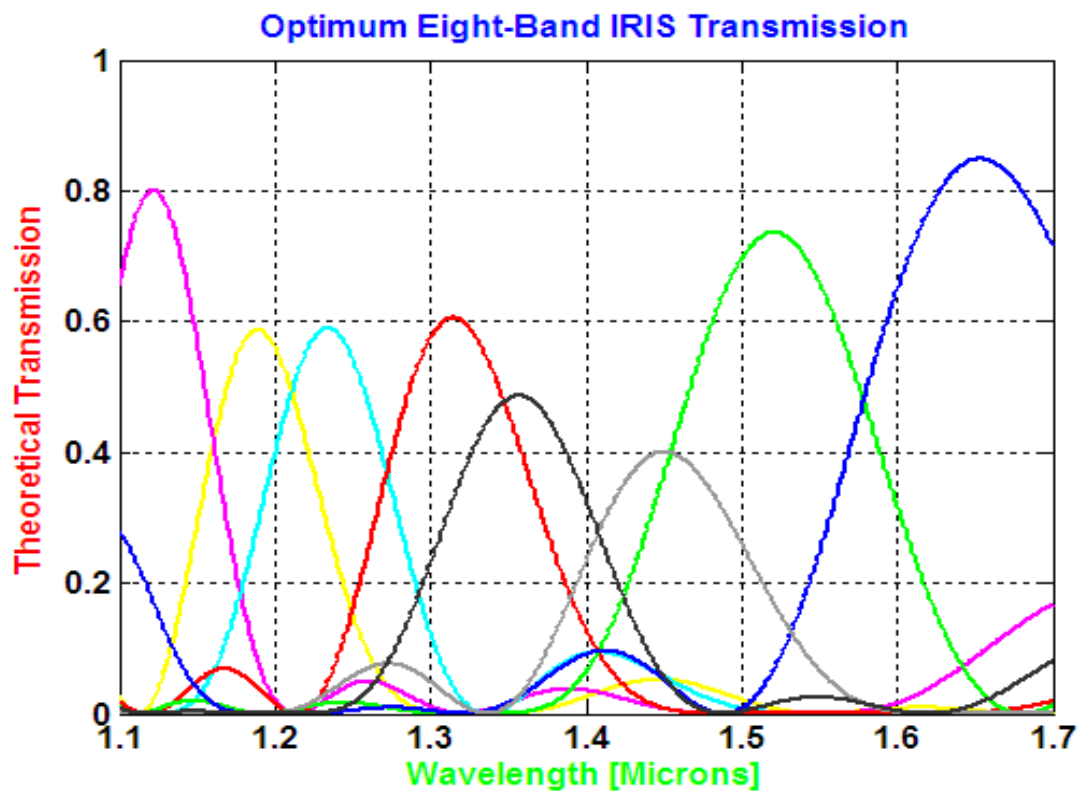
Figure 3-23: Truncated wavelength range STCs for the optimum depths of **275**, **384** and **701 μm**
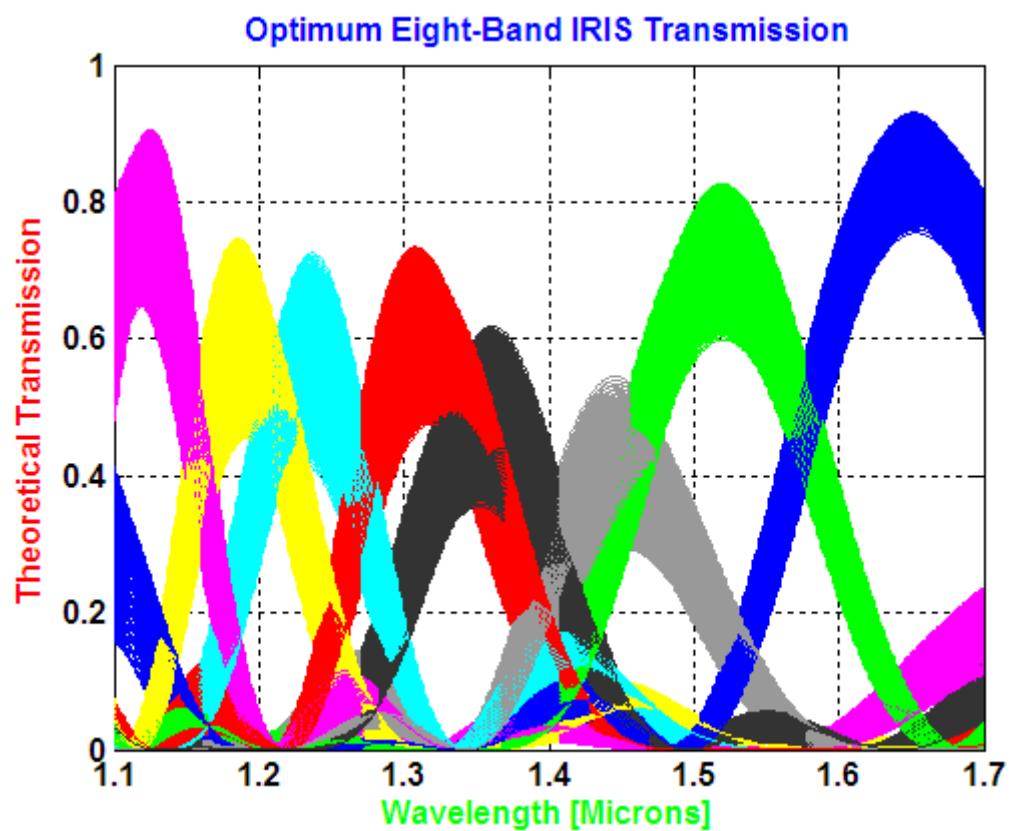

Figure 3-24: Sensitivity analysis for an error envelope of 10 µm distributed about the optimal depths. One thousand possible combinations of waveplate depths are displayed on this tolerance graph.

3.3 Birefringent Materials for Prisms

For paraxial or collimated light incident on a Wollaston prism, the splitting angle θ is a function of the physical wedge angle β. Wollaston prism splitting is shown in Figure 3-25 and the wedge angle is given by:

$$\beta_{i,j}\left(a_i, f_{con}, n_{i,j}, \lambda_{Min}\right) = \left|\tan^{-1}\left(\frac{\theta_{i,j}}{2B\left(\lambda_{Min}\right)}\right)\right| = \left|\tan^{-1}\left(\frac{\tan^{-1}\left(\dfrac{a_i}{4\ f_{con}n_{i,j}}\right)}{n_e\left(\lambda_{Min}\right) - n_o\left(\lambda_{Min}\right)}\right)\right| \tag{23}$$
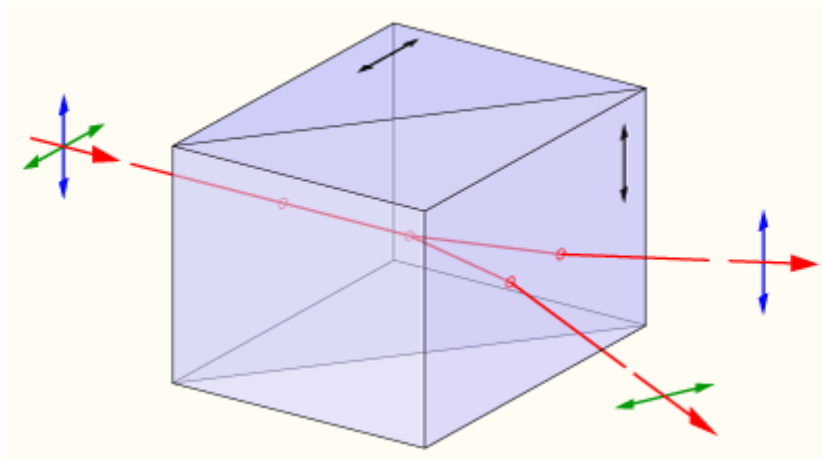
Figure 3-25: Wollaston prism splitting with annotated optical axes and polarisation states

Referring back to Figure 2-14 within Chapter Two, the main lobe and side lobes present in the STFs create smearing. The λ-dependence of birefringence causes variations in the splitting angle across the STFs for each sub-image, which contribute to the chromatic aberration of the sub-images.

The wedge angle β is a function of birefringence, which itself is dependent upon the wavelength of incident photons. Observing typical STCs for IRIS wavebands from Figure 2-14, it is known that the full-width at half-maximum (FWHM) can extend over 100 nm. The wedge angle must allow the spatial separation of all replicated sub-images, given the lowest birefringence at the shortest wavelength of 1.1 µm. Since birefringence increases with wavelength, the splitting angle will also be greater. This prevents any overlapping sub-images, but care should be taken not to exceed the FPA boundaries – enforcing a border region or frame would prevent this.

The most suitable material for the prisms was chosen from a pre-selected range given cost and availability limitations. This range was formed after consultation with in-house material experts and optical suppliers. Several quantitative and qualitative criteria were

subjectively judged by the author and contributing peers. These include ease of machining, availability in required dimensions, toxicity and affordability, along with meaningful values of birefringence [53,55,56]. The pre-selected range is as follows:

1) Beta-Barium Borate BaB_2O_4
2) Calcium Carbonate (Calcite) $CaCO_3$
3) Gallium Selenide Ga_2Se_3
4) Lithium Niobate $LiNbO_3$
5) Magnesium Fluoride MgF_2
6) Silicon Dioxide (Quartz) SiO_2
7) Potassium Dideuterium Phosphate KD_2PO_4
8) Potassium Dihydrogen Phosphate KH_2PO_4
9) Potassium Titanyl Phosphate $KTiOPO_4$
10) Aluminium Oxide (Sapphire) Al_2O_3
11) Silver Gallium Selenide $AgGaSe_2$
12) Silver Gallium Thiogallate $AgGaS_2$
13) Yttrium Vanadium Orthovanadate YVO_4
14) Zinc Germanium Phosphide $ZnGeP_2$

An appropriate measure for assessing this shortlist of materials is the Abbe numbers. The Abbe number *V*, or constringence, is a measure of dispersion, with respect to the refractive index variation:

$$V\left(n_C, n_D, n_F\right) = \frac{n_D - 1}{n_F - n_C} \qquad (24)$$

It is usually defined by the refractive indices (n_D,n_F,n_C) at the Fraunhofer spectral lines (DFC) at 589, 486 and 656 nm respectively. Since this was not useful for N-IRIS, the appropriate wavelength bounds in the SWIR region were substituted. The DFC lines henceforth map to 1.1, 1.7 and 1.4 µm respectively to enable a relevant Abbe number to be found from Equation (24). Birefringent materials exhibit two Abbe numbers *V* for the two optical axes and so the difference in Abbe numbers Δ*V* between both optical axes is taken as calculated by:

$$\Delta V\left(n_e^C, n_e^D, n_e^F, n_o^C, n_o^D, n_o^F\right) = \left(\frac{n_e^D - 1}{n_e^F - n_e^C}\right) - \left(\frac{n_o^D - 1}{n_o^F - n_o^C}\right) \qquad (25)$$

Minimising ΔV will minimise prism dispersion across both of the splitting directions. Sellmeier equations are then used to calculate refractive indices for the Wollaston prism materials [55,56]. For reference, the majority of the equations sourced were full or truncated Sellmeier-type forms, while a few were of full and truncated Laurent-Cauchy forms. This variation in forms arises from the discrepancy in methods of curve fitting utilised by previous researchers, which has no material impact on accuracy. Potassium Titanyl Phosphate (KTiOPO$_4$) possessed tri-refringence and was considered as three pairs of vectors (**x,y**), (**y,z**) and (**z,x**). The Laurent equations for the extraordinary $n_e(\lambda)$ and ordinary axes $n_o(\lambda)$ of Calcium Carbonate CaCO$_3$ are given by [55,56]:

$$n_e(\lambda) = \left(2.18438 + \frac{0.0087309}{\lambda^2 - 0.01018} - 0.0024411 \cdot \lambda^2 \right)^{\frac{1}{2}} \tag{26}$$

$$n_o(\lambda) = \left(2.69705 + \frac{0.0192064}{\lambda^2 - 0.01020} - 0.0151624 \cdot \lambda^2 \right)^{\frac{1}{2}} \tag{27}$$

The Sellmeier equations for Zinc Germanium Phosphide ZnGeP$_2$ are similarly given by:

$$n_e(\lambda) = \left(8.0929 + \frac{1.8649 \cdot \lambda^2}{\lambda^2 - 0.41468} + \frac{0.84052 \cdot \lambda^2}{\lambda^2 - 452.05} \right)^{\frac{1}{2}} \tag{28}$$

$$n_o(\lambda) = \left(8.0409 + \frac{1.68625 \cdot \lambda^2}{\lambda^2 - 0.40824} + \frac{1.2880 \cdot \lambda^2}{\lambda^2 - 611.05} \right)^{\frac{1}{2}} \tag{29}$$

A final measure in selecting a material is provided by a first-order estimate of spectral smear, given in absolute pixel units for expediency where each pixel is 30 µm square:

$$\begin{aligned} Smr_i &= \left| \frac{\sqrt{10}}{16} \frac{\Delta B(\lambda)}{B_{\text{Min}}(\lambda)} r_i \right| = \left| \frac{\sqrt{10}}{16} \frac{B(\lambda_2) - B(\lambda_1)}{B(\lambda_1)} r_i \right| \\ &= \left| \frac{\sqrt{10}}{16} \left[\left\{ \frac{n_e(\lambda_2) - n_o(\lambda_2)}{n_e(\lambda_1) - n_o(\lambda_1)} \right\} - 1 \right] \frac{a_i}{n_{i,j}} \right| \end{aligned} \tag{30}$$

Equation 30 was derived by Fletcher-Holmes and Harvey [45], which provides an intuitive measure of image quality, but is only relevant for a given detector array in a given dimension, as it is dependent on the overall array size and the number of pixels. To provide a new effective measure and enable a more straightforward comparison of smear, an upper value of smear Smr_{AVG}, independent of direction, was calculated from the (**x,y**) directions by:

$$Smr_{\text{Avg}}\left(Smr_{\text{X}}, Smr_{\text{Y}}\right)=\sqrt{\left(Smr_{\text{X}}\right)^2+\left(Smr_{\text{Y}}\right)^2} \qquad (31)$$

Table 3-4 following is a summary of all the considerations made for the fourteen pre-selected materials, where KTiOPO$_4$ is defined in terms of its three crystal axes (x,y,z) in cyclical vector fashion. The wedge angle β_{AVG} from (23) is calculated and averaged for all three required prisms. β_{AVG} is an inverse trigonometric function of birefringence, whose mean value B_{Avg} from 1.1 μm to 1.7 μm is given for reference. A small birefringence leads to a relatively large wedge angle and results in thick prisms, which not may be readily obtainable or affordable. For reference here, the clear aperture divided by the tangent of the wedge angle gives the depth required. This is explicitly considered later, but the relative values of birefringence are considered here as one part of the considerations. To assist in minimising bulk material and the potentially the overall cost, a heuristic used was that the prisms should not be thicker than any other orthogonal dimension. This lead to an upper bound of π/4 radians on the wedge angle.

Prism Material	Wedge Angle β_{AVG} (degrees)	Mean Birefringence B_{AVG}	ΔAbbe ΔV	Spectral Smear Smr_{AVG} (pixels)
BaB$_2$O$_4$	29.3	-0.115	-14.95	0.147
CaCO$_3$	23.0	-0.158	109.59	1.443
Ga$_2$Se$_3$	11.3	-0.336	10.10	1.102
LiNbO$_3$	41.5	-0.074	5.08	1.361
MgF$_2$	80.5	0.010	-3.72	0.597
SiO$_2$	82.3	0.008	-2.71	1.667
KD$_2$PO$_4$	65.8	-0.031	46.18	5.781
KH$_2$PO$_4$	72.7	-0.027	50.40	12.672
KTP (x,y)	83.9	-0.007	4.40	3.739
KTP (y,z)	38.7	-0.082	8.89	1.313
KTP (z,x)	36.6	0.089	-13.28	1.512
Al$_2$O$_3$	82.7	-0.008	-0.283	0.257
AgGaSe$_2$	64.3	-0.027	-5.35	10.220
AgGaS$_2$	49.7	-0.053	-2.75	0.172
YVO$_4$	17.9	0.205	-4.30	0.587
ZnGeP$_2$	56.3	0.046	-2.08	6.078

Table 3-4: Calculated values of metrics used to select a suitable prism material

The difference in Abbe numbers ΔV is a comparative measure indicating which crystal axis is more constringent. As stated previously it is only a relative indicator of mean values, being intuitively formed as a first-order gauge of dispersion but is useful nevertheless. The estimated spectral smear from Equation 31 may lead to only a lower bound of smear, since implicit within this expression is an assumption that birefringence follows a linear progression from two known points, which may be a simplistic assumption in this case.

Considering cost constraints and the minimisation of physical envelope, the heuristic of $\beta \leq \pi/4$ eliminates nine potential choices that would result in prisms longer than they are wide or high. The remaining options are BaB_2O_4, $CaCO_3$, Ga_2Se_3, $LiNbO_3$, YVO_4, and $KTiOPO_4$ (not xy-orientation) as potential materials for further selection. Disregarding any outlying and extreme values of ΔV eliminates $CaCO_3$, which yields relatively high smear and dispersion.

The final stage involved considering the spectral smear, thus resulting in the conclusion that BaB_2O_4 is the most suitable material. It possesses the smallest value of spectral smear comparable to the values of the remaining choices. Consultation with suppliers further supported this choice, with BaB_2O_4 prisms being both relatively affordable and easily obtainable. Only SiO_2 and $CaCO_3$ are superior on availability, but fail to meet the optical requirements on the wedge angle upper limit and spectral smear respectively. For completeness, it must be reiterated that the prevalent beta-phase crystal β-BaB_2O_4, rather than the alpha-phase, is being referred to here. The latter type differs in barium-ion positioning, leading to optical changes and is more difficult to manufacture. Further investigation of BaB_2O_4 did not highlight any features of concern for N-IRIS, such as thermo-optical response or nonlinear coefficients [55,56,57,58]. Table 3-5 concludes this section, before optical design using ray-tracing software is discussed. Table 3-6 is a reference table of key N-IRIS optical and design parameters as a summary.

Splitting (i,j)	Splitting Angle (deg)	Wedge Angle (deg)
X-Dimension (1,1)	7.908°	30.780°
Initial Y-Split (2,1)	4.947°	20.437°
Second Y-Split (2,2)	9.876°	36.645°

Table 3-5: Summary of splitting and wedge angles required for BaB_2O_4 prisms

Optical Parameter	Value of Parameter
Full Field of View	1.6°×1.0°
Objective Focal Length	250 mm
Objective F-Number	F4.9
Field-Stop Size	6.91 × 4.32 mm
Collimator Focal Length	50 mm
Collimator F-Number	F1.7
Wollaston-Prism Material	$\beta\text{-BaB}_2\text{O}_4$
Waveplate Material	SiO_2 quartz
Waveplate #1 Thickness	275.0 μm
Waveplate #2 Thickness	384.4 μm
Waveplate #3 Thickness	700.8 μm
Prism #A Wedge Angle	30.78°
Prism #B Wedge Angle	20.44°
Prism #C Wedge Angle	36.65°
Condenser Focal Length	25 mm
Condenser F-Number	F2.0
InGaAs FPA Dimensions	7.68 × 9.6 mm
InGaAs FPA Pixel Pitch	30 μm

Table 3-6: Summary table of selected key optical and design parameters

3.4 Ray Tracing of N-IRIS System

Following waveband selection and prism design, *Zemax* software was used for optical modelling and ray tracing. This allowed an accurate design of N-IRIS, along with predictions of optical performance such as the modulation transfer function (MTF). The optical prescription for the *XenICs* lens was not available and could not be integrated into a full design. Required design parameters included surface number, radius of curvature, thickness to next surface, glass type or medium, any aspheric data, and semi-diameters with decentre and tilt data if applicable. Decoupling the lens effects was however needed to assess correctly the impact of the N-IRIS optics upon image quality, so this deficiency was acceptable although not optimal. Paraxial lenses were substituted for their defined real equivalents in *Zemax* software during this initial modelling.

Figure 3-26 is the N-IRIS design from the field-stop onwards, showing the layout of the SiO_2 retarders and BaB_2O_4 prisms. Figure 3-27 show the FPA division of the eight sub-images, with the design yielding no vignetting. Figure 3-28 and Figure 3-29 show the spectral smear in the sub-images, where the outer boxes signify each vertex and the middle box represents the centroid. The box length matches the pixel pitch and confirms that the smear calculated within Table 3-4 is consistent. The geometric and RMS spreads across all sub-images reside between one-third and one-sixth of a single pixel. Figure 3-30 is the polychromatic MTF in conventional format, where the upper black line denotes the diffraction limit. Figure 3-31 shows the surface MTF response for object orientations other than purely sagittal or tangential. Figure 3-30 and Figure 3-31 indicate an MTF response that suggests an acceptable contrast quality, without any characteristics of concern such as zeros or suppression.

Figure 3-32 is the polychromatic PSF for a typical centroid ray, illustrating that smear does not overwhelm the formed image of a point source. Figure 3-33 is the culmination of the previous factors, being a geometric image analysis of an alphabetic target. This enables qualitative interpretation, aggregating all optical effects into the single measure of the image quality expected at the focal plane. As can be seen from Figure 3-33, the characters are legible and suggest that the N-IRIS design is feasible at least with high-quality lenses. Figure 3-34 and Figure 3-35 are the respective worst-case and best-case chromatic focal shifts for N-IRIS at the image plane using paraxial lenses. Additional measures included optical path difference (OPD) and ray aberration, but these exhibited no significant negative features and did not affect the conclusion of viability.
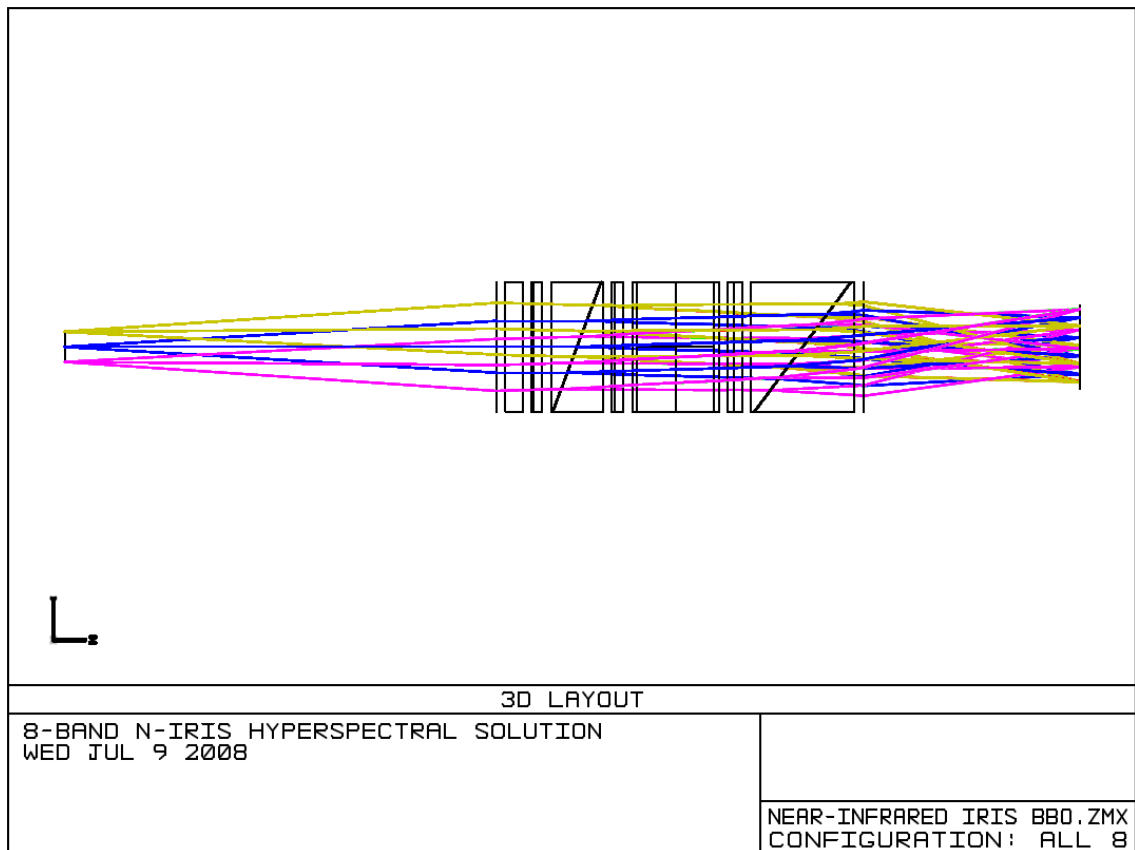
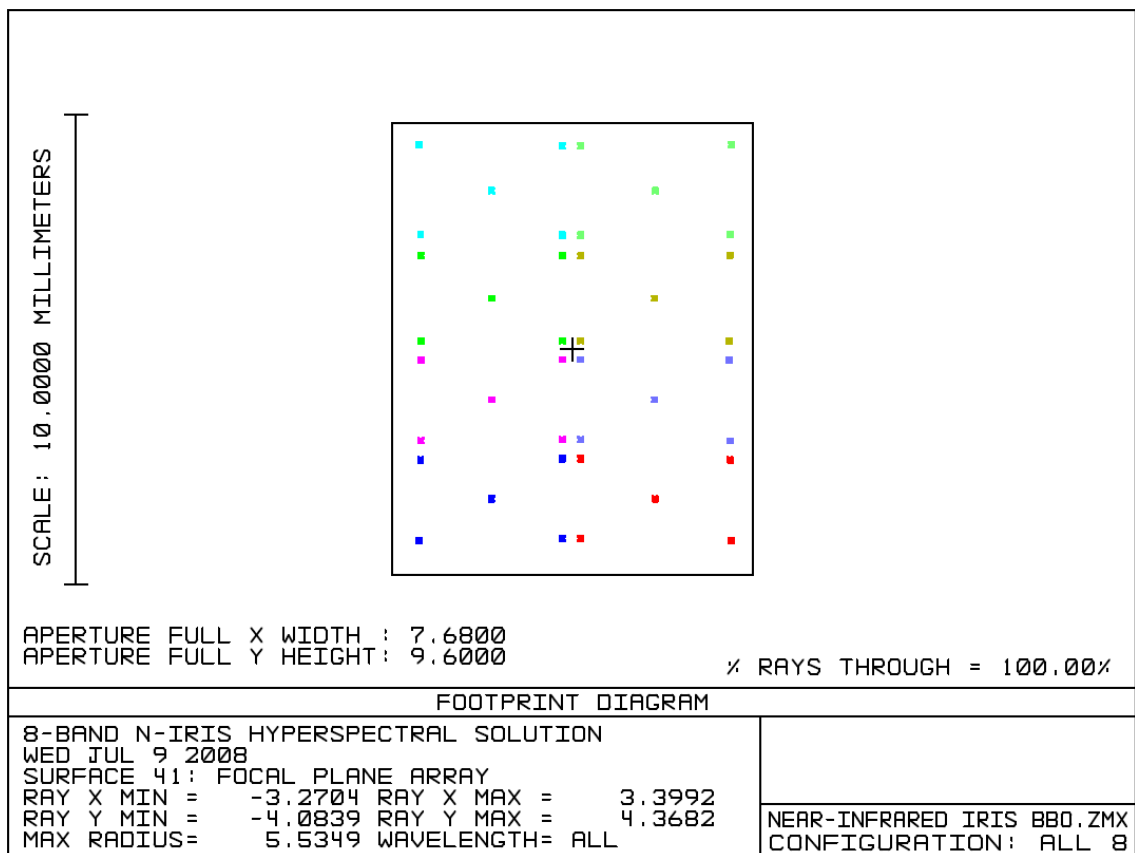**Figure 3-26:** Schematic layout for N-IRIS from field stop onwards employing paraxial lenses

Figure 3-27: Footprint diagram showing colour-coded distribution of the eight sub-images
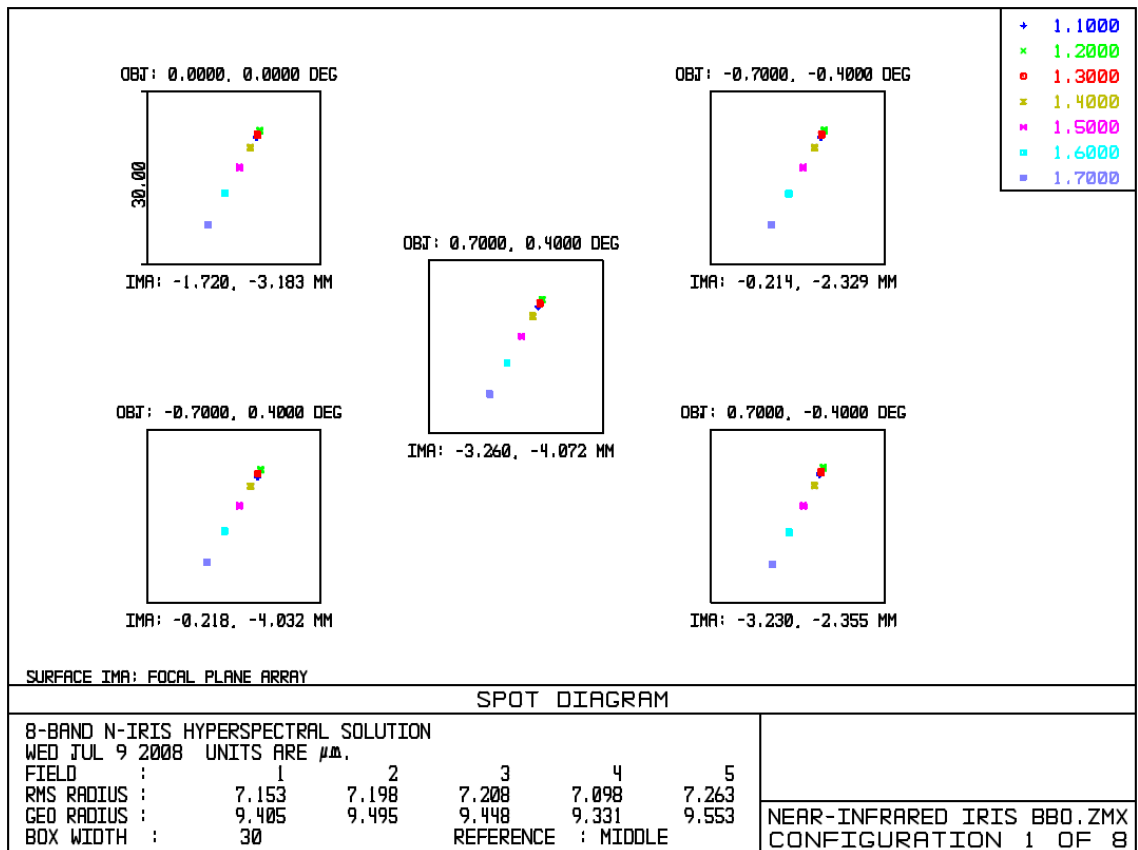
Figure 3-28: Maximal smear expected of 19.1 µm – the solid boxes represent one 30 µm pixel
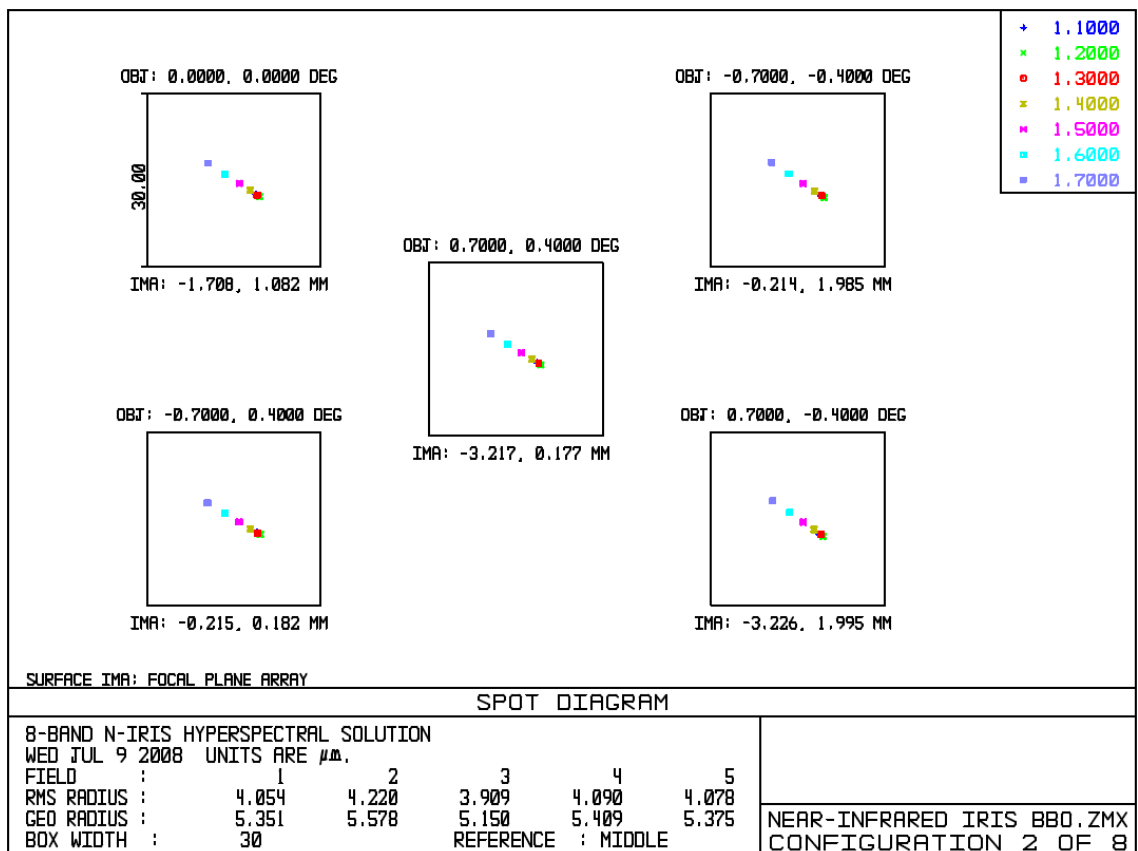

Figure 3-29: Minimal smear expected of 10.8 µm – the solid boxes represent one 30 µm pixel
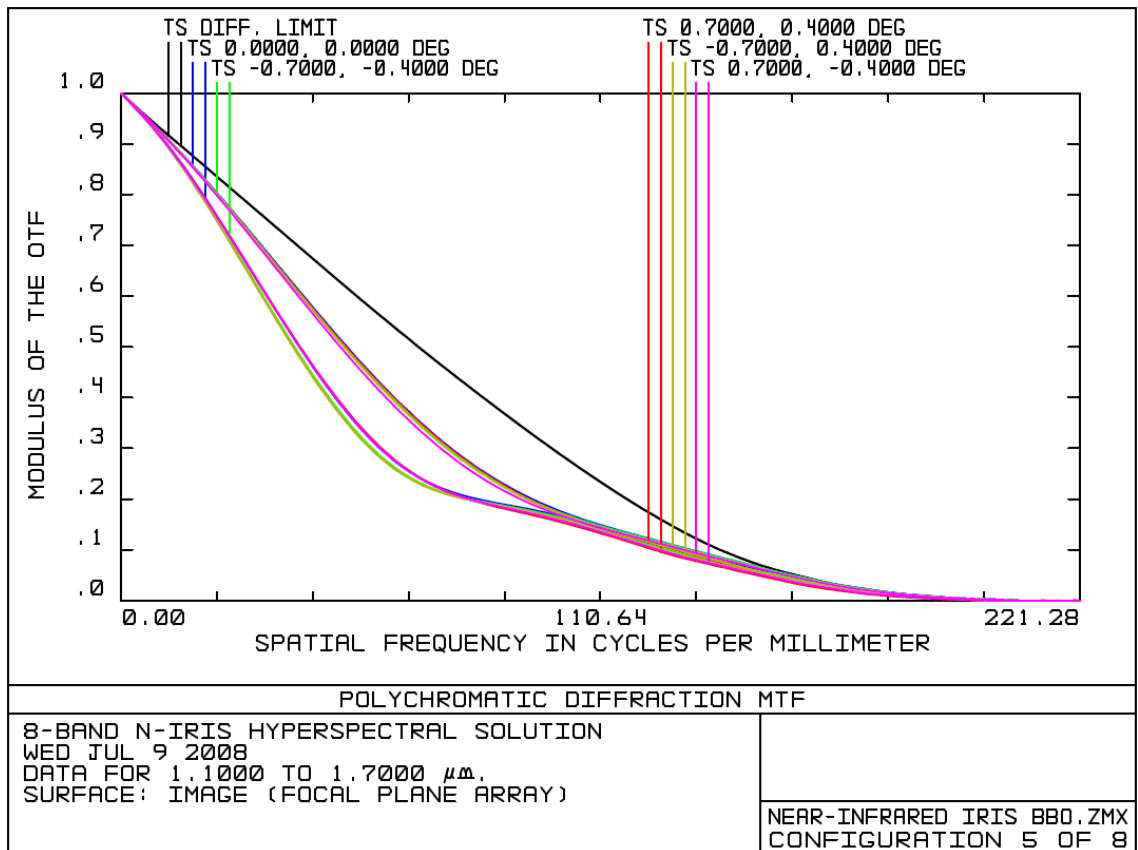
Figure 3-30: Polychromatic MTF with diffraction limit for typical N-IRIS subimages
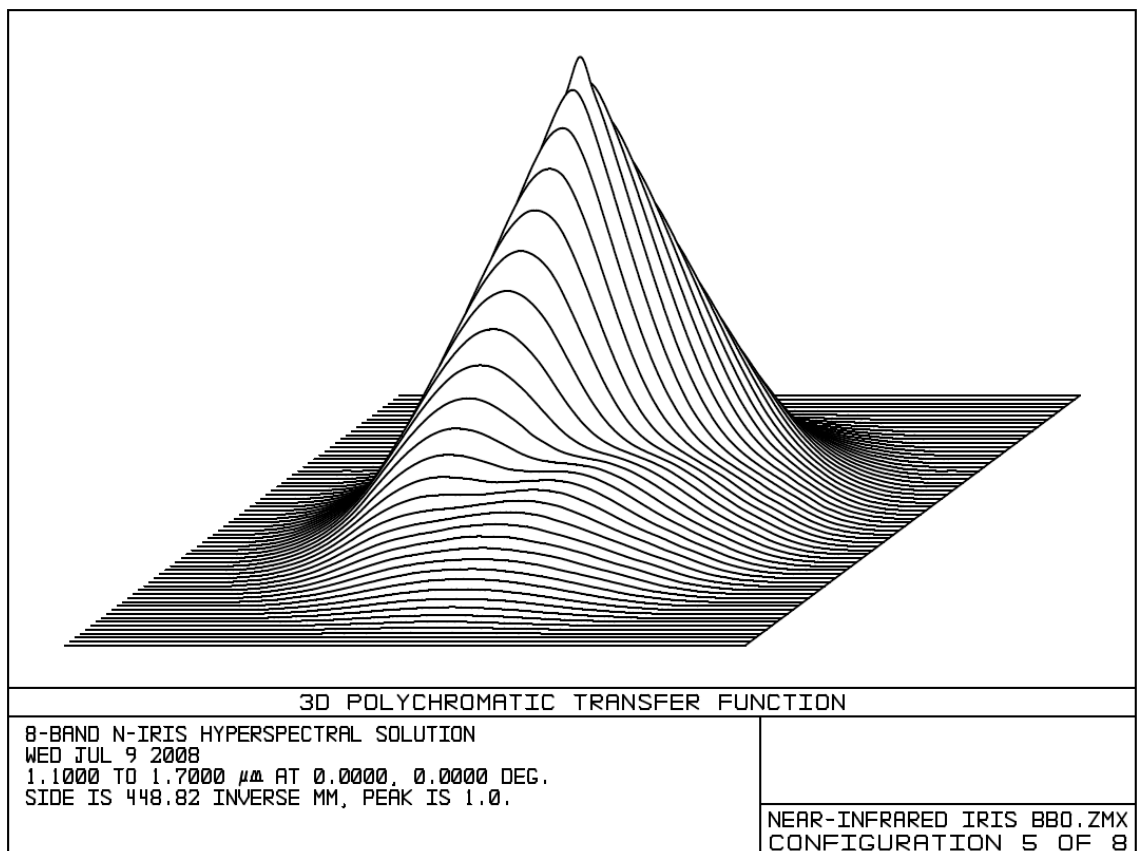
Figure 3-31: 3D rendering Surface MTF (polychromatic) for typical centroid ray

POLYCHROMATIC FFT PSF

| 8-BAND N-IRIS HYPERSPECTRAL SOLUTION
WED JUL 9 2008
1.1000 TO 1.7000 μm AT 0.0000, 0.0000 DEG.
SIDE IS 135.60 μm.
SURFACE: IMAGE (FOCAL PLANE ARRAY)
REFERENCE COORDINATES: -1.70380E+000, -1.07072E+000 | NEAR-INFRARED IRIS BBO.ZMX
CONFIGURATION 5 OF 8 |
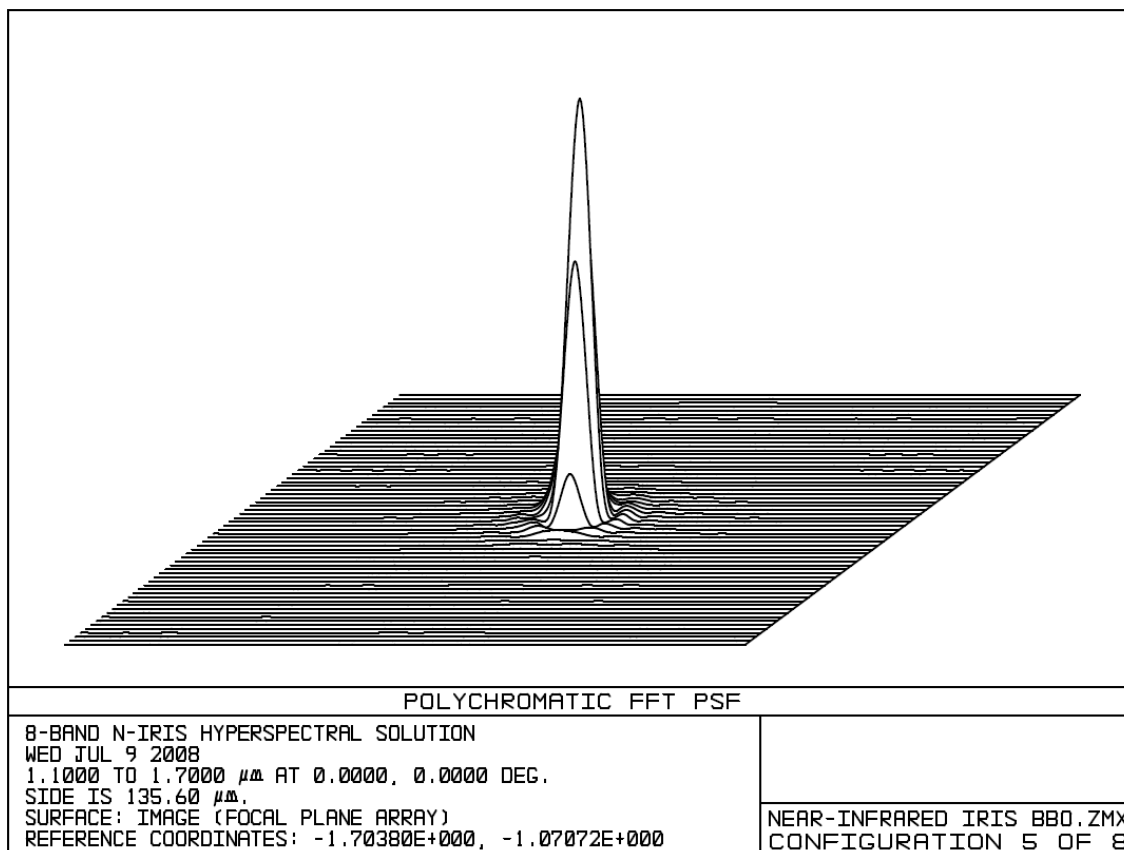
Figure 3-32: 3D rendering of polychromatic PSF for typical centroid ray

IMAGE DIAGRAM

| 8-BAND N-IRIS HYPERSPECTRAL SOLUTION
WED JUL 9 2008
SCALE BAR IS 1.2000 MILLIMETERS.
FIELD POSITION: 0.0000, 0.0000 DEG
EFFICIENCY: 100.000%, TOTAL POWER: 1.000E+000 WATTS
SURFACE: 41 | NEAR-INFRARED IRIS BBO.ZMX
CONFIGURATION: ALL 8 |

Figure 3-33: Geometric image analysis at the focal plane, indicating negligible impact of smearing

Figure 3-34: Worst-case chromatic focal shift for N-IRIS at the image plane using paraxial lenses

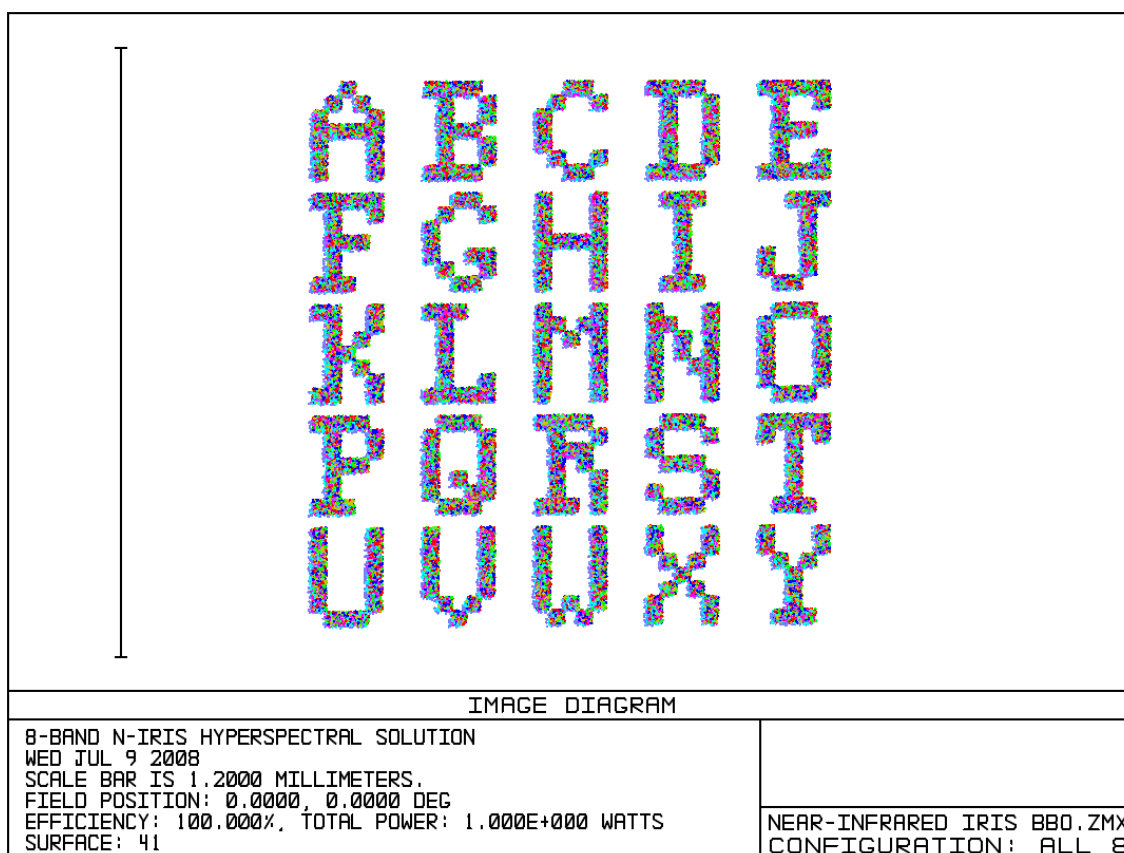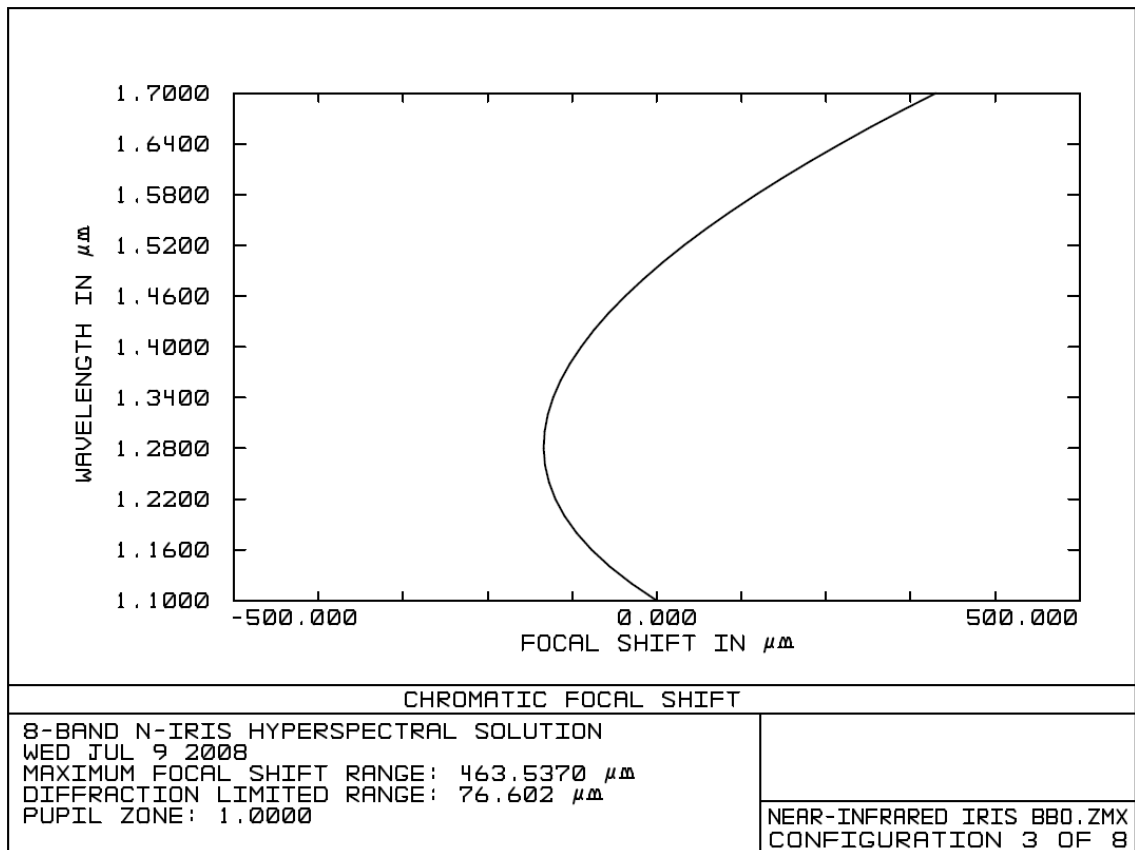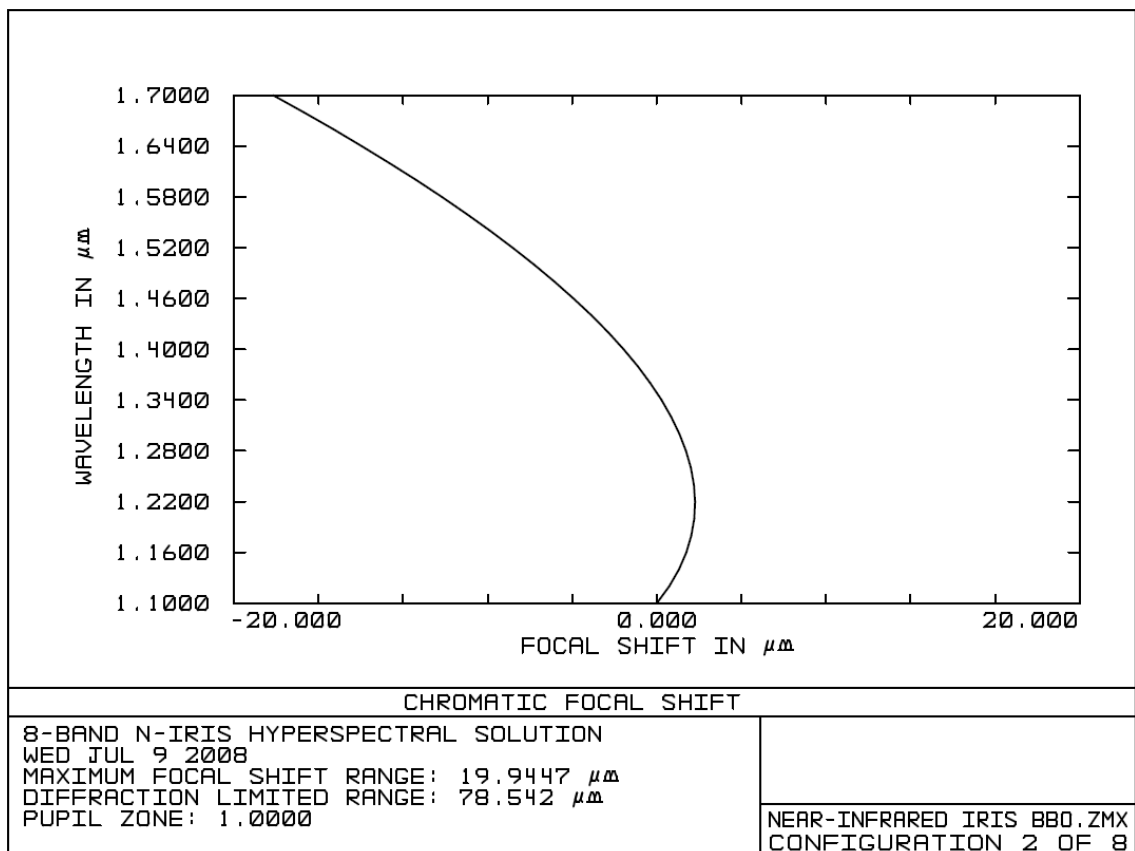**Figure 3-35:** Best-case chromatic focal shift for N-IRIS at the image plane using paraxial lenses

3.5 Integrating Lens Aberration into Model

Aside from the multi-element *XenICs* lens, optical performance data were found from the manufacturer website for the COTS lenses used as collimator and condenser. Along with respective lens prescriptions, graphs were obtained of the chromatic focal shifts, geometric spot diagrams and polychromatic diffraction MTFs. These are reproduced in Figure 3-36 to Figure 3-41 for both COTS lenses respectively. These lenses are listed as achromatic doublets, compensating for spherical aberration with design wavelengths of 1.016 μm, 1.330 μm and 1.550 μm. N-IRIS for comparison operates from 1.1 μm to 1.7 μm inclusive. It should be noted that the chromatic focal shift for the collimator lens in Figure 3-36 does not reflect the manufacturer claim of achromaticity.

Chromatic focal shifting will cause some sub-images to become defocused, whereby certain sub-images are in optimal focus while the remainder are not. This focal dependence upon wavelength can be visualised using geometric spot diagrams. Such spot diagrams indicate where point source rays will be incident upon an image plane while the MTF is also of key interest. Off-axis spatial contrast may be highly deficient for these telecomm lenses, since they are optimized for on-axis performance for data transmission in three laser wavelengths.

Figure 3-36 indicates that the chromatic focal shift for the collimator lens is extensive. Even within its design range, the longitudinal shift is almost 0.4 mm with respect to the 20 μm depth of field. Figure 3-37 similarly exhibits an extensive longitudinal shift that increases parabolically at longer wavelengths. The overall longitudinal shift is in excess of 0.75 mm with respect to the 154 μm depth of field. Both lenses will introduce significant relative defocus between the N-IRIS wavebands. Figure 3-38 and Figure 3-39 are alternative depictions of chromatic shift respectively, with the latter showing the parabolic focal shift at longer wavelengths.

Figure 3-40 and Figure 3-41 are the respective MTFs for the 'telecom' lenses; each is annotated with the diffraction limit. As can be expected from these lenses, the MTFs highlight the lack of contrast transfer from an object. Since the MTF is defined as the Fourier transform magnitude of the PSF, the resolution is significantly worse than the diffraction limit. An interim conclusion is that alternative lenses designed for imaging would significantly improve the optical performance and image quality from N-IRIS.
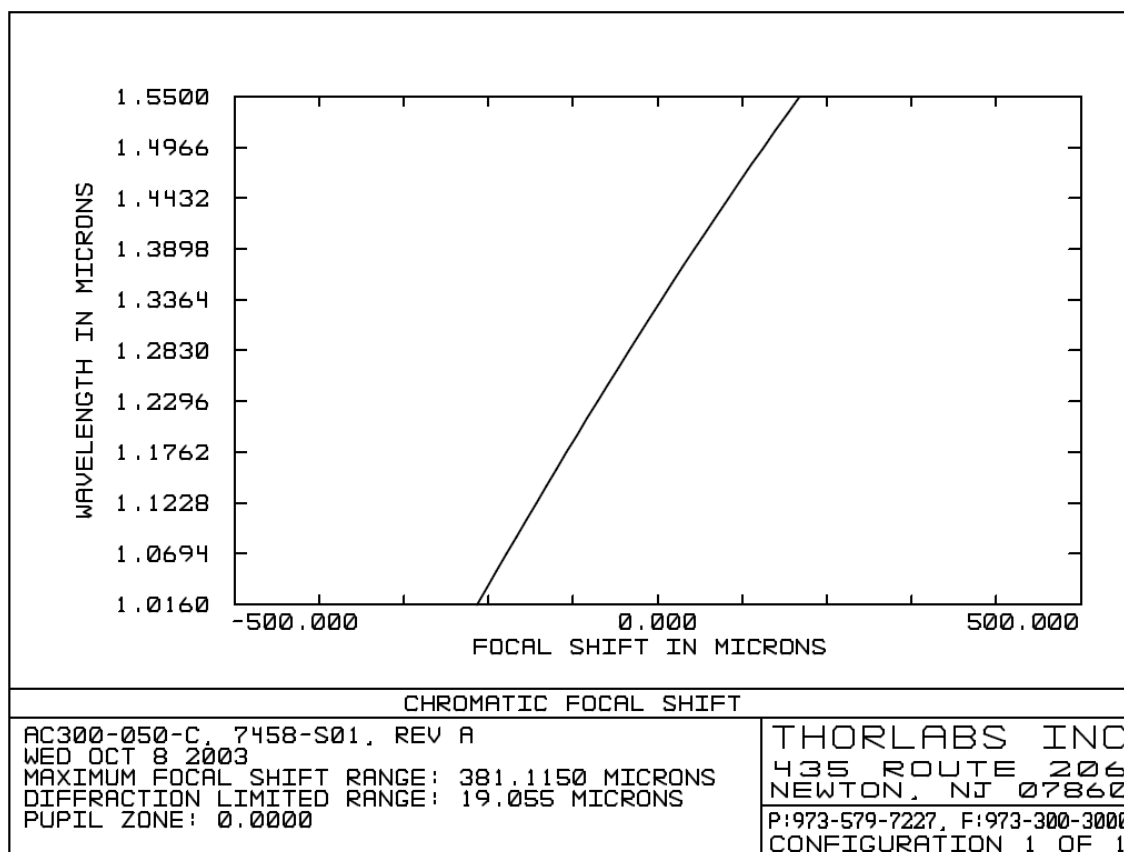
Figure 3-36: Chromatic focal shift for F=50mm collimator telecom lens
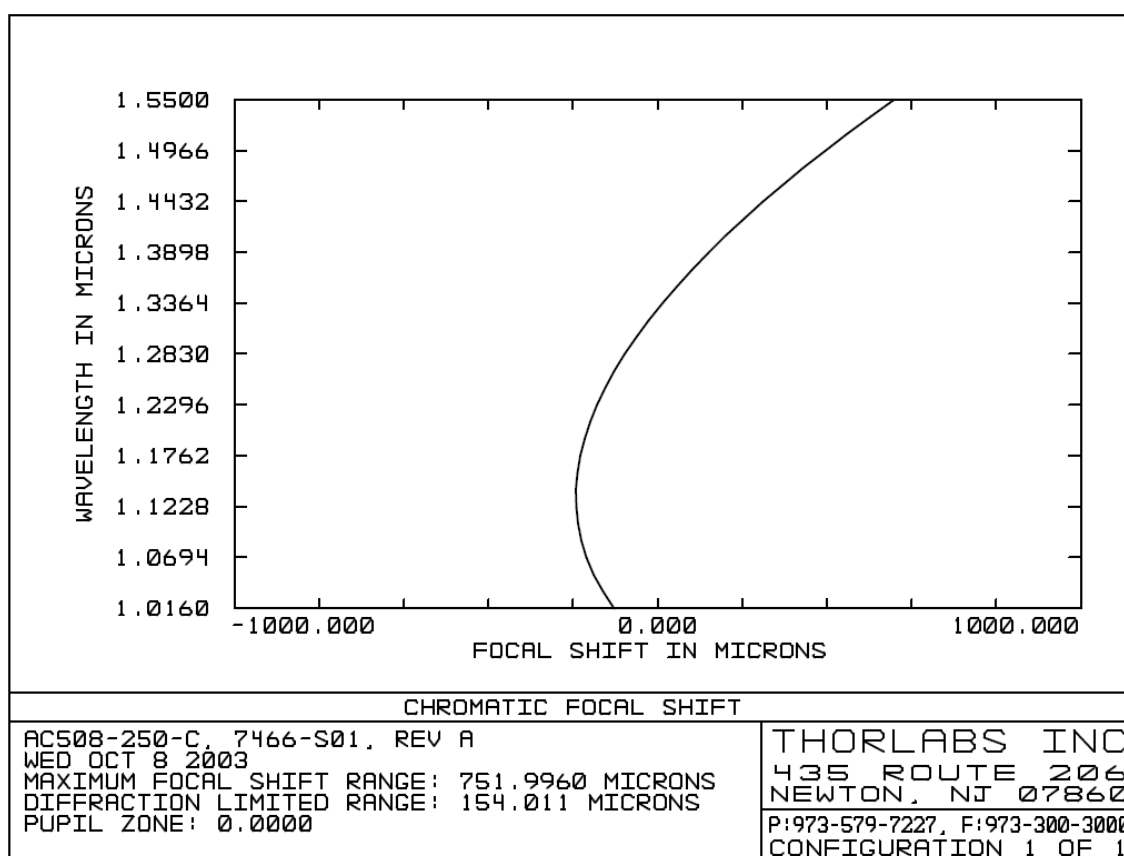
Figure 3-37: Chromatic focal shift for F=250mm objective telecom lens
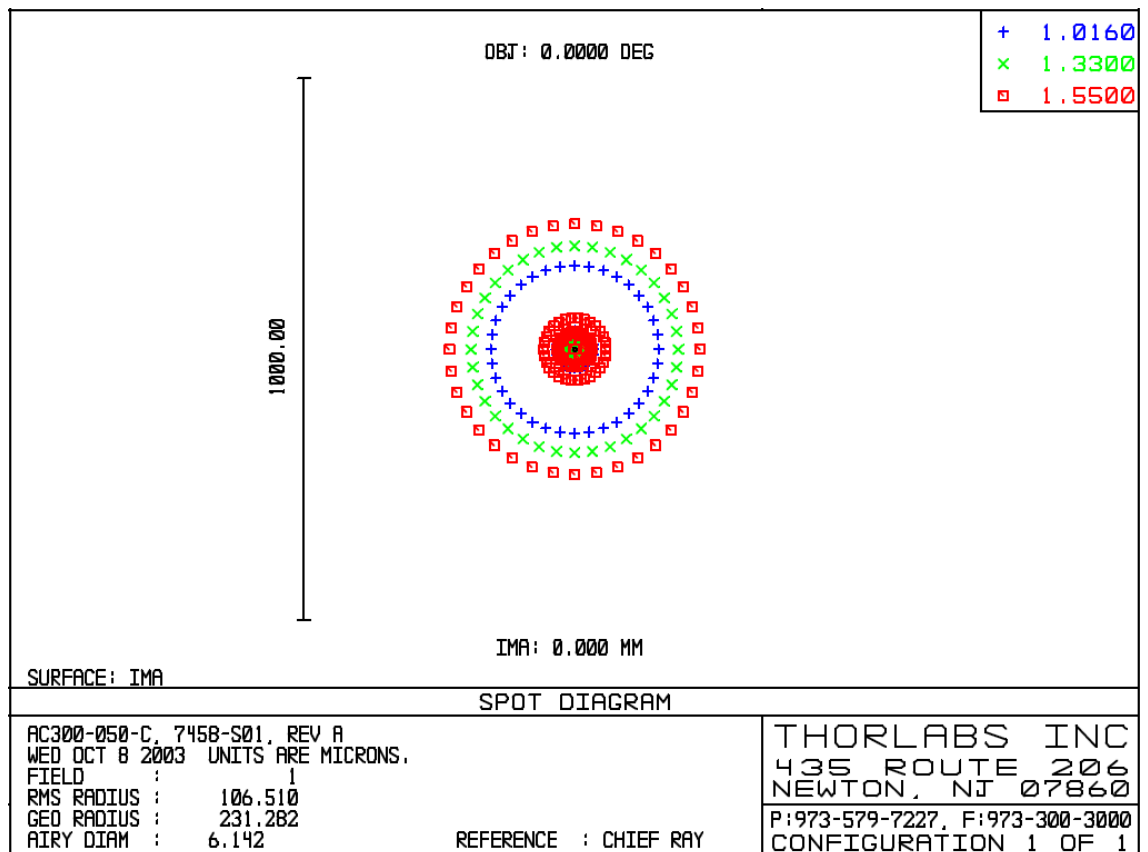
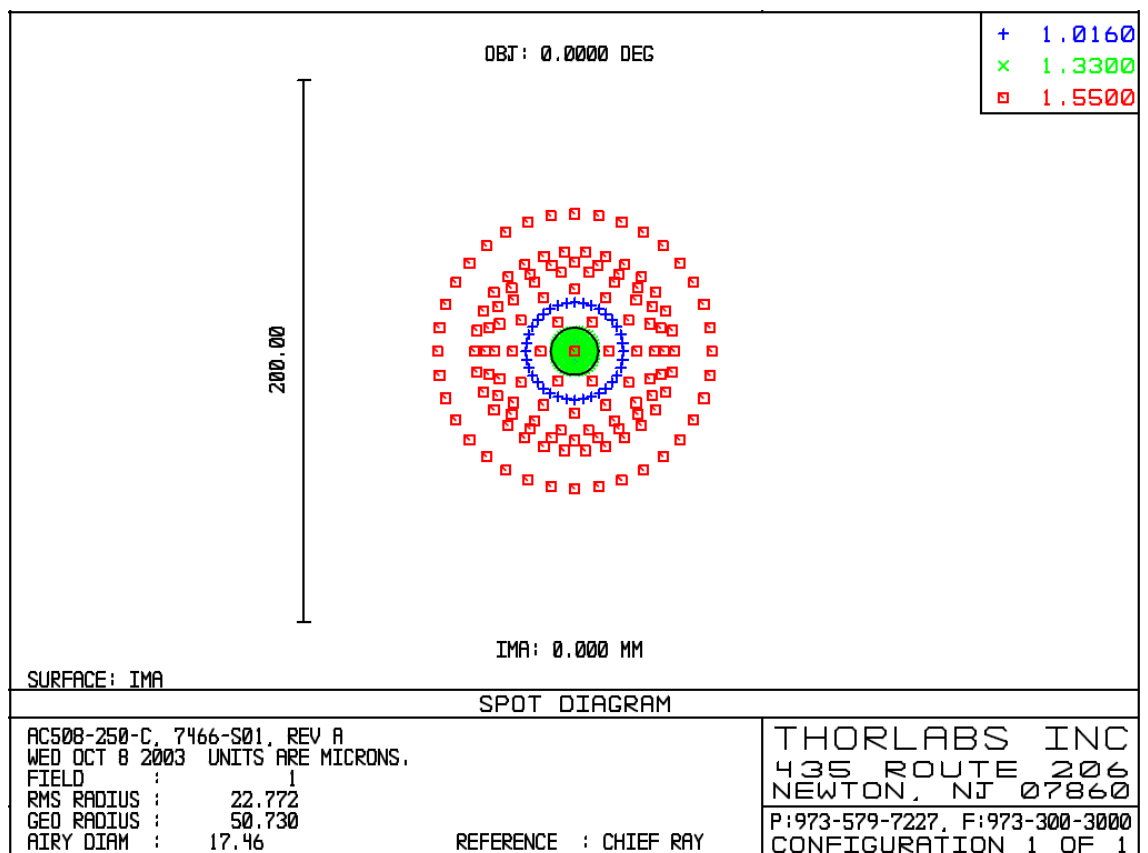**Figure 3-38:** Geometric spot diagram for F=50mm collimator telecom lens

Figure 3-39: Geometric spot diagram for F=250mm objective telecom lens
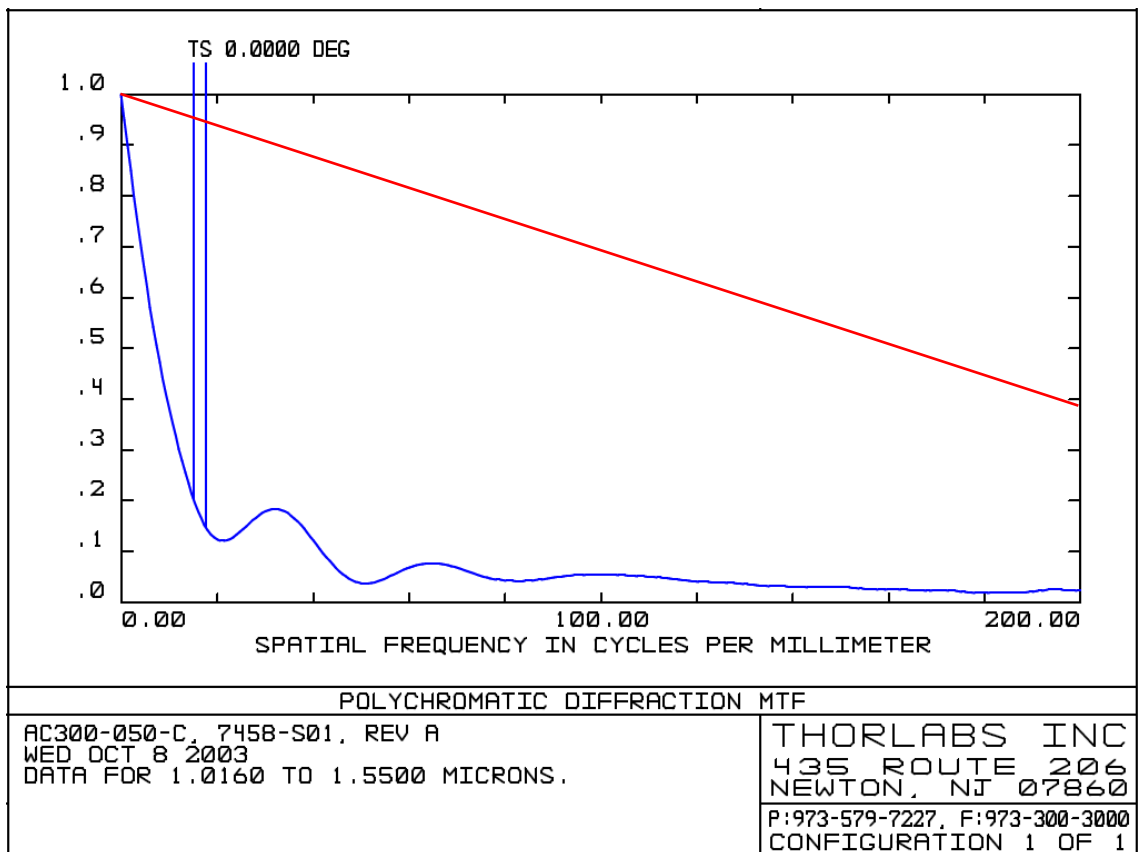
Figure 3-40: Polychromatic MTF for F=50mm collimator telecom lens, annotated with diffraction limit
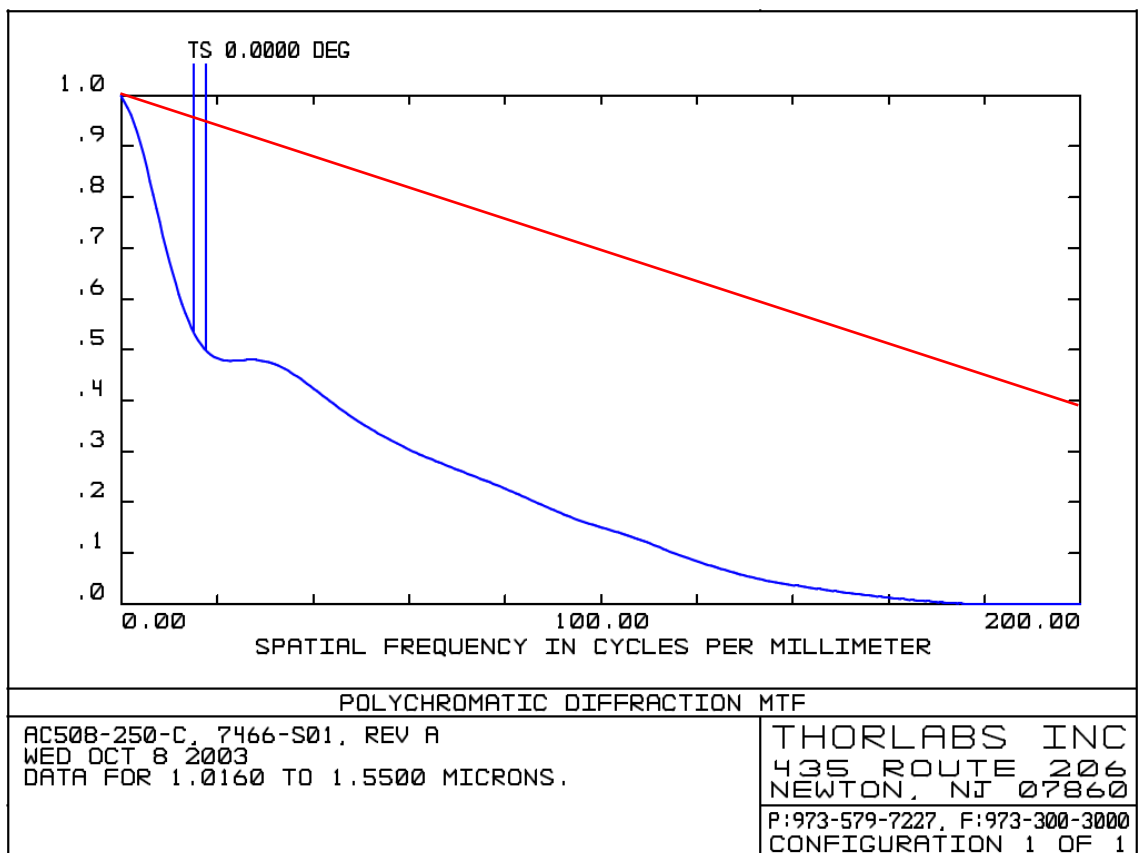
Figure 3-41: Polychromatic MTF for F=250mm objective telecom lens, annotated with diffraction limit

With this information for the real lenses assessed, they can be integrated into the main optical model, with the MTF ray-traced results given by Figure 3-42. Compared with the paraxial case of Figure 3-30, the effects of the telecomm doublets are detrimental with respect to imaging lenses. This can be observed as significant deviation from the diffraction limit, which will become manifest within imagery as notable contrast loss. The MTF is better visualised in Figure 3-43 and its Fourier transform yields the PSF as shown in Figure 3-44. An indicative spot diagram followed by a geometric image analysis is given in Figure 3-45 and Figure 3-46 respectively. Figure 3-47 is the worst-case chromatic shift of 1.16 mm, which leads to large defocus effects. Figure 3-48 is the optimal scenario for comparison.

Comparison between these graphs and those for the paraxial lens case clearly show the degradation of N-IRIS imagery when using sub-standard lenses. Financial constraints entailed the mandatory use of these lenses. The following section now details the acceptance testing for the N-IRIS sensor as initially assembled. Two key tasks are to compare the spatial MTF and spectral STCs of the actual sensor, with those predicted by theory using the model, before more work could be considered.
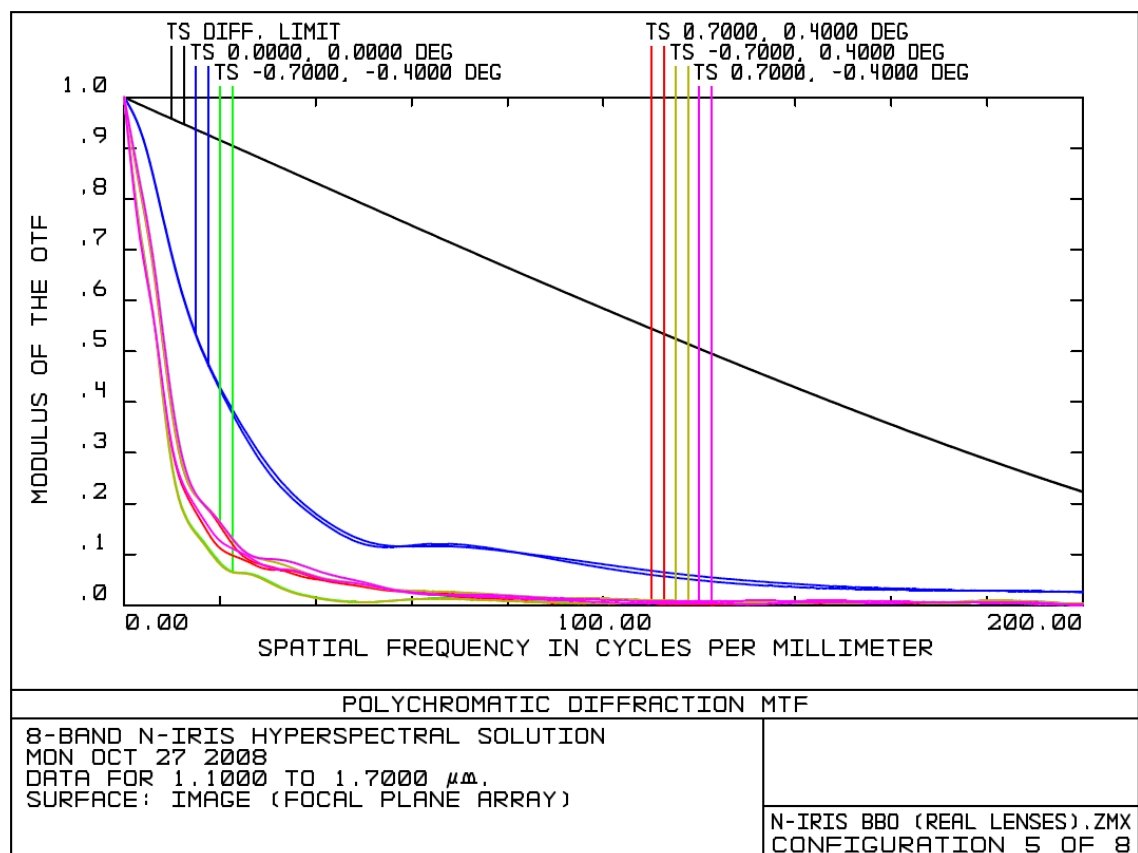
Figure 3-42: Polychromatic MTF and diffraction limit, as predicted for N-IRIS across all wavelengths

3D POLYCHROMATIC TRANSFER FUNCTION

8-BAND N-IRIS HYPERSPECTRAL SOLUTION
MON OCT 27 2008
1.1000 TO 1.7000 μm AT 0.0000, 0.0000 DEG.
SIDE IS 788.92 INVERSE MM, PEAK IS 1.0.

N-IRIS BBO (REAL LENSES).ZMX
CONFIGURATION 5 OF 8
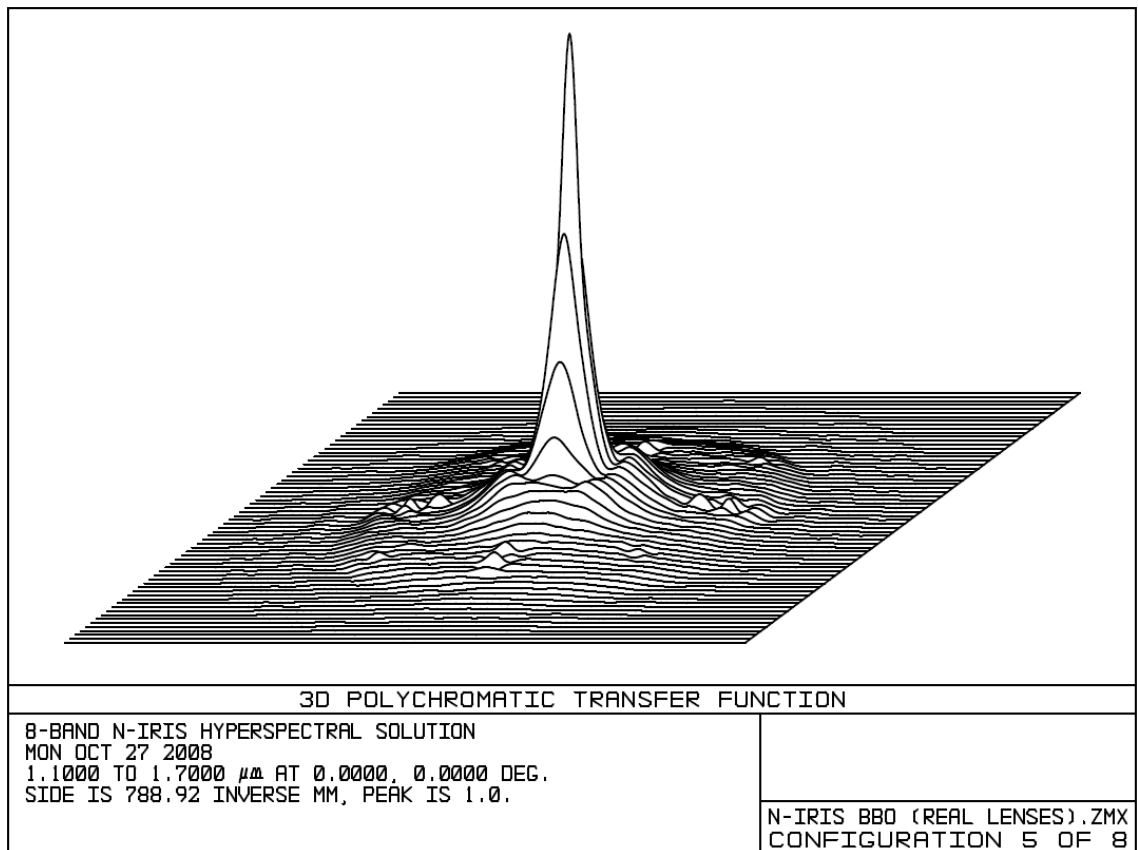
Figure 3-43: Polychromatic MTF considering real lenses and exhibiting substantial contrast loss

POLYCHROMATIC FFT PSF

8-BAND N-IRIS HYPERSPECTRAL SOLUTION
MON OCT 27 2008
1.1000 TO 1.7000 μm AT 0.0000, 0.0000 DEG.
SIDE IS 19.71 μm.
SURFACE: IMAGE (FOCAL PLANE ARRAY)
REFERENCE COORDINATES: -1.69261E+000, -1.03834E+000

N-IRIS BBO (REAL LENSES).ZMX
CONFIGURATION 5 OF 8
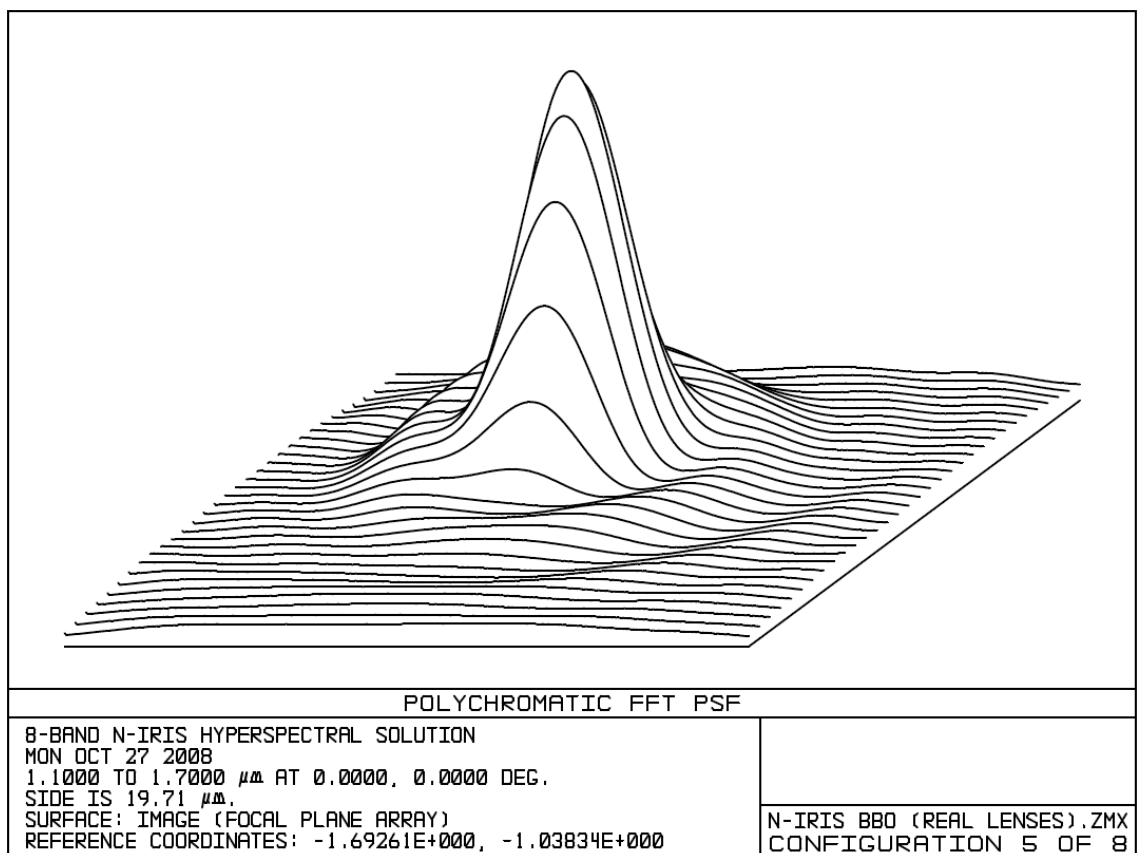
Figure 3-44: Polychromatic PSF taking real lenses into account – note the extensive dispersion
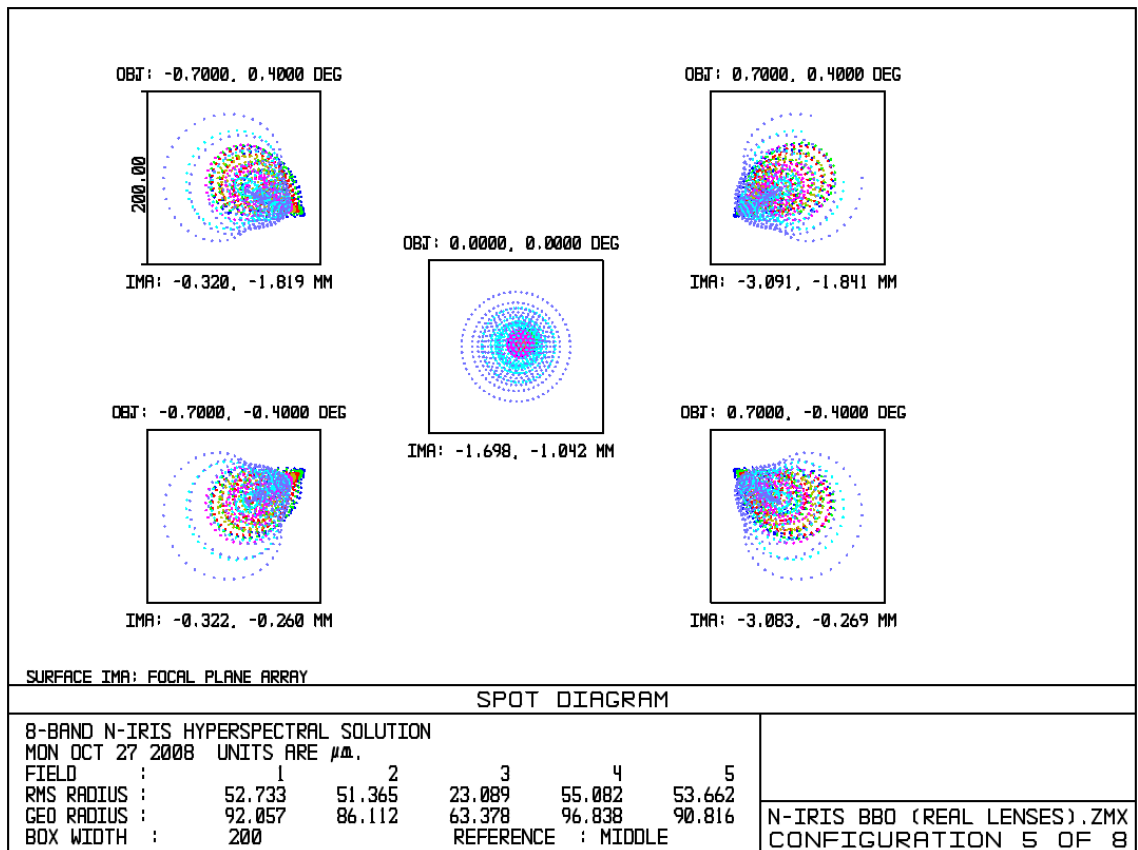
Figure 3-45: Spot diagram illustrating massive aberrations of nearly 200 µm in extent (six pixels)
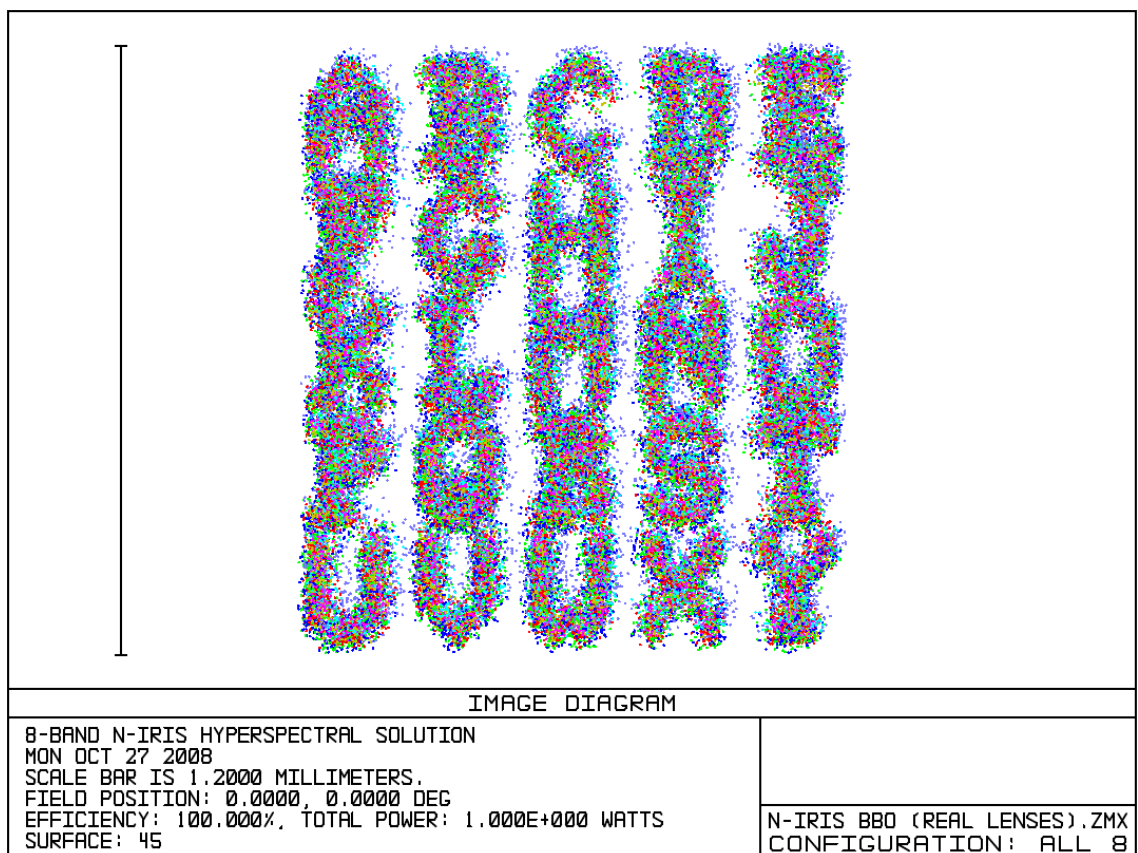
Figure 3-46: Geometric image analysis at the focal plane, indicating the huge impact of deficient lenses

CHROMATIC FOCAL SHIFT

8-BAND N-IRIS HYPERSPECTRAL SOLUTION
MON OCT 27 2008
MAXIMUM FOCAL SHIFT RANGE: 1156.2279 μm
DIFFRACTION LIMITED RANGE: 33.768 μm
PUPIL ZONE: 1.0000

N-IRIS BBO (REAL LENSES).ZMX
CONFIGURATION 3 OF 8
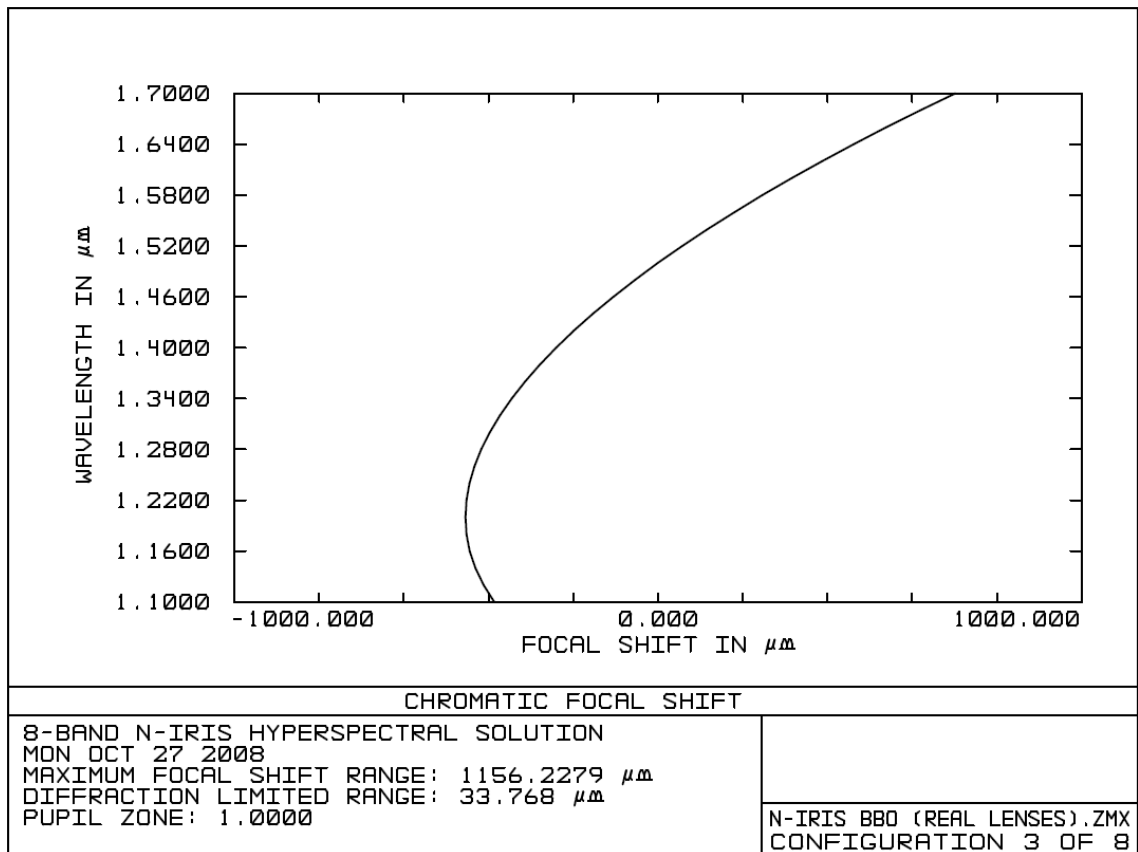
Figure 3-47: Worst-case chromatic focal shift for N-IRIS at the image plane using real lenses

CHROMATIC FOCAL SHIFT

8-BAND N-IRIS HYPERSPECTRAL SOLUTION
MON OCT 27 2008
MAXIMUM FOCAL SHIFT RANGE: 38.6215 μm
DIFFRACTION LIMITED RANGE: 37.386 μm
PUPIL ZONE: 1.0000

N-IRIS BBO (REAL LENSES).ZMX
CONFIGURATION 8 OF 8
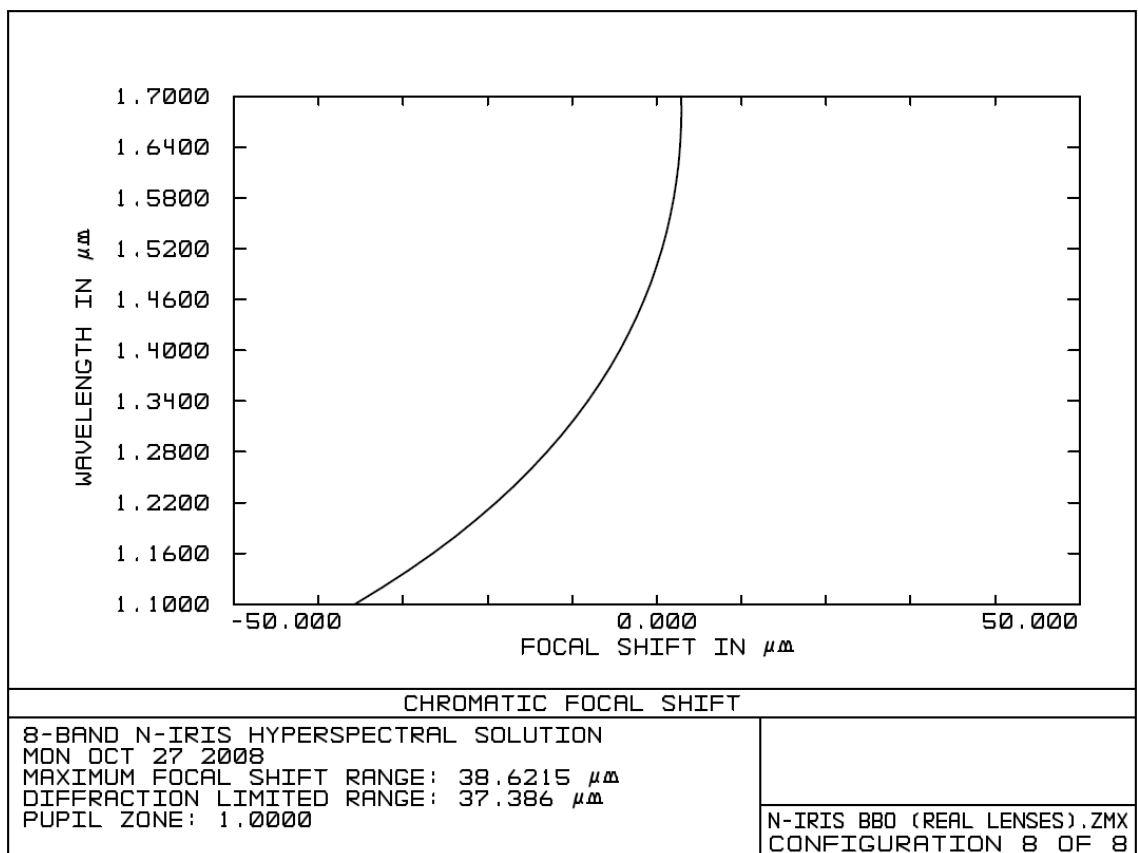
Figure 3-48: Best-case chromatic focal shift for N-IRIS at the image plane using real lenses

3.6 Assembly Testing of Initial Prototype

Figure 3-49 and Figure 3-50 are images of N-IRIS after it was assembled using COTS components. Project cost limitations resulted in the initial need for rail-mounting using suboptimal positioners and manual coarse adjustment without scale markings.
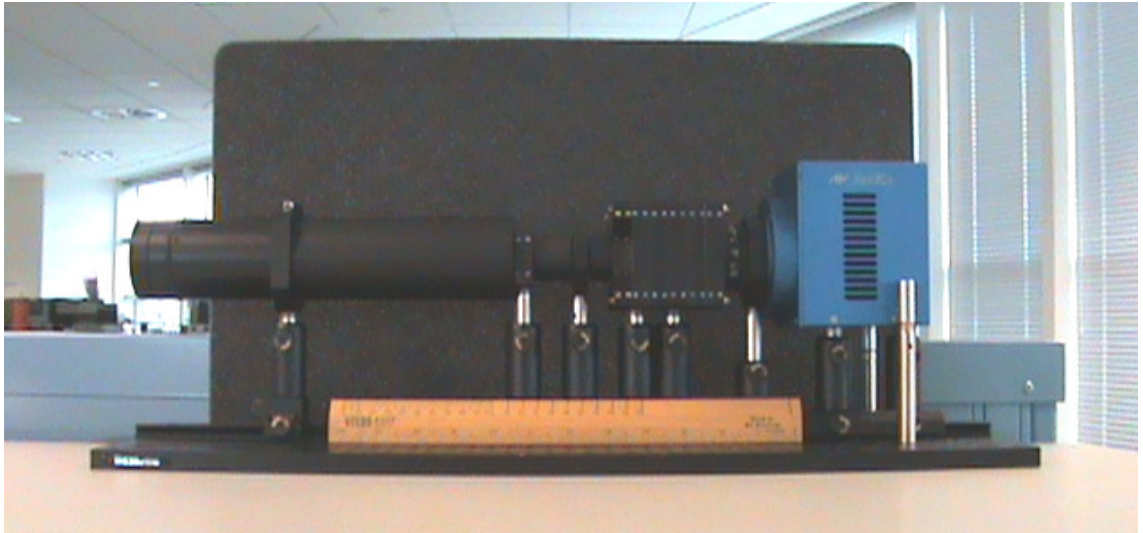
Figure 3-49: In-situ image of N-IRIS, with 30cm ruler for scale perspective (input aperture on left)
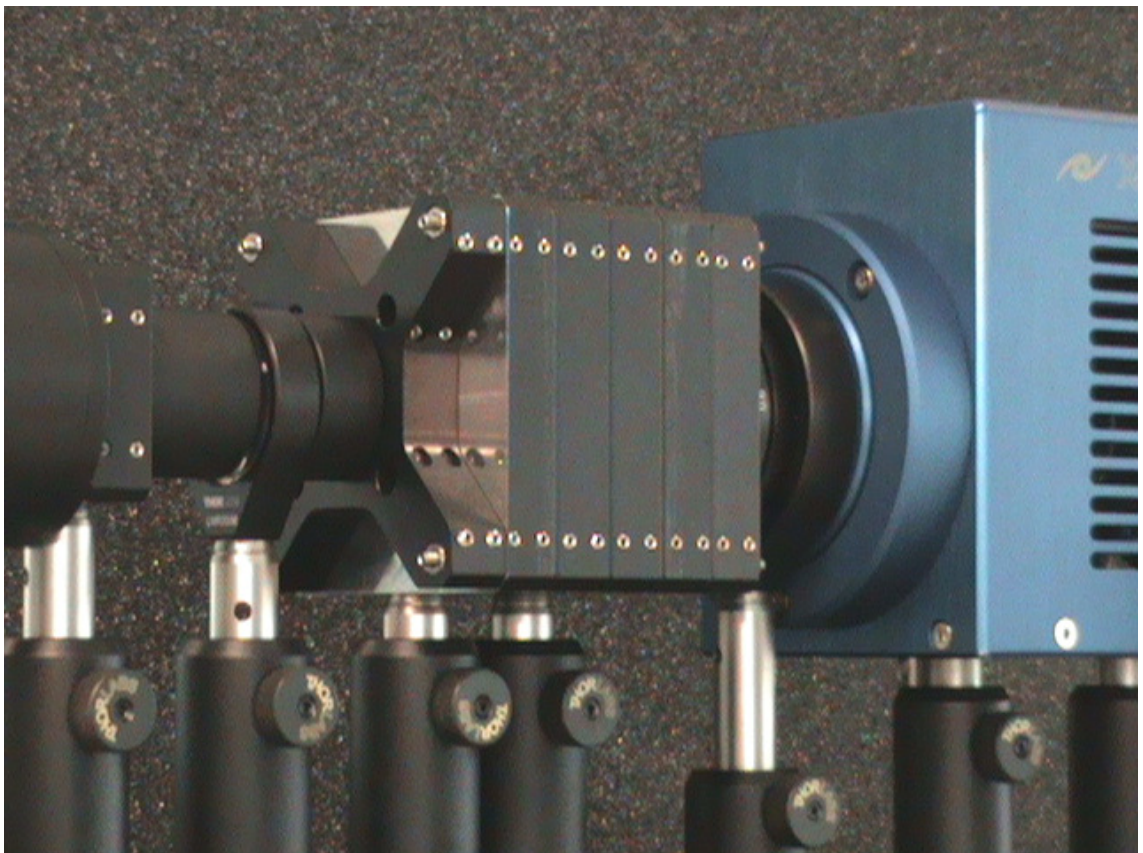
Figure 3-50: Close-up image of the retarder-prism block, situated ahead of the *XenICs* camera (blue)

The first task in completing the acceptance testing for N-IRIS was to assess the image quality and compare it against predictions. The MTF may be calculated from a slanted feature through an edge-gradient algorithm. The algorithm used was provided by the I3A (International Imaging Industry Association) that also publishes ISO (International Organization for Standardization) standards for electronic imaging. This MTF algorithm conforms to the intent of their ISO 12233 and ISO 16067 standards for spatial resolution measurements [59,60]. Figure 3-51 is the test chart used for calculating the MTF, while Figure 3-52 is an actual image from N-IRIS.
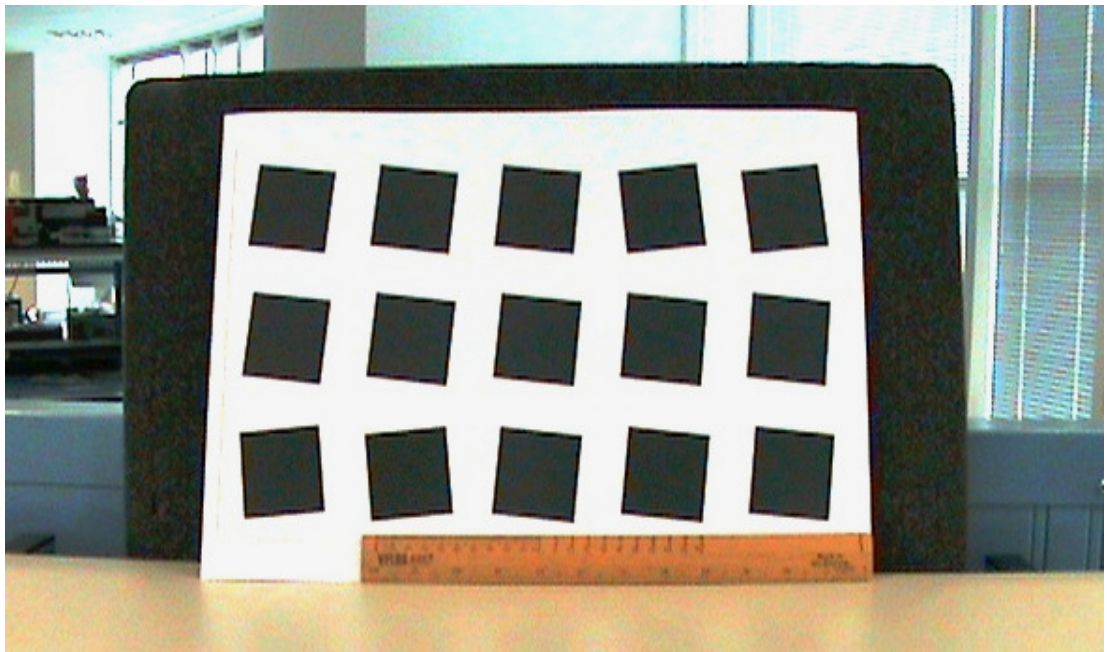
Figure 3-51: Colour image of ISO-standard test chart, with 30cm ruler for scale

Figure 3-52: N-IRIS test image of slanted edge target for MTF calculations, where the central lower-left image is in optimal focus given lens limitations

Figure 3-53 shows the predicted MTF for a central ray within an N-IRIS sub-image at the median wavelength of 1.4 μm. Although the polychromatic MTF across all sub-images is more indicative of overall image quality, it is not suitable for practical verification of MTF. The chromatic aberration that is manifest as focal shifts at the image plane means that only one sub-image is within focus at any point. Attempting to calculate an MTF for a defocused image would yield misleading results.

Considerations of broadband MTF are not suitable for N-IRIS, whose purpose is to clearly separate the incident flux into distinctive wavebands. The average wavelength was taken since the IR lamp used exhibits a blackbody spectrum through ohmic heating. The sub-image optimally within focus was used to calculate the MTF, yielding a single curve for comparison with predictions. Analysis of additional sub-images did not reveal significant and material differences.
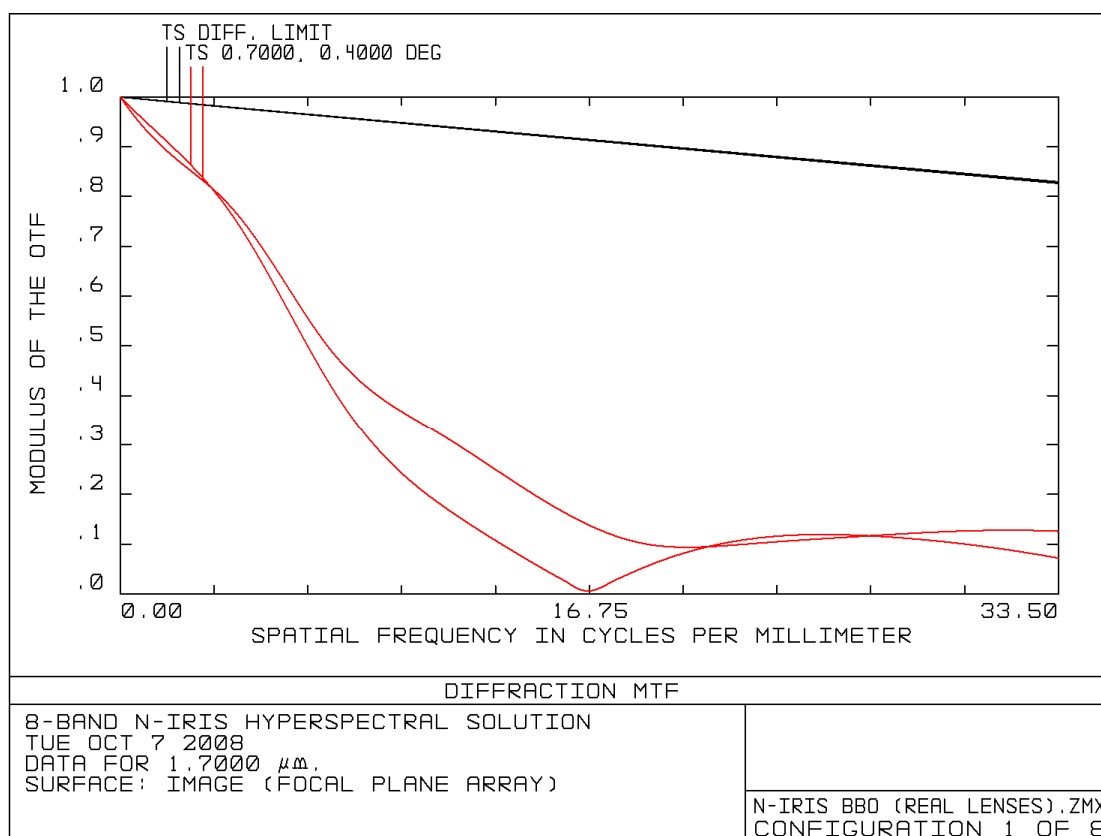
Figure 3-53: Predicted MTF and diffraction limit for N-IRIS using real lenses.

33.5 cycles per pixel corresponds to one cycle per pixel (assuming 30μm pitch)

Figure 3-54 is the calculated MTF from the N-IRIS image of the slanted-edge test chart, showing good agreement between predictions from the optical model and actual results. This is compatible with the degraded spatial contrast that was anticipated from using the telecom COTS lenses available for inclusion into N-IRIS as objective and collimator.

It can be concluded that the lenses are indeed a significant source of lens aberration, as anticipated *a priori* and from ray-tracing using available manufacture specifications. Significant improvement would potentially be possible from using SWIR imaging lenses, which are optimised for remote imaging over a panchromatic wavelength range.
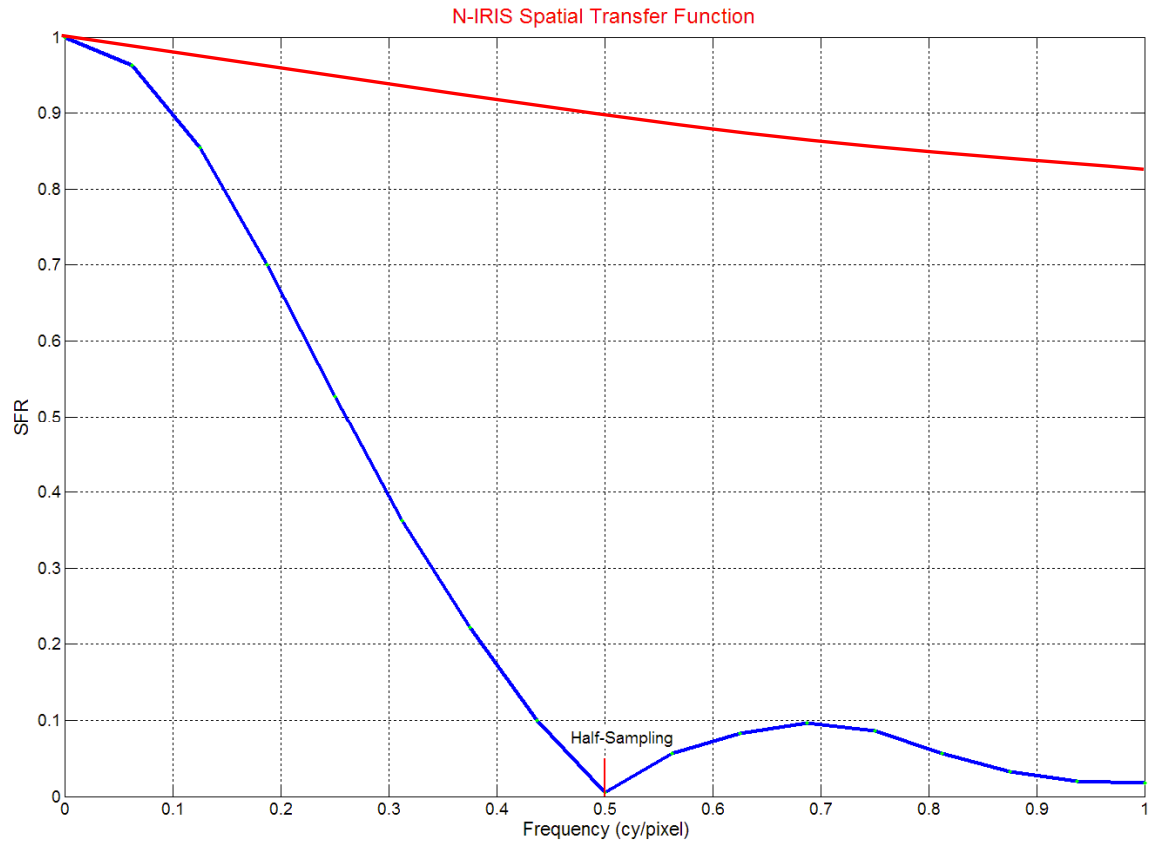
Figure 3-54: Calculated MTF with diffraction limit for N-IRIS using best sub-image from Figure 3-52

The second task needed to finish the acceptance testing of N-IRIS was to consider the spectral performance over the wavelength range of interest. Since N-IRIS is unique in the SWIR, there are no standards or metrics available for testing. It was hence necessary to devise a method for finding the spectral response of each sub-image. The following procedure outlines the basis developed for finding the STCs for N-IRIS.

1) Setup an appropriate laser with tuneable wavelength output, with a spatially diffused beam being incident upon a diffusely flat surface to reduce speckle from the laser.

2) Setup N-IRIS and defocus the objective such that the diffuse reflection is uniformly present throughout the entire FoV, as observed through the FPA for all sub-images.

3) At constant power output from the laser, record N-IRIS imagery at suitable intervals across the wavelength range of interest – maintain FPA gain and integration timings.

4) Remove the retarder-prism assembly only and repeat Step 3, in order to determine a baseline for the tuneable laser and non-IRIS components such as the SWIR lenses.

5) Calculate the mean STCs for each of the sub-images. This is achieved by averaging the intensity across each sub-image at each wavelength increment.

6) Repeat the analysis for the baseline run without the N-IRIS retarder-prism assembly, in order to determine a response curve to allow normalisation of the measured STCs.

7) Normalise the eight sub-image STCs using the baseline laser response for N-IRIS, along with calculated Fresnel losses and bulk attenuation of the removed optics.

The laser employed for this task was the *Opolette 355-II* from *Opotek Incorporated*, which is a tuneable OPO (optical parametric oscillator) laser with turnkey operation. It is based upon a Q-switched Nd:YAG pump at 355nm, coupled into an OPO to yield a range of 410nm to 2400nm. The polarisation of the required idler wave was vertical and matched the polariser orientation for N-IRIS. The laser rate was fixed at 20Hz with a pulse length of 5ns, 3mm beam diameter and 3mJ peak energy – all these values are nominal and variable.

This could have created issues for N-IRIS imaging, in that a diffuse and consistent source was desired to flood the FoV uniformly for statistical averaging. Such a source would negate localized spatial artefacts such as laser speckle. Henceforth the beam was diffused onto a white balance chart with flat spectral albedo and a diffusely flat surface to prevent specular reflection. N-IRIS was also defocused using the objective lens to enhance the spatial uniformity over each sub-image to improve measurement accuracy.

Temporal averaging of the 20Hz rate was achieved by maximising the integration time of the *XenICs* camera to one second. Images should therefore encompass 20 pulses, which is the highest possible to negate variations in pulse timing and power for the following reasons. Lesser amounts of temporal averaging were observed to create excessive flickering as pulses on occasion fell outside the integration window due to two causes.

The first is a short yet variable downtime between two frames, caused by electronic jitter and charge-coupled device (CCD) operation. The second cause is that the laser repetition rate is also variable due to timing jitter from Q-switching, whereby there is a delay in pulse formation after switch opening. These two causes combine cumulatively

from an inability to synchronise source and sensor. Employing a large integration time was required to negate variations in pulse timing and power, which could be minimised but not fully eliminated.

The particular nature of the laser required that it be operated at full power to reduce eratic changes and variation in average power over time. To protect the FPA from damage, the laser beam required attenuation to a level undetectable by a power meter. The actual laser operation is credited to EngD colleague James Beedell, who had the required authorisation and laser safety clearance.

Figure 3-55 replicates Figure 3-23 for the optimal STCs chosen for N-IRIS, in order to maximise average peak power against total power. As stated in Section 3.2, this metric minimises the power transmitted by side-lobes relative to the main transmission lobes, in order to limit the effect of spectral dispersion on image quality. Figure 3-56 is the normalized graph for the STCs measured using the tuneable laser over the same range.
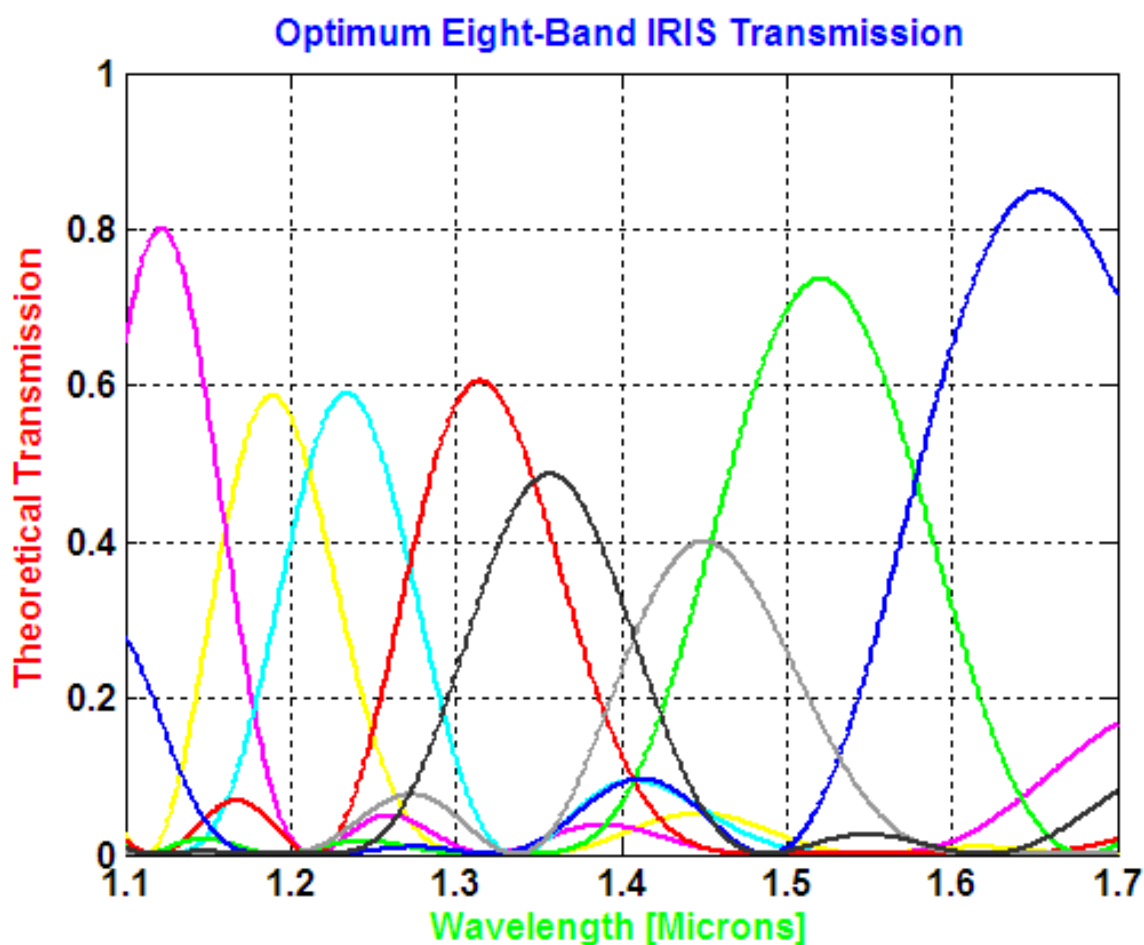
Figure 3-55: Optimum STCs for N-IRIS as predicted by theory, using paraxial lenses and ideal optics
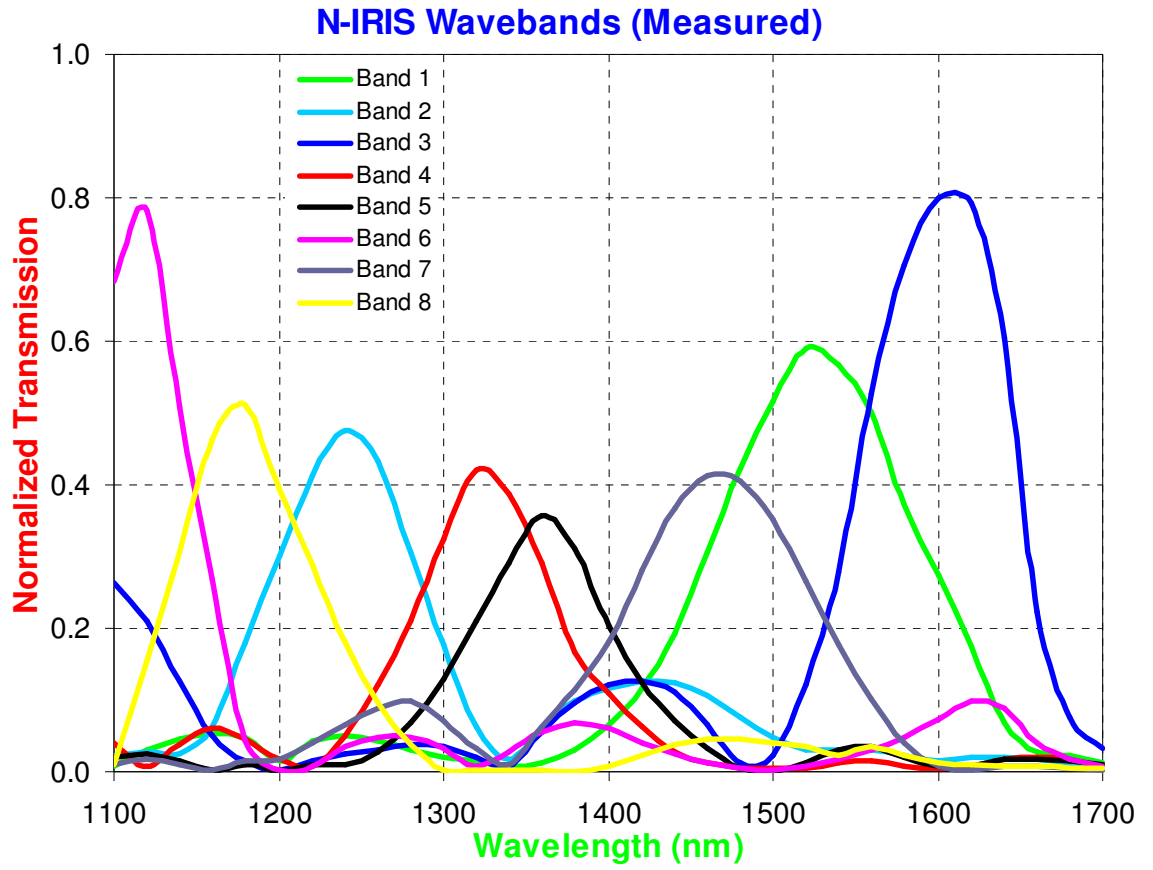
Figure 3-56: Measured STCs for N-IRIS from experiment, using non-imaging telecom lenses

Figure 3-57: Eight-band (X,Y) layout for the assembled N-IRIS, annotated with STF combinations

Figure 3-57 is the layout for the eight sub-images of the assembled N-IRIS, annotated with the STF combinations in truncated form. These annotations were made by comparing the STCs within Figure 3-56 with the theoretical plots of Figure 3-54. Recalling the STF forms given within Chapter Three, cosine terms are denoted by C and sine terms are represented by S. An example STF, which would be denoted as CCC in Figure 3-57 is:

$$T_1(\lambda, d_1, d_2, d_3) = \cos^2\left[d_1\pi\left\{\frac{n_e(\lambda) - n_o(\lambda)}{\lambda}\right\}\right]\cos^2\left[d_2\pi\left\{\frac{n_e(\lambda) - n_o(\lambda)}{\lambda}\right\}\right]\cos^2\left[d_3\pi\left\{\frac{n_e(\lambda) - n_o(\lambda)}{\lambda}\right\}\right] \quad (32)$$

Comparison with Figure 3-18 will show a $\pi/2$ rotation of the (x,y) sub-image layout, which is now 4×2 instead of 2×4 sub-images respectively. This post-design rotation was due to mounting particulars and did not affect any optical attributes – merely an exchange of X and Y unit vectors.

Aside from an unanticipated cut-off towards 1.7 µm, the measured wavebands in Figure 3-56 exhibit agreement with the predictions of Figure 3-55. The peak positions are within the limits derived from the design stage shown previously in Figure 3-24 and reproduced in Figure 3-58, using manufacturing tolerances from suppliers. Recall that these waveband limits were computed from sensitivity analysis and yielded an error envelope as given within Figure 3-24 previously. The unexpected cut-off towards 1.7 µm resulted from an extremely sharp cut-off from the *XenICs* array.
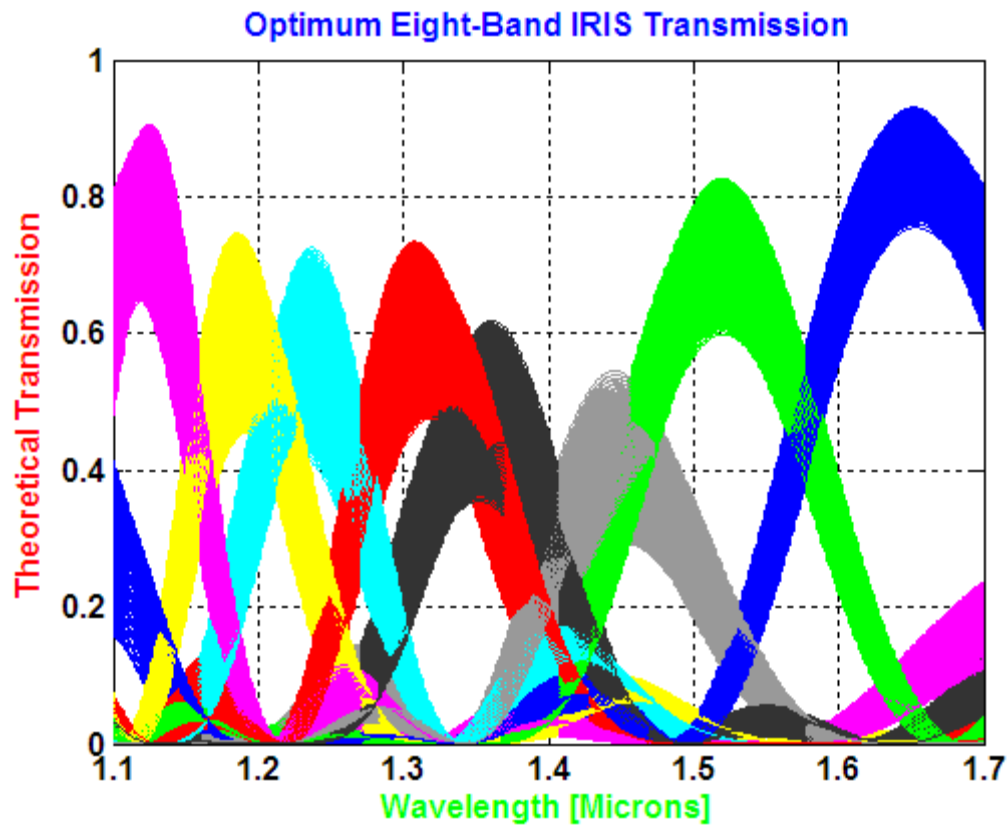
Figure 3-58: Sensitivity analysis for an error envelope of 10 µm distributed about the optimal depths. One thousand possible combinations of waveplate depths are displayed on this tolerance graph.

Recalling the design stage, the supplier did not provide spectral response data for the camera and a tuneable laser was not available for use during that period. It was taken upon confidence that the cut-off stated of 1.7 µm was the limit of signal-to-noise. Extensive searches did not yield affordable COTS bandpass filters that could provide transparency towards 1.7 µm for further investigation of the sharp cut-off.

This cut-off caused a reduction in the upper bound of wavelength range for N-IRIS from 1.7 µm down towards 1.65 µm. This limit was taken as being the wavelength at which the waveband three attenuates to half of its measured peak value. This 50 nm or 8.3% reduction in wavelength range had the added benefit in that the spectral dispersion from waveband three would be less than it otherwise would have been in the ideal case.

3.7 Upgrading towards Finalised Prototype

As stated within Section 3.1 and studied in Section 3.5, sub-standard COTS lenses were initially employed for use to maintain cost-effectiveness for N-IRIS. The objective and collimator lenses were achromatic telecomm doublets for paraxial use at specific wavelengths, with focal lengths of 250mm and 50mm respectively. Following the acceptance testing of the preceding section, funding became available to upgrade both the non-imaging lenses and non-rigid mountings. This provided promise for improved image quality and robustness for field use.

Optec SpA (*Società per Azioni*) of Italy was chosen as the preferred supplier by the author for military-grade SWIR lenses for imaging, tracking and surveillance [61]. *Optec SpA* was commissioned with producing two lenses as direct replacements for the current lenses. The collimator and objective were to be substituted for two F-1.4 lenses with the same focal lengths from *Optec SpA*. This direct substitution had no effect on the *Zemax* software ray-trace geometry as developed within this Chapter. The optical performance of these lenses was optimised with respect to cost, for high transparency and MTF resolution with respect to civilian COTS counterparts. These lenses also exhibited low reflection, vignetting, distortion and chromatic aberration – again when contrasted with civilian COTS counterparts.

Since the collimator lens is focussed upon the field-stop and is decoupled from the objective, a change in focal length for its replacement was enacted to increase the FoV. An arbitrary value-judgement was taken to increase the full-field FoV from 1.4°×0.8° to 1.7°×1.0° that led to a new 200mm objective, as a 250mm lens was not available from *Optec SpA*. The revised optical model confirmed no significant or discernable changes in ray-geometry other than the intended FoV angles. In addition to the lens upgrades, mounting components such as goniometers were procured, to further ruggedize N-IRIS and improve stability [61].

Both the objective and collimator lenses were supplied in due course and the interim upgraded N-IRIS layout with these improved lenses can be observed in Figure 3-59.
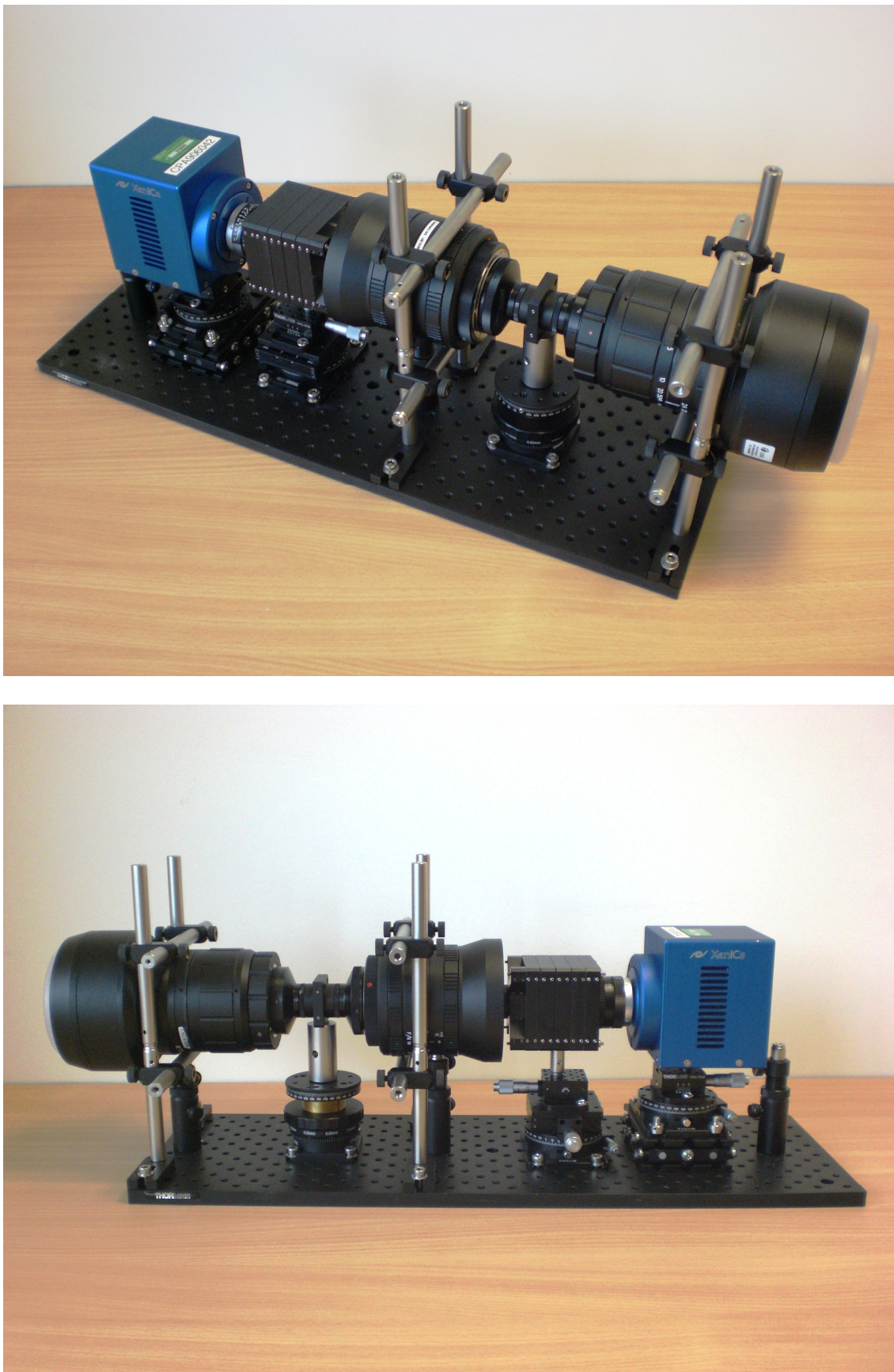
Figure 3-59: Image of the interim N-IRIS with custom imaging lenses and micrometer mountings

A direct replacement for the condenser lens was not possible. The net result was the urgent need for an alternative, *in lieu* of the 25mm F-1.4 lens that was commissioned but not supplied. Many COTS lenses were not suitable for a variety of factors, including unsuitable apertures, wavelength ranges and IR filtering. Figure 3-60 illustrates the corner vignetting still created by the deficient condenser lens, with the image taken from a separate research task into material discrimination and assisted anomaly detection.
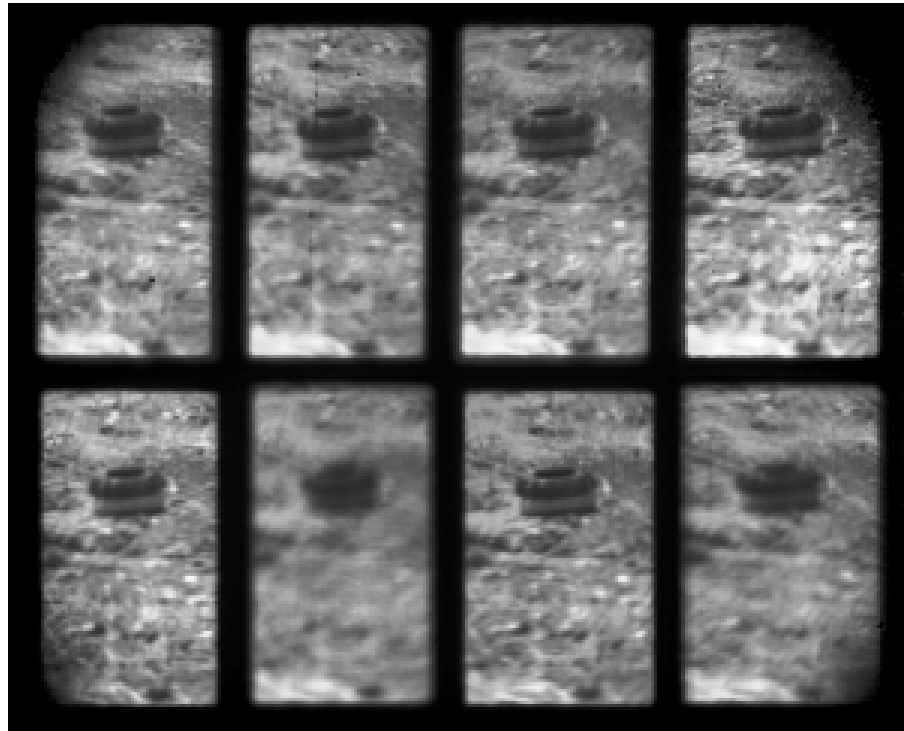
Figure 3-60: Example image from the interim N-IRIS, highlighting chromatic aberration and vignetting. The scene involved is an inert VS90 anti-personnel landmine, which is lying on a surface of bare earth.

The Canon L-Series range was discovered as a suitable replacement, despite being designed for SLR (single-lens reflex) operation in the visible. These lenses incorporated CaF_2 aspheric elements that are transparent in the SWIR region with low dispersion with respect to alternatives. A short loan allowed the investigation of the Canon 24mm F-1.4 lens by mounting it to N-IRIS and manually comparing any improvements. It was then found that the recorded images were virtually vignetting-free. Considering time constraints, it was deemed that the marginal cost of further searching exceeded the marginal benefits to be gained. The Canon L-Series lens was then obtained and mounted accordingly, allowing the project to advance and progress, although without an optimal SWIR condenser lens. Figure 3-61 is the otherwise finalised configuration for N-IRIS, with the substitute condenser lens mounted. Figure 3-62 and Figure 3-63 are two indicative examples of N-IRIS imagery after the upgrade of the condenser lens.

Figure 3-61: In-situ images of the finalised N-IRIS prototype, with Canon L-Series and *Optec* lenses

Figure 3-62: Example output from N-IRIS (post-condenser upgrade) with notable spectral differences of vegetation between the sub-images

Figure 3-63: Example output from N-IRIS (post-condenser upgrade) of a heavy good vehicle, at a distance of approximately 250m

3.8 Testing of Finalised Prototype

In an analogous manner to Section 4.6, the MTF was calculated using an ISO-standard algorithm operating upon the captured image of a binary slanted-edge target. The slant target (16cm × 27cm) was imprinted within the margins of A4 card at a distance of 9 m, allowing for an incidental check on the 1.7°×1.0° FoV for N-IRIS, which was observed to be as expected from *Zemax* software. Figure 3-64 is the N-IRIS captured image of the slant target, while Figure 3-67 is the graph showing the MTF curves for N-IRIS against measured baseline curves from the Canon L-Series and consumer TV lenses alone, to understand the effects of these components. The MTF curve for N-IRIS was determined by using the best-focussed sub-image from eight different captures, which was a central sub-image. It can be observed that the previous frequency null point at 0.5 pairs per pixel in Figure 3-65 is no longer present, thus highlighting the improved MTF.

The TV lens exhibits deficient response beyond 0.5 pairs per pixel where the actual real response is zero and spurious aliasing dominates. With respect to the Canon L-Series alone, N-IRIS exhibits slight degradation towards higher frequencies but maintains an MTF response towards higher frequencies. This degradation is minor considering the additional optics required by N-IRIS, of which the two high-grade SWIR lenses were anticipated to have a negligible impact upon MTF due to their high-performance design.

Figure 3-64: N-IRIS test image of slanted edge target for MTF calculations with reduced vignetting
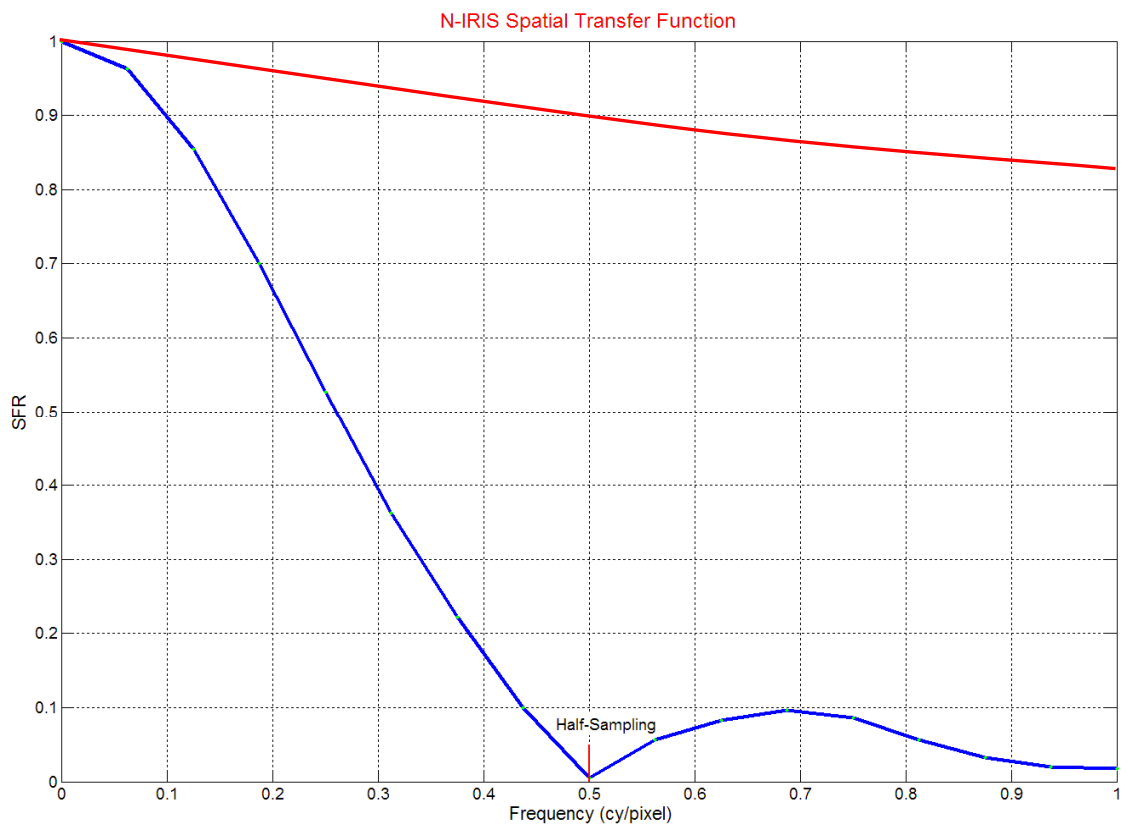
Figure 3-65: Previously calculated MTF with diffraction limit for
N-IRIS using non-imaging telecomm achromatic doublet lenses
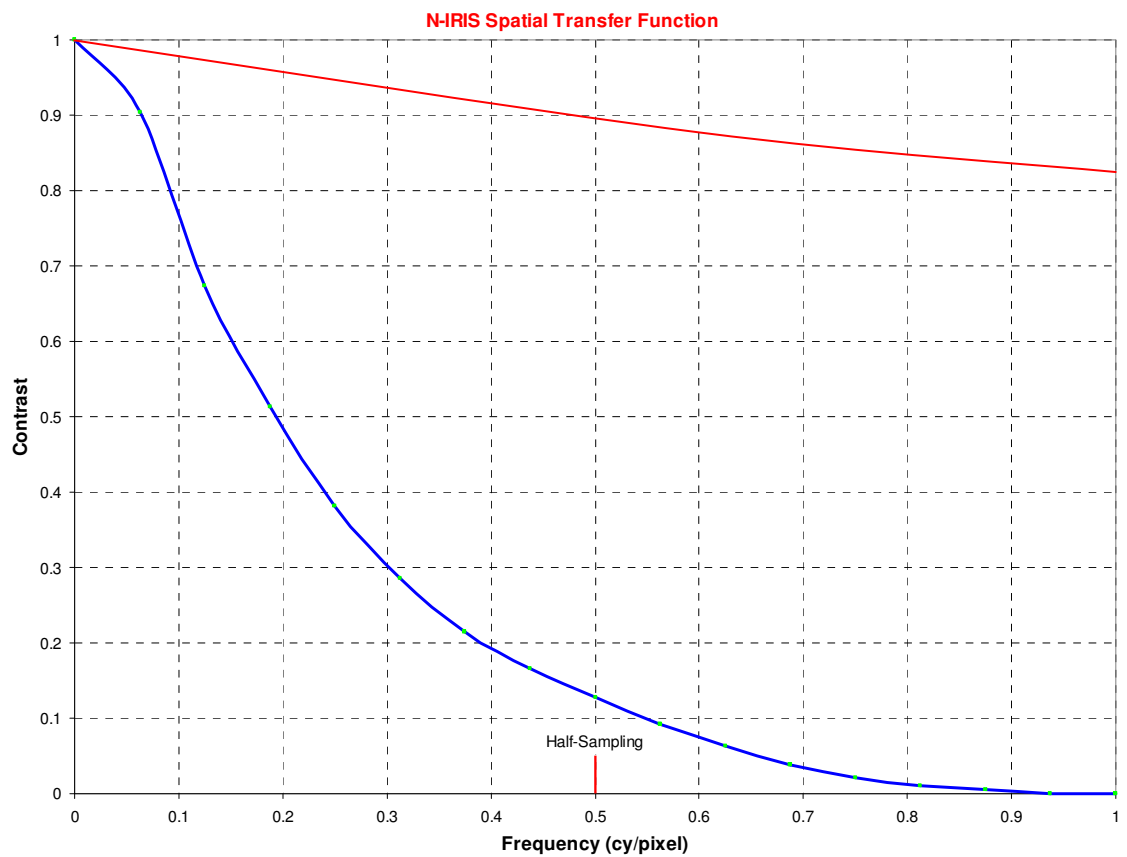
Figure 3-66: Calculated MTF with diffraction limit for N-IRIS using optimal subimage from Figure 3-64
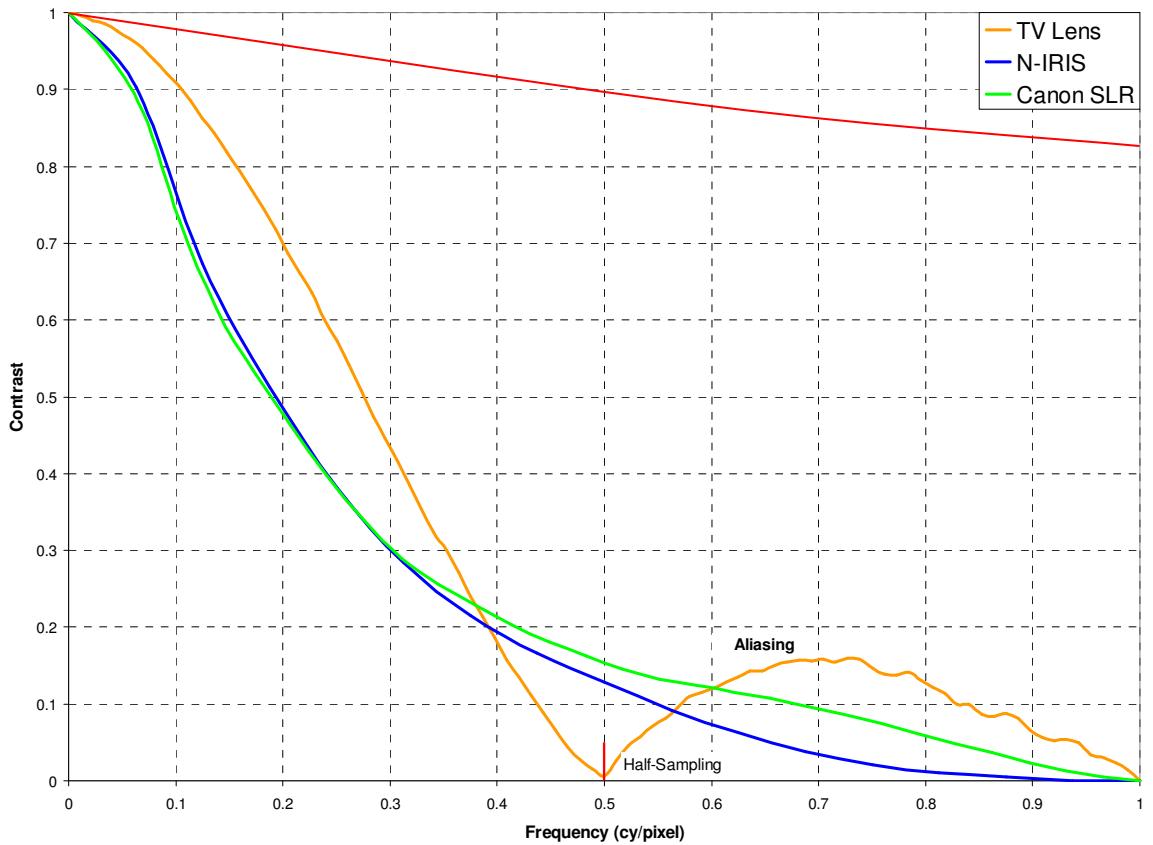
Figure 3-67: MTF comparison of finalised N-IRIS prototype and lens baselines (*TV* and *Canon L-Series*)

With the finalised N-IRIS prototype designed and assembled, Chapter Four describes experiments testing if the performance of N-IRIS is sufficient for SWIR snapshot HSI. One objective was to consider the extraction of the sub-images and co-registering them into a hypercube for eventual input into anomaly detection algorithms, the evaluation of which is outwith the principle scope of this thesis. The main objective is analysis of variance (ANOVA) testing to disprove the hypothesis that "N-IRIS cannot provide additional spectral information beyond its broadband counterpart".

> **CONCLUSION** – This chapter described the N-IRIS design and verification process, with the supplied SWIR camera and lenses acting as the starting point for the design process. The required splitting arrangement to achieve eight subimages was described, along with the necessary field stop size and resultant pixel spread length at a given distance. The choice of quartz was made for the waveplates with their thicknesses optimised to minimise the ratio of sidelobes to main peaks for a uniform passband distribution. Based on cost considerations and image quality, beta barium-borate was selected as the most suitable prism material for N-IRIS. Ray-trace optical modelling was performed for N-IRIS with paraxial and real lenses respectively, with key optical parameters reported. The eventual assembled prototype was tested for basic verification, before and after the integration of upgraded lenses that were available to N-IRIS after the initial prototype.

Chapter 4:
Experiments for Necessary and Sufficient Performance of N-IRIS Prototype

ABSTRACT – This chapter describes work to demonstrate the necessary and sufficient performance of N-IRIS for SWIR snapshot HSI. The extraction and co-registration of hypercubes from N-IRIS imagery is examined to determine the issues affecting the exploitation of imagery in anomaly detection or classification algorithms. A potential solution in the form of optical mapping is examined as a solution to issues of subimage warping. Using open-source databases, simulated N-IRIS responses enable an initial consideration of material discrimination performance. This is further studied with an ANOVA (analysis of variance) experiment to disprove the null hypothesis that "N-IRIS cannot provide additional spectral information beyond its panchromatic counterpart". Three-party collaborative work on snapshot anomaly detection is described to highlight consideration of the practical exploitation of N-IRIS imagery for publishable scenarios.

4.1 Hypercube Extraction and Co-Registration

Although the focus of this thesis has been upon the N-IRIS sensor, it was appropriate for completeness to consider processing and exploitation. Significant research work has already been undertaken concerning image processing for ophthalmology [62]. The focus here is the understanding of basic processing and exploitation. To exploit N-IRIS imagery for most applications, the objective is to return co-registered hypercubes for either anomaly detection or spectral classification. Figure 4-68 highlights the problem to be addressed in registering the optically distorted subimages expected from N-IRIS at the FPA plane.
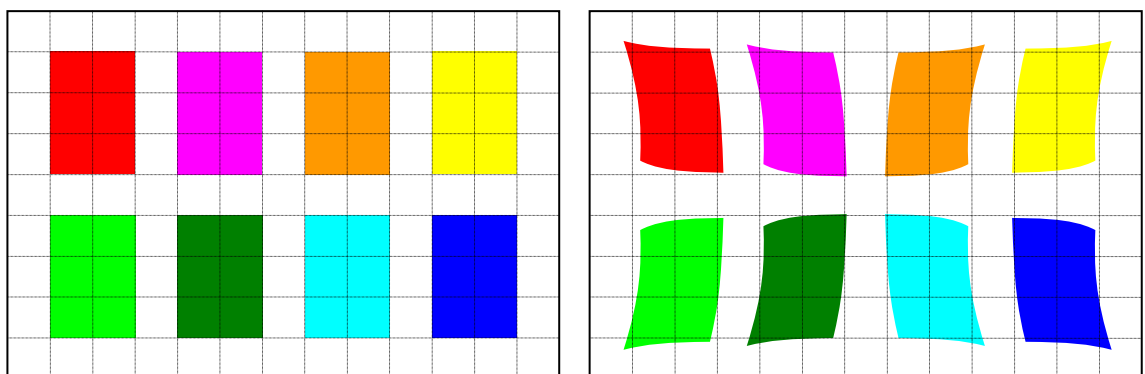
Figure 4-68: Examples of *ideal* co-registration and (pincushion) distorted image mis-registration

In contrast to automated techniques [62], the approach adopted here was to use the manual input of critical reference points for simplicity at this stage. The initial step is to define opposing corner points and one centrally located common point, which is selected according to an identifiable feature that is common to the subimages. Although higher-order image distortions require correction, an initial linear co-registration was needed before progressing to image dewarping and co-registration. Figure 4-69 depicts this initial linear alignment, through the definition of the mutually inclusive (gray) area that is common to all the subimages. Using the standard functions provided by *MatLab* software, the eight subimages were cropped via their corner points and their common points were correlated between the eight subimages. The process returned seven subimage matrices, which were aligned to an eighth arbitrary reference subimage.

Exploiting the proprietary tools in *MatLab* software, pairs of subimages were then aligned with each other through the manual selection of multiple tie-points against any arbitrary reference subimage, in the absence of a geo-rectified or truthed image. Tie-points are those points within the distorted image for which their corresponding positions within the reference image are known.
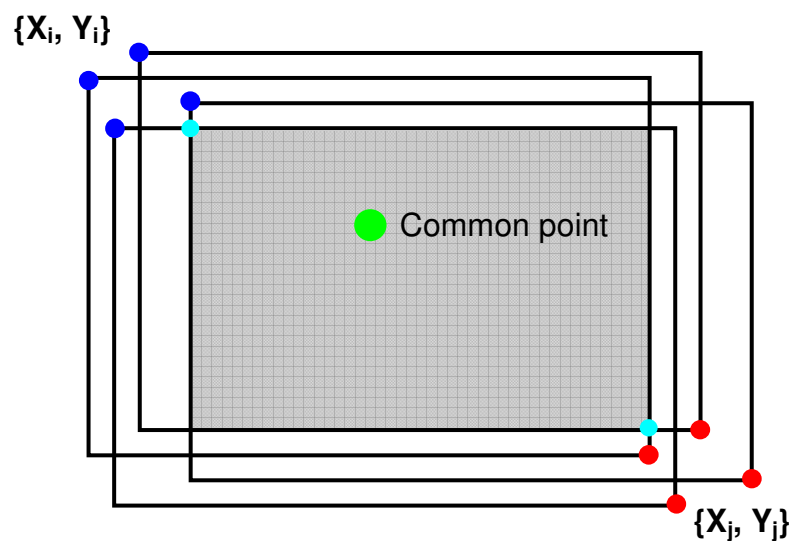
Figure 4-69: Overlay diagram of linear alignment and cropping of N-IRIS subimages

These tie-points were defined through the capture of dot targets arranged onto a grid pattern, with different sets being created using varying dot size and pitch for diversity. After judicious empirical testing with polynomials of varying order, it was discovered that fitting the distortions to second-order polynomials returned the least distorted hypercubes for use in detection or classification. The metric chosen was a visual balance between co-registration and geometric distortion introduced by the process itself. Third-

order correction required ten tie-points as a minimum, but it was found that at least twenty points for each subimage pair were needed to prevent excessive distortion.

The higher polynomial orders enabled an improved fit (to fourth order), but the result increased the geometric distortion and reduced image validity. Furthermore, it was impractical to define more than two dozen accurate points on the sub-images, which were equal to or less than 128×80 pixels. Second-order correction was determined to be an optimal although compromised solution, considering the resolution limits of N-IRIS in its then current configuration. This low resolution was coupled with the need for reference features comprised of many pixels, which enabled the cross-correlation of features to sub-pixel accuracy as opposed to single-pixel points. Using the latter would introduce quantization error and aliasing within the subimages, as each pixel is approximately 1% of the image height and width. A trade-off became apparent between larger dots for images that directly related to the scene, yet were mis-registered, versus many smaller dots for accurate co-registration, but with geometric image distortion.

Distortions were still however present within the final hypercube and originated from two main causes – spurious boundary cropping and double-images. The former resulted from null values used for output pixels when the matching transformed location in the output image was outside the input image boundaries. This problem was solved by taking borders around subimages into consideration and then manually cropping.

The second issue of double-images or "ghosting" derives from prominent sidelobes in the passbands for N-IRIS, which is due to Wollaston-prism dispersion and multiple sidelobes (described in Section 2.2.3). Correlation could not consistently select between two ghosted dots that were prominent in certain subimages. Figure 4-70 is an example of second-order correction, where the 8D hypercube has been summed for easier viewing than eight separate images. The first image is a greyscale rendering of all eight layers, while the second is a false RGB (red-green-blue) rendering of three randomly chosen layers. This RGB image allows more detail to be observed that may not be apparent due to the greyscale rendering (subject to printing limitations here).
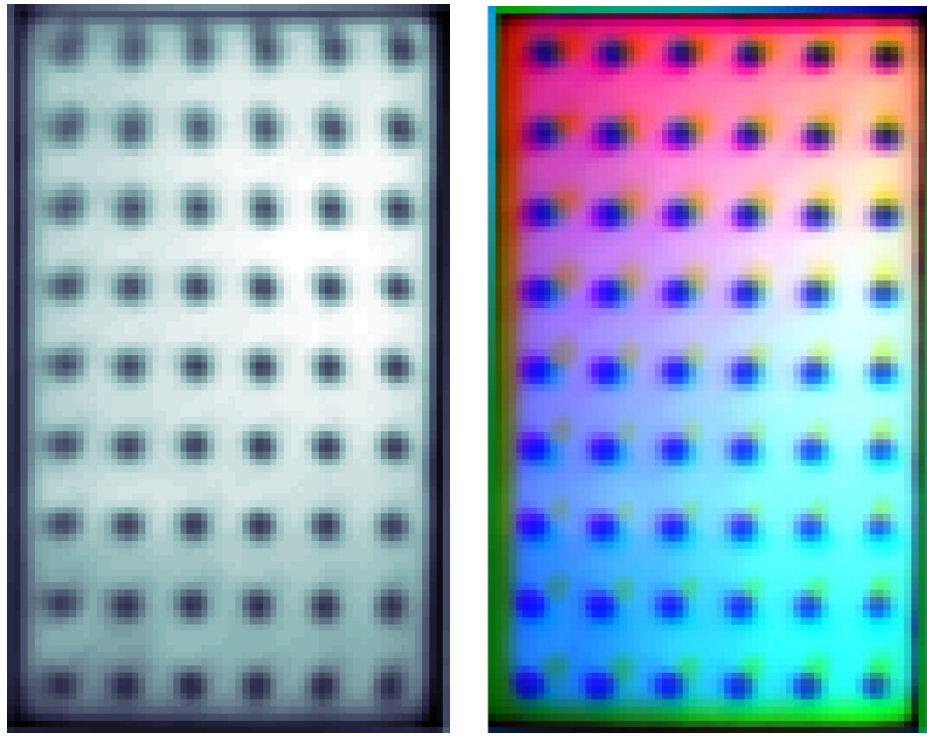
Figure 4-70: Examples of best co-registration given current limitations – images are summed layers of the 8D hypercube, both full (all eight) in greyscale and three random layers as false RGB respectively

Of note within Figure 4-70 are spurious border regions, coupled with registration artefacts from ghosted dot targets, as observed within both the top row and first column of the first image. They are also seen within the top-half of the RGB image, subject to the colour limitations of the printing process. The approach described can be termed as relative alignment, where seven of the subimages are co-registered to an arbitrary reference subimage. Any final hypercube will still contain the distortion of the reference frame, but will be valid for anomaly detection. Although absolute dewarping is not currently required, it is accepted that some applications may need more exact mapping between the output and remote scene. One such example is designating hidden objects of interest using a UAV equipped with an N-IRIS sensor and an infrared or visible laser.

An absolute approach using an aligned dot target or similar would initially appear to provide the solution, by allowing truthed correction to quantified real-world features. This method would still suffer from the trade-off between the quality of chosen tie-point pairs and the optimal numbers for polynomial correction. Fourth-order and up to eighth-order polynomials are generally sufficient to describe lens distortion accurately [63]. Considering these imaging aberrations from an optical viewpoint, potential solutions are described within the next section.

4.2 Modelled N-IRIS Response from Spectral Databases

To determine the capability of N-IRIS for material discrimination, spectral data was needed to predict the theoretical spectral response. These predictions provide an objective first-order consideration and learning exercise before actual testing against materials. Accurate spectral databases were required for this task, *in lieu* of access to a SWIR spectrometer for the ground-truthing of test materials. Spectral databases from the United States Geological Service (USGS) and the National Aeronautics and Space Administration (NASA) were selected [64,65].

The raw dataset entries were uploaded, formatted and graphed for review before the planned multiplication with the N-IRIS passbands to reach the theoretical response. The list below details the selected material albedos for mapping to the N-IRIS passbands. Figure 4-71 and Figure 4-72 illustrates these albedos from ASTER (NASA) and USGS.

ASTER: Conifer needles, bare red brick, aluminium, olive green paint (matt and gloss)

USGS: Particle board, pine plywood, black tar paper, cardboard, galvanised metal, white HDPE (high-density polyethylene) plastic, white cotton, white PVC (polyvinyl chloride) plastic, nylon carpet (gray and brown)
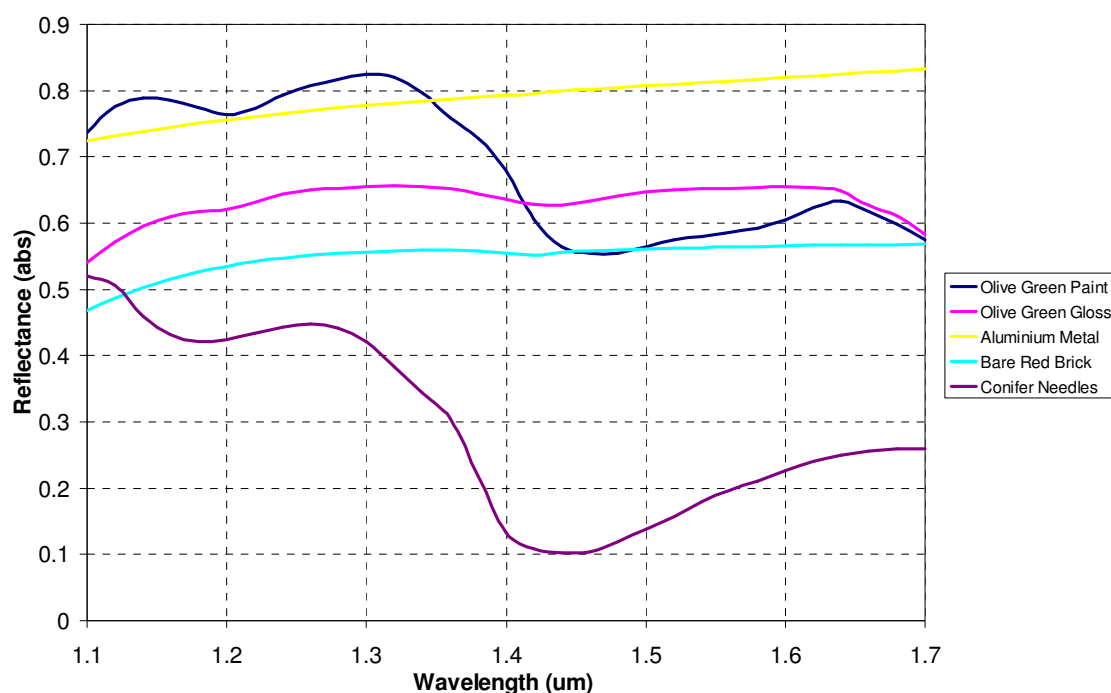
Figure 4-71: Normalised ASTER albedos for selected materials over the N-IRIS wavelength range
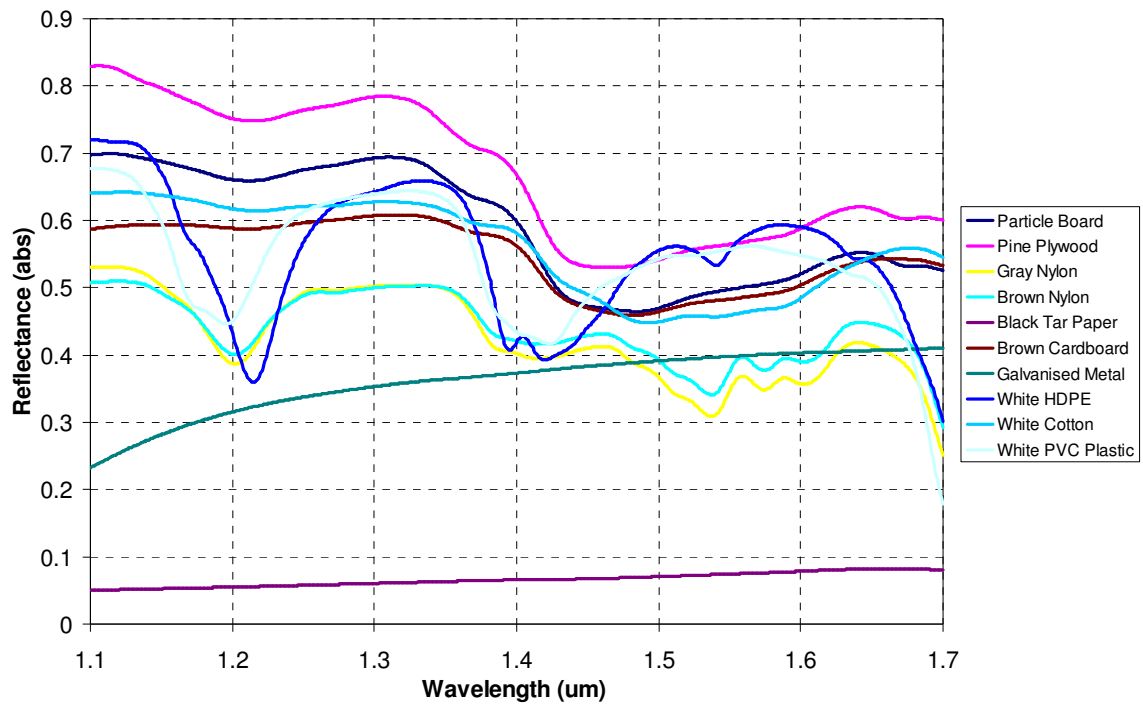
Figure 4-72: Normalised USGS albedos for selected materials over the N-IRIS wavelength range

Figure 4-73 and Figure 4-74 are the subsequent transmitted albedos from respectively multiplying the ASTER and USGS datasets with the theoretical N-IRIS passbands. These predictions provide the relative intensity expected for these generic materials.
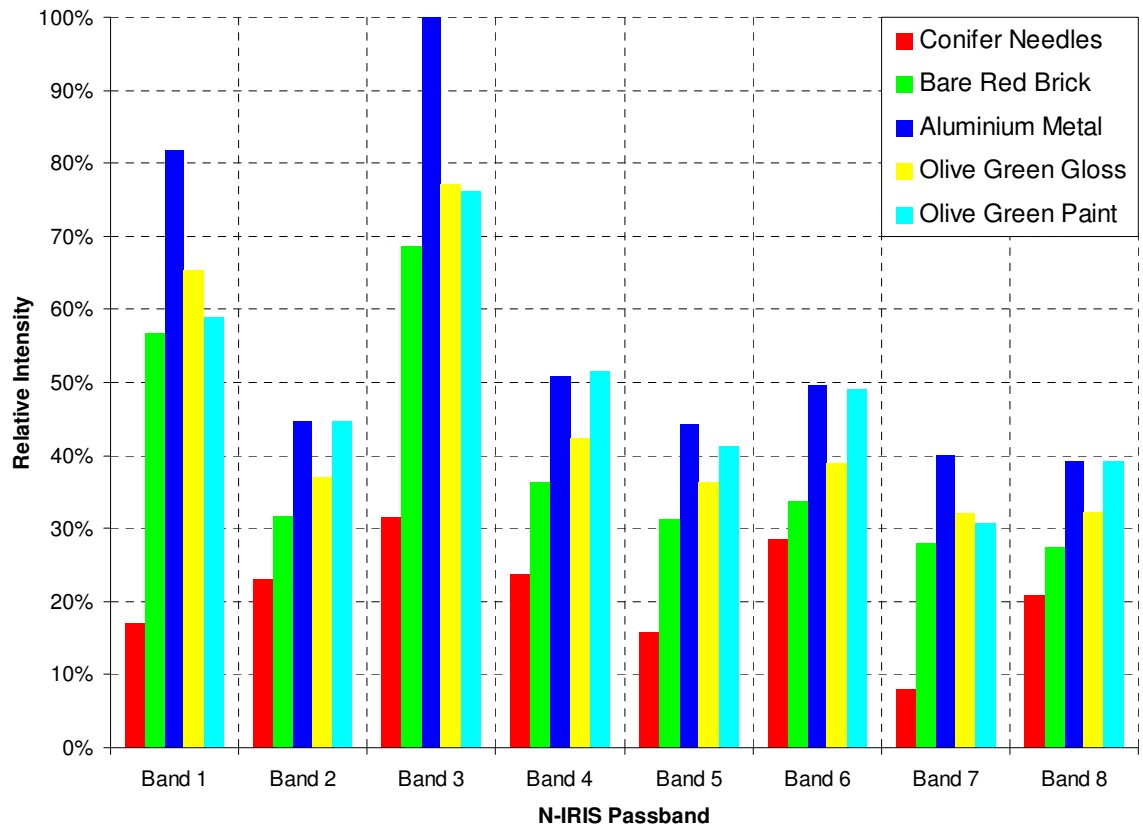
Figure 4-73: Normalised intensities of ASTER spectra for selected materials over each N-IRIS passband
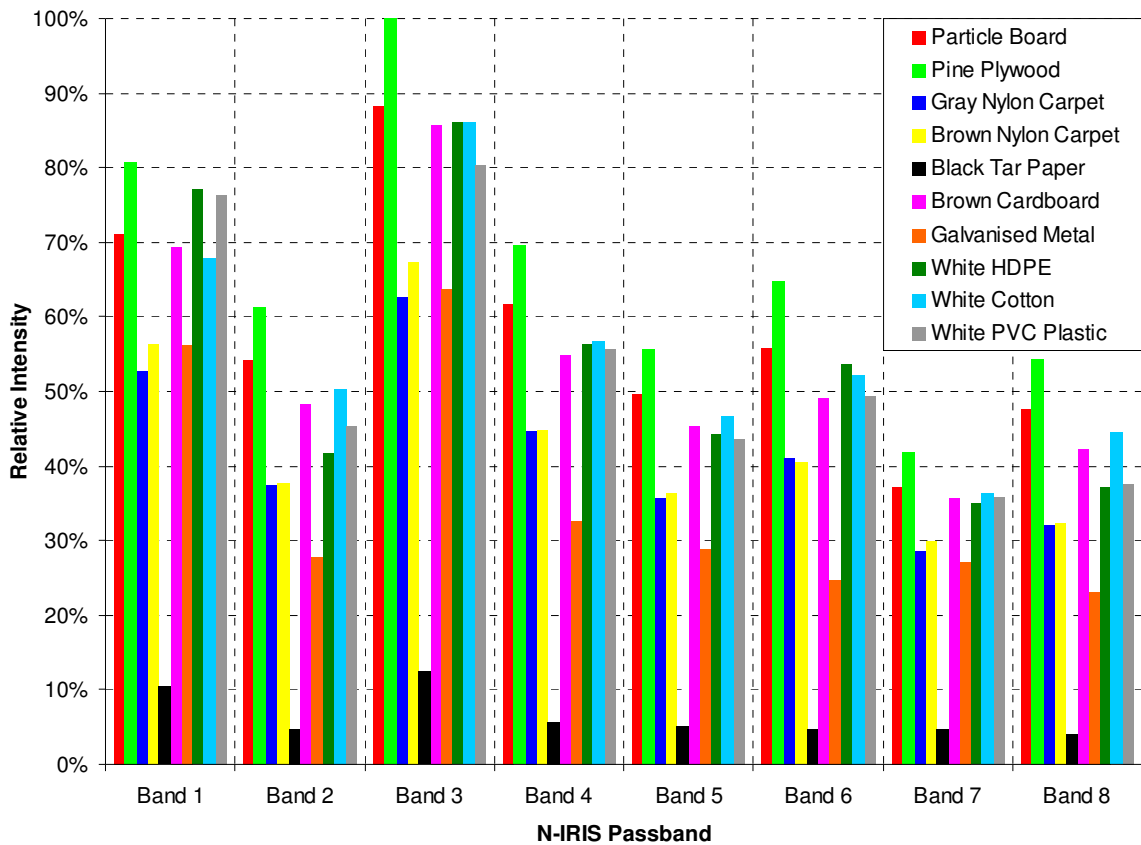
Figure 4-74: Normalised intensities of USGS spectra for selected materials over each N-IRIS passband

For each material in Figure 4-71 and Figure 4-72, the theoretical N-IRIS passbands were multiplied with the spectral albedo taken from the databases. Each curve is then numerically integrated across the wavelength range of interest to yield eight scalar values. These values yield Figure 4-73 and Figure 4-74. The results suggest that for the limited subset of materials considered and under ideal conditions, detector noise and bit-depths are likely pivotal for spectral discrimination. Across each N-IRIS passband, the relative differences between the generic materials are small.

The low spectral resolution of N-IRIS attenuates spectral features with respect to higher resolution spectrometers. Empirical observation of Figure 4-73 and Figure 4-74 does enable the discrimination of materials with respect to each other. It can also be observed that Bands One and Three return a relatively higher response with respect to the others. Although this would reduce the available intensity for the other bands, the waveband selection process in Chapter Three explicitly minimised sidelobes for image quality. The trade-off as evidenced in this brief study is a loss of responsivity in certain bands. This could negatively affect the ability of N-IRIS to distinguish between certain materials whose defining spectral features are concentrated within those bands. Such trade-offs should be considered in future prototypes for application specific designs, rather than the generic imaging here for proof-of-concept SWIR snapshot HSI.

Although these modelled differences could be further quantified by comparing the Mahalanobis distances between pairs of materials, the following section describes the Analysis of Variance (ANOVA) for controlled testing within a laboratory environment.

4.3 Analysis of Variation (ANOVA) Testing

In addition to unpublished testing with surrogate landmines by the author in an external environment, additional controlled testing within a laboratory environment was also completed. The method used was Analysis of Variance (ANOVA) in order to test the hypothesis that "N-IRIS cannot provide any additional spectral information beyond a panchromatic imager" [66]. ANOVA requires that hypothesises which are to be tested are framed in the negative. Hypotheses cannot be proven correct, as there a counter-point case may always exist, even with infinitesimal probability.

For this testing, one-way ANOVA was used to determine whether "applying" N-IRIS to the baseline *XenICs* SWIR camera creates a statistically *significant* change in the data at a given confidence level for various materials tested. With an intractable number of potential materials that could be sampled, this initial test is indicative only at best and another reason why negative framing of the N-IRIS hypothesis is necessary. In the following discussion of ANOVA theory, "treatments" refer to capturing data using N-IRIS and *XenICs* respectively. Treatments are analogous to "applying" these sensors to the underlying information that exists independently of the collection method used.

One-way ANOVA compares the variation between treatment groups with the variation within each treatment group. If the variation between treatments is greater than within them at some level of significance, then the differences between the treatment means must be significantly greater than would be expected by random processes. Treatments can be considered as having had a significant influence on the values taken by the variable. The treatment groups are unlikely to have come from populations with the same mean, which is identical to coming from one common population.

The ANOVA testing initially requires the total variation of all observations, regardless of the treatments from which they come. The following description of the ANOVA method uses the conventional notation style within statistical literature [66]. This total sum of squares (*SSY*) is calculated as

$$SSY\left(x_{ij}\right) = \sum \left(x_{ij} - \bar{x}\right)^2 \tag{33}$$

where the x_{ij} are the observations (x_{ij} being the ith observation in the jth treatment), and $\bar{x}$ is the grand mean of all observations. The variance also known as the sum of squares between treatments (generally referred to as SST) is calculated as

$$SST\left(N, x_j\right) = N\sum\left(\bar{x}_j - \bar{x}\right)^2 \tag{34}$$

where x_j is the mean of the jth treatment and N is the number of observations. SST measures the variation between group means using the deviations between group means and the grand mean. The variance within treatments is known as the error sum of squares (SSE). The calculation is made over all observations as for SSY, but each deviation is measured with respect to its treatment mean rather than the grand mean. To simplify the calculation of SSE, it can be shown that $SSY = SST + SSE$ that is referred to as partitioning the sums of squares.

The next step is calculating the mean squares (the treatment mean squares, TMS, and the error mean squares, EMS) from the sums of squares (SST and SSE). A mean square is a sum of squares divided by the degrees of freedom. The degrees of freedom of $SST = c - 1$ (where c = number of treatments), one being lost because of the presence of the grand mean; the degrees of freedom of SSE is $(r-1)\cdot c$ (where r = number of observations for each treatment), one being lost from each treatment because of the treatment mean.

$$TMS\left(N, x_j, c\right) = \frac{N\sum\left(\bar{x}_j - \bar{x}\right)^2}{(c-1)} \tag{35}$$

$$EMS\left(N, x_{ij}, x_j, c, r\right) = \frac{\left[\sum\left(x_{ij} - \bar{x}\right)^2\right] - \left[N\sum\left(\bar{x}_j - \bar{x}\right)^2\right]}{(r-1)c} \tag{36}$$

The mean squares enable a significance test to determine whether explained variation between treatments is significantly different from unexplained variation within those treatments. This is because it can be shown that the ratio between TMS and EMS follows an F-distribution. The significance test makes the hypothesis that all treatments come from populations with the same mean, or from a common population. If the observed F value (TMS/EMS) lies beyond the critical value, at a given level of significance, then the hypothesis is rejected: the treatments do have a significant effect. If the observed F value is less than the critical value then the hypothesis is accepted: there is not a significant difference between the treatment means.

It can be shown that *TMS* and *EMS* are two alternative ways of estimating the variance (σ^2) of the common population from which the observations are assumed as taken from. The ratio *TMS/EMS* is the ratio between two variance estimates and thus the *F* test can be used to determine whether they are significantly different. If there were a significant difference between *TMS* and *EMS*, where *TMS* was the larger value, then a significant proportion of the variation between the observations is accounted for by the effect of the different treatments. This contrasts with the variation being a result of random variation between observations. Treatments would then appear to have a significant effect on the means of observations relating to them and there is a difference between their effects. ANOVA is completed by comparing the observed *F* value (from tables) with a critical *F* value for $(c-1,(r-1)\cdot c)$ degrees of freedom from an F-distribution table – conventionally taken at the 2σ or 95% confidence level, with example configurations as in Figure 4-75.
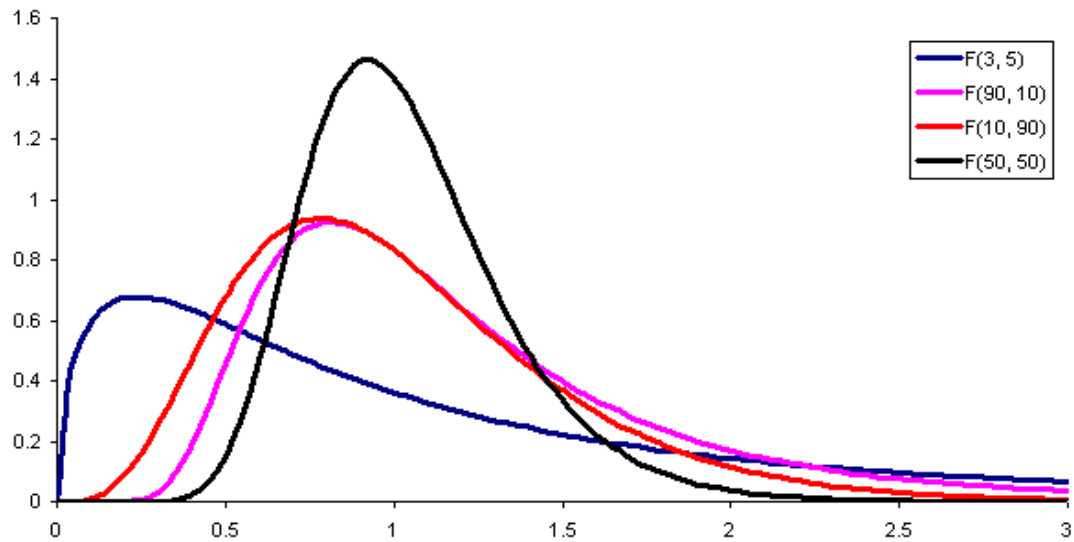
Figure 4-75: Examples of the F-distribution, whose exact form varies dependent on the two degrees of freedom (c-1) and (r-1)·c respectively for a given situation.

The following sets of points briefly outlines the steps taken in data capture and post-processing for ANOVA testing of N-IRIS, to test the hypothesis that "N-IRIS cannot provide any additional spectral information beyond a panchromatic imager".

Data Capture Steps:

1) Using an ISO/NIST (National Institute of Standards and Technology) white-balance target, determine the *XenICs* settings that avoid saturation under broadband lighting when operating with and without N-IRIS while imaging various materials.

2) These *XenICs* settings should maximise the captured range of intensity information – this will likely be different for different materials.

3) The white-balance target should appear as an image element in all captures either with or without N-IRIS to provide normalisation factors.

4) Under constant lighting conditions if possible, capture images both with and without N-IRIS using those suitable *XenICs* parameters as found previously.

5) The captured images should incorporate a variety of identifiable materials, which should cover a large range of common and accessible materials where possible.

Post-Processing Steps:

1) For all of the following considerations, homogenous regions within an image will be selected to be as large as possible to help to minimise random intensity variations.

2) The white-balance target within each capture will be averaged into a single value (or vector for N-IRIS) and used for normalisation of data.

3) For N-IRIS images, regions of imaged materials will be averaged and then normalised to provide an eight-element vector, where each such element is expected to contain varying spectral information.

4) For *XenICs*-alone, large regions of materials will be averaged from eight separate captures, with each then normalised to provide an eight-element vector, to enable a more accurate comparison with N-IRIS images (compared with only a scalar value).

5) With these N-IRIS and *XenICs*-alone vectors, execute ANOVA analysis for each material being tested – where each type of sensor represents one treatment and each vector element representing one block.

6) For each material of interest, compare the observed F-value with the critical F-value for the required degrees of freedom (DoFs) from an F-distribution table.

7) Using the mean observed *F*-values for the *N* materials tested, infer the confidence level that "treatment" with N-IRIS does significantly provide more information than broadband SWIR.

The rationale for this experimental method is accurately test the discrimination ability of N-IRIS against the panchromatic *XenICs* SWIR camera as a reference point, instead of another camera with different characteristics or specifications. Common and accessible materials were used due to budget limitations on acquiring truthed spectral test targets.
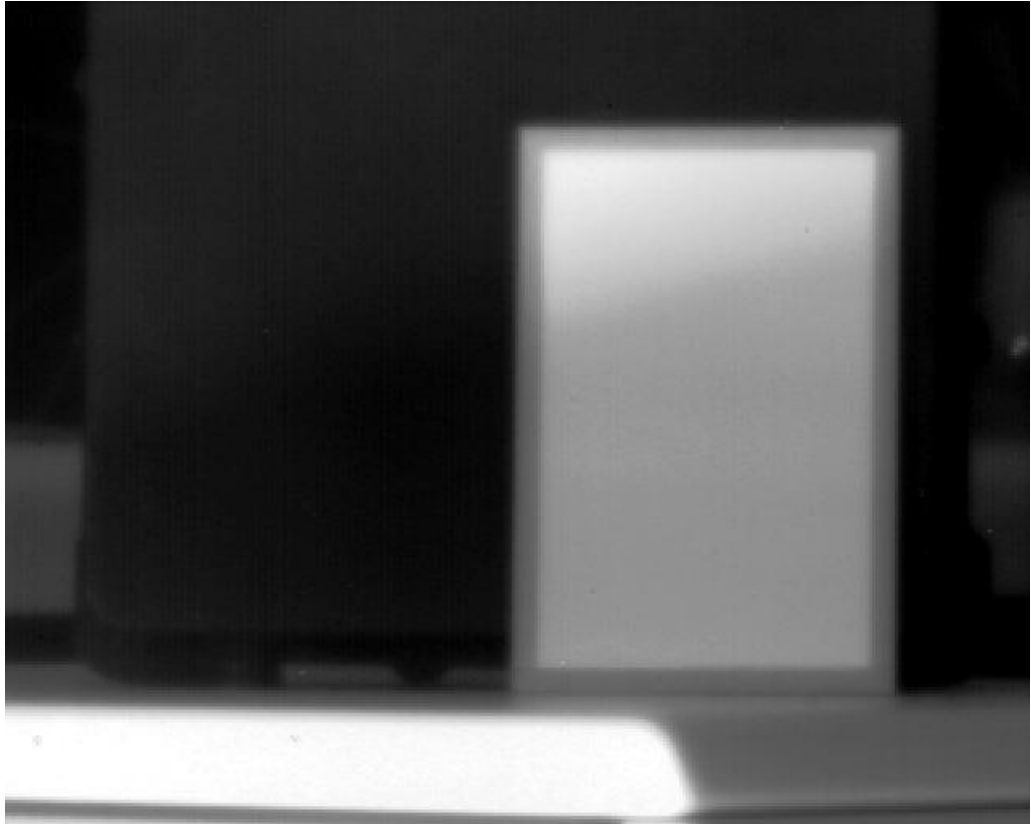
Figure 4-76: Example of *XenICs* capture of white-balance card against olive green metal
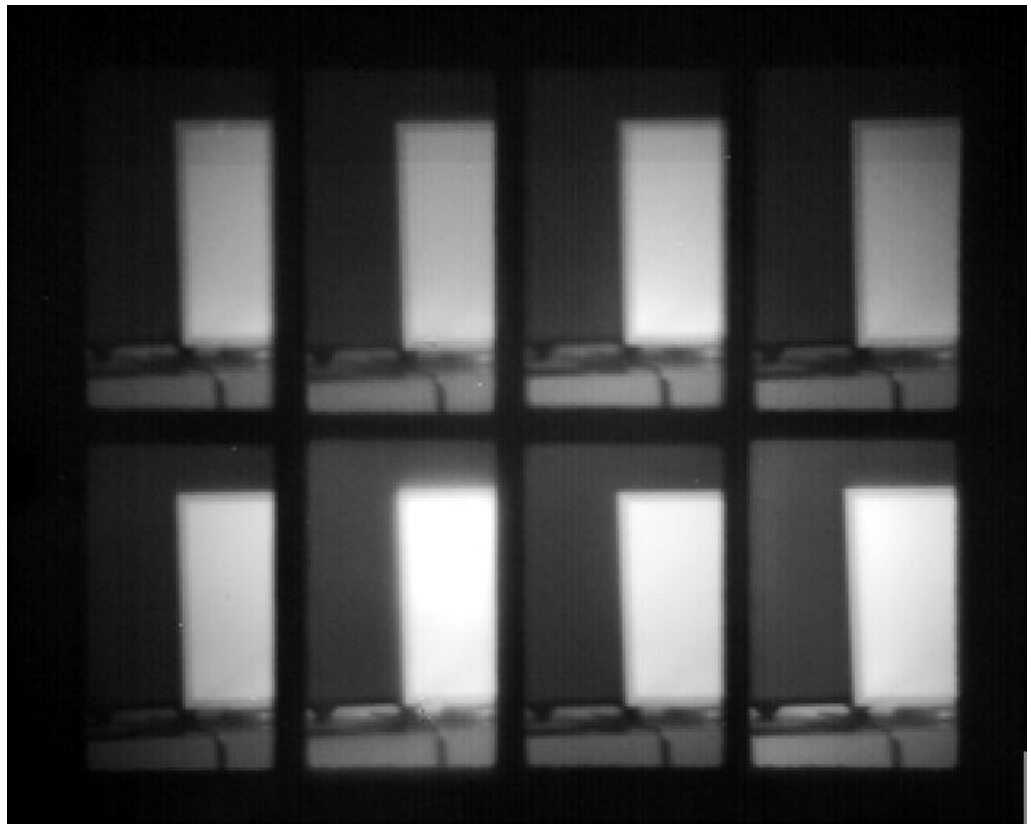
Figure 4-77: Example of N-IRIS capture of white-balance card against olive green metal, the image is aberrated due to the use of a sub-optimal COTS condenser lens designed for the visible waveband

List of Materials Tested

The following list of tested materials is representative of common materials. This choice of selected materials was primarily influenced by both their accessibility and portability at the time of ANOVA testing. Organic materials were also desirable but were not made available due to laboratory restrictions.

1) Black nylon-based textile
2) Blue nylon-based textile
3) UK-style camouflaged bag
4) Corrugated brown cardboard
5) Back of circuit breadboard
6) Front of circuit breadboard
7) Cover of dark blue laboratory notebook
8) Sheet of gray polyvinyl-chloride based plastic
9) Green felt-type textile
10) Matt-finished unpainted aluminium
11) Olive green painted aluminium
12) Pink packing foam
13) Large sandstone pebble
14) Standard wide masking tape
15) White painted masonry wall
16) White cotton-based textile
17) (Dirty) yellow tarpaulin jacket
18) Inside of yellow tarpaulin jacket

Results from Materials Tested

For $(c-1)=1$ and $(r-1)\cdot c=7$ in this ANOVA test, where $c=2$ is the number of treatments and $r=8$ is the number of observations, then the critical F-values for acceptance or rejection at the 5% and 1% confidence levels are 5.59 and 12.25 respectively. The confidence in rejecting the negatively framed hypothesis is 95% and 99% respectively. 95% is generally used without *a priori* requirements for different values while 99% can be used for pharmaceutical testing and other critical applications. It is assumed that 95% confidence is "effective" in this case, while $\geq 70\%$ is "acceptable" but only in a subjective sense in this discussion without prior qualification. Table 4-7 are the results of the ANOVA trials showing the calculated F-value, confidence level and inferred result, while Figure 4-78 illustrates one worked example for completeness.

Material	F-Value	Confidence	Result
Black nylon-based textile	0.44	0.471	Not effective
Blue nylon-based textile	6.97	0.967	Effective
UK-style camouflaged bag	7.89	0.974	Effective
Corrugated brown cardboard	1.62	0.757	Acceptable
Back of training-style circuit board	0.84	0.609	Inconclusive
Front of training-style circuit board	1.29	0.706	Acceptable
Dark blue laboratory notebook	0.49	0.495	Not effective
Gray polyvinyl-chloride plastic	8.71	0.979	Effective
Green felt-type textile	1.24	0.698	Acceptable
Matt-finished unpainted aluminium	4.21	0.921	Effective
Olive green painted aluminium	24.35	0.998	*Highly* effective
Pink packing foam	6.03	0.956	Effective
Large sandstone pebble	4.82	0.936	Effective
Standard wide masking tape	2.69	0.855	Effective
White painted masonry wall	1.28	0.704	Acceptable
White cotton-based textile	5.63	0.951	Effective
(Dirty) yellow tarpaulin jacket	2.29	0.826	Effective
Inside of yellow tarpaulin jacket	2.64	0.852	Effective

Table 4-7: Results of ANOVA trial showing the calculated F-value, confidence level and inferred result

Since the results show that at least one material can be discriminated by N-IRIS, the null hypothesis that "N-IRIS cannot provide additional spectral information beyond its panchromatic counterpart" is clearly disproven. Recall that it is not possible to prove strictly the inverse formulation of the hypothesis, as there are an intractable number of possible materials to test under varying environmental conditions. It would not be practical to test N-IRIS against every material under every condition, even if both variables could be fully known in entirety and exhaustively specified.

Only one counter-example of a spectrally indistinguishable material would invalidate the strict hypothesis that "N-IRIS can provide additional spectral information beyond its panchromatic counterpart", hence the traditional use of a null hypothesis. It is also clear that N-IRIS in its current configuration can provide with confidence ($\geq 95\%$ or $\geq 99\%$),

improved spectral discrimination of certain materials with respect to its panchromatic counterpart. Even though it is unknown how many materials N-IRIS is effective against, it is superior to its panchromatic counterpart on spectral discrimination by disproving the null hypothesis through counter-examples of materials that it can discriminate well.

	Xen-WB	IRIS-WB	Avg			XenICs	N-IRIS	Avg
SI #1	2201.9	2190.5	2196.2		SI #1	0.102048	0.249989	0.176018
SI #2	2155.3	2215.9	2185.6		SI #2	0.097666	0.205424	0.151545
SI #3	2181.2	2718.8	2450		SI #3	0.100174	0.185045	0.14261
SI #4	2150.3	1688.3	1919.3		SI #4	0.096545	0.142688	0.119616
SI #5	2214.7	1031.2	1622.95		SI #5	0.102136	0.261055	0.181595
SI #6	2188.9	1795.2	1992.05		SI #6	0.098223	0.193182	0.145702
SI #7	2125.8	1439.9	1782.85		SI #7	0.096011	0.20175	0.148881
SI #8	2137.9	1253	1695.45		SI #8	0.09528	0.156824	0.126052
Avg	2169.5	1791.6			Avg	0.09851	0.199495	0.149002
	Xen-Raw	IRIS-Raw	Avg			Xen-Var	IRIS-Var	Avg
SI #1	224.7	547.6	386.15		SI #1	1.25E-05	0.00255	0.001281
SI #2	210.5	455.2	332.85		SI #2	7.13E-07	3.52E-05	1.79E-05
SI #3	218.5	503.1	360.8		SI #3	2.77E-06	0.000209	0.000106
SI #4	207.6	240.9	224.25		SI #4	3.86E-06	0.003227	0.001615
SI #5	226.2	269.2	247.7		SI #5	1.31E-05	0.00379	0.001901
SI #6	215	346.8	280.9		SI #6	8.27E-08	3.99E-05	2E-05
SI #7	204.1	290.5	247.3		SI #7	6.25E-06	5.09E-06	5.67E-06
SI #8	203.7	196.5	200.1		SI #8	1.04E-05	0.001821	0.000916
Avg	213.7875	356.225			Total	4.98E-05	0.011676	0.011726
					SST	SSB	SSE	SS
					0.040791	0.006481	0.011726	0.058998

Variation	DoF	Σ Sqrs	μ-Sqr	F-Stats
Trtmnts	1	0.040791	0.040791	24.35127
Blocks	7	0.006481	0.000926	0.552742
Error	7	0.011726	0.001675	
Total	15	0.058998		

Trtmnts Critical	F-Obs	F-Val (5%)	F-Val (1%)	Cnf Level	Inverse
	24.35127	5.59	12.25	0.2%	99.8%

Blocks Critical	F-Obs	F-Val (5%)	F-Val (1%)	Cnf Level	Inverse
	0.552742	3.79	7.00	77.4%	22.6%

Figure 4-78: Worked example of ANOVA statistical analysis with an F-distribution test, using olive-green aluminium sample. Not shown is the algorithm source-code for the *MatLab* software that extracts homogenous portions of both the sample and white balance target.

4.4 Collaborative Project on Snapshot Anomaly Detection for N-IRIS

The following section is reproduced from a published paper[2] covering collaborative work between Heriot-Watt University, SELEX Galileo Ltd and Waterfall Solutions Ltd. Minor modifications to the published text have been carried out for improved clarity, along with renumbering of references and figures for consistency in EngD thesis.

Important contributions by the author was informing the requirements and reviewing the outputs from Waterfall Solutions Ltd [20,21]. Additional contributions were the optical design, assembly and provision of the N-IRIS sensor, in addition to support for the sensor and consultation regarding its operation.

In collaboration with Waterfall Solutions Ltd (WS), N-IRIS was integrated with COTS computer hardware and multi-threaded WS algorithms into an anomaly detection demonstrator. The major output of the collaboration was the HSI Prototype Unit (HPU), which is the processing unit to extract the subimages from N-IRIS and perform anomaly detection. This HPU was then coupled to N-IRIS and resulted in a practical system, capable of detecting targets based upon spectral anomalies at video frame rates of 25Hz.

An example of output quality is presented within Figure 4-79, which highlights the improvements in anomaly detection and reduction in background clutter, as compared to the industry standard RX (Reed and Yu) algorithm [67]. Figure 4-80 illustrates the major COTS components within the HPU, without the need for custom or bespoke hardware.

Although not fully ruggedized, the system has been designed for demonstration in real-world scenarios and the compact and semi-rugged build reflects this. The HPU can thermally dissipate up to 130W under full processing load and this is vented from slots milled into the side of the mini-ITX housing.

---

[2] **G Wong**, **AR Harvey**, **R Pilkington** and **R Rickman**, "Real-Time SWIR Hyperspectral Imaging with Polarimetric Capability" *Proceedings of SPIE*, Vol. 7812, 781204 (2010)

Figure 4-79: From left to right respectively – (a) False RGB composite from three random subimages of a person pushing a bicycle, (b) baseline RX anomaly detection and (c) temporal anomaly detection. Note that all of these outputs are achieved at video frame rates ≥ 25 Hz within the SWIR region.

External
12V PSU

COTS Mini-ITX
Quad Core

Rugged mini-ITX enclosure
(W21.5cm x D26.5cm x H7.5cm)
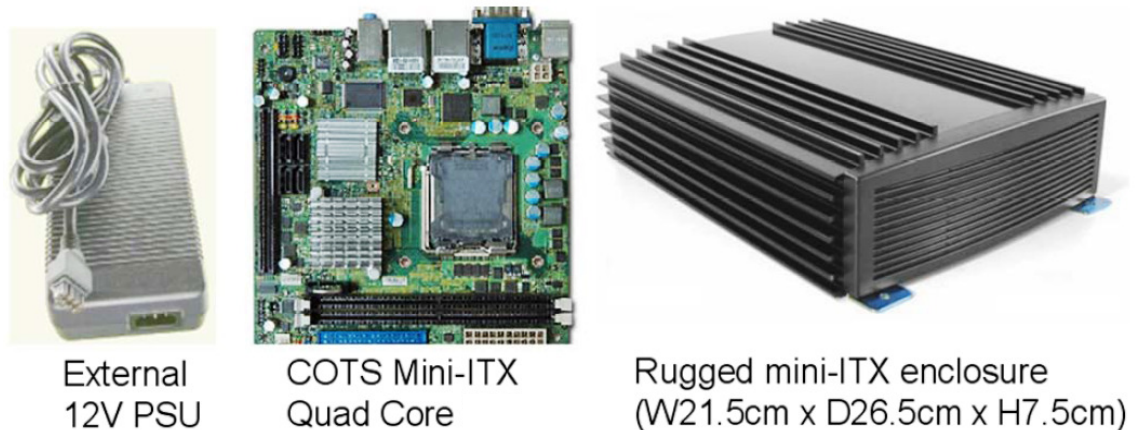
Figure 4-80: Major hardware components of the HPU, selected for compactness and portability – the PSU is rated at 150W, while the COTS processor exploits an L2 cache of 12 Mb and 4GB of RAM, which both enable the high bandwidth processing needed here

The WS real-time software is implemented as a complete suite of interconnected and concurrent threaded processes. The complete software architecture has been broken down into five processes, where each process thread communicates and synchronizes with other threads running in parallel during normal operation. An overview of the entire processing architecture is shown in Figure 4-81, within which are the embedded process threads that are now described as follows.

Figure 4-81: An overview of the software processing architecture, consisting of five concurrent threaded processes (not shown here)

The acquisition thread polls for the availability of data from the *XenICs* XEVA camera and double-buffers the image, so that data can be made available for subsequent processing whilst downloading another image from the camera. The registration thread crops the incoming frame using sub-image boundaries that are pre-defined during offline calibration. 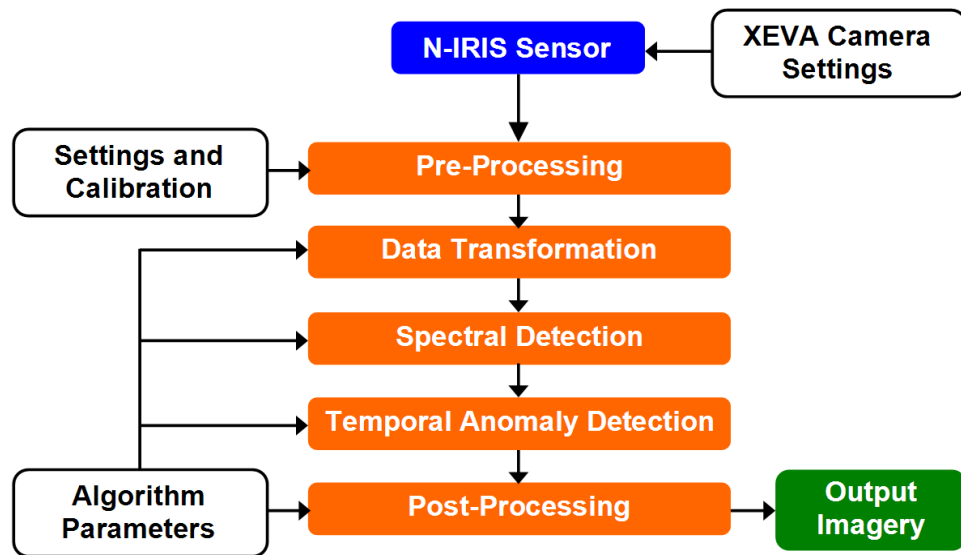This thread then de-warps and registers each image to a reference sub-image to form a hyperspectral cube using proprietary techniques undisclosed to the author. The processing thread then ensures that the hyperspectral cube is processed appropriately and the output imagery buffered for display – the HPU presently employs the RX baseline algorithm, along with proprietary temporal and spatial WS processes. The RX algorithm is an industry standard for anomaly detection, using the Mahalanobis distance to measure the statistical similarity for two N-dimensional points [68,69]. The recording thread enables the recording of raw unprocessed sub-images and the resultant HSI processed output. The final graphical user interface (GUI) thread reacts to any user commands, displaying both the raw sub-images and the processed output image.

During data gathering exercises and acceptance testing, some points were noted that could increase the synergy between the N-IRIS sensor and the HPU hardware. These offer the potential for the further development of both the sensor and processing hardware, for either improved stand-alone performance or operating as an entire system. Automatic registration is of paramount importance for practical working systems and this applies to both N-IRIS and other hyperspectral sensors, whether snapshot or otherwise in their operation.

In the case of N-IRIS, formation of the hyperspectral cube also requires the accurate registration of all sub-images. One of the great benefits of spectral-based techniques for target detection is that they offer the potential for sub-pixel detection. This is especially important where the pixel count of the imagery is comparatively low-resolution, as is the case for N-IRIS imagery. Sub-pixel target detection requires very accurate spatial registration and any misalignment will invariably degrade the performance of such a system, so future iterations or revisions should improve upon the current N-IRIS sensor.

During various data-gathering trials, imagery of deliberately moistened earth was recorded to determine if an improvised explosive device (IED) could be detected in disturbed earth by virtue of the fact that moisture content was higher than in undisturbed material. Whilst water does indeed elicit a local absorption peak in the 1450nm region (within the N-IRIS sensor bandwidth), this band is also absorbed by atmospheric moisture and may not be readily distinguishable in very humid environments or during precipitation. It is known however, that features of disturbed earth are usually manifest around 2.2μm for SWIR, which can be incorporated into future revisions. The optics of N-IRIS are capable of functioning to 2.3μm, with only an upgraded SWIR camera and new quartz waveplates.

The hardware architecture outlined within Figure 4-80 and Figure 4-81 support the multi-threaded software architecture, which processes the imagery from the N-IRIS camera in real-time and displays the results via a GUI. The GUI also permits N-IRIS imagery to be recorded and stored within the unit so that the HSI-detection algorithms can be run in real-time using recorded sequences. The GUI also allows the user to select which algorithm variant (RX or otherwise) is used to process the imagery. The relative merits of the respective algorithms can henceforth be assessed qualitatively by the user on-line with live camera imagery or off-line with recorded sequences. The processed output imagery may also be stored as a sequence of images for subsequent playback.

To better realise the potential of the system, it was judged that there was usefulness in exploiting simulated datasets. To this end, the "Low Altitude" dataset from NASA's publically available AVIRIS (Airborne Visible and Infrared Imaging Spectrometer) HSI database was acquired and suitable modifications were made to generate synthetic N-IRIS datasets. This enabled the subsequent analysis and optimization of WS algorithms, along with demonstrating what could perhaps be achieved from an airborne system.

The "Low Altitude" AVIRIS data consisted of eighty-two distinct bands of spectral data between 900nm to 1700nm. The spectral transmission curves of the N-IRIS bands were simulated by selecting waveplate thicknesses that optimized the spectral response and coverage of the eight wavebands within this range. The relationship between these waveplate thicknesses, their refractive indices and the response curves was laid out previously within Chapter Three. Waveband orthogonality was not a factor within these optimization criteria, but an undisclosed WS optimization indicated that the following thicknesses would satisfy the aforementioned criteria: 180μm, 216μm and 490μm. This yielded the simulated N-IRIS response curves as shown in Figure 4-82 and the synthetic hypercube was created from the AVIRIS data by applying these transmission curves across the 82 bands for the complete spectral cube of the scene shown in Figure 4-83.
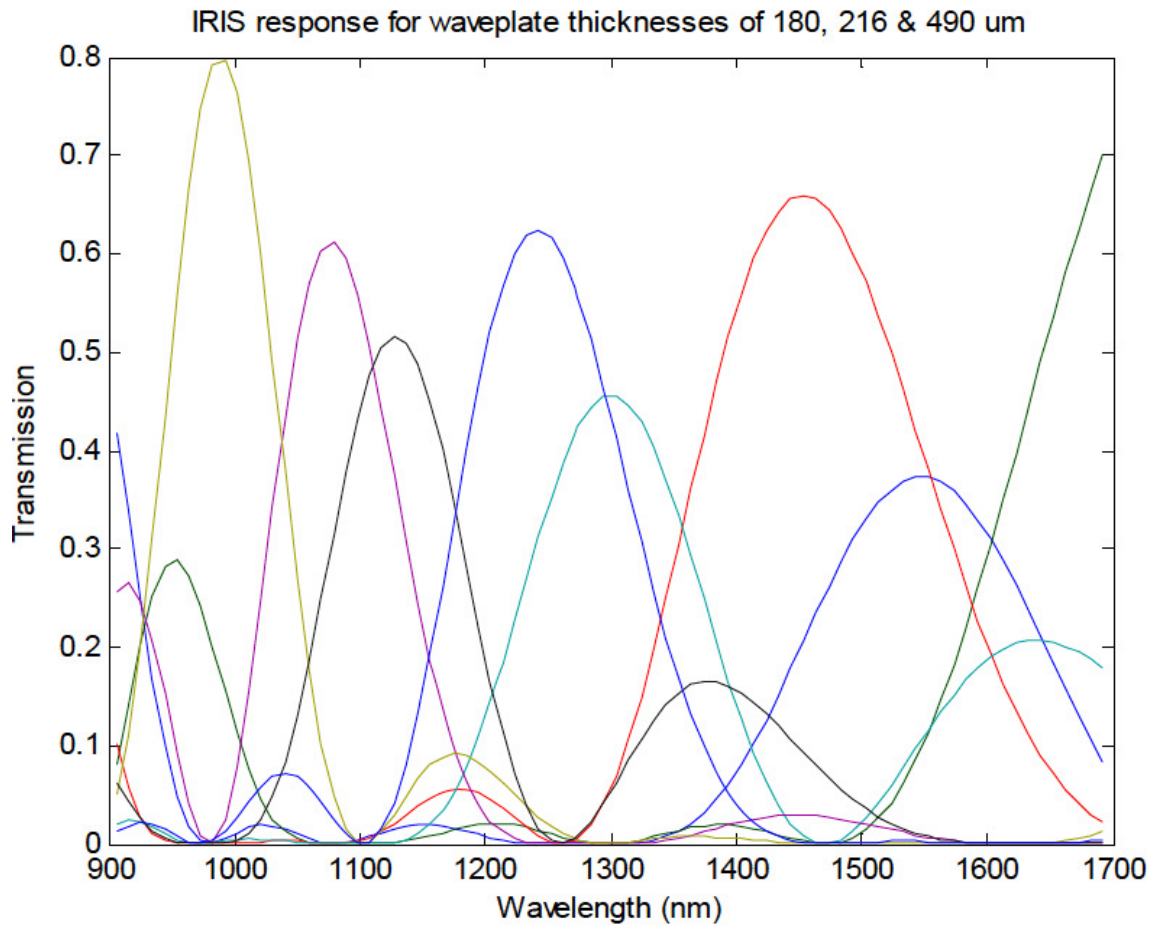

Figure 4-82: Simulated wavebands used in the dataset synthesised from the AVIRIS dataset

Figure 4-83: AVIRIS scene used as the basis of the simulated N-IRIS data

This scene consisted of a diverse range of spectral features ranging from rivers to arable land, roads, pasture and various types of (unidentified) vegetation. A small sub-section of this scene, consisting of a river and vegetation, outlined by a green rectangle, was used as the basis of this analysis. Within this scene, spectral signatures extracted from a section of the road (outlined by the green circle) were then superimposed at various levels of transparency to simulate varying degrees of sub-pixel mixing. The objective was to develop a set of scenarios to analyze and show how spectral anomalies can be identified using the WS algorithms in the presence of noise and clutter within the scene, as described in the following paragraphs.

A grid of single-pixel spectral samples of the road (within the green circle) was super-imposed upon the image outlined within the green rectangle. Each anomaly has the same level of transparency with respect to the background vegetation so that the target pixel spectral variance is due to background variation. The base grid of (road) anomalies and the scene upon which they are super-imposed are shown in Figure 4-84. A range of clutter-limited grids was produced by modelling the grids with a varying degree of

transparency, ranging from 0% through to 100%. Two moving targets were also defined as an out-of-scene target of (anomalous) road spectra with 75% transparency moving down the river, along with an in-scene target of vegetation spectra with 100% fill-factor moving upwards through the vegetation. Additive white Gaussian noise was then added to the scene in the form of five analogue-to-digital units (ADU).
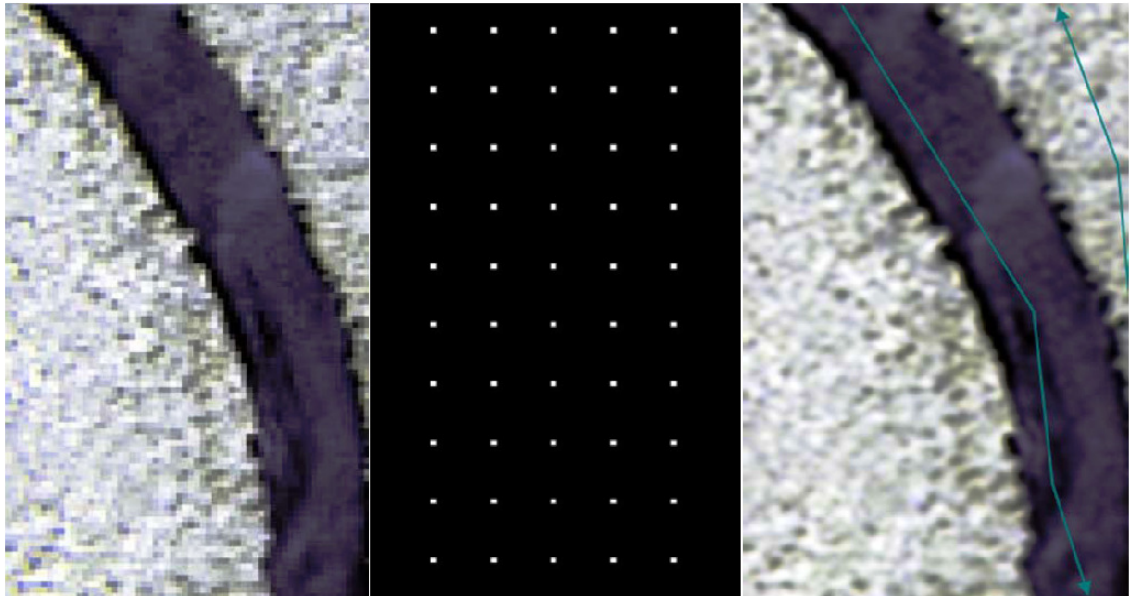
Figure 4-84: (Left to right respectively) AVRIS selection, static grid of sampled road spectra and superposition of two temporal targets

Temporal anomaly detection was performed on the entire fifty frames of the synthesized sequence that was created, which shows the target moving down the river and the other moving up through the vegetation. The results are best observed as a movie sequence to highlight the snapshot capability, although frame 25 is shown in Figure 4-85 to illustrate the benefit of the WS approach. These results demonstrate the advantage of temporal algorithms over the baseline RX algorithm, with the reduced clutter rendering the moving target within the vegetation more visible. The amount of clutter and false alarms is significantly reduced, but not at the expense of true target detections. Such temporal anomaly detection is not possible when using time-sequential HSI sensors.

Figure 4-85: (Left to right respectively) Target detection of two moving targets by the baseline RX algorithm and the WS temporal algorithm, with a greater level or false alarms by the RX algorithm

Temporal anomaly detection was again performed on the entire fifty frames of the synthesized sequence with moving targets as before, but now in addition to a grid of static target anomalies. The results from frame 25 of the complete fifty-frame sequence are shown in Figure 4-86. The temporal algorithm is able to detect both the static and moving anomalies within the scene whilst the baseline RX algorithm does not detect the temporal anomalies.

This collaborative project has successfully implemented temporal HSI algorithms onto COTS processing hardware to produce the HSI Prototype Unit. The hardware and software design has exploited quad-core processors and multi-threaded real-time software architecture. This unit has then been integrated with the N-IRIS sensor to provide an effective and practical demonstrator capable of detecting targets in real-time at frame rates of 25Hz.
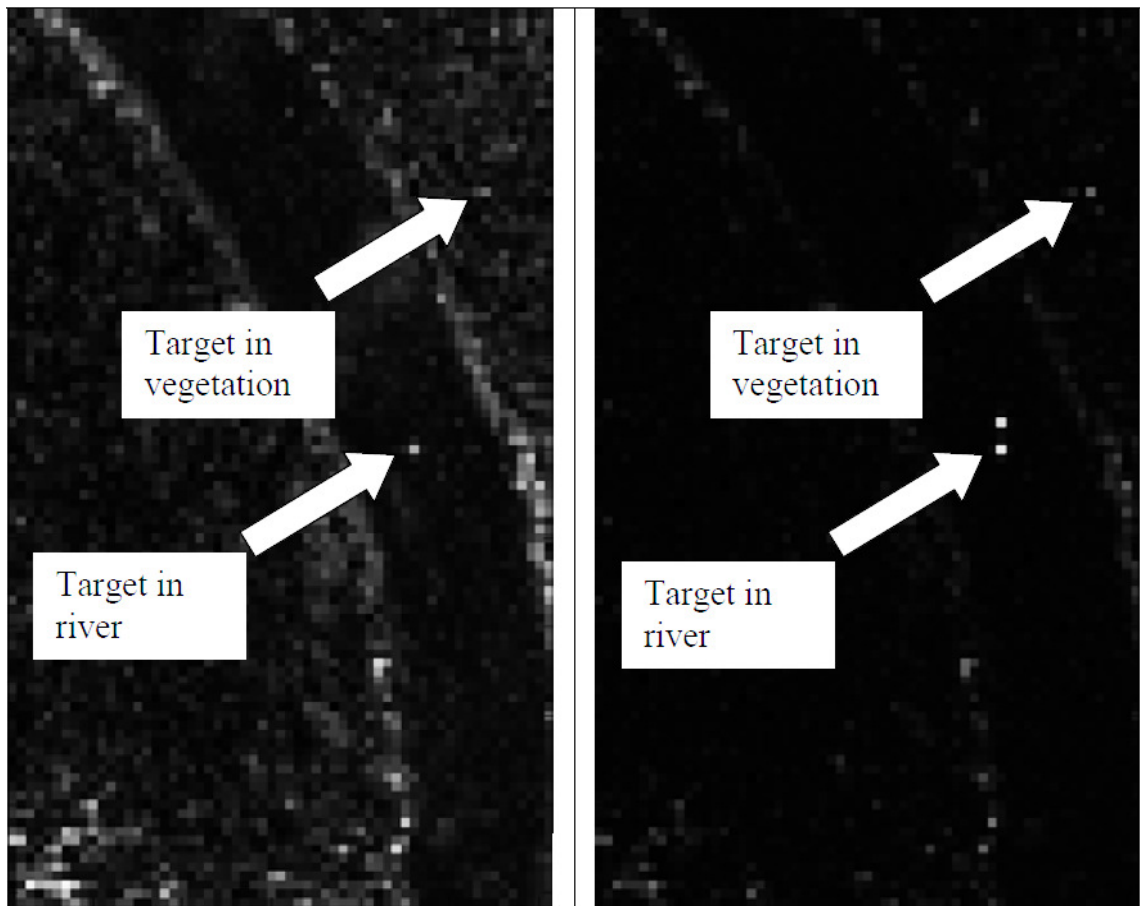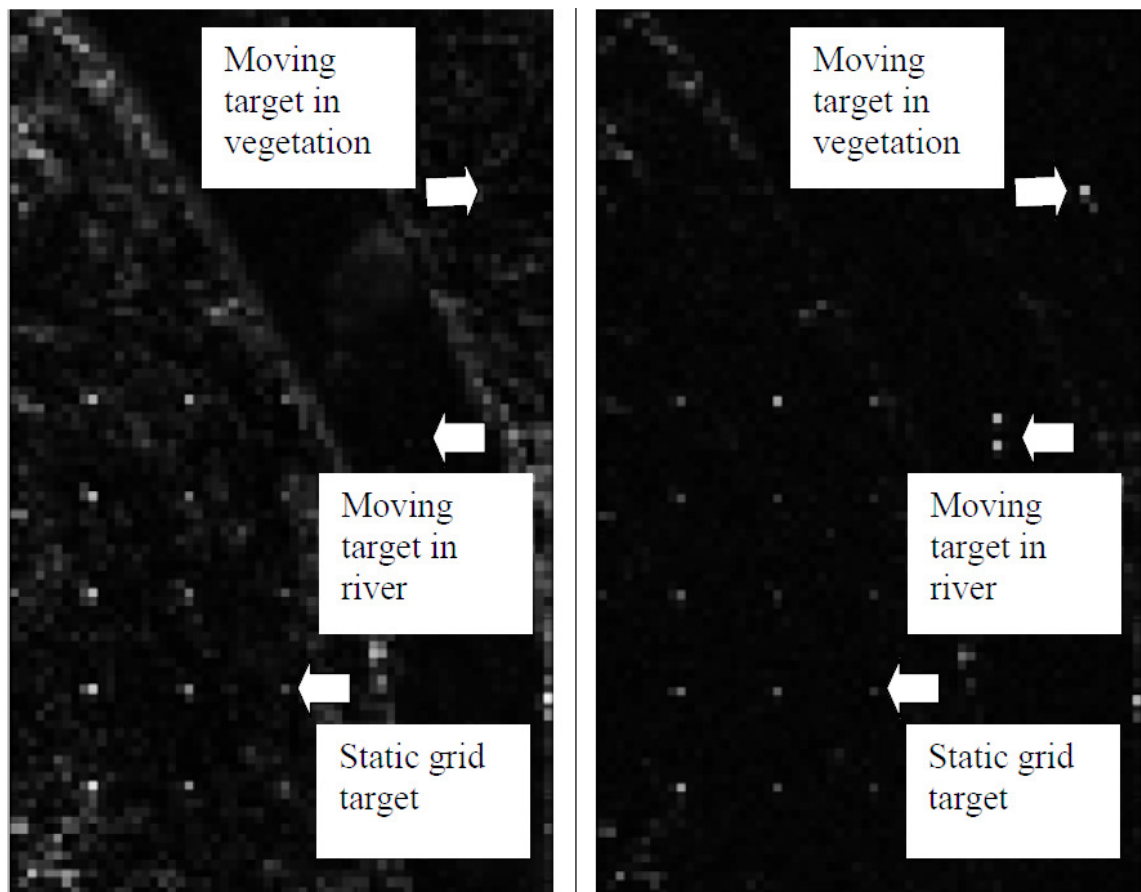
Figure 4-86: (Left to right respectively) Target detection of moving/static targets by the RX algorithm and the temporal algorithm, with both moving targets missed by the baseline RX algorithm

Temporal algorithms deliver a significant improvement in anomaly detection performance compared to conventional but widely used approaches to HSI. This is particularly true of the detection of anomalous moving targets where the conventional techniques are not able to detect moving targets that have spectral signatures similar to that of the background. The temporal algorithms as implemented by WS can detect such targets because the detection is based both on spectral and temporal anomalies. A key aspect of the HSI processing is the registration of sub-images to form the hypercube. In the current system, spatial registration of the sub-images is calculated off-line as temporal registration is not necessary at this stage. An improved demonstrator system will require the calculation of the warping coefficients to be performed on-line and automatically, which is the next stage of development for real-time HSI.

CONCLUSION – This chapter described work undertaken to demonstrate the necessary and sufficient performance of N-IRIS for SWIR snapshot HSI. The extraction and co-registration of hypercubes from N-IRIS imagery was examined to determine the issues affecting the exploitation of imagery in anomaly detection or classification algorithms. A potential solution in the form of optical mapping was examined as a solution to issues of subimage warping. Using open-source databases, simulated N-IRIS responses enable an initial consideration of material discrimination performance. This was further studied with an ANOVA experiment to disprove the null hypothesis that "N-IRIS cannot provide additional spectral information beyond its panchromatic counterpart". Three-party collaborative work on snapshot anomaly detection was also described to highlight consideration of the practical exploitation of N-IRIS imagery for publishable scenarios.

Chapter 5:
Solutions to Dispersive Spectral Smear

ABSTRACT – The convenience of the approximately co-linear polarizing beamsplitting of Wollaston prisms has led to their widespread use in areas such as imaging polarimetry, optical instrumentation and laser systems. The chromatic variation in their splitting angles can however introduce detrimental effects such as the spectral blurring of broadband images. The achromatisation of Wollaston prisms to reduce this angular dispersion is described in this chapter within the context of current solutions to spectral smear. The analytical theory is presented with an example application where a six-fold reduction in dispersion is achieved for wavelengths in the region 400nm to 1.7μm. The principle is generally applicable from ultraviolet to thermal-IR wavelengths. Experimental proof of concept is demonstrated and spectral dispersion of extended images recorded through cascaded Wollaston prisms for IRIS is shown to be reduced by nearly an order of magnitude.

5.1 Cost-Effective Visible IRIS Sensor

Recalling the N-IRIS design choices of Chapter Three, the supplier of the BBO prisms required for splitting offered a second identical prism set at negligible marginal cost. It was decided that this additional set would be obtained and a cost-effective IRIS sensor in the visible regime would be assembled. This new sensor would be designated as VIS-IRIS and serve as a demonstrator, using the remaining funds from the N-IRIS budget. It would also allow the examination of dispersive spectral smear, which is relatively more convenient to investigate with respect to longer wavelengths beyond human perception. The design of VIS-IRIS will be described, followed by an assessment of the dispersive spectral smear, before the technique of achromatising Wollaston prisms is presented.

A low-cost 1.97 megapixel camera in the visible regime (400 to 700 nm) was obtained from *Lumenera Corporation*, with the model being the Infinity 2-2M in universal serial bus (USB) format. The monochrome camera employed a 1616×1216 pixel CCD with a pitch of 4.4 μm, leading to the nominal FPA dimensions of 7.11×5.35 mm respectively. Table 5-8 gives the wedge angles β that are identical to the N-IRIS prisms, but where the splitting angles θ for the infrared regime are no longer applicable here. Unlike the N-IRIS design process where the splitting requirement θ controlled the prism wedge angles β, the splitting angle was found from the wedge angle by:

$$\beta_{i,j}(a_i, f_{con}, n_{i,j}, \lambda_{Min}) = \left| \tan^{-1}\left(\frac{\theta_{i,j}}{2B(\lambda_{Min})} \right) \right| = \left| \tan^{-1}\left(\frac{\tan^{-1}\left(\frac{a_i}{4 f_{con} n_{i,j}} \right)}{n_e(\lambda_{Min}) - n_o(\lambda_{Min})} \right) \right| \quad (37)$$

Using the birefringence B at the shortest wavelength of 400 nm, the splitting angles have been recalculated from the Sellmeier expressions for BaB_2O_4 as follows:

$$n_e(\lambda) = \left(2.3753 + \frac{0.01224}{\lambda^2 - 0.01667} - 0.01516 \cdot \lambda^2 \right)^{\frac{1}{2}} \quad (38)$$

$$n_o(\lambda) = \left(2.7359 + \frac{0.01878}{\lambda^2 - 0.01822} - 0.01354 \cdot \lambda^2 \right)^{\frac{1}{2}} \quad (39)$$

Recall that the wedge angle β must enable the spatial separation of the replicated sub-images over the entire wavelength range of interest. This prevents any overlapping sub-images, particularly between those at shorter wavelengths.

Splitting (i,j)	Wedge Angle β (deg)	Splitting Angle θ (deg)
X-Dimension (1,1)	30.780°	7.978°
Initial Y-Split (2,1)	20.437°	4.991°
Second Y-Split (2,2)	36.645°	9.964°

Table 5-8: Wedge angles reproduced from Table 3-5, with splitting angles calculated for the visible range

With the detector array and splitting angles known, the next step was to determine the collimator COTS lens needed to ensure the correct splitting of centroid rays. FPA size, splitting angle and condenser lens are related by Equation (14) in Chapter Three where:

$$\theta_{i,j}(a_i, f_{con}, n_{i,j}) = 2\tan^{-1}\left(\frac{c_{i,j}}{2 f_{con}} \right) = 2\tan^{-1}\left(\frac{a_i}{4 f_{con} n_{i,j}} \right) \quad (40)$$

The required focal length for the single X-split and both Y-splits were 19.18mm and 20.39mm respectively. An SLR 20mm condenser was chosen as the optimal COTS lens, since it is widely available within the field of amateur photography and was inexpensive to obtain. Selecting an appropriate field stop and collimator lens for VIS-IRIS is more problematic, as shown by Equation (16) in Chapter Three where:

$$k_i(a_i, f_{col}, f_{con}, n_{i,j}) = \frac{s_i}{m} = \left(\frac{f_{col}}{f_{con}} \frac{a_i}{n_{i,j}} \right) \quad (41)$$

This single expression contains the two unknown quantities and an arbitrary choice must be made to fix one of these values. Since the field-stop would require bespoke manufacture regardless, the decision was made to use a 50mm collimator. Any other choice would also be equally viable, but 50mm SLR lenses are inexpensive to obtain and are widely available.

The field stop size was chosen as 4.6×3.1 mm, subjectively trimmed from 4.8×3.2 mm after modelling within *Zemax* software to ensure a sufficient border in-between all sub-images. This prevented any sub-image overlapping on the FPA and offered a margin of error against manufacturing variations of the prisms. With reference to the remaining equations within Chapter Three, the objective chosen was a 100mm SLR lens, after modelling with various focal lengths around that value. The arbitrary choice was made for a full-FoV of 2.76°×1.83° that was deemed suitable for longer-range imaging. For completeness, the PSL was 0.396 m^2 and the GSD was 241×160 metres at a reference distance of five kilometres. Figure 5-87 is the VIS-IRIS design from the field-stop onwards, while Figure 5-88 is a reference image of the assembled VIS-IRIS.
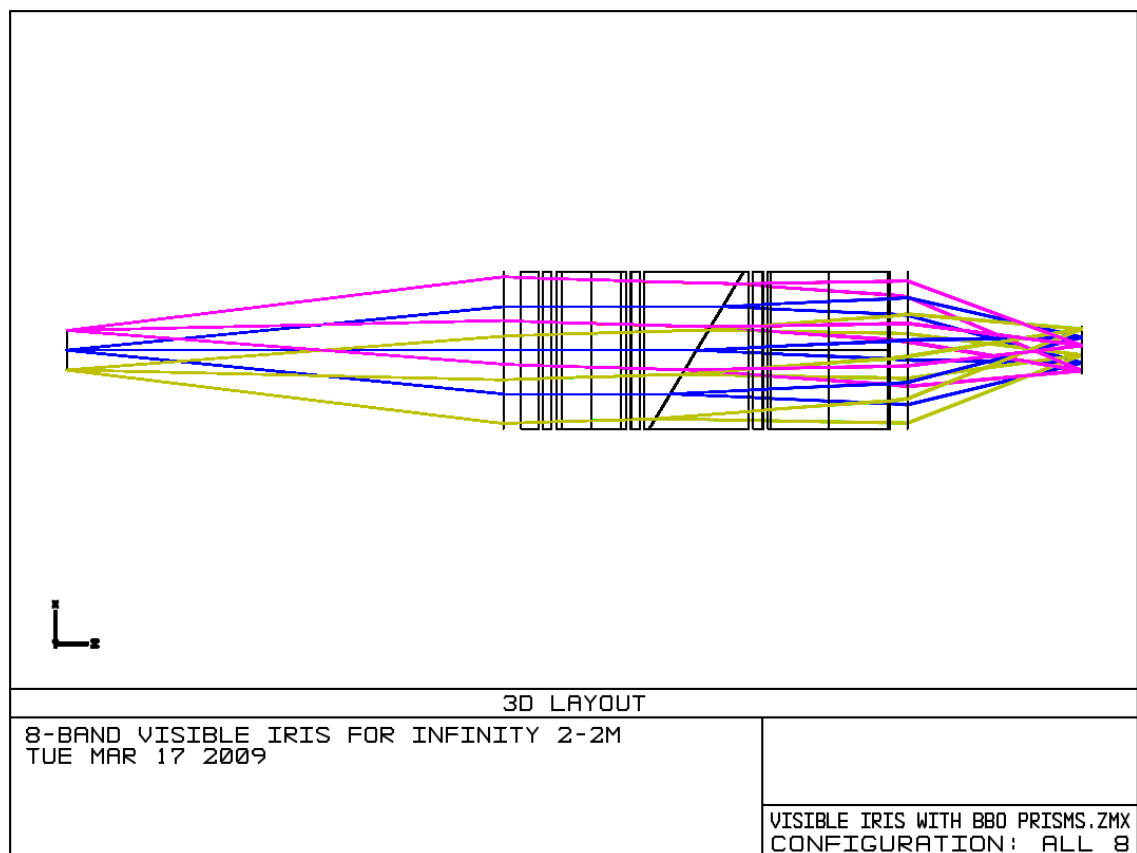

3D LAYOUT

8-BAND VISIBLE IRIS FOR INFINITY 2-2M
TUE MAR 17 2009

VISIBLE IRIS WITH BBO PRISMS.ZMX
CONFIGURATION: ALL 8

Figure 5-87: Schematic layout for VIS-IRIS from field stop onwards employing paraxial lenses
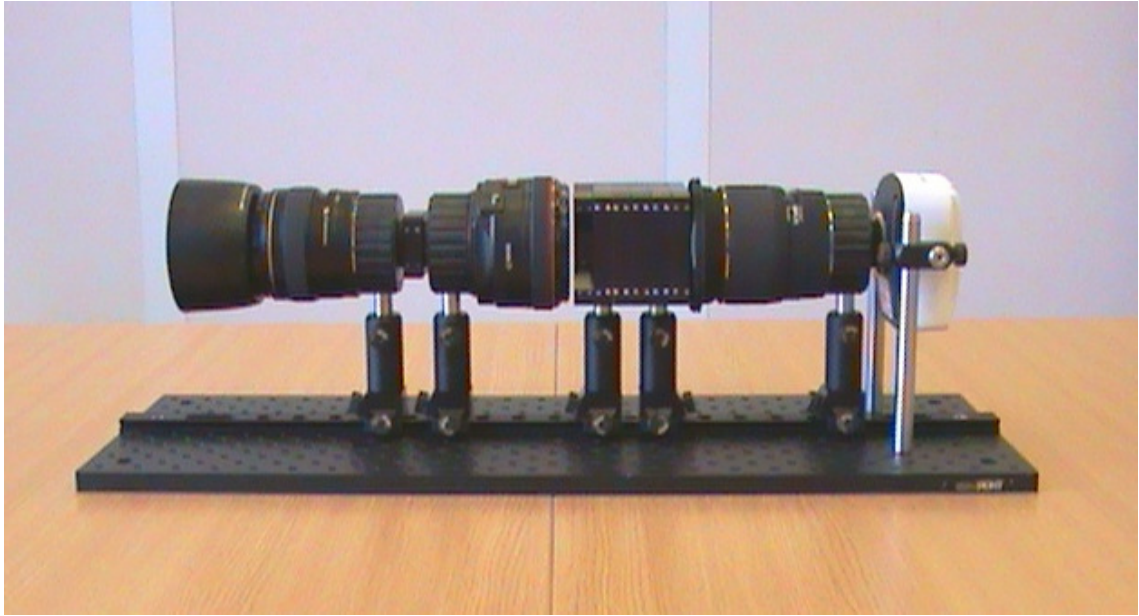
Figure 5-88: In-situ image of Vıs-IRIS, with input aperture on left and FPA on right hand-side

5.2 Assessment of the Problem

As with the development of the preceding N-IRIS that initially used COTS lenses, the design schematics for the procured SLR lenses were proprietary. Ideal lenses were substituted for their real equivalents to enable construction of ray-tracing models. Figure 5-89 to Figure 5-91 demonstrate the extent of spectral blurring, which is much greater within the visible regime than the previous near-IR region beyond 1μm. This chromatic smear is intrinsic to Wollaston prisms, since the passband spectra are not orthogonal components. This is evidenced by the presence of sidelobes in the STCs of sub-images, which are not the idealised rectangular windows.

The resultant dispersion smears the point-spread function (PSF) in the direction of splitting, causing an overall blurred image. Spectral contrast is generally reduced and image quality significantly degraded because of smearing. The steps within Section 3.3 for prism material selection were repeated for Vis-IRIS and BBO was confirmed as the most suitable substance. This was expected since BBO was also optimal for N-IRIS in terms of balancing optical qualities with availability in the non-thermal SWIR region.

Using paraxial lenses in the optical model along with BBO prisms, the blurring was so large that PSF and MTF calculations in *Zemax* software failed. Interrupt errors were returned and attempts at workarounds proved to be unsuccessful. These analyses were however secondary at the time for the blurring problem at hand, which overwhelmed the consideration of specific optical aspects such as PSF and MTF. As evidenced by Figure

5-89 and Figure 5-90, the maximum smear varied from around 14 to 45 pixels between sub-images. The geometric image analysis of an alphabet target became significantly degraded as seen in Figure 5-91. Even if the lenses designs were available, it would only serve to further compound a challenging optical situation.
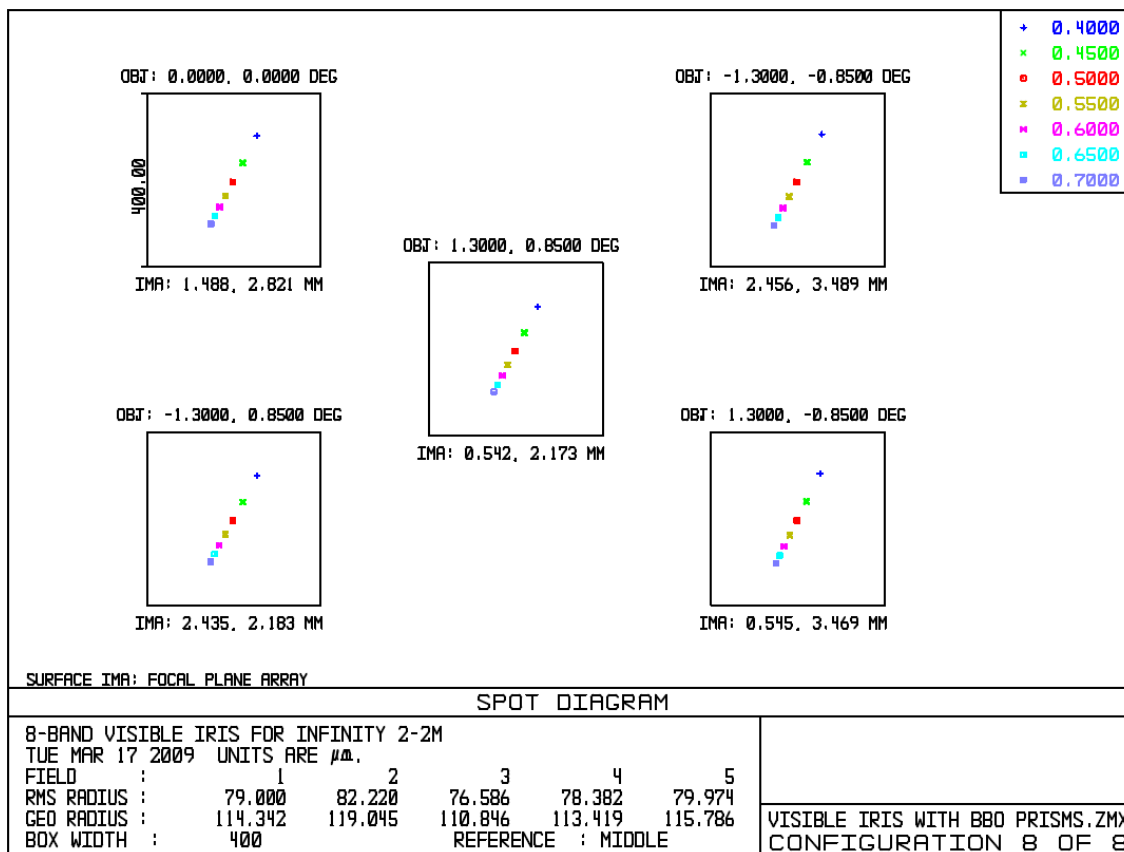
Figure 5-89: Maximal smear expected, with 115 µm geometric and 80 µm RMS radial extent
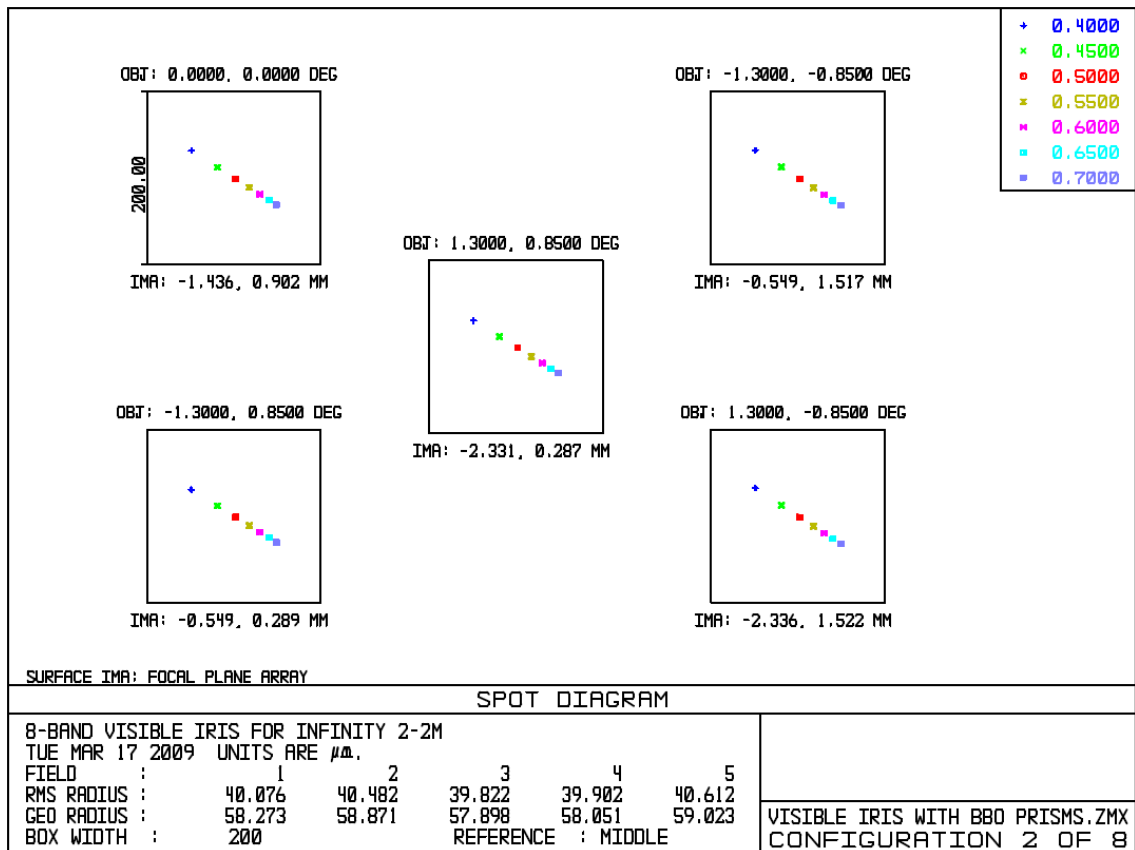
Figure 5-90: Minimal smear expected, with 60 µm geometric and 40 µm RMS radial extent
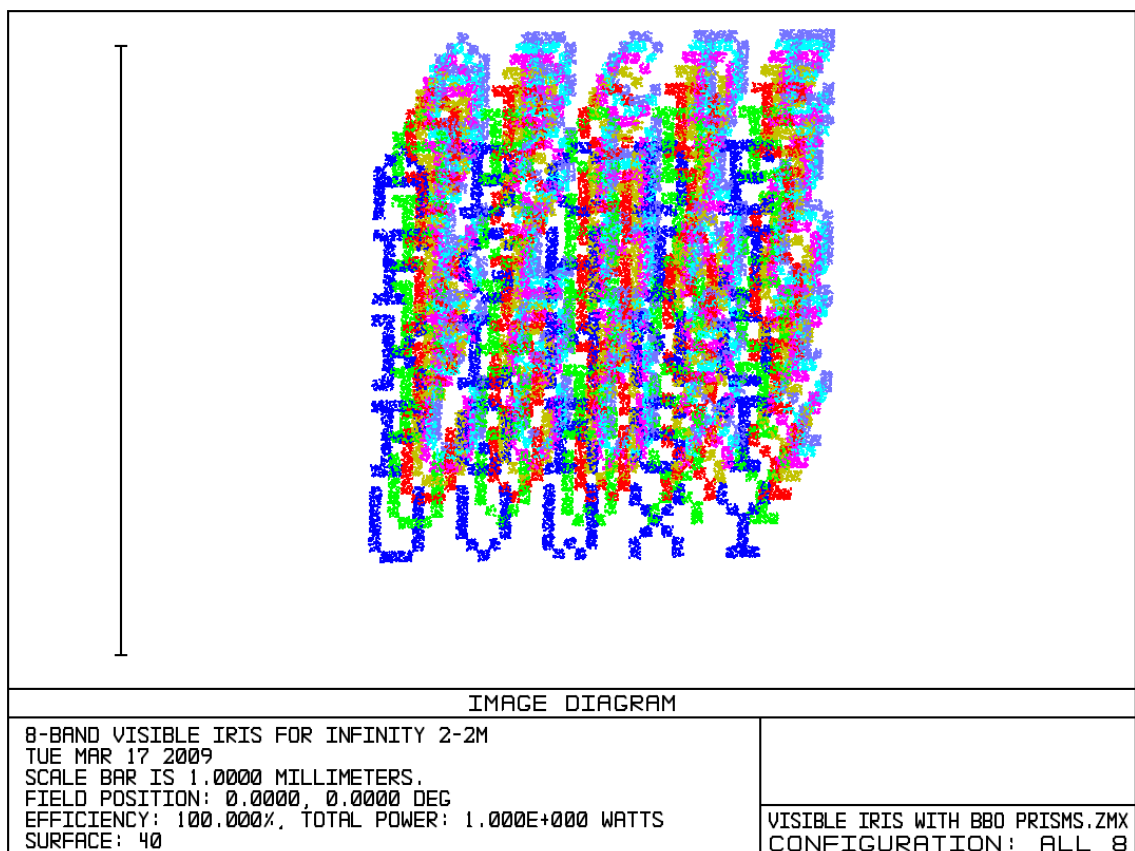
Figure 5-91: Geometric image analysis at the focal plane, indicating the impact of spectral smear

Figure 5-92 is a test image recorded with Vis-IRIS of two traffic signs, situated at a distance of around 150 metres. Figure 5-93 and Figure 5-94 are enlarged sub-images, which are rendered into false RGB for clarity of comparison between the limit cases of minimum and maximum smear. These limits of smear were empirically measured as 14 and 35 pixels respectively for the preceding images, thus according well with the prediction of 14 to 45 pixels. The following section now briefly relates three possible solutions to smear that have been suggested [62].
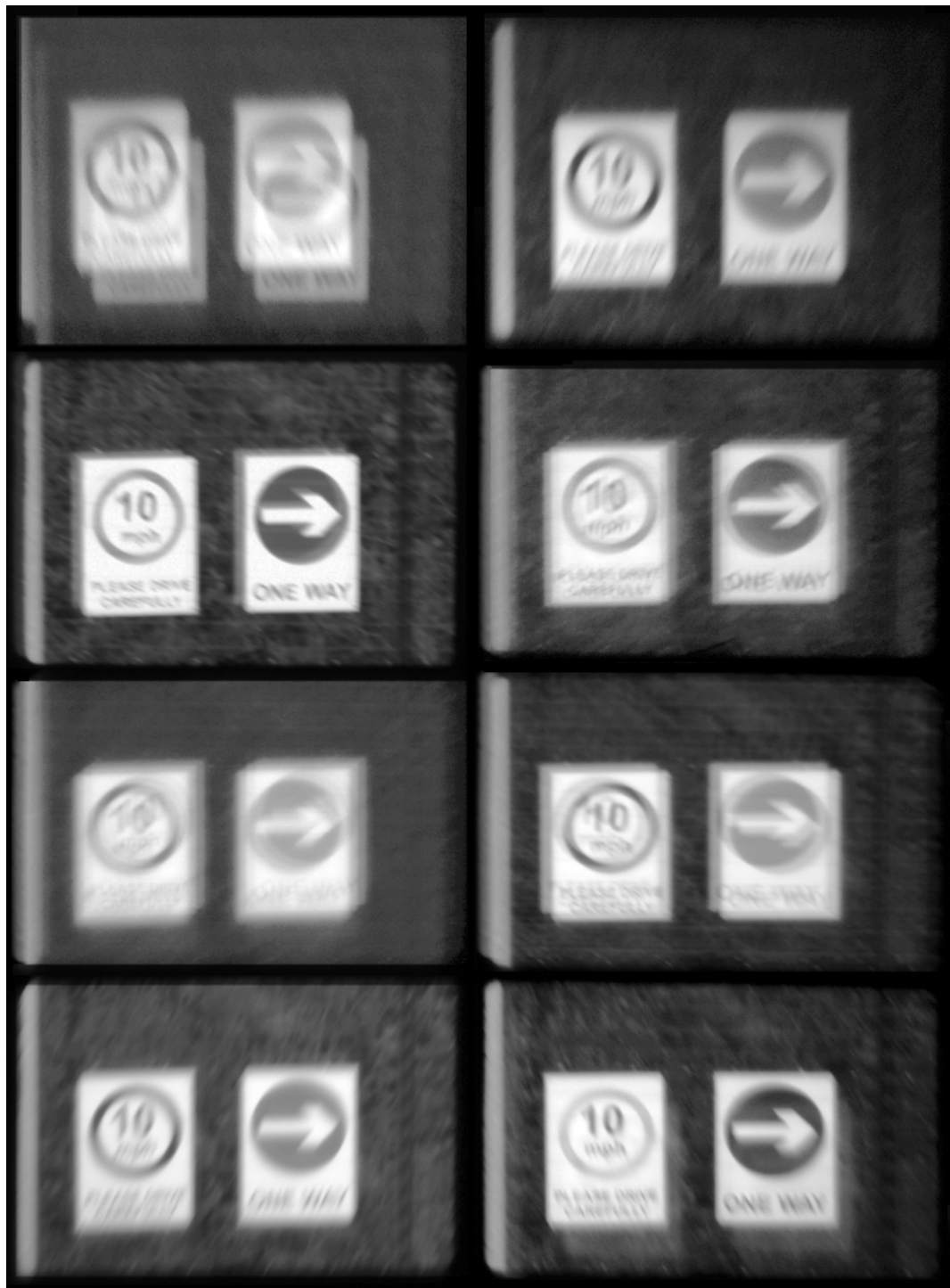
Figure 5-92: VIS-IRIS capture of 2 traffic signs at a distance of around 150 meters – note the dispersion

Figure 5-93: VIS-IRIS image exhibiting lowest dispersion, rendered into false RGB for clarity

Figure 5-94: VIS-IRIS image showing the highest dispersion – upper left portion from Figure 5-92

5.3 Present Solutions and Remedies

The first proposal involves employing prisms to provide counter-dispersion, which greatly reduces but may not fully eliminate the spectral smearing [45]. Figure 5-95 demonstrates this principle of counter-dispersion, where the dashed lines represent the defocused rays *w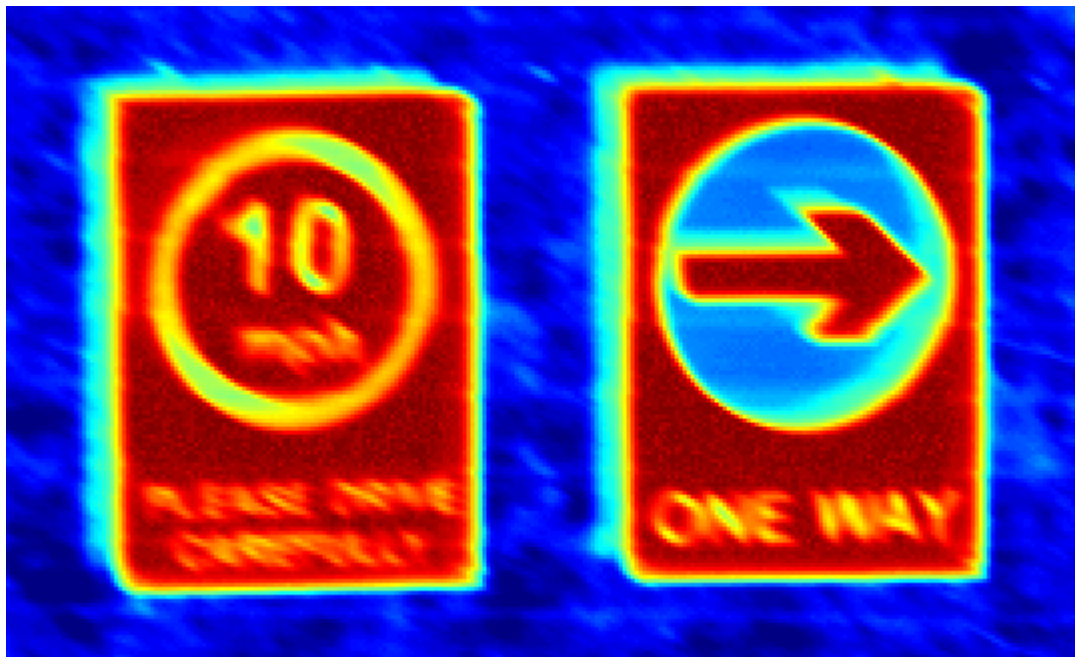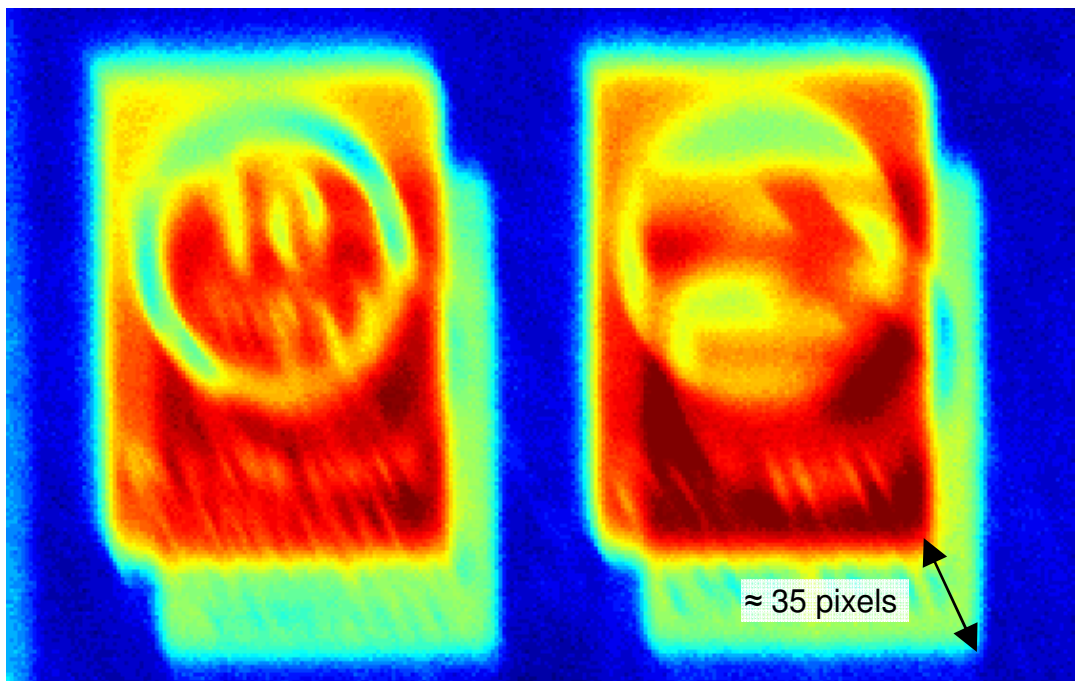ithout* correction, while the prism compensates the solid rays as shown. At present in this regard, no further developments in this area are known to have been advanced by the inventors of this method.
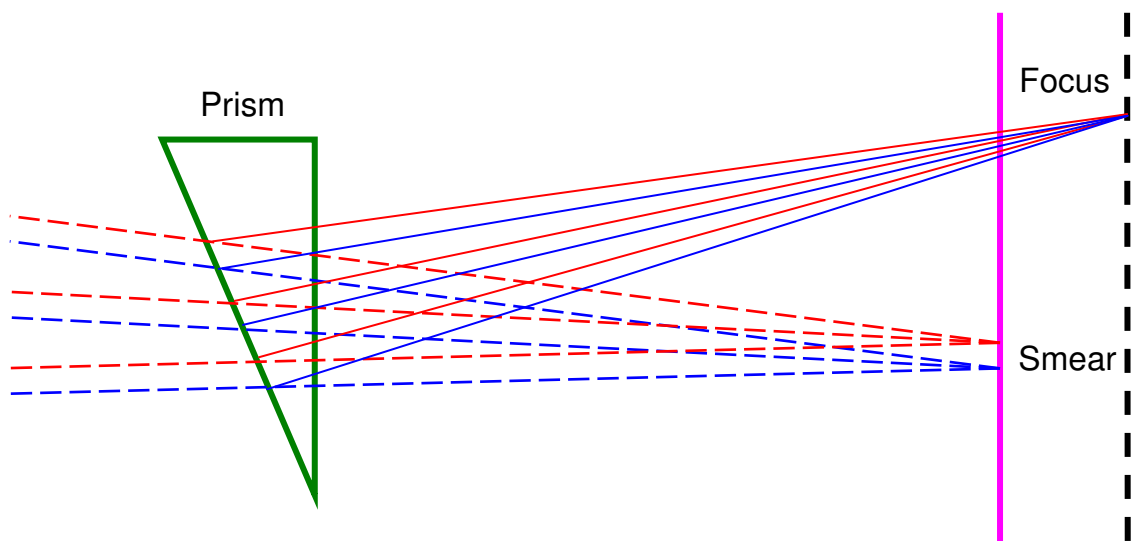
Figure 5-95: The correction of spectral smear by a dispersive prism – note that the image plane may shift

The second method of resolving smear is to deploy a mosaic filter onto the FPA, whereby eight tiles of interference filters are assembled onto a single planar element. Bandpass regions for these filters can be selected to assist in transmitting the main STC peaks while rejecting their side-lobes. This approach reduces the lateral smear across the FPA caused by the spectrally dispersed splitting angles within the Wollaston prisms. An issue with this method is locating suitable filters that are both micro-machinable and possess the required bandpass window, notwithstanding the cost of bespoke filters.

Additional glass tiles can be stacked along with these filters to compensate for optical path differences (OPD) between sub-images of varying wavebands upon the FPA. These glass spacers compensate for chromatic aberration introduced by lenses and this mosaic approach shown in Figure 5-96 is effective, but achromatised prisms may offer a simpler method with higher optical throughput. The further particulars of this mosaics approach, including design and merit assessment, have been investigated and published by fellow researchers [62].
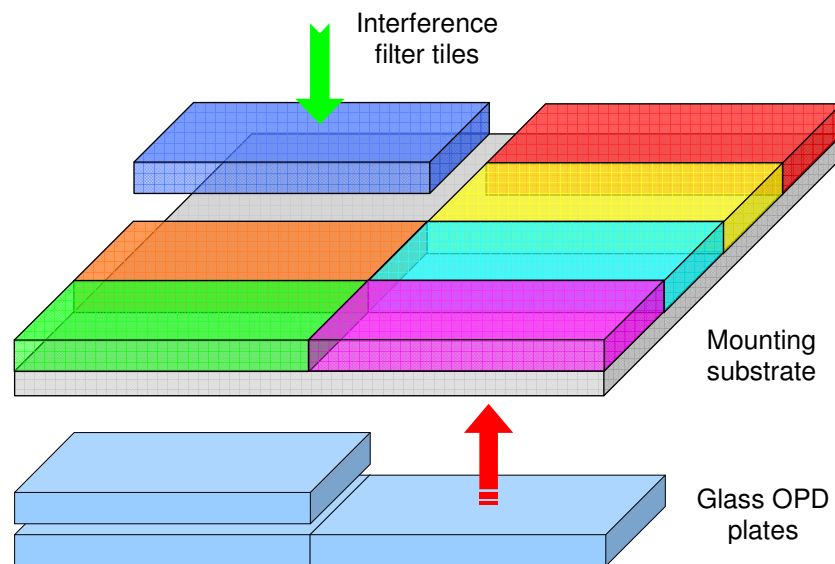
Figure 5-96: Mosaic filter assembly with interference filter tiles and glass OPD plates

The third solution is software-based correction, based upon the fact that each sub-image pixel involves spectral mixing between sub-images. Considering each STF could be represented within an 8D spectral space, the corresponding unit vectors would not be orthonormal. In other terms, the STCs are not functions that divide a spectrum into eight mutually exclusive pieces without spectral overlap. Each resultant sub-image that primarily represents a given waveband contains a portion of every other waveband. This spectral mixing between the eight sub-images is not trivial to resolve.

The unmixing process will however degrade the images by amplifying detector noise. Further particulars of this approach, including design and merit assessment, are detailed in reference [62]. The following sections outline a fundamental remedy, which can replace or reduce the need for retrofitted solutions to resolve spectral smear. As will be discussed, this solution relies upon an innovative approach to polarising beam splitting, which can also provide benefit to other applications and areas of photonics.

5.4 Achromatisation of Wollaston Prisms

The IRIS requirement for the beamsplitter is to split symmetrically an incoming beam into orthogonal polarisations. As discussed in Chapter Two, chromatic variation in the splitting angle (CVSA) leads to image blurring or smear. The advance in reducing CVSA was in recognising that positive and negative dispersive prisms can contribute to the needed splitting. As will be shown, this can reduce CVSA by an order of magnitude, whilst retaining key conveniences such as high extinction ratios and acute-angle polarization beam splitting [22,23]. Two prisms with a certain pair of wedge angles β can combine to yield an overall splitting angle θ, such that the angular deviation $\Delta\theta$ with wavelength λ is minimised. For a single prism and for use in later considerations when formulating a master equation for achromatised prisms, this deviation is given by:

$$\Delta\theta(\beta,\lambda) = 2\tan(\beta)\left[n_e(\lambda_2) + n_o(\lambda_1) - n_e(\lambda_1) - n_o(\lambda_2)\right] \qquad (42)$$

For a small wedge angle β and normal incidence, the splitting angle θ for a Wollaston prism is $\theta(\lambda) \approx 2b(\lambda)\tan(\beta)$, where birefringence is $b=n_o(\lambda)–n_e(\lambda)$, n_o and n_e are the ordinary and extraordinary refractive indices respectively [70] and the approximations improve with reducing θ [71]. In the approximation that the dispersion in birefringence is constant within the range $\{\lambda_1,\lambda_2\}$, the CVSA is given by $\Delta\theta \approx 2(\lambda_2-\lambda_1)\,db/d\lambda\,\tan\beta$.

Achromatisation can be achieved by combining two prisms of opposite CVSA [72] as illustrated in Figure 5-97. We describe a method for determining the optimal parameters for achromatic prisms with a given resultant splitting angle for a compound instrument employing multiple achromatic prisms and an extended field of view, together with numerical and experimental validation [22,23]. The achromatisation of prisms requires that at a nominal central wavelength,

$$\frac{db_1}{d\lambda}\tan(\beta_1) + \frac{db_2}{d\lambda}\tan(\beta_2) = 0 . \qquad (43)$$

The suffixes refer to the first and second prisms of the achromatic prism pair respectively. This is analogous to the achromatisation of doublet lenses using crown and flint glasses. Material selection is based on a combination of acceptable residual CVSA, material properties, financial cost, availability and magnitude of birefringence. Approximate achromatisation is achieved using analytical approximations and

optimized achromatisation is subsequently obtained using rigorous ray tracing over a finite spectral band and over an extended range of angles of incidence.
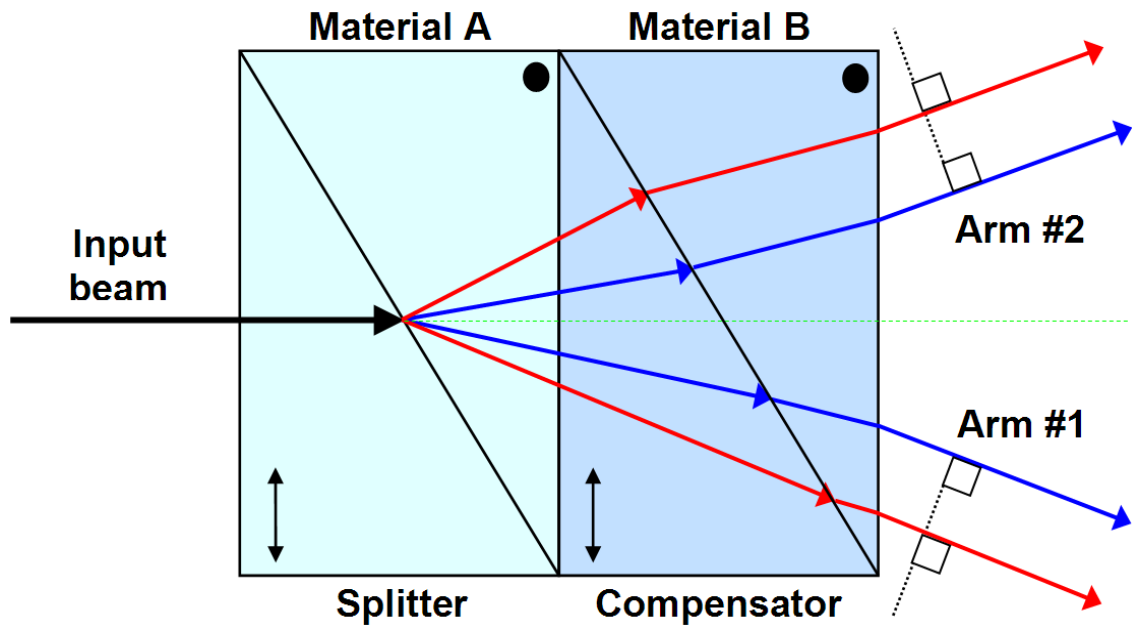
Figure 5-97: Illustration of achromatisation principle – all features are exaggerated and are not to scale

Recalling the design stage for N-IRIS, there were a number of materials highlighted as suitable for single prisms, but not all of their transmission curves extend into the visible region. Consideration of the remaining material options yielded the shortlist in Table 5-9, where $KTiOPO_4$ is defined in terms of its three crystal axes (x,y,z) in cyclical vector fashion. The final chosen pair of β-BaB_2O_4 with YVO_4 was based on factors such as cost, availability and birefringence. Their respective birefringences are also well matched against each other and relatively large with respect to the other materials, to minimise bulk material and hence cost. Other potential materials shortlisted to be paired with YVO_4 were Ga_2Se3, $AgGaSe_2$ and $CaCO_3$, however the former suffers from instability and toxicity and all three are higher cost than β-BaB_2O_4.

Prism Material	Birefringence B_{AVG}
Al_2O_3	-0.008
BaB_2O_4	-0.120
$CaCO_3$	-0.175
$LiNbO_3$	-0.090
MgF_2	0.011
SiO_2	0.009
KD_2PO_4	-0.039
KH_2PO_4	-0.042
$KTiOPO_4$ (x,y)	-0.011
$KTiOPO_4$ (y,z)	-0.101
$KTiOPO_4$ (z,x)	0.112
YVO_4	0.117

Table 5-9: Calculated values of metric used to dispersion-match two materials in the visible regime

The CVSA of the achromatic prisms can be determined and optimized using rigorous ray tracing through the two prisms in sequence for a range of pertinent incident angles, but it is physically insightful to use analytical expressions as a first approximation for starting parameters. Starting from expressions in [71] and [73], it can be shown that the splitting angle θ for an achromatic prism pair for an initial normally incident ray is:

$$\theta(\lambda,\beta_A,\beta_B) = \delta(\lambda,\beta_A,\beta_B) + \theta^A(\lambda,\beta_A) \tag{44}$$

where

$$\delta(\lambda,\beta_A,\beta_B) = 2\sin^{-1}\left(n_o^B(\lambda) - \frac{n_e^B(\lambda)}{2} - \frac{n''(\lambda)}{2} \right) \left\{ \frac{\cos(\Psi(\lambda,\beta_A))}{\cos\left[\theta^A(\lambda,\beta_A)\right]} \right\}$$
$$\times \left[\tan(\Psi(\lambda,\beta_A)) - \tan(\beta_B + \Psi(\lambda,\beta_A)) \right] \tag{45}$$

where

$$\Psi(\lambda,\beta_A) = \sin^{-1}\left(\frac{n_o^A(\lambda) + n_e^A(\lambda)}{2\bar{n}*} \sin\left[\theta^A(\lambda,\beta_A)\right] \right) \tag{46}$$

where

$$\bar{n}*(\lambda,\beta_A) = \frac{1}{2}\left[n_o^A(\lambda) + n''(\lambda) \right] \tag{47}$$

where

$$n''(\lambda, \beta_A) = n_e^B(\lambda) \left\{ 1 - \left(\frac{1}{n_o^B(\lambda)^2} - \frac{1}{n_e^B(\lambda)^2} \right) \sin^2 \left[\theta^A(\lambda, \beta_A) \right] \right\} \qquad (48)$$

where

$$\theta^A(\lambda, \beta_A) = \sin^{-1} \left[B^A(\lambda) \tan \beta_A \right] \qquad (49)$$

and

$$B^A(\lambda) = n_e^A(\lambda) - n_o^A(\lambda). \qquad (50)$$

β_A and β_B are the wedge angles for prisms A and B, while their refractive indices are denoted by n^A and n^B respectively with Sellmeier or Laurent-Cauchy equations for each material. As in the case of large-angle splitting with Wollaston prisms [71], it is necessary to define the refractive index for the extraordinary ray as a function of the directions of both the incident ray and the optical axis [73]. A normally incident ray is assumed here with refraction approximated using mean refractive indices and Snell's Law, which although not physically correct yields accurate approximations [73].

5.6 Optimisation and Design of Prisms

Consider broadband incident light with a wavelength range of $\{\lambda_1, \lambda_2\}$ for a splitting angle requirement $\theta(\bar{\lambda})$ for an application where $\bar{\lambda} = (\lambda_1 + \lambda_2)/2$. Optimization involves finding those combinations of β_1 and β_2 that yield the required nominal splitting angle $\theta(\bar{\lambda})$ and are optimized for minimum CVSA across the full waveband $\{\lambda_1, \lambda_2\}$.

The constraint between both wedge angles to satisfy the splitting angle requirement $\theta(\bar{\lambda})$ simplifies the search from the 2D space of $\{\beta_1, \beta_2\}$ to a search in only one variable (β_1 or β_2). For each value of β_1 (or β_2 instead) there is given CVSA and the optimization goal is to minimize the CVSA for $\{\lambda_1, \lambda_2\}$. The optimization metric yielding a first-order approximation of CVSA for use in rigorous ray-tracing optical models is henceforth given for a prism pair by

$$\Delta\theta = \theta(\beta_2(\lambda_2), \beta_1, \lambda_2) - \theta(\beta_2(\lambda_1), \beta_1, \lambda_1). \qquad (51)$$

This expression provides the means for an approximate optimization of the prism pair, prior to a rigorous ray-traced optimization across an extended field of view. For each field-angle, ray tracing is expedient to account for the first wedge angle that is perturbed by the required angle of incidence, which is also compounded by the refraction through

the first surface. It is not tenable to consider field angles analytically, since refraction and splitting will be different as refractive indices are a function of the directions of an incident ray and the optical axis [73].

In applications involving the transmission of light through multiple achromatised prisms, due to the interaction of CVSA between each achromatic prism, it is necessary to perform the optimization for the entire prism train or complete system. As with matching the CVSA between the prisms within an isolated achromatic pair, the residual CVSA between two or more pairs can be optimized such that the net CVSA is minimized by cancellation. For $2N$ prisms matched into N achromatic pairs, there are N free variables as one angle within each prism pair is constrained such that the splitting angle requirement can be satisfied. In conjunction with mathematical packages, optical ray-trace modelling software (such as *Zemax*) is effective in the optimization of multiple prism pairs with non-paraxial field angles. The averaging of refractive indices, net beam splitting and refraction that was initially used for analytical simplicity can be substituted for rigorous ray tracing for both the ordinary and extraordinary rays.

It is noteworthy that whilst the angular splitting introduced by Wollaston prisms is usually taken as approximately symmetrical, the differing refraction encountered by the ordinary and extraordinary rays results in asymmetry in both dispersion and splitting. For the achromatic prisms, this asymmetry can be reduced through the optimization process. It should also be noted that the optimization process allows positive and negative wedge angles, where the two angles within an achromatised pair do not have to be of the same sign or magnitude.

5.7 Proof-of-Concept Demonstration

To reduce costs, it was decided to design and obtain a test prism that could be compared against one of the existing VIS-IRIS prisms. The prism chosen to act as a reference was the largest prism from VIS-IRIS, which recalling the values in Table 5-8, yielded the splitting angle of 10° from the 36.7° wedge angle. The visible regime provided ease of measurement, since the previously used tuneable OPO laser was no longer available for testing in the SWIR or visible wavelengths.

Assuming that variations in $\partial b/\partial \lambda$ are sufficiently small, then the paraxial approximation of $-\partial b_1/\partial \lambda \, \tan(\beta_1) \approx \partial b_2/\partial \lambda \, \tan(\beta_1)$ will be satisfied over an extended wavelength range. At an indicative centre wavelength of 0.625 μm, $\partial b/\partial \lambda$ for β-BaB$_2$O$_4$ with YVO$_4$ are equal to 0.01442 and -0.08032 respectively and achromatisation is achieved when $\tan(\beta_2)/\tan(\beta_1) \approx -\partial b_1/\partial b_2 \approx 5.570$. This can be combined with Equation (51) and solved numerically to yield a unique combination of β_1 and β_2 that yields the required net splitting angle θ. Rigorous optimization based on ray tracing and minimization of CVSA for the range 400 nm $\leq \lambda \leq$ 850 nm yielded the splitting angles shown in Figure 5-98 and the parameters in Table 5-10. The ratio $\tan(\beta_2)/\tan(\beta_1)$ in this case differs by about 5% from that calculated using the approximations given in equations (44) to (50).
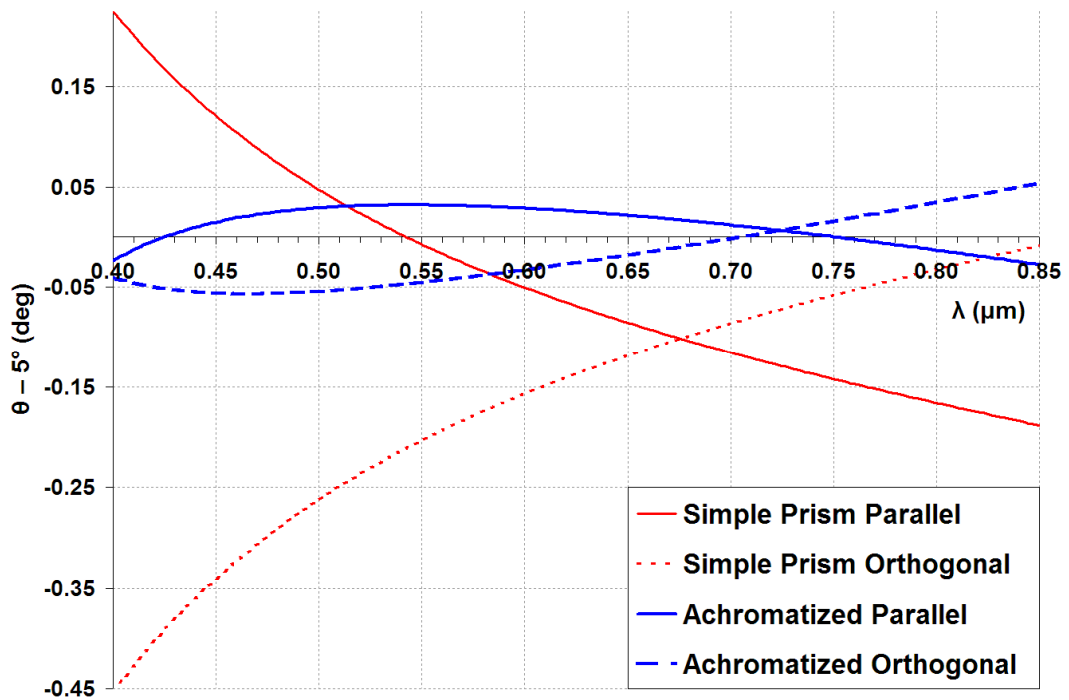

Figure 5-98: Spectral variation of the ray angles of exitance with respect to the surface normal, for the traditional and achromatised prism (optimized for 400 nm to 700 nm).

Using an iterative search of the 2D angle space for the achromatic pair with manual intervention as needed, the required wedge angles were discovered. These angles were constrained to yield the same 10° splitting angle as the baseline prism and are given in Table 5-10. Figure 5-99 and Figure 5-100 are the respective spot diagrams for both the baseline and achromatic prisms, showing a predicted reduction of 82% in this case. These diagrams pertain to a planar projection at an arbitrary distance of two metres, being what would be seen on a flat surface normal to the central axis at that distance.

Achromatic Prism	Prism Material	Wedge Angle β	Nominal Splitting $\theta(\beta)$	Net Splitting $\theta(\beta_1,\beta_2)$
Prism 1	β-BaB_2O_4	47.6°	14.78°	10.0°
Prism 2	YVO_4	10.62°	4.78°	

Table 5-10: Wedge angles β, nominal splitting angles $\theta(\beta)$ for single Wollaston prisms at 625 nm, and overall net-splitting angle $\theta(\beta_1,\beta_2)$ for an achromatic prism for 400 nm $\leq \lambda \leq$ 850 nm

To validate this achromatisation experimentally, imaging was done with a pinhole back-illuminated using a white light source that was band-pass filtered to transmit only in the range 400-700 nm. The achromatised Wollaston was situated 400mm in front of the aperture of a photographic lens with focal length 50 mm. This SLR lens was used to focus the collimated light from the pinhole after splitting onto a 27.9×18.6 mm FPA. The actual testing procedure would be to focus at infinity through the prism to the source for only one of the two resultant rays, due to the level of symmetry in this simple proof case. The spectral dispersion at the detector was ray-traced as 0.30 mm for the standard prism and 0.05 mm for the achromatic prism. These absolute values are again particular to the SLR lens and 16.1 megapixel array, but the relative reduction by over a factor of six remains the same for all cases.

With reference to Table 5-10, the preferred supplier for IRIS prisms (*Dr Sztatecsny STZ GmbH*) manufactured the proof-of-concept design. Surface flatness, planar finish and optical cementing were all emphasised to ensure conformance to the theoretical model as far as possible. The angular tolerance was minimised to the physical limits of manufacturing techniques at the time.
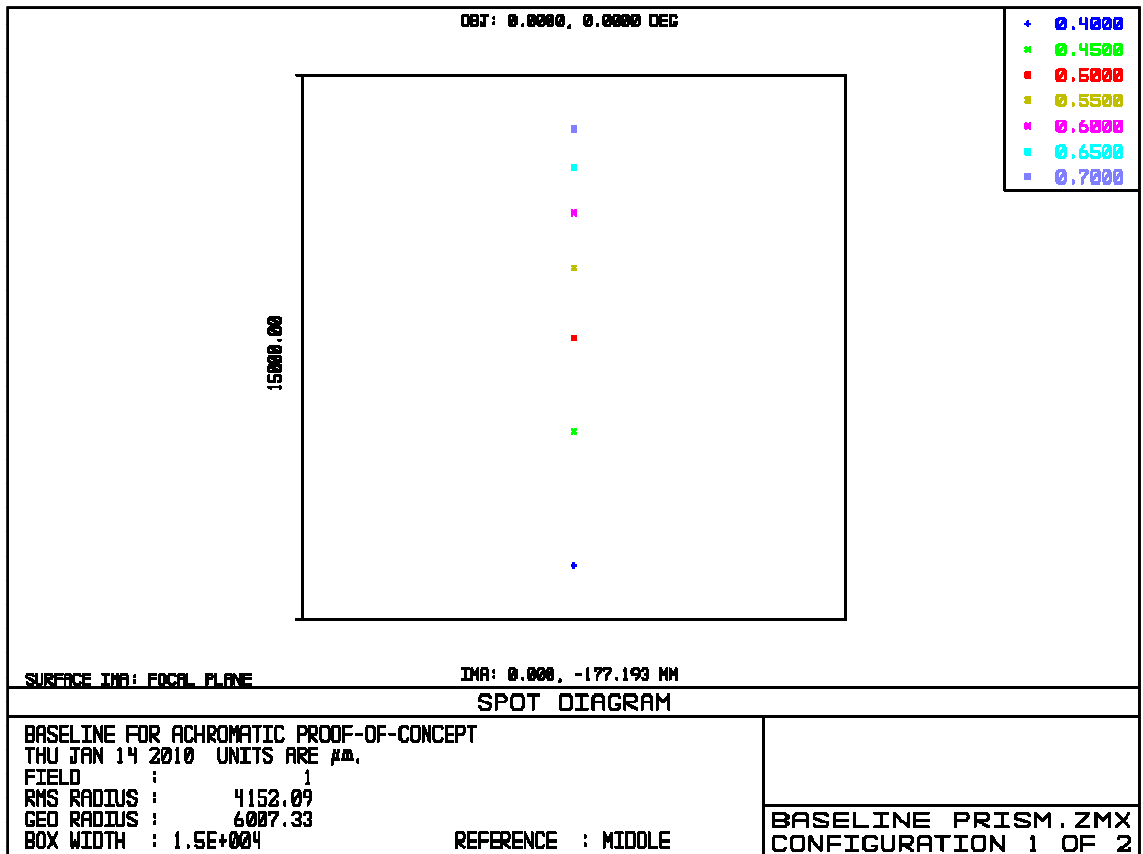
Figure 5-99: Large chromatic dispersion of 1.22cm at 2m for regular prism with wedge angle of 36.7°
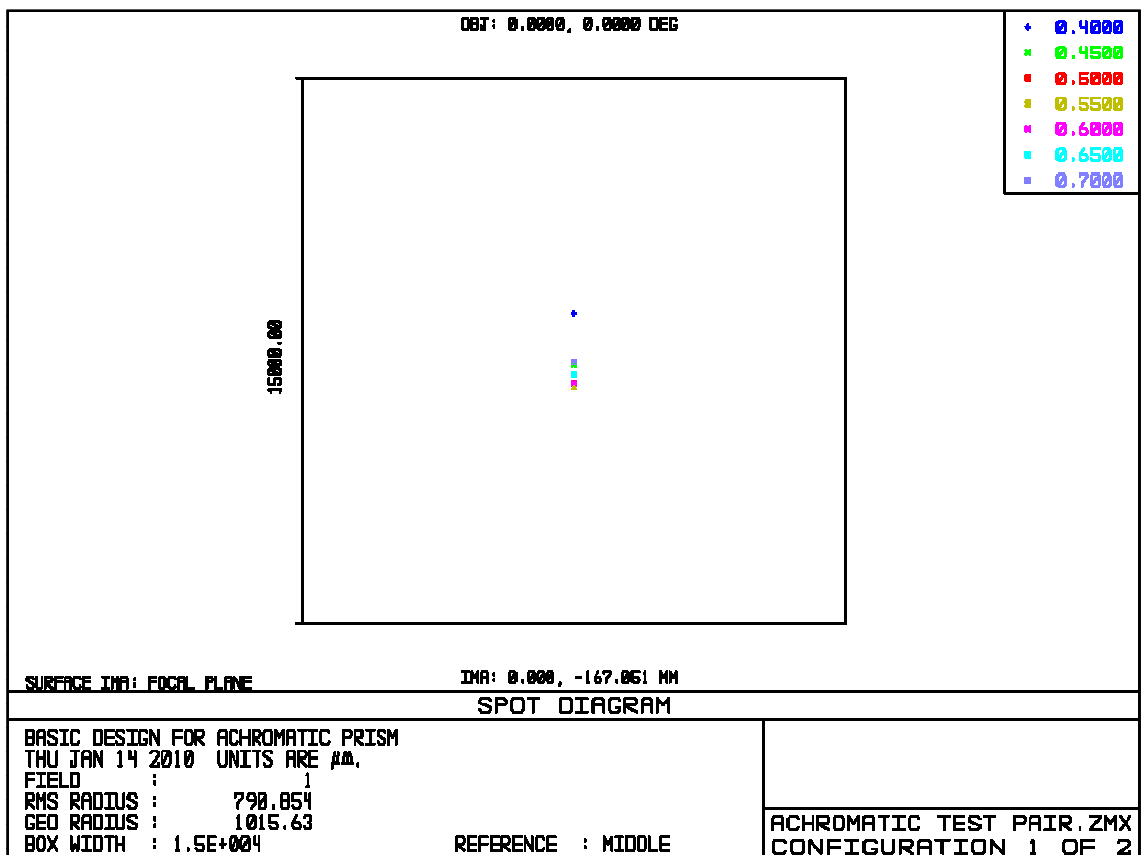

Figure 5-100: Lower dispersion of 0.22cm at 2m for achromatic prism – predicted reduction of 82%

Figure 5-101 shows the image captures for the dispersion of these two cases respectively, which are both in agreement with the predictions made earlier, as evidenced in Figure 5-100 from the rigorous ray-tracing model. The comparison and analogy with doublet lenses can be made here, where focal length variation over wavelength is minimized by using glasses of differing refractive indices. The innovation in this technique is the exploitation of birefringence variation for true symmetric beamsplitting, whether for imaging polarimetry or laser-based applications.

As can be observed within Figure 5-101, the dispersion for the standard prism is linear in wavelength for the splitting plane. The achromatised prism however exhibits a turning point in the CVSA, as can be seen in Figure 5-98. This is evidenced through the faint magenta, orange, and green hues on three points of the imaged pinhole – similar to the previous comparison and analogy of doublet lenses.
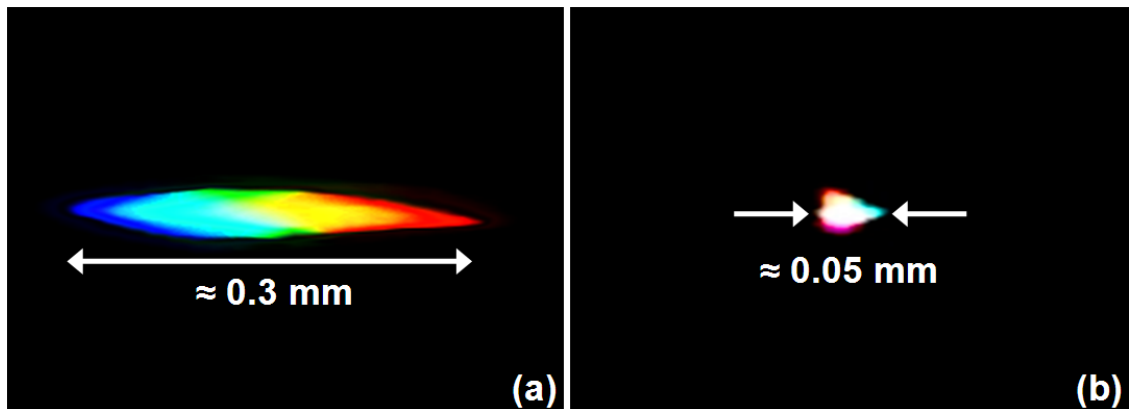

Figure 5-101: Colour captures of the chromatic dispersion from the traditional (a) and achromatised prism (b) over 400nm to 700nm respectively

5.8 Modelling and Optimisation of Wollaston Prisms

Designing a solution for VIS-IRIS required three pairs of achromatised prisms and since imaging is taking place, ray bundles covering each vertex of the entire FoV needed consideration, rather than one single ray that is initially incident along the central axis. For white light, the residual smear from the first prism set can be manifested as ray fans entering the second prism set, where each ray within an arc is of a different wavelength. Assuming five fans (corners and middle) in the initial FoV, there will be forty such arcs for the eight sub-images. They must all be optimised concurrently, whereby every sub-image and each fan within them are balanced in terms of minimising smear.

The overall smear for each sub-image is not a linear addition of the smear from each prism pair, since its effects are compounded through N-IRIS along with propagation through the quartz waveplates and their glass substrates. The problem required a computational solution in the form of optical modelling and ray tracing. *Zemax* software was used to carry out this constrained search in 6D angular space, to determine the six most suitable prism angles.

Figure 5-102 is the optical schematic for the upgraded VIS-IRIS, now named ACHRO-IRIS. Compared to Figure 5-87 for VIS-IRIS, the additional elements are apparent in the layout where each BBO splitter is immediately followed by the thinner YVO compensators. Table 5-11 following lists the details of each ACHRO-IRIS prism from front to back. It is analogous to Table 3-5 and Table 5-8 for the two previous IRIS systems, with the exception of the nominal angle $\theta(\beta)$. This represents the splitting achieved at the longest wavelength of 700 nm for a normally incident ray, to give a point of reference for a standard prism.
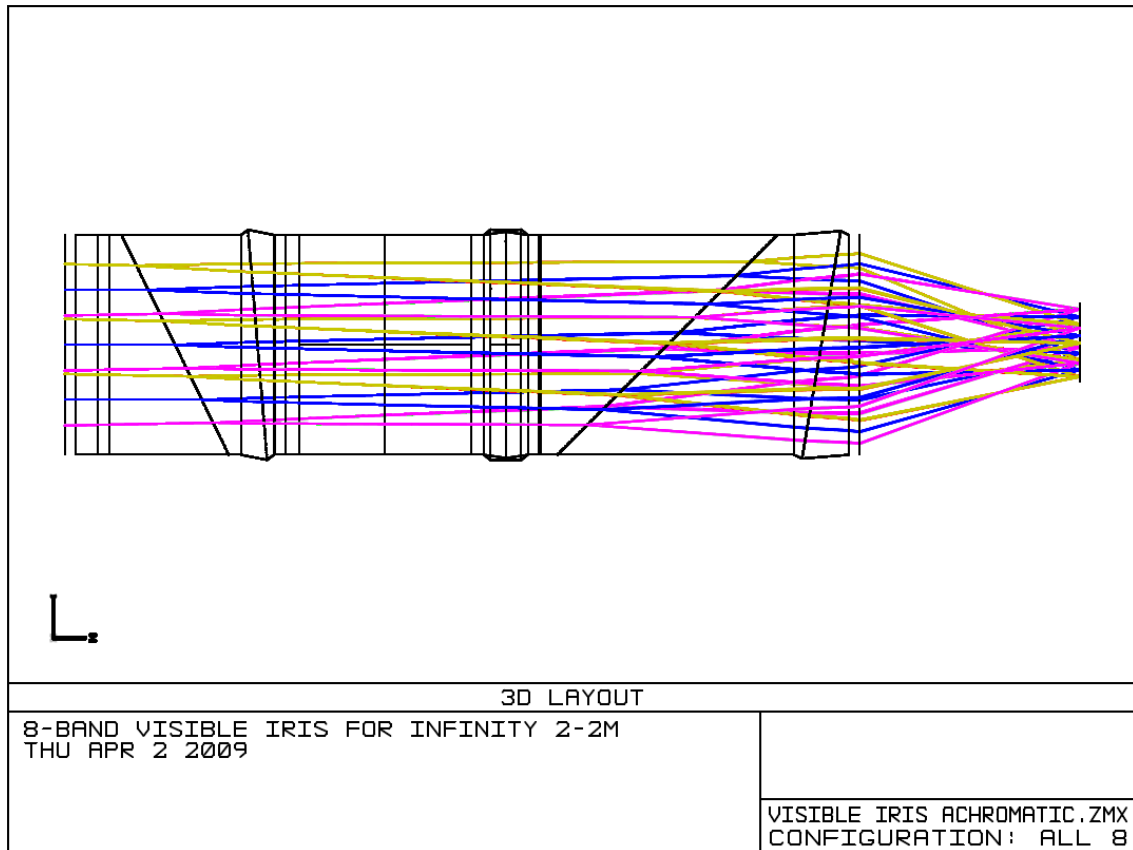
```
                              3D LAYOUT
8-BAND VISIBLE IRIS FOR INFINITY 2-2M
THU APR 2 2009

                                        VISIBLE IRIS ACHROMATIC.ZMX
                                        CONFIGURATION:  ALL  8
```

Figure 5-102: Schematic layout for ACHRO-IRIS from collimator onwards with paraxial lenses

Achromatic Prism	Prism Material	Wedge Angle β	Nominal Splitting $\theta(\beta)$	Net Splitting $\theta(\beta_1,\beta_2)$
Splitter Prism 1a	β-BaB$_2$O$_4$	-26.0°	6.533°	5.0°
Compensator 1b	YVO$_4$	-4.76°	2.082°	
Splitter Prism 2a	β-BaB$_2$O$_4$	38.0°	10.464°	8.0°
Compensator 2b	YVO$_4$	7.61°	3.340°	
Splitter Prism 3a	β-BaB$_2$O$_4$	45.0°	13.394°	10.0°
Compensator 3b	YVO$_4$	9.65°	4.251°	

Table 5-11: Wedge angles β, nominal splitting angles $\theta(\beta)$ for single Wollaston prisms at 700 nm, and overall net-splitting angle $\theta(\beta_1,\beta_2)$ for each achromatic prism pair within an eight-band snapshot imager operating over the range 400 nm $\leq \lambda \leq$ 700 nm

Referring back to Section 5.2, regarding VIS-IRIS smear, the following figures highlight the reduction in image degradation from achromatisation of prisms. Figure 5-103 is the same geometric analysis as Figure 5-91 and clearly shows the improvement with respect to the latter. Figure 5-104 and Figure 5-105 are similarly the corresponding spot

diagrams for Figure 5-89 and Figure 5-90 respectively. Recall that the maximum smear varied from around 14 to 55 pixels between the sub-images for Vis-IRIS, given a nominal 4.4 μm pixel pitch.

ACHRO-IRIS exhibits a decreased maximum smear from 2.7 to 6.4 pixels for the eight sub-images, which is a factor reduction of between five and nine respectively. These bounds on smear are for the indicative range of 400nm to 700nm. Each sub-image will actually exhibit lesser smear, dependent upon the wavebands selected. Assuming the presence of only one large side-lobe within the STCs, the smear could potentially be reduced further by also using mosaic filters as given in Section 5.3 previously.

IMAGE DIAGRAM

8-BAND VISIBLE IRIS FOR INFINITY 2-2M
THU APR 2 2009
SCALE BAR IS 0.7000 MILLIMETERS.
FIELD POSITION: 0.0000, 0.0000 DEG
EFFICIENCY: 100.000%, TOTAL POWER: 1.000E+000 WATTS
SURFACE: 61

VISIBLE IRIS ACHROMATIC.ZMX
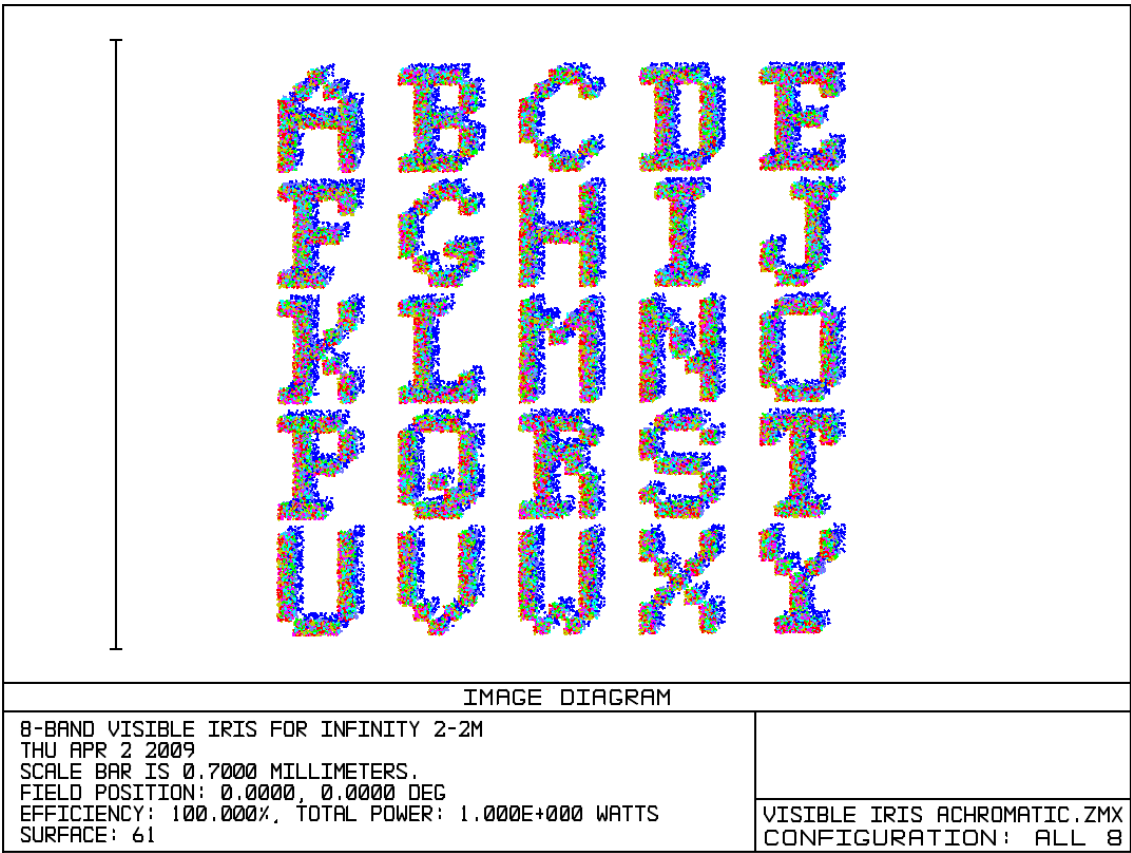CONFIGURATION: ALL 8

Figure 5-103: Geometric image analysis at the focal plane, indicating reduced impact of CVSA
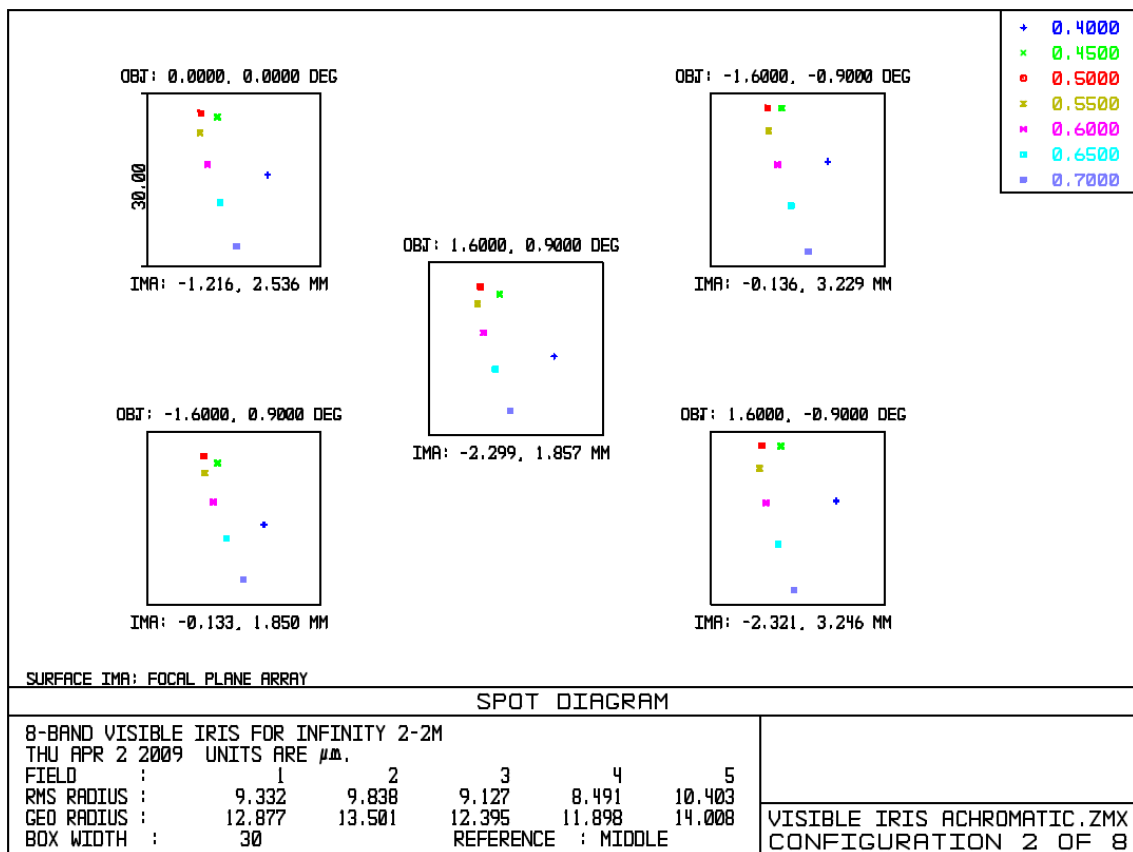
Figure 5-104: Maximal smear expected, with 14 µm geometric and 10 µm RMS radial extent
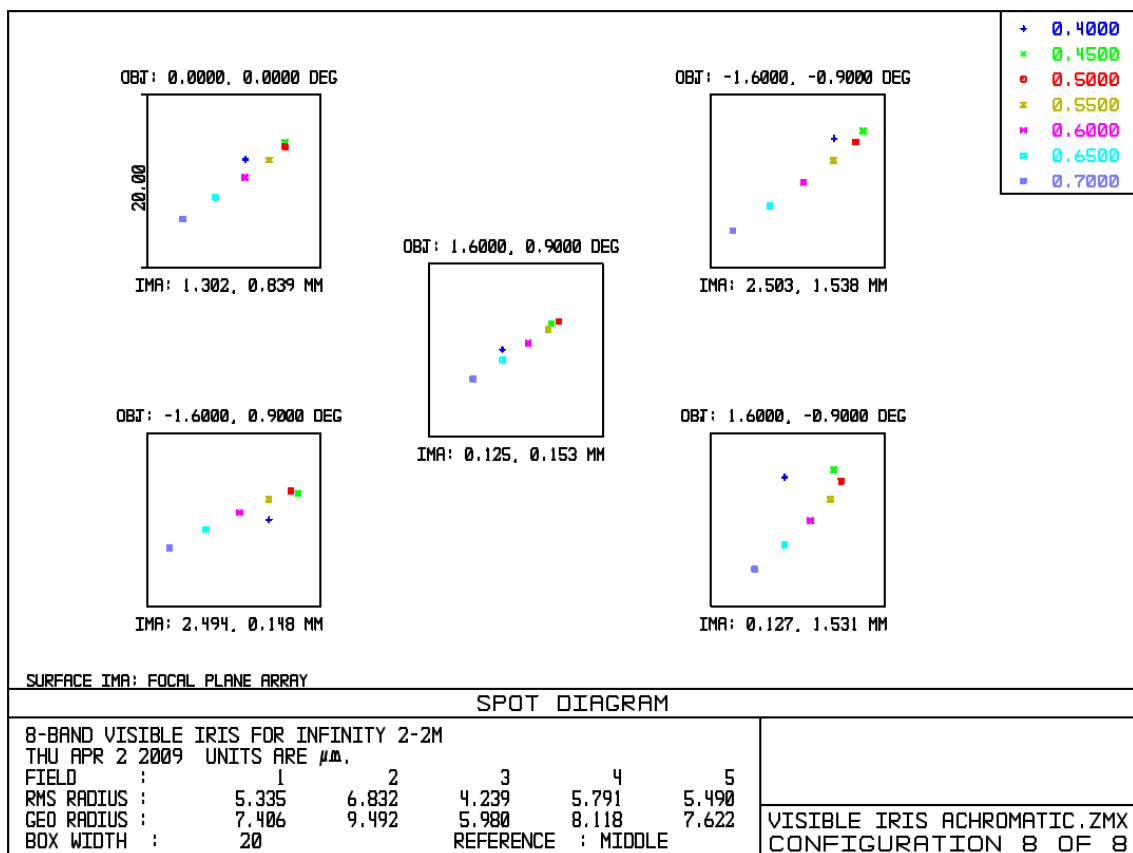

Figure 5-105: Minimal smear expected, with 6 µm geometric and 4 µm RMS radial extent

5.9 Achromatisation of N-IRIS Prisms

The application of achromatic prisms to N-IRIS was considered in a design study, which also factored in an extension in the operating range to 2.5 µm. This increase in wavelength range was to be achieved by a direct substitute of the *XenICs* InGaAs camera with its HgCdTe counterpart also from *XenICs*. The proposed camera features exactly the same FPA size as the current detector, along with an unchanged pixel pitch. Figure 5-106 is the normalized spectral response for a generic HgCdTe array [74], since detailed data from the supplier was not forthcoming. The upgraded SWIR lenses were designed to operate up to 3 µm, which would remove the need for new lenses.

Although the detector could operate towards 800 nm in wavelength, the range was curtailed at 1.4 µm due to two factors. The spectral response below this point was under the arbitrary chosen threshold of 50% response for FPA efficiency. Another factor was the presence of H_2O absorption bands below 1.4 µm as shown in Figure 5-107, which combines with the diminishing FPA response to reduce contrast.
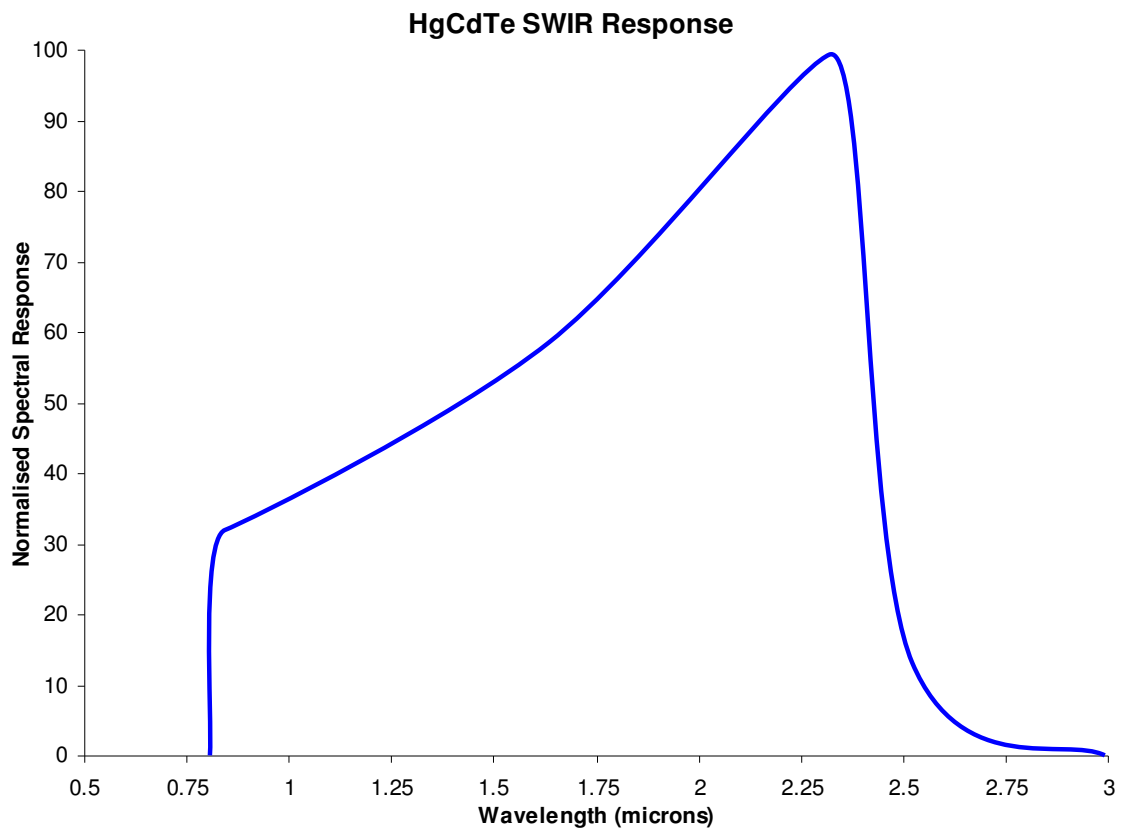

Figure 5-106: Normalised spectral response for generic 320×256 pixel HgCdTe arrays at T=175K [74]
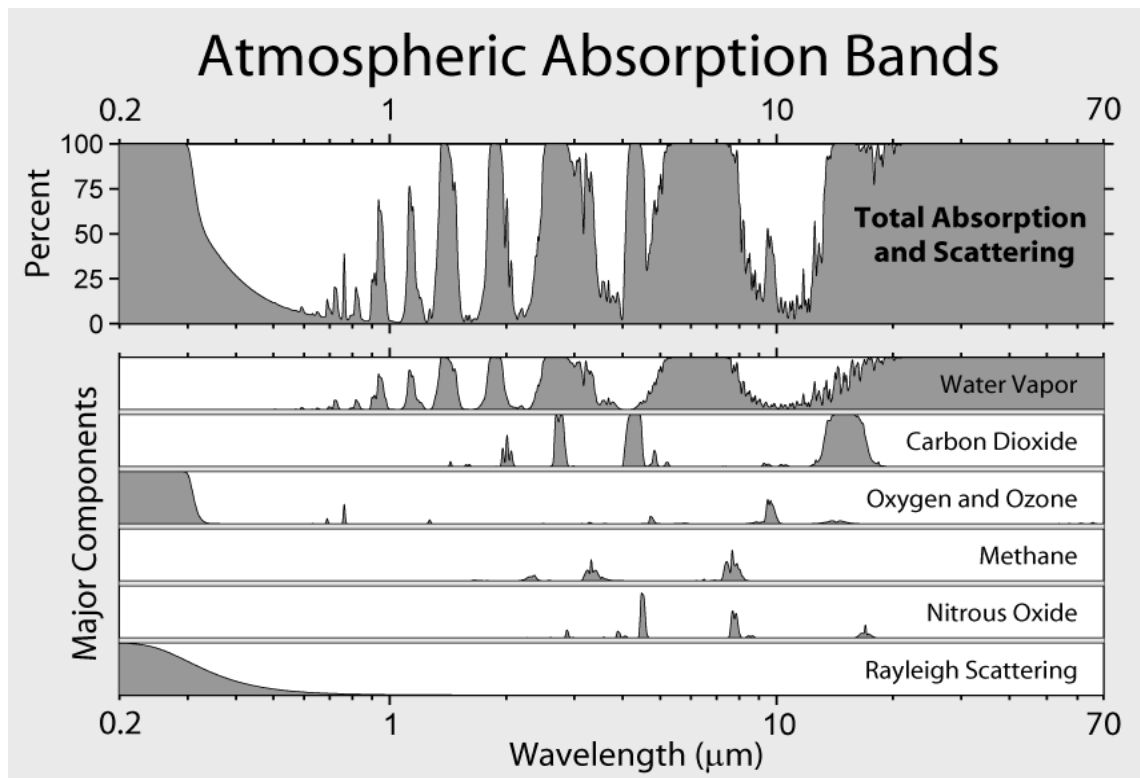
Figure 5-107: Absorption and scattering through one standard atmosphere to sea level [75]

The absorption region and falling FPA response below 1.4 µm suggested limiting N-IRIS to this point, so that spectral resolution could be increased in the remainder to 2.5 µm with the same number of passbands. Consideration of atmospheric effects was prompted by suggestions regarding possible field trials onboard airborne platforms. The N-IRIS at the time of writing was aimed at proof-of-concept and validation of the optical design. Using the same steps as in the design of ACHRO-IRIS, the pairing of BaB_2O_4 and YVO_4 was found to the most suitable for the range of 1.4 µm to 2.5 µm. Using the same birefringent materials as ACHRO-IRIS would also help to reduce costs.

The search within the 6D angle-space to determine the most appropriate angles for the three achromatic pairs was initially troublesome. Two solution sets were discovered for the six prism angles, each of which would satisfy the needed sub-image FPA splitting. In other words, two local minima lay relatively nearby to each other on the constrained search path. Recall that three angles are constrained by three other angles, in order to achieve the necessary net splitting between prism pairs. This simplifies a continuum search within a 6D volume of possible angles towards what can be considered as a constrained search for non-global minima.

The problem discovered was that the returned solution would oscillate between or orbit about two local minima, but never rest or converge upon one solution entirely. Each set

of optimal angles to reduce dispersion lay marginally outside the constrained search path, which ensures that pairs of angle yield the required nominal splitting. Upon attempting to converge to either solution, the constraint upon three angles would block further movement and force the search towards the other local minima.

Manual intervention was needed to successfully terminate the search, consider each solution and select the one with the lowest overall smear. Table 5-12 and Table 5-13 relate the optimal angles for each of the two solutions, in the same layout as for ACHRO-IRIS previously. Figure 5-108 to Figure 5-110 are the corresponding spot diagrams for the minimal expected dispersion from each solution, along with the baseline case for objective comparison. The first solution can be observed to yield the lowest intra-pixel smear, which is around 35% smaller than the second solution and about 75% less than the baseline respectively. These results conclude that the achromatisation of Wollaston prisms is a relatively simple and effective method of reducing CVSA. It is not mutually exclusive to the previously solutions given in Section 5.3 and may synergise with them.

Achromatic Prism	Prism Material	Wedge Angle β	Nominal Splitting $\theta(\beta)$	Net Splitting $\theta(\beta_1,\beta_2)$
Splitter Prism 1a	β-BaB$_2$O$_4$	17.0°	4.15°	7.91°
Compensator 1b	YVO$_4$	-9.5°	2.27°	
Splitter Prism 2a	β-BaB$_2$O$_4$	18.0°	4.41°	9.88°
Compensator 2b	YVO$_4$	-14.3°	3.46°	
Splitter Prism 3a	β-BaB$_2$O$_4$	12.0°	2.89°	4.95°
Compensator 3b	YVO$_4$	-5.5°	1.31°	

Table 5-12: 1ST SOLUTION – Wedge angles β, nominal splitting angles $\theta(\beta)$ for single Wollaston prisms at 1.95 μm, and overall net-splitting angle $\theta(\beta_1,\beta_2)$ for each achromatic prism pair within an eight-band snapshot imager operating over the range 1.4 μm $\leq \lambda \leq$ 2.5 μm

Achromatic Prism	Prism Material	Wedge Angle β	Nominal Splitting $\theta(\beta)$	Net Splitting $\theta(\beta_1,\beta_2)$
Splitter Prism 1a	β-BaB$_2$O$_4$	17.0°	4.15°	7.91°
Compensator 1b	YVO$_4$	-9.5°	2.27°	
Splitter Prism 2a	β-BaB$_2$O$_4$	24.5°	6.05°	9.88°
Compensator 2b	YVO$_4$	-10.1°	2.37°	
Splitter Prism 3a	β-BaB$_2$O$_4$	10.0°	2.34°	4.95°
Compensator 3b	YVO$_4$	-6.6°	1.54°	

Table 5-13: 2ND SOLUTION – Wedge angles β, nominal splitting angles $\theta(\beta)$ for single Wollaston prisms at 1.95 μm, and overall net-splitting angle $\theta(\beta_1,\beta_2)$ for each achromatic prism pair within an eight-band snapshot imager operating over the range 1.4 μm ≤ λ ≤ 2.5 μm
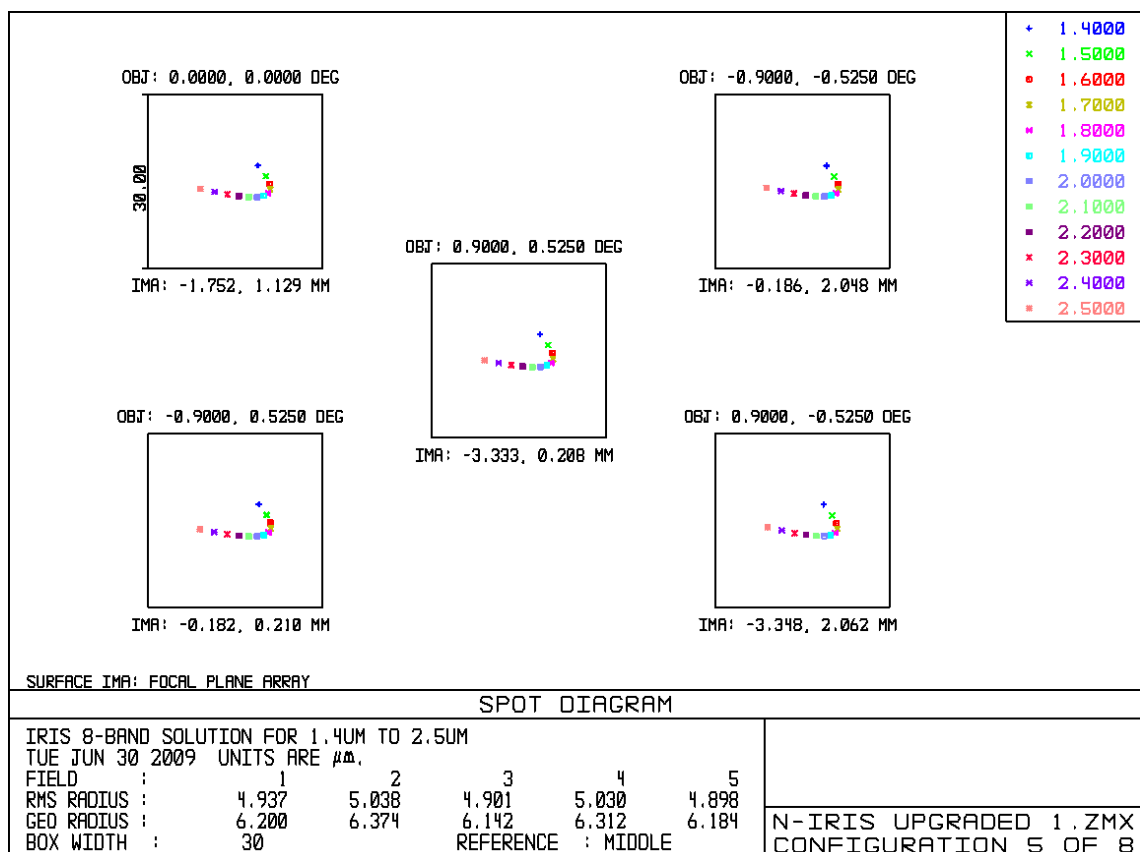

Figure 5-108: Minimal smear from first solution, with 6μm geometric and 5μm RMS radial extent
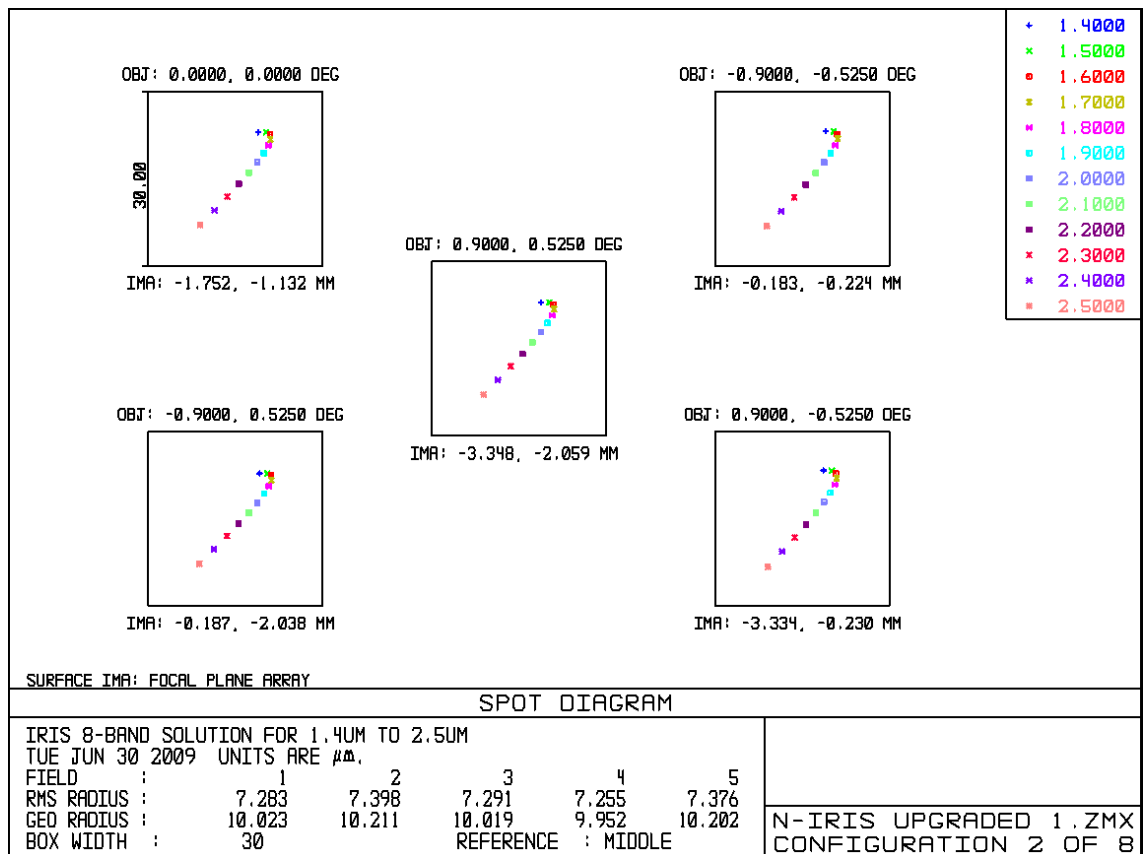
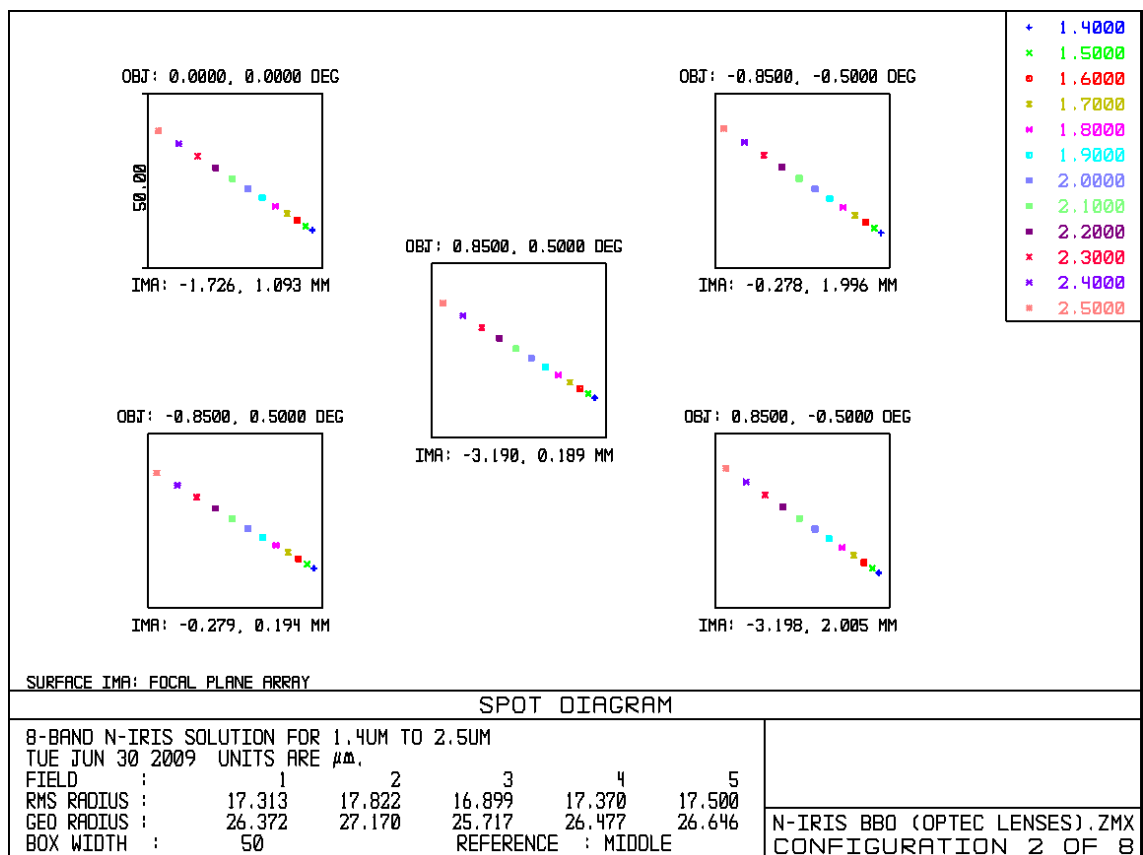**Figure 5-109:** Minimal smear from second solution, with 10µm geometric and 7µm RMS radial extent

Figure 5-110: Minimal smear with no achromatic prisms, with 27µm geometric and 17µm RMS extent

5.10 Future Areas for Achromatisation Work

At the time of writing, the complete implementation of achromatic prisms was only a design exercise due to the costs involved. The concepts within the preceding section are however an excellent opportunity for a follow-up project. There exists potential for advancing the design further into the infrared wavelengths and for non-defence IRIS applications, such as retinal imaging and diagnosis of epidermal cancers. Certain areas of microscopy and laser physics could potentially benefit from a symmetric polarising beamsplitter, with a relatively high extinction ratio that exhibits reduced variation with input wavelength. Synergies would be realised whereby this development contributes to the wider field of photonics. It is suggested here that triplet achromatic prisms (and higher orders) are feasible for IRIS sensors and other dispersion-sensitive applications or imaging systems.

CONCLUSION – The approximately co-linear polarizing beamsplitting of Wollaston prisms has led to their widespread use in areas such as imaging polarimetry, optical instrumentation and laser systems. Their CVSA can however introduce detrimental effects such as the spectral blurring of broadband images. The achromatisation of Wollaston prisms to reduce this angular dispersion was described in this Chapter within the context of current solutions. The analytical theory was presented with an example application where a six-fold reduction in dispersion was achieved for wavelengths in the region 400nm to 1.7μm, although the principle is generally applicable from ultraviolet to thermal infrared wavelengths. Experimental proof of concept was demonstrated and spectral dispersion of extended images recorded through cascaded Wollaston prisms for IRIS was shown to be reduced by nearly an order of magnitude.

Chapter 6:
Conclusions and Future Opportunities

Recalling the seven suggested requirements in Chapter One to enable SWIR snapshot HSI for defence applications such as anomaly detection, it has been shown in this thesis that N-IRIS can optimally meet these requirements with respect to the alternatives considered in Chapter Two. The N-IRIS sensor builds upon previous efforts, enabling a new method of snapshot HSI in the SWIR region that was not demonstrated previously.

1) Passive and snapshot HSI without any spectral or spatial scanning

2) Operation beyond visual wavelengths into the IR spectrum with $1\mu m \leq \lambda \leq 2\ \mu m$

3) Maximise optical transmission and SNR over the entire waveband of operation

4) Compact size, low mass and power-efficient with respect to alternatives

5) Static operation without any moving parts or elements sensitive to vibration

6) Minimise processing overhead and resource requirements to extract hypercubes

7) Raw imagery to be recognisable and interpretable by an operator at video rates

Chapter Three outlined the design process and choices made for N-IRIS, including the selection of crystalline quartz for the waveplates and β-BaB$_2$O$_4$ for the prisms. Optical ray tracing was used to predict certain performance aspects, firstly with ideal lenses and secondly with the provided telecom lenses. Basic MTF testing and spectral waveband measurements were carried out for the N-IRIS initial prototype. Upgraded lenses were then made available and subsequently integrated into N-IRIS, followed by further basic testing to verify the improvement in the image quality of the finalised N-IRIS prototype.

Necessary and sufficient experiments to provide the proof-of-concept of SWIR snapshot HSI for N-IRIS were documented in Chapter Four. Issues of sub-image extraction and co-registration were considered, with resolution limitations being identified as a critical factor in successfully generating a hypercube. A potential solution for co-registration using dewarping models is postulated and outlined as a future component of N-IRIS. USGS and NASA databases were exploited to provide a first-order study of N-IRIS spectral performance, with the result that intra-band sensitivity is important for material discrimination. This was further considered with an ANOVA experiment that disproved the null hypothesis that "N-IRIS cannot provide any additional spectral information beyond its panchromatic counterpart".

The chromatic variation in splitting angle (CVSA) of Wollaston prisms degrades image quality, especially for the low-cost VIS-IRIS demonstrator. This problem is considered in Chapter Five and can be generalised to broadband applications that exploit the polarising beamsplitting of Wollaston prisms. To formulate a novel solution in the form of achromatised prisms, analytical theory was presented alongside the choice of β-BaB_2O_4 and YVO_4 as the optimal material pairing for N-IRIS. The optimisation and modelling of a proof-of-concept achromatic prism was followed by the experimental confirmation of a predicted six-fold reduction in dispersion. This was followed by the design and optimisation of three achromatised prisms for N-IRIS, which required a search in 6D angular space, to determine the optimal six prism angles. Optical ray tracing demonstrated an order-of-magnitude improvement in FPA blurring.

Future opportunities to develop N-IRIS include integrating a full set of achromatised prisms to improve image quality, alongside an upgrade in FPA resolution to address the challenge of hypercube co-registration. Fully bespoke lenses with disclosed prescriptions will enable the comprehensive ray tracing of N-IRIS, without relying upon COTS lenses for which optical prescriptions are not available. Material discrimination capability can be improved by a design study and subsequent upgrade to sixteen wavebands for increased spectral resolution. Any potential improvement can be further augmented by optimising the waveband selection for a specific application requirement.

Medium-term research includes removing the front polariser such that dual polarimetric and spectral snapshot data can be captured. The concurrent capture of spatial, temporal, polarimetric and spectral information may offer significant potential for discrimination of highly camouflaged or obscured targets of interest. Longer-term objectives include operation in the mid-wave IR region, although suitable birefringent materials, cooling requirements and reduction of stray radiation will require new design considerations.

Nonetheless, N-IRIS has demonstrated SWIR snapshot HSI and has disproved the null hypothesis that "N-IRIS cannot provide any additional spectral information beyond its panchromatic counterpart". The invention of achromatised Wollaston prisms for highly symmetric beamsplitting can potentially benefit optical applications beyond IRIS, such as imaging polarimetry, optical instrumentation and laser systems.

References and Bibliography

[1] **Gerald Wong**, Hyperspectral Imaging, Nexus News: *Institute of Physics*, autumn 2nd edition, featured article **#4**, pages 27-30 (December 2009)

[2] **Randall B Smith**, Introduction to Hyperspectral Imaging, *and references therein*, MicroImages Inc (July 2006)

[3] **Rick S. Blum** and **Zheng Liu**, Multi-Sensor Image Fusion and Applications, CRC Francis & Taylor Group, page 330 (July 2005)

[4] **Michael T Eismann** *et al*, Target Detection in Desert Backgrounds: Infrared Hyperspectral Measurements and Analysis, *Proceedings of SPIE*, Volume 2561, pages 80-87 (1995)

[5] **G Koh** and **JR Ballad**, Disturbed Soil Signatures for Mine Detection, *US Army Engineer Research and Development Centre*, document ADA432261 (Dec 2004)

[6] **J Cederquist** *et al*, Infrared Multispectral Target and Background Measurements, *IRIS Speciality Group Meeting on Targets, Background and Discrimination* (Feb 1994)

[7] **Roger L Roy** and **Shaye K Friesen**, Historical Uses of Antipersonnel Landmines: Impact on Land Force Operations, *Directorate Land Strategic Concepts*, Department of National Defence, Canada (October 1999)

[8] **Jacqueline MacDonald** *et al*, Alternatives for Landmine Detection, *RAND Corporation*, ISBN 0833033018 (25th May 2003)

[9] **James Trevelyan**, Demining Research, University of Western Australia (2005)

[10] **A Ascherio** *et al*, Deaths and Injuries caused by Landmines in Mozambique, *The Lancet*, Volume 346, Issue 8977, pages 721 – 724 (September 1995)

[11] **N Andersson**, **CP Da Sousa** and **S Paredes**, Social Cost of Landmines in Four Countries, *British Medical Journal*, Volume 311, Issue 718 (September 1995)

[12] **United Nations Mine Action Service**, Mine Action Standards*, United Nations* (19th March 2007)

[13] **Bob French**, The Business of Landmine Clearing, *Economics of Peace and Security Journal*, Volume 1, Issue 2, pages 54 – 57 (June 2006)

[14] **A Mahmoud** and **H Farouk**, Efficient Detection and Classification Method for Landmine Types Based on IR Images Using Neural Networks, *International Journal of Geology*, Volume 10, Issue 4, pages 91 – 95 (2010)

[15] **USAF** and **US Army**, Weather Support for Army Tactical Operations, *Field Manual*, Reference FM 34-81/AFM 105-4 (31st August 1989)

[16] **John R Jensen**, Remote Sensing of the Environment: An Earth Resource Perspective, *2nd Edition, Prentice Hall,* ISBN 0131889508 (21st May 2006)

[17] **AG Huizing** *et al*, Compact Scalable Multifunction RF Payload for UAVs with FMCW Radar and ESM Functionality, *RADAR International Conference* (Oct 2009)

[18] **Frank Pinkney** *et al*, UAV Communications Payload Development, *MILCON 97 Proceedings*, Volume 1, pages 403-407 (November 1997)

[19] **Gerald Wong**, Low-Cost Snapshot Hyperspectral Imaging with the N-IRIS Sensor, *presentation*, *5th* Annual PGR Conference, Heriot-Watt University (June 2010)

[20] **Gerald Wong**, **Andrew R Harvey**, **Roger Pilkington** and **Rick Rickman**, Real-Time Hyperspectral Imaging in the SWIR Band, *oral slide presentation*, Institute of Physics *Photon-10* conference, University of Southampton (August 2010)

[21] **Gerald Wong**, **AR Harvey**, **Roger Pilkington** and **Rick Rickman**, Real-Time SWIR Hyperspectral Imaging with Polarimetric Capability, *Proceedings of SPIE*, volume **7812**, paper 781204 (August 2010)

[22] **Gerald Wong**, **Roger Pilkington** and **A R Harvey**, Achromatization of Wollaston polarizing beam splitters, *Optics Letters*, volume 36:8, pages 1332 – 1334 (April 2011)

[23] **Gerald Wong**, **Andrew R Harvey** and **Roger Pilkington**, Achromatic Wollaston Prisms for Snapshot Multispectral Imaging, *oral presentation*, IoP *Spectral Imaging* meeting, *Photonex-10* conference, Telford International Centre (November 2010)

[24] **Fabrizio Vagni**, Survey of Hyperspectral & Multispectral Imaging Technologies, *Technical Report*, NATO Research and Technology, ISBN 9283700715 (May 2007)

[25] **Alexandre Y Fong** and **Elliot Wachman**, Hyperspectral Imaging for the Life Sciences, *Biophotonics International*, Volume 15, Num #3, pages 38-41 (March 2008)

[26] **Nahum Gat**, Imaging Spectroscopy Using Tuneable Filters, *Proceedings of SPIE*, Volume 4056, pages 50-64 (2000)

[27] **Chris L Hart** and **William J Slough,** Review of Hyperspectral Imagers and Comparison with Respect to Real-Time Processing, *Proceedings of SPIE*, Volume 3389, pages 139-149 (1998)

[28] **Mauri Aikio**, Hyperspectral Prism-Grating-Prism Imaging Spectrograph, *Doctor of Technology dissertation*, University of Oulu and VTT Electronics (June 2001)

[29] **Michael Descour** and **Eustace Dereniak**, Non-Scanning No-Moving-Parts Imaging Spectrometer, *Proceedings of SPIE*, Volume 2480, pages 48-64 (1995)

[30] **William Johnson** *et al*, All-Reflective Snapshot Hyperspectral Imager for Ultraviolet and Infrared Applications, *Optics Letters*, Volume 30, Number 12, pages 1464-1466 (June 2005)

[31] **William Johnson** *et al*, Spatial-Spectral Modulating Snapshot Hyperspectral Imager, *Applied Optics*, Volume 45, Number 9, pages 1898-1908 (March 2006)

[32] **William Johnson** *et al*, Snapshot Hyperspectral Imaging in Ophthalmology, *Journal of Biomedical Optics*, Volume 12, Number 1, Article 014036 (February 2007)

[33] **CE Volin** *et al*, Demonstration of a MWIR High-Speed Non-Scanning Imaging Spectrometer, *Proceedings of SPIE*, Volume 3718, pages 480-489 (1999)

[34] **SITIS Information System**, Hyperspectral/Multispectral Imaging for Transient Events, *Research Project Details*, Program SBIR, Topic MDA05-004, US DoD (2007)

[35] **Eustace Dereniak** and **James George**, Visible Spectrometer Measurements of the PAC III Intercept of Hera at WSMR on 31-Mar-2001, *Final Progress Report* ADA415180, Arizona University and Space Missile Defence Command (March 2001)

[36] **Latsavongsakda Sethaphong**, Large Format CTIS in Real Time, *Masters MSc Thesis*, Graduate School of Vanderbilt University (May 2008)

[37] **B Ford** *et al*, Large-Image-Format Computed Tomography Imaging Spectrometer for Fluorescence Microscopy, *Optics Express*, Volume 9, pages 444-453 (2001)

[38] **Harvey C Schau**, Field Multiplexed Dispersive Imaging Spectrometer, *United States Patent 7092088* (15th August 2006) – International Reference WO/2005/015140

[39] **ME Gehm** *et al*, Single-Shot Compressive Spectral Imaging with Dual-Disperser Architecture, Optics Express, Volume 15, Number 21, pages 14013-14027 (Oct 2007)

[40] **A Wagadarikar** *et al*, Single Disperser Design for Coded Aperture Snapshot Spectral Imaging, *Applied Optics*, Volume 47, Number 10, pages B44-51 (April 2008)

[41] **Leah Goldsmith**, Coded Aperture Snapshot Spectral Imaging (CASSI), *website* at http://www.disp.duke.edu/projects/CASSI/index.ptml (2nd June 2009)

[42] **Matthias Tecza** *et al*, An Image Slicer-Based Integral-Field Spectrograph for EPICS, *Proceedings of SPIE*, Volume 7735, paper 77357B (2010)

[43] **Neelam Gupta**, **PR Ashe** and **Songsheng Tan**, Miniature Snapshot Multispectral Imager, *Optical Engineering*, **50**:3, paper 033203 (March 2011)

[44] **Neelam Gupta**, **Philip Ashe** and **Songsheng Tan**, Development of a Miniature Snapshot Multispectral Imager, *Army Research Laboratory*, technical report ARL-TR-5320 (September 2010)

[45] **DW Fletcher-Holmes** and **AR Harvey**, The Feasibility of an LWIR IRIS II System, Commercial report RM/02/9, Heriot-Watt University (February 2003)

[46] **Andrew R Harvey** *et al*, Spectral Imaging in a Snapshot, *Proceedings of SPIE*, Volume 5694, pages 110-119 (2005)

[47] **AR Harvey**, **DW Fletcher-Holmes** and **A Gorman**, Generalization of the Lyot Filter: Application to Snapshot Spectral Imaging, *Advanced Optical Imaging – EOS Meeting*, Imperial College London, (June/July 2005)

[48] **Andrew Harvey** and **David Fletcher-Holmes**, Imaging Apparatus, *International Patent* WO2004 005870 A1 (2004)

[49] **AR Harvey** *et al*, Imaging Spectrometry at Visible and Infrared Wavelengths using Image Replication, *Proceedings of SPIE*, Volume 5612, pages 190-198 (2004)

[50] **Gerald Wong**, Snapshot Hyperspectral Imaging and Practical Applications, Journal of Physics: *Conference Series*, volume **178**, paper 012048 (July 2009)

[51] **Alistair S Gorman**, Snapshot Spectral Imaging using Image Replication and Birefringent Interferometry, *PhD thesis*, Heriot-Watt University (October 2010)

[52] **AR Harvey** *et al*, Technology Options for Imaging Spectrometers, *Proceedings of SPIE*, Volume 4213, Number 13, pages 13-24 (2000)

[53] **Valentin Dmitriev** *et al***,** Handbook of Nonlinear Optical Crystals, *Third Edition*, Springer Science & Business Media, ISBN 3540653945 (July 1999)

[54] **Ian Hodgkinson** and **Qi-Hong Wu**, Birefringent Thin Films and Polarizing Elements, *World Scientific Publishing Company*, ISBN 9810229062 (February 1998)

[55] **Michael Bass** (*Editor*), Handbook of Optics: Volume Two, *Optical Society of America* and *McGraw-Hill Professional*, ISBN 0070479747 (September 1994)

[56] **David Nikogosyan**, Nonlinear Optical Crystals: Complete Survey, *First Edition*, Springer Science & Business Media, ISBN 0387220224 (February 2005)

[57] **DN Nikogosyan**, Beta Barium Borate (BBO), *Applied Physics A: Materials Science and Processing*, Volume 52, Number 6, pages 359-368 (June 1991)

[58] **K Kato**, Second-Harmonic Generation to 2048 Å in β-Ba2O4, *IEEE Journal of Quantum Electronics*, Volume 22, Issue 7, pages 1013-1014 (July 1986)

[59] **Technical Committee ISO/TC-42**, ISO 12233: Picture Resolution Measurement, *International Organisation for Standardisation* (31st August 2000)

[60] **Technical Committee ISO/TC-42**, ISO 16067: Spatial Resolution Measurement, *International Organisation for Standardisation* (21st October 2004)

[61] **Gerald Wong**, Spectral Imaging with N-IRIS: Optical Design & Spiral Upgrades, *oral presentation*, EngD Annual Conference, Heriot-Watt University (August 2009)

[62] **Alistair S Gorman**, Snapshot Spectral Imaging using Image Replication and Birefringent Interferometry, *PhD Thesis*, Heriot-Watt University (October 2010)

[63] **Patrick Maeda**, **Peter Catrysse** and **Brian Wandell**, Integrating Lens Design with Digital Camera Simulation, *Proceedings of SPIE*, Volume 5678, paper 48 (2005)

[64] **Roger N Clark**, USGS Digital Spectral Library, *Online database*, United States Geological Service, http://speclab.cr.usgs.gov/spectral-lib.html (September 2007)

[65] **AM Baldridge**, **SJ Hook**, **CI Grove** and **G Rivera**, The ASTER Spectral Library Version 2.0, *Remote Sensing of Environment*, Volume 113, pages 711-715 (2009)

[66] **Alan Grafen** and **Rosie Halls**, Chapter 1: Introduction to Analysis of Variance, *Modern Statistics for the Life Sciences*, Oxford University Press (2002)

[67] **Gerald Wong**, Anomaly Detection Rudiments for the Application of Hyperspectral Sensors in Aerospace Remote Sensing, Journal of Physics: *Conference Series*, volume **178**, paper 012051 (July 2009)

[68] **Prasanta Chandra Mahalanobis**, On the Generalized Distance in Statistics, *Proceedings of the National Institute of Science of India*, Vol 12, pages 49-55 (1936)

[69] **Heesung Kwon** and **Nasser M Nasrabadi**, Kernel RX-Algorithm: A Nonlinear Anomaly Detector for Hyperspectral Imagery, *IEEE Transactions on Geoscience and Remote Sensing*, Volume 43, Number 2 (February 2005)

[70] **M Françon** and **S Mallick**; Appendix A: Angular splitting Between E and O Rays Produced by a Wollaston Prism, *Polarisation Interferometry*, Wiley-Interscience, 147–148 (1971)

[71] **MC Simon**; Wollaston Prism with Large Split Angle, *Applied Optics*, **25**:3, pages 369-376 (1986)

[72] **EN Ebizuka**, **H Yokota**, **F Kajino**, **KS Kawabata**, **M Iye**, **S Sato**, Novel Direct Vision Prism and Wollaston Prism Assembly for Diffraction Limit Applications, *Proceedings of SPIE*, **7018**, 70184S (2008)

[73] **MC Simon**, Ray Tracing Formulas for Monoaxial Optical Components, *Applied Optics*, Volume **22**:2, 354–360 (1983)

[74] **Philippe Chorier** and **Philippe M Tribolet**, High-Performance HgCdTe SWIR Detectors for Hyperspectral Instruments, *Proceedings of SPIE*, Volume 4540, pages 328-341 (Sept 2001)

[75] **Robert A Rohde**, *GNU Free Documentation Licence*, Version 1.3 (11th June 2007)